Dynamics and stability of a thin liquid lithium flow within a tokamak divertor

Davin Lunz
Mansfield College
University of Oxford

A thesis submitted for the degree of

Doctor of Philosophy

Trinity 2019

For my family

Abstract

Nuclear fusion has the potential to be the reliable, clean, safe, and fuel-abundant source of baseload power necessary to meet the ever-increasing global energy demand. One technological roadblock is dealing with the heat load that escapes the core confinement region and must be exhausted within the vessel on a component known as the divertor, without causing it excessive damage. A thin liquid metal film covering a solid divertor substrate is one promising direction that may be capable of sustaining the predicted heat loads. It is therefore of great scientific and industrial interest to study the dynamics and stability of a thin liquid metal film within a tokamak (toroidal plasma confinement device).

In this thesis we develop a model of the liquid-metal divertor. We derive the equations governing the flow of a liquid metal on a substrate in the presence of a strong magnetic field. Focusing on the asymptotic limit in which the film is thin compared to its length, and the induced magnetic fields are relatively weak, we derive a generalised thin-film equation governing the film thickness and study the stability of such flows in configurations not previously analysed.

We extend the model to capture the transfer of heat and momentum to the fluid film as the core plasma is exhausted onto the divertor. This allows us to study how the free surface of the fluid is displaced, and whether it may be maintained in a sufficiently stable state. In particular, we analyse the effect on the liquid film of an oscillating plasma jet, and determine how operating parameters may be tuned to minimise the resulting free-surface displacements. We also show how the cooling channels within the divertor may be designed so as to minimise displacements.

Acknowledgements

I would like to sincerely thank Prof. Peter D. Howell for the deep insight and sagely direction he unfailingly brought to this project. I count myself truly lucky to have been able to work with him, and learn from him, during these last three years.

This project would not have been possible without the patient help and advice of Dr. Peter F. Buxton from Tokamak Energy. I would like to thank him for his consistent enthusiasm, engagement, and willingness to explain and re-explain the basics of plasma physics.

This project has benefited from several fruitful discussions with Prof. Julian C. R. Hunt, Prof. John R. Ockendon, and Dr. David J. Allwright, whom I also wish to thank.

I would like to thank friends and family who have supported and encouraged me along the windy way. To the Lic, who has been kind, supportive, and provided much food for thought, I owe many thanks. To my parents most of all, who have been eternally generous in supporting my journey, I am so appreciative. Ten times the writer could not capture one tenth my gratitude.

Contents

List of Figures

List of Tables

Chapter 1

Introduction

The world's population is expected to reach almost 10 billion by 2050, and to further urbanise [203, 204]. The accompanying increase in energy demand must be met with environmentally sustainable forms of production. At present, some 85% of the world's energy comes from fossil fuels [32]. Fossil fuel supplies are diminishing and are not environmentally sustainable. Burning fossil fuels leads to the greenhouse effect and acidic pollution, damaging the environment. Moreover, there are often severe geopolitical instabilities in areas rich in fossil fuels. All of these reasons demand alternative energy sources.

Nuclear fission is one such alternative that produces no carbon emissions; however its growth could be curtailed by issues of public and political acceptability due to the enriched fuel required and the waste products. Renewable energy sources, including solar, wind, and hydro, are reliant on environmental conditions, are subject to the technological challenges of energy storage, and often require vast, vacant, and distant areas of land or sea [124]. Renewables must play a key role in future energy grids; however nuclear fusion has the potential to solve many of the present issues and constraints.

Nuclear reactions release about one million times more energy per mass of fuel than chemical reactions such as the burning of coal, oil or gas [124, 156]. Moreover, fusion offers a secure, long-term source of energy, with zero carbon emissions and no long-lived radioactive waste. The fusion reaction itself produces no waste directly, although the high-energy neutrons that are released make the vessel radioactive. Suitable choice of construction materials allows for a low neutron activation, giving the irradiated components short half-lives and making them recyclable within decades. The fusion process is inherently much safer than fission since it is thermally self-limiting, so no chain reaction can occur, and no reactor meltdown or far-reaching disaster is possible. There is an almost unlimited supply of fuel, as we will describe, with no need for enriched material.

There are many potential nuclear fuels that could be fused to produce energy (see [84]). To choose from among the options, there are various criteria by which we compare reactant fuels, including the amount of energy released per reaction, the conditions required to bring about the reaction, and the abundance of fuels [70]. Deuterium–Tritium (D–T) is a popular focus at this stage of fusion development, since it achieves the highest reactivity at the lowest temperature and releases a lot of energy (although not the most). Both of these reactants are isotopes of hydrogen: deuterium contains one neutron in its nucleus and is stable, while tritium has two neutrons and is unstable, with a half-life of approximately 12.3 years. Deuterium is naturally abundant in seawater, affording easy extraction. On the other hand, since tritium is unstable it is much more rare. However it can be bred during a fusion reaction by allowing the high-energy neutrons released to react with lithium atoms. There are sufficient stores of lithium in the oceans to last more than one million years [124].

There are various criteria required for a fusion reaction to be feasible. For two reactant particles to fuse, their nuclei must obtain sufficient kinetic energy to overcome their electric repulsion. If they then come close enough to one another for the attractive nuclear strong force to dominate the Coulomb repulsion, the particles then fuse. For a typical D–T reaction, a temperature on the order of 10^8 K is required. At this temperature the fuel has ionised to form a plasma – a state of matter where negatively charged electrons move independently from the positively charged ions, as these are no longer bound within the atom. The temperature of an entire plasma expresses the average temperature of all the ions comprising the plasma, whose individual kinetic energies lie in a Maxwell-Boltzmann distribution [70]. Thus the critical ignition temperature, whereby significant fusion reactions occur within the plasma, is on the same order of magnitude but somewhat lower than the critical Coulomb barrier, as fusion will take place between ions at the high-energy tail of the Maxwellian distribution. Moreover, for the reaction to be *self-sustaining*, Lawson's criterion [108] dictates that the ignition temperature must be maintained at high enough density for long enough time [98]. To obtain this critical density, the plasma must be confined. The temperature requirement rules out the possibility of solid-wall confinement, since the reactants would cool down in contact with a solid wall, and the wall itself would melt, losing its structure and leaking impurities

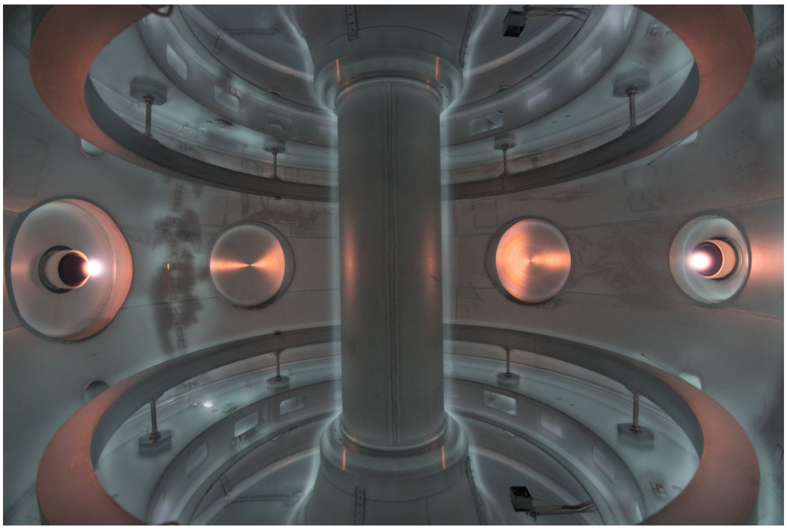

Figure 1.1: The inside of Tokamak Energy's spherical tokamak ST40. The central column and two poloidal coils are clearly visible, as well as circular ports around the vessel that are used for various diagnostics and particle injection.

into the plasma. However, the electromagnetic state of the plasma allows magnetic confinement. There are many different designs of vessels and magnetic fields (stellarators, tokamaks, etc. see figures 1.1 and 1.2), all attempting to stably confine a dense toroidal plasma.

Magnetically-confined fusion reactions have been achieved and are well established. The Joint European Torus (JET), for example, produced 16 MW of fusion power in 1997 [215]. The ultimate fusion goal, yet to be achieved, is to sustain a nuclear fusion reaction that produces more energy than it consumes. This would prove that engineered nuclear fusion is a viable source of energy. One of the main challenges in achieving a sustained reaction is having a sufficiently resilient vessel. The vessel needs to maintain its structural integrity under intense neutron bombardment from the nuclear reactions occurring in the plasma, and minimise impurities entering the plasma [119]. Much work is being done on what materials best satisfy all of these criteria, and how various treatments can enhance performance.

While confinement is important to attain critical densities for the fusion reaction to occur, the magnetic confinement of the plasma is not perfect, and transport across the edge of the confined region is inevitable [28, 99, 235]. As long as this loss of plasma is not too great, the leakage can actually be used to flush the plasma of impurities and nuclear by-products that accumulate in the core, which is vital for an operating reactor. These losses are compensated by injecting fuel directly back into

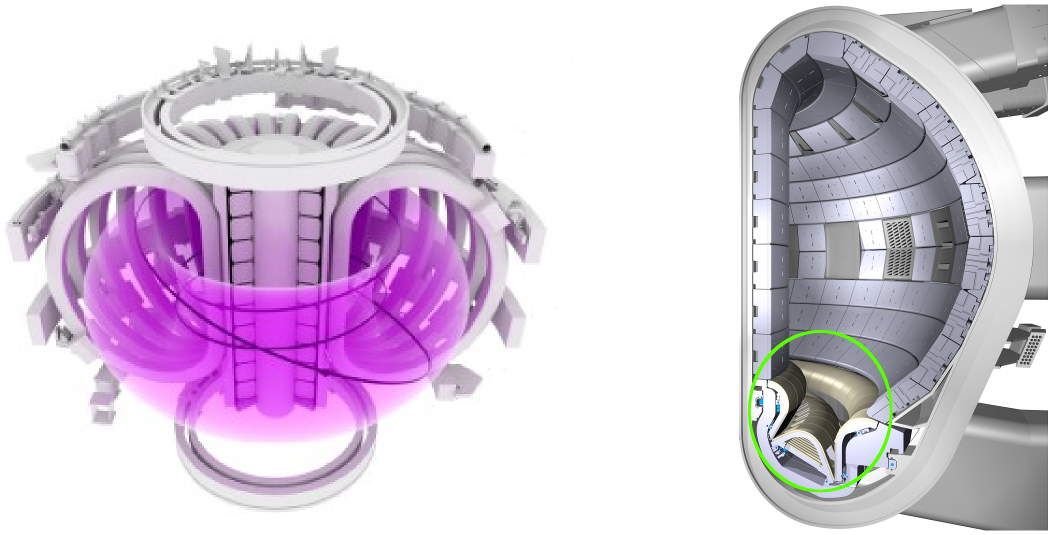

(a) (b)

Figure 1.2: (a) A schematic of the field coils in JET as well as the plasma in purple (image courtesy of EUROfusion, `http://www.euro-fusion.org/`). (b) A cross-section of the ITER vessel showing the blanket modules surrounding most of the vacuum region and covering the inner wall, and the divertor plates highlighted in green at the bottom (image courtesy of ITER Organization, `http://www.iter.org/`).

the core. The leaking particles remain at high temperatures, and must be diverted via the magnetic field to a region of the vessel that can absorb these immense thermal fluxes. This region is known as the divertor, and often comprises specially engineered solid plates designed to handle the thermal loads (see figure 1.2). While the solid divertor plates provide a solution for short-time fusion reactions, they suffer sufficient surface damage to cause concern that they will not suffice for a commercially viable reactor [91].

Currently, many tokamaks use cryopumps to help maintain plasma purity. A cryopump is typically a porous material cooled to 4 K, placed near the divertor with some shielding so that it does not directly encounter hot particles. When a relatively cool particle hits it, the particle imparts much of its kinetic energy to the cooled material, allowing van der Waals forces to dominate and causing it to stick to the plate. This transition of a gas particle in the vacuum to the solid state will be effective up to very low pressures matching the saturation pressures at 4 K. These pumps become saturated and require regenerating, whereby they are heated up and desorption causes the trapped particles to be liberated. They can then be cooled down again and reused. Clearly, this will not work in steady-state, and the divertor's ability to flush plasma impurities becomes even more crucial [38, 76].

An alternative to both solid divertor plates and cryopumps is to have liquid metal cover the plasma-facing surface [157]. This avoids the issues of melting and structural integrity since liquids are immune to surface damage, and any mass loss can be easily replenished. A liquid metal allows for effective heat dissipation, while protecting solid surfaces from overheating. A liquid metal would also be able to absorb discharges from the plasma, including impurities that are directed towards the divertor, thereby shielding the underlying materials. The liquid would be easier to extract and process, enabling an effective heat exhaust, fuel recycling and impurity filtering.

The performance of the divertor is crucial for the viability and success of the entire fusion enterprise [1, 216], and the ability to maintain a specified liquid metal thickness and velocity is crucial to the success of a free-surface liquid metal divertor. The expected difficulties in maintaining a stable free surface [57, 148] have led many fusion projects to pursue a capillary-porous system (CPS) [47, 64]. The behaviour is being explored intensively both theoretically and experimentally [10, 11, 44–46, 48, 123, 136, 143, 160, 234]. However, there is still experimental evidence that flow along a predominantly flat substrate can be achieved [52]. In this thesis we explore the dynamics of such a fully-developed, free-surface flow of liquid metal within a divertor, in the presence of a strong magnetic field. The behaviour of the liquid is governed by the coupling of fluid dynamics and electrodynamics, which has been thoroughly researched in the last 80 years.

1.1 Literature review

While various propositions, observations, and calculations pertaining to the motion of a conducting fluid in a magnetic field had been made earlier [20, 107, 137, 154, 167, 217], fundamental research in the field truly began with the pioneering work of Hartmann [73, 74]. The subsequent few decades served to establish the fundamental theory of magnetohydrodynamics (MHD). The significant contributions of Alfvén [4, 5], applying MHD to astrophysical regimes, shed light on star formation, behaviour and destruction, as well as stellar dust, auroras, and many other phenomena. In some stellar regimes, the plasma can exhibit anisotropies in the stress tensor, requiring extensions to the standard MHD formulation [19, 39]. Dynamo theory explaining geomagnetism has a well developed literature [97, 169].

Other important works include the books [169] and [179]. Industrial applications of MHD flows followed the theoretical development, and extended well beyond the scope of fusion. MHD has been routinely used in metallurgy to heat, pump, stir, stabilise, repel and levitate liquid metals [34, 35, 96, 131, 139, 150]. MHD has been successful in non-intrusively controlling solidification in crystal growth processes [106]. MHD pumps, generators, propulsion systems, and flow-meters have also been developed [92, 214] (and references within [214]).

Fusion-oriented research into liquid metal MHD flows has placed great emphasis on MHD flow through closed channels [150]. Hartmann first showed experimentally and analytically that MHD flow between two planes in a transverse magnetic field exhibits a near uniform velocity profile in the bulk, accompanied by boundary layers near the top and bottom [73], subsequently called Hartmann layers. Shercliff extended the model to include side walls and found an analytical solution in this rectangular geometry with insulating walls [177]. This work predicts the existence of boundary layers along the side walls, in which high-speed jets may develop [85]. Chang and Lundgren, and later on Hunt, extended the model to conducting duct walls [30, 85]. Many analytical results followed for various other geometries, wall conductivities and wall thicknesses [83, 178, 195–197]. It became clear that wall conductivity greatly influences the flow in affecting how current loops are closed and thus changing the current distribution throughout the flow. Free shear layers can be induced within the flow by changing wall conductivity (see [87] and references therein).

If the liquid metal is to be pumped through a complex geometry of closed ducts with bends, expansions and contractions, the MHD flow becomes fully 3D and significantly more complex [22, 23, 138, 150]. When the liquid metal acts as the primary coolant, it is generally expected that the flow rate must be higher. High-speed jets have been considered for this self-cooled regime [80, 227]. The retarding effect of the magnetic field makes pumping less efficient and may induce high mechanical stress if the liquid metal needs to be pumped at higher velocities. Ways to mitigate this problem have been explored [24, 194]. While the main focus has been on modelling a single closed channel, it was shown that coupling adjacent channels leads to current leakage and has global effects [14, 125] (and references within [14]).

Another important aspect of liquid metal coolants is the effectiveness of their heat extraction. The magnetic field may act to suppress turbulent motion [34, 59, 110, 112, 165, 178], promoting laminar flow and resulting in poor thermal mixing [60]. Various turbulence-inducing mechanisms have been assessed to induce mixing and thus improve heat transfer [188]. The effects of MHD on heat transfer have been explored both analytically [105, 226, 233] and numerically [186].

Important experimental work has served to validate the theoretical development in the field [151]. Free-surface flow has been part of this experimental portfolio since the beginning [8, 153, 161]. Theoretical free-surface MHD flow was modeled much later [56, 63, 144, 145, 147] (and references within [145]), along with numerical simulations of free-surface flow [57, 58, 62, 135, 149]. However, as we will point out in this thesis, much of this early work is incomplete and, in places, inconsistent. Thus there is great interest in extending what has been done with more comprehensive modelling.

Shercliff pioneered the study of thermoelectric magnetohydrodynamics (TEMHD) in channel flows [179–182], incorporating the thermoelectric effect into the MHD equations. Initially, this line of research found traction in the solidification literature with applications to crystal growth [94, 111, 140]. More recently, the fusion community have also modelled the influence of the thermoelectric effect and compared the theory with experiments [89, 90, 173, 224].

Hydrodynamic and magnetohydrodynamic stability as well as free-surface flows have a richly developed literature [29, 41, 207]. In particular, thin films of fluid and their stability are widely encountered in both the natural world and industrial processes, and have been studied extensively [33, 152, 158]. The existing literature provides a solid foundation for this thesis to develop and analyse a thin-film free-surface thermoelectric MHD model.

1.2 Thesis Outline

In this thesis we derive a model describing the dynamics of a fully-developed free-surface flow, allowing for a subsequent stability analysis. We perform a systematic derivation of the governing equations without assuming, *a priori*, a constant magnetic field or magnetic field gradient or a constant film thickness. We do not make a thin-wall assumption, but arrive at a similar boundary condition from the full governing equations. We include magnetic stresses exerted on the free-surface due to different magnetic permeabilities of the liquid metal and the surrounding free space. We do not at present model side walls in our channels, as has been done in some previous work. Our simplified 2D configuration makes many realistic extensions tractable. An analytical asymptotic treatment of these phenomena does not appear to have been carried out before.

In §2.1 we present the equations and boundary conditions governing the dynamics of a liquid metal in the presence of a strong magnetic field. In §§ 2.2 and 2.3 we consider separately the canonical cases of purely "toroidal" fields and purely "poloidal" fields, where the fields have components that are only orthogonal and tangential to the fluid motion, respectively. In both cases we use asymptotic analysis to simplify the MHD equations in the limit where the liquid film is thin compared to the length of the divertor substrate. We also leverage the physically relevant limit that the induced field is asymptotically smaller than the applied field, which allows us to obtain closed-form solutions in both cases.

In chapter 3 we consider unsteady solutions and their stability. In particular, we perform a comprehensive analysis of the stability of the flow in the presence of the toroidal field, where the literature appears most incomplete. We find that, while the flow is stable to the simplest family of perturbations, perturbations of high frequency for which inertia is important may be unstable. We quantify how the magnetic field acts to suppress these perturbations.

In chapter 4 we unite the poloidal and toroidal applied fields in an axisymmetric magnetic field with both components, and find that a flow must be driven also in the toroidal direction. Additionally, we extend the model to account for temperature via relevant thermal and thermoelectric effects, enabling the model to capture a crucial interaction between the plasma and the liquid metal layer.

In chapter 5 we further extend the model to incorporate the momentum transferred from the plasma to the liquid metal, allowing us to explore the effects of these dominant interactions between the core plasma and the flowing liquid metal. Of particular interest is the practical case where the incoming plasma is directed to oscillate up and down the liquid metal layer. We analyse the deflections this may induce in the free surface, and find that there are three canonical regimes depending on the frequency of the oscillations, each characterised by distinct deflection magnitudes.

Having seen that thermal effects influence the free-surface deflections, in chapter 6 we consider an optimal control problem, asking how we can best design the substrate cooling to minimise the free-surface deflections. We uncover a fascinating control structure that is not possible to engineer, and thus have to consider regularisations that are physically realisable.

Finally, in § 3.4 we summarise the findings of the thesis, and discuss directions for further study.

We note that the material in §§ 2.3 and 3.3 has been published in [122], and some of the material in chapter 5 has been published in [121].

1.3 Notation

Throughout this thesis, scalar values are typeset in a regular font, vectors, (in $\mathbb{R}^3$), are typeset in bold, and tensors (in $\mathbb{R}^{3\times3}$) are in bold with an overline. Examples of these three, respectively, are ρ, $\boldsymbol{B}$, and $\overline{\boldsymbol{m}}$. Dimensional quantities are denoted with an asterisk. For example, dimensional and dimensionless flow velocity vectors are denoted $\boldsymbol{u}^*$, and $\boldsymbol{u}$, respectively. Typical orders of magnitude are denoted with a calligraphic font style, so for example, the characteristic magnetic field strength is written $\mathscr{B}^*$.

To distinguish them from citations, parameter ranges are bookended by floor and ceiling parentheses, for example, a temperature range between 250 K and 700 K is denoted $\lfloor 250,\ 700 \rceil$ K. A scientific notation may also be adopted, for example, $\lfloor 2.5,\ 7.0 \rceil \times 10^2$ K.

Chapter 2

Gravity-Driven Thin-Film MHD Flows

In this chapter we develop the base model describing the flow of the liquid film coating the solid substrate in the divertor region. First, in § 2.1, we establish the governing equations that model the flow of a liquid metal in a magnetic field. In § 2.1.3 we write down a concrete formulation of the problem statement, applying the governing equations to each region of the divertor configuration. We then solve two distinct instances separately, distinguishing between two canonical applied field orientations. In §2.2 we take a poloidal applied field (tangential to the plane of fluid motion), while in § 2.3 we take a toroidal applied field (orthogonal to the plane of motion). In both cases we use asymptotic analysis to simplify the governing equations in the limit where the film is thin, and the induced field is much weaker than the applied field. We then solve the leading-order equations and discuss qualitative features of the flow and induced magnetic fields. Finally, in § 2.4 we compare the two cases and summarise our findings.

2.1 MHD equations and boundary conditions

To analyse the flow of a conducting fluid in the presence of electric and magnetic fields, we first outline the governing equations of motion, namely the magnetohydrodynamic (MHD) equations, as well as the appropriate boundary conditions.

2.1.1 Governing equations

Electrodynamics

We begin with Maxwell's equations governing the electrodynamic fields [128],

$$\boldsymbol{\nabla}^* \cdot \boldsymbol{D}^* = \varrho^*, \qquad \boldsymbol{\nabla}^* \times \boldsymbol{E}^* = -\frac{\partial \boldsymbol{B}^*}{\partial t^*}, \tag{2.1.1a,c}$$

$$\boldsymbol{\nabla}^* \cdot \boldsymbol{B}^* = 0, \qquad \boldsymbol{\nabla}^* \times \boldsymbol{H}^* = \boldsymbol{j}^* + \frac{\partial \boldsymbol{D}^*}{\partial t^*}, \tag{2.1.1b,d}$$

where $\boldsymbol{E}^*$ is the electric field, $\boldsymbol{D}^*$ is the displacement field, $\boldsymbol{B}^*$ is the magnetic field, $\boldsymbol{H}^*$ is the magnetising force, ϱ^* is the charge density, and $\boldsymbol{j}^*$ is the current density. We assume constant linear constitutive relations [68], whereby

$$\boldsymbol{H}^* = \frac{\boldsymbol{B}^*}{\mu^*}, \qquad \boldsymbol{D}^* = \varepsilon^* \boldsymbol{E}^*, \tag{2.1.2a,b}$$

where μ^* denotes magnetic permeability and ε^* electric permittivity. The magnetic permeability is also written as

$$\mu^* = \mu_0^* \left(1 + \chi\right), \tag{2.1.3}$$

where μ_0^* is the permeability of free space and χ is the magnetic susceptibility. Generally the materials of interest in this thesis are very slightly paramagnetic, so χ is typically small (see tables 2.2 and 2.3); however, in a strong magnetic field even this small deviation in the magnetic permeability may impact the system, as we will describe.

Considering (2.1.1d), we make the quasi-steady approximation that displacement currents are negligible, that is, the term $\partial \boldsymbol{D}^*/\partial t^*$ can be neglected. To justify this, we perform a dimensional analysis of (2.1.1c–d). Assuming a dominant balance in (2.1.1c) requires

$$\frac{\mathscr{E}^*}{\mathscr{L}^*} \approx \frac{\mathscr{B}^*}{\mathscr{T}^*}, \tag{2.1.4}$$

where the calligraphic font denotes typical orders of magnitude: $\mathscr{E}^*$, $\mathscr{B}^*$, $\mathscr{L}^*$, and $\mathscr{T}^*$ are characteristic magnitudes of the electric field, magnetic field, length-scale, and time-scale, respectively. Then the ratio of the displacement current term on

Parameter	Symbol	Typical value range	Unit
Fluid thickness	$\mathscr{H}^*$	$\lfloor 0.1,\, 1.0 \rceil \times 10^{-3}$	m
Fluid length	$\mathscr{L}^*$	$\lfloor 0.1,\, 1.0 \rceil$	m
Fluid velocity	$\mathscr{U}^*$	$\lfloor 0.01,\, 1.0 \rceil \times 10^{-1}$	m/s
Time-scale	$\mathscr{T}^*$	$\mathscr{L}^*/\mathscr{U}^* \in \lfloor 0.001,\, 1.0 \rceil \times 10^{3}$	s
Magnetic field	$\mathscr{B}^*$	1	T
Substrate inclination angle	θ	$\lfloor 0,\, \pi/4 \rceil$	rad
Temperature range	ΔT^*	$\lfloor 1.0,\, 5.0 \rceil \times 10^{2}$	K

Table 2.1: Characteristic system properties. The film thickness is based on calculations from the fusion literature [157] *that have been established experimentally* [161].

the right-hand side of (2.1.1d) to the left-hand side is given by

$$\frac{\varepsilon^* \mathscr{E}^* / \mathscr{T}^*}{\mathscr{B}^* / \mu^* \mathscr{L}^*} \approx \frac{\varepsilon^* \mu^* {\mathscr{L}^*}^2}{{\mathscr{T}^*}^2}. \tag{2.1.5}$$

One fundamental relation from electrodynamics is that

$$c^* = \frac{1}{\sqrt{\varepsilon^* \mu^*}} \approx 3.0 \times 10^8\,\mathrm{m/s}, \tag{2.1.6}$$

which is the speed of light. Since $\mathscr{T}^*$ is at least of order 1 s, and $\mathscr{L}^*$ from 10 cm to 1 m (see table 2.1), the ratio in (2.1.5) is at most of order 10^{-17}, and thus can be neglected. The quasi-steady approximation filters out electromagnetic radiation, which we consider to radiate across the length of our system effectively instantaneously with respect to the time-scale of interest [169].

Taking the divergence of (2.1.1d) with the quasi-steady approximation gives the continuity equation for current,

$$\boldsymbol{\nabla}^* \cdot \boldsymbol{j}^* = 0. \tag{2.1.7}$$

Another fundamental electromagnetic constitutive relation is Ohm's law. When considering a conductor in motion with velocity $\boldsymbol{u}^*$, this takes the form [169],

$$\boldsymbol{j}^* = \sigma^*(\boldsymbol{E}^* + \boldsymbol{u}^* \times \boldsymbol{B}^*), \tag{2.1.8}$$

where σ^* is the electrical conductivity, which we assume to be constant. Equa-

Parameter	Symbol	Value range	Unit
Density	ρ^*	$\lfloor 4.7,\, 5.2 \rceil \times 10^2$	$\mathrm{kg/m^3}$
Electrical conductivity	σ^*	$\lfloor 2.7,\, 4.0 \rceil \times 10^6$	S/m
Kinematic viscosity	ν^*	$\lfloor 0.6,\, 1.1 \rceil \times 10^{-6}$	$\mathrm{m^2/s}$
Thermal diffusivity	κ^*	$\lfloor 2.0,\, 2.8 \rceil \times 10^{-5}$	$\mathrm{m^2/s}$
Thermal conductivity	k^*	$\lfloor 4.0,\, 6.0 \rceil \times 10$	W/m K
Specific heat	c^*	4.2×10^3	J/K kg
Surface tension	γ^*	$\lfloor 3.4,\, 4.0 \rceil \times 10^{-1}$	N/m
Surface tension gradient	$\mathrm{d}\gamma^*/\mathrm{d}T^*$	1.2×10^{-4}	N/m K
Seebeck coefficient	S^*	$\lfloor 2.0,\, 2.7 \rceil \times 10^{-5}$	V/K
Seebeck gradient	$\mathrm{d}S^*/\mathrm{d}T^*$	1.3×10^{-8}	$\mathrm{V/K^2}$
Magnetic permeability	μ^*	1.3×10^{-6}	H/m
Magnetic susceptibility	χ	2.1×10^{-5}	–
Electric permittivity	ε^*	8.9×10^{-12}	F/m

Table 2.2: Material properties of liquid lithium in the temperature range $\lfloor 180,\, 600 \rceil$°C *(taken from* [37, 179, 184]*).*

tion (2.1.8) is a nonrelativistic approximation, appropriate when $(\mathscr{U}^*/c^*)^2 \ll 1$, which is certainly true in our case, where $\mathscr{U}^*$ is significantly less than 1 m/s (see table 2.1).

Ohm's law in the form (2.1.8) neglects the so-called Hall effect, describing the deflection that current experiences in the presence of an applied magnetic field. According to the classical Drude model, the Hall effect is incorporated through Ohm's law by adding a term of the form $\sigma^* {R_H}^* \boldsymbol{j}^* \times \boldsymbol{B}^*$ to the right-hand side of (2.1.8), where ${R_H}^*$ is the Hall coefficient [12]. The ratio of the magnitudes of this term and the current is $\sigma^* {R_H}^* \mathscr{B}^* \approx 10^{-4}$ in liquid lithium in the temperature range of interest [69]. Thus we neglect the Hall effect henceforth in this thesis.

The induction equation

It is well known that, with the quasi-steady approximation, the role of (2.1.1a) is reduced to determining ϱ^* as a function of the solution vector fields [169]. It is common to further simplify the electrodynamics by isolating $\boldsymbol{E}^*$ from (2.1.8) and

Parameter	Symbol	Material	Value range	Unit
Electrical conductivity	σ^{s*}	Stainless steel	$\lfloor 0.9,\ 1.3 \rceil \times 10^{6}$	S/m
		Copper	$\lfloor 1.7,\ 5.9 \rceil \times 10^{7}$	
Magnetic susceptibility	χ^{s}	Stainless steel	$\lfloor 3.0,\ 4.0 \rceil \times 10^{-3}$	–
		Copper	-1.0×10^{-6}	
Thermal conductivity	k^{s*}	Stainless steel	$\lfloor 1.5,\ 2.1 \rceil$	W/m K
		Copper	$\lfloor 3.5,\ 3.8 \rceil \times 10^{2}$	
Thermal diffusivity	κ^{s*}	Stainless steel	$\lfloor 3.7,\ 5.0 \rceil \times 10^{-6}$	m^2/s
		Copper	$\lfloor 0.9,\ 1.1 \rceil \times 10^{-4}$	
Seebeck coefficient	S^{s*}	Stainless steel	$\lfloor -3.7,\ -1.3 \rceil \times 10^{-6}$	V/K
		Copper	$\lfloor 2.8,\ 5.2 \rceil \times 10^{-6}$	

Table 2.3: Substrate material properties, in a temperature range of $\lfloor 0,\ 600 \rceil$°C *(taken from* [15, 18, 25, 51, 67, 79, 127, 176, 185, 191]*).*

substituting it into (2.1.1c). Then, using the vector identity

$$\boldsymbol{\nabla}^* \times (\boldsymbol{\nabla}^* \times \boldsymbol{B}^*) = \boldsymbol{\nabla}^* (\boldsymbol{\nabla}^* \cdot \boldsymbol{B}^*) - \boldsymbol{\nabla}^{*2} \boldsymbol{B}^*, \tag{2.1.9}$$

while incorporating (2.1.1b,d), we find that the electrodynamics is described by the induction equation

$$\frac{\partial \boldsymbol{B}^*}{\partial t^*} = \boldsymbol{\nabla}^* \times (\boldsymbol{u}^* \times \boldsymbol{B}^*) + \eta^* \boldsymbol{\nabla}^{*2} \boldsymbol{B}^*, \tag{2.1.10}$$

where η^* is the magnetic diffusivity, given by

$$\eta^* = \frac{1}{\sigma^* \mu^*}. \tag{2.1.11}$$

Equation (2.1.10) effectively eliminates $\boldsymbol{E}^*$ and $\boldsymbol{j}^*$ leaving $\boldsymbol{B}^*$ as the only electromagnetic state variable for which we need to solve. This comes at the cost of (2.1.10) being second order, which requires more boundary conditions for $\boldsymbol{B}^*$, to be deduced from boundary conditions for $\boldsymbol{j}^*$, using (2.1.1d).

Magnetic stress tensor

The final law that is required alongside Maxwell's equations is that the Lorentz force, $\boldsymbol{f}_L^*$, the force per unit volume exerted by an electromagnetic field on a conductor, is given by [169]

$$\boldsymbol{f}_L^* = \varrho^* \boldsymbol{E}^* + \boldsymbol{j}^* \times \boldsymbol{B}^*. \tag{2.1.12}$$

We compare the magnitudes of the two terms on the right-hand side of (2.1.12). From (2.1.1a) we use $\mathscr{R}^* = [\varrho^*] \approx \varepsilon^* \mathscr{E}^* / \mathscr{L}^*$ as the characteristic magnitude of charge density, and from (2.1.1d) we use $\mathscr{J}^* = [\boldsymbol{j}^*] \approx \mathscr{B}^* / \mu^* \mathscr{L}^*$ for current density. Then from (2.1.5) and (2.1.6) it follows that

$$\frac{\mathscr{R}^* \mathscr{E}^*}{\mathscr{J}^* \mathscr{B}^*} \approx \varepsilon^* \mu^* \left(\frac{\mathscr{E}^*}{\mathscr{B}^*} \right)^2 \approx \left(\frac{\mathscr{L}^*}{c^* \mathscr{T}^*} \right)^2 \ll 1, \tag{2.1.13}$$

which is the same magnitude as the negligible ratio in (2.1.5). We therefore neglect the contribution of the electric field to the Lorentz force (2.1.12). We note that care must be taken in assuming that $[\boldsymbol{j}^* \times \boldsymbol{B}^*] \approx [\boldsymbol{j}^*]\,[\boldsymbol{B}^*]$ if the currents run near parallel to the magnetic field.

It is worth noting that the term $\boldsymbol{j}^* \times \boldsymbol{B}^*$ in (2.1.12) has an alternative expression. From (2.1.1b), (2.1.1d), and (2.1.2a) one can show [169] that

$$\boldsymbol{j}^* \times \boldsymbol{B}^* = \boldsymbol{\nabla}^* \cdot \overline{\boldsymbol{m}}^*, \tag{2.1.14}$$

where $\overline{\boldsymbol{m}}^*$ is the magnetic stress tensor, given by

$$\overline{\boldsymbol{m}}^* = \frac{1}{\mu^*} \left(\boldsymbol{B}^* \otimes \boldsymbol{B}^* - \frac{1}{2} \left| \boldsymbol{B}^* \right|^2 \overline{\boldsymbol{I}} \right), \tag{2.1.15a}$$

where we have denoted the tensor product by $\otimes$ and the identity tensor by $\overline{\boldsymbol{I}}$. In Cartesian coordinates, this takes the form

$$\overline{\boldsymbol{m}}_{ij}^* = \frac{1}{\mu^*} \left(\boldsymbol{B}_i^* \boldsymbol{B}_j^* - \frac{1}{2} \left| \boldsymbol{B}^* \right|^2 \delta_{ij} \right), \tag{2.1.15b}$$

where the Kronecker delta function is denoted by δ_{ij}. The full Maxwell stress tensor includes contributions also from the electric field, $\boldsymbol{E}^*$; however, these have been neglected by the above dimensional argument. The stress formulation (2.1.14) will be used to obtain the correct stress balance at the free surface.

Hydrodynamics

To model the fluid flow, we use the incompressible Navier–Stokes equations [169],

$$\boldsymbol{\nabla}^* \cdot \boldsymbol{u}^* = 0, \tag{2.1.16a}$$

$$\rho^* \left(\frac{\partial \boldsymbol{u}^*}{\partial t^*} + (\boldsymbol{u}^* \cdot \boldsymbol{\nabla}^*)\boldsymbol{u}^* \right) = \boldsymbol{\nabla} \cdot (\overline{\boldsymbol{\tau}}^* + \overline{\boldsymbol{m}}^*) + \boldsymbol{f}^*, \tag{2.1.16b}$$

where ρ^* is the fluid density, $\overline{\boldsymbol{\tau}}^* + \overline{\boldsymbol{m}}^*$ is the total stress tensor given by the sum of the viscous and magnetic stresses, and $\boldsymbol{f}^*$ is the external body force per unit volume. We consider an incompressible Newtonian fluid, in which the viscous stress tensor, $\overline{\boldsymbol{\tau}}^*$, is given by

$$\overline{\boldsymbol{\tau}}^* = -p^* \overline{\boldsymbol{I}} + \rho^* \nu^* \left(\boldsymbol{\nabla}^* \boldsymbol{u}^* + (\boldsymbol{\nabla}^* \boldsymbol{u}^*)^T \right), \tag{2.1.17}$$

where ν^* is the kinematic viscosity of the fluid. We assume that ρ^* and ν^* are constant and apply a gravitational body force, $\boldsymbol{f}^* = \rho^* \boldsymbol{g}$, where $\boldsymbol{g}^*$ is acceleration due to gravity. Then (2.1.16b) becomes

$$\rho^* \left(\frac{\partial \boldsymbol{u}^*}{\partial t^*} + (\boldsymbol{u}^* \cdot \boldsymbol{\nabla}^*)\, \boldsymbol{u}^* \right) = -\boldsymbol{\nabla}^* p^* + \rho^* \nu^* \boldsymbol{\nabla}^{*2} \boldsymbol{u}^* + \boldsymbol{j}^* \times \boldsymbol{B}^* + \rho^* \boldsymbol{g}^*. \tag{2.1.18}$$

2.1.2 Boundary conditions

We are interested in the free-surface flow of a conducting liquid metal layer on a conducting solid substrate as illustrated in figure 2.1. The free surface is in contact with an insulator (a vacuum), while the bottom of the fluid is in contact with a solid conductor. We need to consider the relevant boundary conditions at all material interfaces, and assume vanishing far-field conditions for the induced electromagnetic fields.

Electrodynamics

We denote the unit vector normal to a material surface by $\boldsymbol{n}$, where the normal points from below the interface upwards, i.e. such that $\boldsymbol{n} \cdot \boldsymbol{g}^* \leq 0$. We also denote the jump across a boundary of quantity q by $[q]_-^+ = q|_+ - q|_-$, the value above the boundary minus the value below it.

The electrodynamic boundary conditions are effectively jump conditions for the partial differential equations (2.1.1) and (2.1.7), at an interface across which the ma-

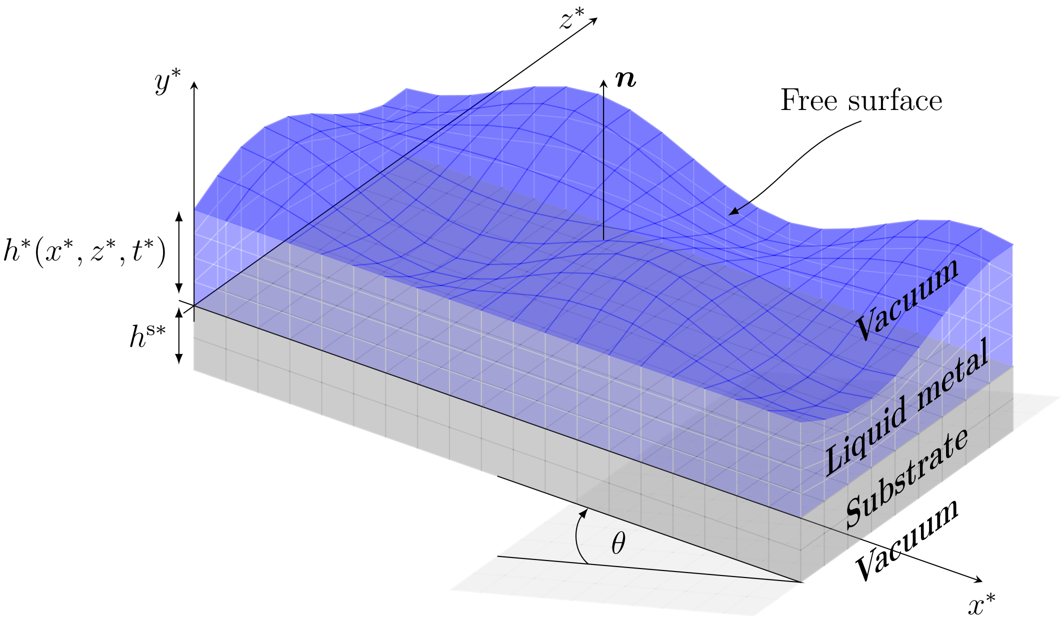

Figure 2.1: Schematic of the fluid film (shaded blue) flowing on the solid substrate (shaded grey) inclined at an angle θ from the laboratory horizontal. The thicknesses of the fluid and substrate layers as well as the normal to the free surface are labelled.

terial parameters μ^*, ε^*, and σ^* are discontinuous. First, corresponding to equations (2.1.1b–d), we have the conditions $[\boldsymbol{B}^* \cdot \boldsymbol{n}]_-^+ = 0$ and $[\boldsymbol{E}^* \times \boldsymbol{n}]_-^+ = [\boldsymbol{H}^* \times \boldsymbol{n}]_-^+ = \boldsymbol{0}$. Next, from the current conservation equation (2.1.7) we have $[\boldsymbol{j}^* \cdot \boldsymbol{n}]_-^+ = 0$. Then from (2.1.8) it follows that $[\sigma^* \boldsymbol{E}^* \cdot \boldsymbol{n}]_-^+ = -[\sigma^* (\boldsymbol{u}^* \times \boldsymbol{B}^*) \cdot \boldsymbol{n}]_-^+$. In particular, at the interface between the liquid metal and the solid substrate we impose the no-slip condition $\boldsymbol{u}^* = \boldsymbol{0}$. Thus $[\sigma^* \boldsymbol{E}^* \cdot \boldsymbol{n}]_-^+ = 0$ at such a boundary, and, in general, there must be a jump in $\boldsymbol{D}^* \cdot \boldsymbol{n}$ at any interface between materials with different conductivities. The jump in $[\boldsymbol{D}^* \cdot \boldsymbol{n}]_-^+$ corresponds to a surface charge ξ^* localised at the interface. Importantly, just as ϱ^* is to be obtained from the solution of the system, so too ξ^* is to be determined from the solution and need not be specified.

Overall, then, we arrive at the boundary conditions

$$[\varepsilon^* \boldsymbol{E}^* \cdot \boldsymbol{n}]_-^+ = \xi^*, \qquad [\boldsymbol{E}^* \times \boldsymbol{n}]_-^+ = \boldsymbol{0}, \tag{2.1.19a,b}$$

$$[\boldsymbol{B}^* \cdot \boldsymbol{n}]_-^+ = 0, \qquad \left[\frac{1}{\mu^*}\boldsymbol{B}^* \times \boldsymbol{n}\right]_-^+ = \boldsymbol{0}, \tag{2.1.19c,d}$$

$$[\boldsymbol{j}^* \cdot \boldsymbol{n}]_-^+ = 0, \qquad \left[\frac{1}{\sigma^*}\boldsymbol{j}^* \times \boldsymbol{n}\right]_-^+ = [(\boldsymbol{u}^* \times \boldsymbol{B}^*) \times \boldsymbol{n}]_-^+ . \tag{2.1.19e,f}$$

In (2.1.19d), the right-hand side is zero since we do not model surface currents, as by the induction equation, (2.1.10), these are not sustained, but rather diffuse into current density within the material [30, 170]. It is worth noting that we have included the boundary conditions for all the state variables $\boldsymbol{E}^*$, $\boldsymbol{B}^*$, and $\boldsymbol{j}^*$; however, just as there is redundancy between these quantities in (2.1.1) and (2.1.8), so too the boundary conditions (2.1.19) are not all independent.

Hydrodynamics

For the fluid flow, we assume a no-slip condition on the liquid–substrate interface, $y^* = 0$ (see figure 2.1),

$$\boldsymbol{u}^* = \boldsymbol{0}. \tag{2.1.20}$$

At the free surface we impose the kinematic condition

$$\frac{\partial h^*}{\partial t^*} + \left(\frac{\partial h^*}{\partial x^*}\boldsymbol{x} - \boldsymbol{y} + \frac{\partial h^*}{\partial z^*}\boldsymbol{z}\right) \cdot \boldsymbol{u}^* = 0, \tag{2.1.21}$$

where $\boldsymbol{x}$, $\boldsymbol{y}$ and $\boldsymbol{z}$ are unit vectors in the x^*, y^*, and z^* directions, respectively, and where the free surface is represented by $y^* = h^*(x^*, z^*, t^*)$. The normal and tangential stress balances at the free surface [109], are given respectively by

$$[(\overline{\boldsymbol{\tau}}^* + \overline{\boldsymbol{m}}^*) \cdot \boldsymbol{n}]_-^+ \cdot \boldsymbol{n} = \gamma^* \varkappa^*, \tag{2.1.22a}$$

$$[(\overline{\boldsymbol{\tau}}^* + \overline{\boldsymbol{m}}^*) \cdot \boldsymbol{n}]_-^+ \times \boldsymbol{n} = \boldsymbol{0}, \tag{2.1.22b}$$

where $\varkappa^*$ is the free-surface curvature and γ^* is the surface tension.

2.1.3 Problem statement

Separating applied and induced magnetic fields

In a tokamak there is a large *applied* field, denoted $\boldsymbol{B}^{\mathrm{a}*}$, imposed by external electromagnets. In addition there is a (typically somewhat smaller) *induced* magnetic field, denoted $\boldsymbol{B}^{\mathrm{i}*}$, caused by the interaction of the applied magnetic field with the liquid metal film and divertor substrate. In what follows it is helpful to separate the magnetic field into these two distinct components. We therefore write

$$\boldsymbol{B}^*(x^*, y^*, z^*, t^*) = \boldsymbol{B}^{\mathrm{a}*}(x^*, y^*, z^*) + \boldsymbol{B}^{\mathrm{i}*}(x^*, y^*, z^*, t^*), \tag{2.1.23}$$

where $\boldsymbol{B}^{\mathrm{a}*}$ is assumed to be a known, smooth, specified function of position and $\boldsymbol{B}^{\mathrm{i}*}$ is to be determined from the equations

$$\boldsymbol{\nabla}^* \cdot \boldsymbol{B}^{\mathrm{i}*} = 0, \tag{2.1.24a}$$

$$\frac{1}{\mu^*}\boldsymbol{\nabla}^* \times \boldsymbol{B}^{\mathrm{i}*} = \boldsymbol{j}^*, \tag{2.1.24b}$$

$$\frac{\partial \boldsymbol{B}^{\mathrm{i}*}}{\partial t^*} - \eta^* \boldsymbol{\nabla}^{*2} \boldsymbol{B}^{\mathrm{i}*} = \boldsymbol{\nabla}^* \times \left(\boldsymbol{u}^* \times \left(\boldsymbol{B}^{\mathrm{a}*} + \boldsymbol{B}^{\mathrm{i}*}\right)\right). \tag{2.1.24c}$$

It is worth noting from (2.1.1) and (2.1.24) that we consider only $\boldsymbol{B}^{\mathrm{a}*}$ that is divergence-free and such that the support of the curl is outside the divertor, since we consider $\boldsymbol{j}^*$ to be non-zero only in the liquid metal and divertor substrate.

Next, substituting the decomposition (2.1.23) into the electromagnetic boundary conditions (2.1.19), we find that the induced field satisfies the jump conditions

$$\left[\boldsymbol{B}^{\mathrm{i}*} \cdot \boldsymbol{n}\right]_-^+ = 0, \tag{2.1.25a}$$

$$\left[\frac{1}{\mu^*}\boldsymbol{B}^{\mathrm{i}*} \times \boldsymbol{n}\right]_-^+ = -\boldsymbol{B}^{\mathrm{a}*} \times \boldsymbol{n} \left[\frac{1}{\mu^*}\right]_-^+, \tag{2.1.25b}$$

at the interface between two media, having used the fact that $\boldsymbol{B}^{\mathrm{a}*}$ is continuous across the interface. Thus, as well as by induction due to the flowing metal, additional magnetic fields may be caused by a mismatch in permeability at an interface.

Governing equations and boundary conditions

We now proceed to write down the full problem, comprising the governing equations in each layer and the boundary conditions. The divertor comprises a solid, inclined substrate down which the liquid metal layer flows, a section of which is illustrated in figure 2.1. The divertor sits in a vacuum vessel, and so we consider the region above and below the divertor to be a vacuum extending to the far field. The thicknesses of the fluid layer and substrate are denoted by h^* and $h^{\mathrm{s}*}$, respectively, while the angle of inclination of the substrate is denoted θ.

In the vacuum above and below the divertor, there is no flow and can be no current or charge density, so we have, in $y^* < -h^{\mathrm{s}*}$ and $y^* > h^*(x^*, z^*, t^*)$,

$$\boldsymbol{\nabla}^* \cdot \boldsymbol{B}^{\mathrm{i}*} = 0, \tag{2.1.26a}$$

$$\boldsymbol{\nabla}^* \times \boldsymbol{B}^{\mathrm{i}*} = 0. \tag{2.1.26b}$$

In the substrate there is no flow, but there can be current and charge density, so the equations in $-h^{s*} < y^* < 0$ are

$$\boldsymbol{\nabla}^* \cdot \boldsymbol{B}^{i*} = 0, \tag{2.1.27a}$$

$$\boldsymbol{\nabla}^* \times \boldsymbol{B}^{i*} = \mu^{s*} \boldsymbol{j}^*, \tag{2.1.27b}$$

$$\frac{\partial \boldsymbol{B}^{i*}}{\partial t^*} = \eta^{s*} \boldsymbol{\nabla}^{*2} \boldsymbol{B}^{i*}, \tag{2.1.27c}$$

where the superscript 's' denotes material properties in the substrate. In the liquid film, $0 < y^* < h^*(x^*, z^*, t^*)$, all the dynamics are present, and the governing equations are

$$\boldsymbol{\nabla}^* \cdot \boldsymbol{B}^{i*} = 0, \tag{2.1.28a}$$

$$\boldsymbol{\nabla}^* \times \boldsymbol{B}^{i*} = \mu^* \boldsymbol{j}^*, \tag{2.1.28b}$$

$$\frac{\partial \boldsymbol{B}^{i*}}{\partial t^*} - \eta^* \boldsymbol{\nabla}^{*2} \boldsymbol{B}^{i*} = \boldsymbol{\nabla}^* \times \left(\boldsymbol{u}^* \times \left(\boldsymbol{B}^{a*} + \boldsymbol{B}^{i*} \right) \right), \tag{2.1.28c}$$

$$\boldsymbol{\nabla}^* \cdot \boldsymbol{u}^* = 0, \tag{2.1.28d}$$

$$\rho^* \left(\frac{\partial \boldsymbol{u}^*}{\partial t^*} + \left(\boldsymbol{u}^* \cdot \boldsymbol{\nabla}^* \right) \boldsymbol{u}^* \right) = -\boldsymbol{\nabla}^* p^* + \rho^* \nu^* \boldsymbol{\nabla}^{*2} \boldsymbol{u}^* + \boldsymbol{j}^* \times \left(\boldsymbol{B}^{a*} + \boldsymbol{B}^{i*} \right) + \rho^* \boldsymbol{g}^*. \tag{2.1.28e}$$

At the substrate–vacuum interface, $y^* = -h^{s*}$, the unit normal vector is in the y^* direction, $\boldsymbol{n} = \boldsymbol{y}$. The vacuum is electrically insulating, so the boundary conditions are given by

$$\boldsymbol{j}^* \cdot \boldsymbol{y} = 0, \tag{2.1.29a}$$

$$\left[\boldsymbol{B}^{i*} \cdot \boldsymbol{y} \right]_-^+ = 0, \tag{2.1.29b}$$

$$\left[\frac{1}{\mu^*} \boldsymbol{B}^{i*} \times \boldsymbol{y} \right]_-^+ = -\boldsymbol{B}^{a*} \times \boldsymbol{y} \left[\frac{1}{\mu^*} \right]_-^+. \tag{2.1.29c}$$

At the liquid–substrate interface, $y^* = 0$, the unit normal vector is again $\boldsymbol{n} = \boldsymbol{y}$. Both media are conducting, and there is no slip between the liquid and the substrate, so the boundary conditions are given by

$$[\boldsymbol{j}^* \cdot \boldsymbol{y}]_-^+ = 0, \tag{2.1.30a}$$

$$\left[\frac{1}{\sigma^*}\boldsymbol{j}^* \times \boldsymbol{y}\right]_-^+ = \boldsymbol{0}, \tag{2.1.30b}$$

$$\left[\boldsymbol{B}^{\mathrm{i}*} \cdot \boldsymbol{y}\right]_-^+ = 0, \tag{2.1.30c}$$

$$\left[\frac{1}{\mu^*}\boldsymbol{B}^{\mathrm{i}*} \times \boldsymbol{y}\right]_-^+ = -\boldsymbol{B}^{\mathrm{a}*} \times \boldsymbol{y}\left[\frac{1}{\mu^*}\right]_-^+, \tag{2.1.30d}$$

$$\boldsymbol{u}^* = \boldsymbol{0}. \tag{2.1.30e}$$

At the liquid–vacuum free surface, $y^* = h^*(x^*, z^*, t^*)$, the normal is given by

$$\boldsymbol{n} = \frac{1}{\sqrt{1 + \left(\dfrac{\partial h^*}{\partial x^*}\right)^2 + \left(\dfrac{\partial h^*}{\partial z^*}\right)^2}}\left(-\frac{\partial h^*}{\partial x^*}\boldsymbol{x} + \boldsymbol{y} - \frac{\partial h^*}{\partial z^*}\boldsymbol{z}\right). \tag{2.1.31a}$$

The vacuum is non-conducting and we impose the kinematic and stress conditions (2.1.21) and (2.1.22). From (2.1.19) it follows that $[(\overline{\boldsymbol{m}} \cdot \boldsymbol{n}) \times \boldsymbol{n}]_-^+ = \boldsymbol{0}$ and so the magnetic stress contributes only to the normal stress condition. Therefore, the boundary conditions take the form

$$\boldsymbol{j}^* \cdot \boldsymbol{n} = 0, \tag{2.1.31b}$$

$$\left[\boldsymbol{B}^{\mathrm{i}*} \cdot \boldsymbol{n}\right]_-^+ = 0, \tag{2.1.31c}$$

$$\left[\frac{1}{\mu^*}\boldsymbol{B}^{\mathrm{i}*} \times \boldsymbol{n}\right]_-^+ = -\boldsymbol{B}^{\mathrm{a}*} \times \boldsymbol{n}\left[\frac{1}{\mu^*}\right]_-^+, \tag{2.1.31d}$$

$$\frac{\partial h^*}{\partial t^*} + \left(\frac{\partial h^*}{\partial x^*}\boldsymbol{x} - \boldsymbol{y} + \frac{\partial h^*}{\partial z^*}\boldsymbol{z}\right) \cdot \boldsymbol{u}^* = 0, \tag{2.1.31e}$$

$$(\overline{\boldsymbol{\tau}}^* \cdot \boldsymbol{n}) \cdot \boldsymbol{n} = -\gamma^* \varkappa^* + [(\overline{\boldsymbol{m}}^* \cdot \boldsymbol{n}) \cdot \boldsymbol{n}]_-^+, \tag{2.1.31f}$$

$$(\overline{\boldsymbol{\tau}}^* \cdot \boldsymbol{n}) \times \boldsymbol{n} = \boldsymbol{0}, \tag{2.1.31g}$$

where

$$[(\overline{\boldsymbol{m}}^* \cdot \boldsymbol{n}) \cdot \boldsymbol{n}]_-^+ = \frac{(\boldsymbol{B}^* \cdot \boldsymbol{n})^2}{2}\left[\frac{1}{\mu^*}\right]_-^+ - \frac{|\boldsymbol{B}^* \times \boldsymbol{n}|^2}{2(\mu^*)^2}[\mu^*]_-^+. \tag{2.1.31h}$$

Finally, we require that the induced field vanish in the far field, that is,

$$\left|\boldsymbol{B}^{\mathrm{i}*}\right| \to 0, \quad \text{as} \quad |(x^*,\, y^*,\, z^*)| \to \infty. \tag{2.1.32}$$

In addition to the conservation of mass and momentum, the conservation of energy must also be ensured. For the clarity of the exposition, we delay introducing thermal variations until chapter 4, proceeding, in the first instance, in the isothermal case.

With the problem statement concretely delineated, we proceed in the next sections to consider two-dimensional flow with two canonical cases of the magnetic field: the "poloidal" case, where the field lies in the plane of motion, and the "toroidal" case, where the field is orthogonal to the plane of motion. In both cases, we use asymptotic analysis to simplify the governing equations in the limit where the liquid film is thin compared to its length, and where the induced magnetic field is small compared to the applied field.

2.2 The Poloidal case

2.2.1 2D Cartesian geometry

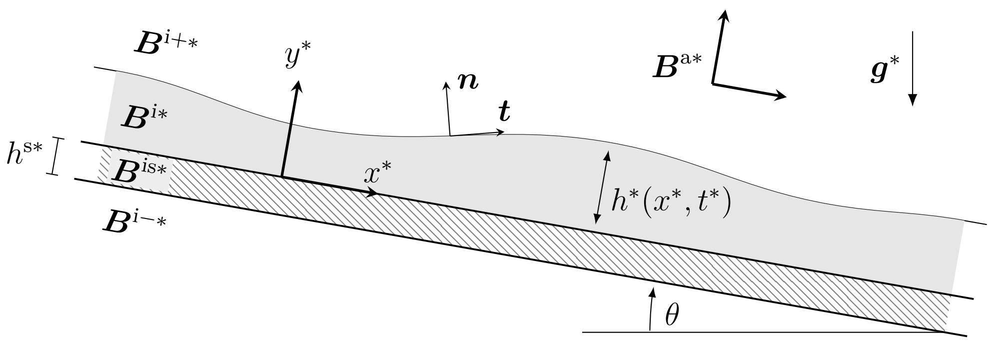

Figure 2.2: Schematic of the two-dimensional geometry where the fluid flows above a solid substrate inclined with angle θ in the presence of a poloidal applied field.

In the first instance, we consider a two-dimensional flow in the (x^*, y^*)-plane, so $\boldsymbol{u}^* = (u^*(x^*, y^*, t^*),\, v(x^*, y^*, t^*),\, 0)^T$ and $h^* = h^*(x^*, t^*)$; see a cross section in figure 2.2. In this case, the free-surface curvature is given by

$$\varkappa^* = -\frac{\partial^2 h^*}{\partial x^{*2}} \left(1 + \left(\frac{\partial h^*}{\partial x^*}\right)^2\right)^{-3/2}. \tag{2.2.1}$$

This geometry exploits the fact that the tokamak is axisymmetric while neglecting the curvature of the device. We further simplify the model by considering in this section an applied magnetic field that has only x^*- and y^*-components. These components are referred to as the poloidal components of the field, while the orthogonal component is called the toroidal component, which will be considered below in §2.3.

Before proceeding with the analysis, we note an exact net mass conservation relation. By integrating (2.1.16a) and imposing (2.1.20) and (2.1.21) we obtain

$$\frac{\partial h^*}{\partial t^*} + \frac{\partial}{\partial x^*}\left(\int_0^{h^*} u^* \, \mathrm{d}y^*\right) = 0. \tag{2.2.2}$$

With this evolution equation for the free surface, we need not solve for v^*. Our aim is to use asymptotic analysis to approximate the horizontal velocity u^*, and then substitute into (2.2.2) to obtain an evolution equation for $h^*(x^*, t^*)$.

We denote the induced field in the vacuum beneath the divertor, in the substrate, in the fluid layer, and in the vacuum above the divertor by $\boldsymbol{B}^{\mathrm{i}-*}$, $\boldsymbol{B}^{\mathrm{is}*}$, $\boldsymbol{B}^{\mathrm{i}*}$, and $\boldsymbol{B}^{\mathrm{i}+*}$, respectively, as in figure 2.2. We denote the applied field

$$\boldsymbol{B}^{\mathrm{a}*} = \left(B_x^{\mathrm{a}*}(x^*, y^*),\, B_y^{\mathrm{a}*}(x^*, y^*),\, 0\right)^T. \tag{2.2.3}$$

We observe that the applied field only appears in the poloidal components of the induction equation and boundary conditions, (2.1.24) and (2.1.25), from which we deduce that the induced magnetic field will likewise only have poloidal components. Using this poloidal form and (2.1.1b), we know that $\boldsymbol{B}^*$ can be written in terms of a vector potential (with a Coulomb gauge) with a single component

$$\boldsymbol{B}^* = \boldsymbol{\nabla}^* \times (0,\, 0,\, A^*(x^*, y^*, t^*))^T = \left(\frac{\partial A^*}{\partial y^*},\, -\frac{\partial A^*}{\partial x^*},\, 0\right)^T. \tag{2.2.4}$$

We consider the magnetic potential to be a combination of the applied and induced potentials

$$A^* = A^{\mathrm{a}*} + A^{\mathrm{i}*}, \tag{2.2.5}$$

with the same restrictions on the associated magnetic fields as detailed in § 2.1.3. Moreover, we use the same notation conventions for the potential in each spatial region as we do for the magnetic field.

2.2.2 Non-dimensionalisation

We scale the system variables with the typical values

$$x^* = \mathscr{L}^* x, \qquad y^* = \epsilon \mathscr{L}^* y, \tag{2.2.6a,b}$$

$$u^* = \mathscr{U}^* u, \qquad v^* = \epsilon \mathscr{U}^* v, \tag{2.2.6c,d}$$

$$p^* = \sigma^* \mathscr{B}^{*2} \mathscr{U}^* \mathscr{L}^* p, \qquad t^* = \left(\mathscr{L}^*/\mathscr{U}^*\right) t, \tag{2.2.6e,f}$$

$$A^{\mathrm{a}*} = \mathscr{L}^* \mathscr{B}^* A^{\mathrm{a}}, \qquad A^{\mathrm{i}*} = \epsilon \,\mathrm{Rm}\, \mathscr{L}^* \mathscr{B}^* A^{\mathrm{i}}, \tag{2.2.6g,h}$$

$$h^* = \epsilon \mathscr{L}^* h, \qquad h^{\mathrm{s}*} = \epsilon \mathscr{L}^* h^{\mathrm{s}}, \tag{2.2.6i,j}$$

where ϵ is the aspect ratio of the system,

$$\epsilon = \frac{\mathscr{H}^*}{\mathscr{L}^*}, \tag{2.2.7}$$

which is small (see table 2.1), while χ and χ^{s} are the magnetic susceptibilities of the liquid metal and substrate, and Rm is the magnetic Reynolds number, defined in table 2.4.

The induced field in all regions is scaled by a factor of $\epsilon\,\mathrm{Rm}$, which reflects the fact that the induction is caused by the fluid flow in the presence of the applied field, and is given by finding a dominant balance in the induction equation (2.1.28c).

The pressure is scaled so that it balances the magnetic terms in the momentum equation (2.1.28e). We consider the dominant balance in (2.1.28e) between the magnetic terms and gravity so that

$$\mathrm{Ha}^2 = \frac{\epsilon^2\,\mathrm{Re}}{\mathrm{Fr}^2}, \tag{2.2.8}$$

where Ha, Re and Fr are the Hartmann, Reynolds, and Froude numbers also defined in table 2.4. From (2.2.8) we deduce the typical velocity scale

$$\mathscr{U}^* = \frac{\rho^*\,|\boldsymbol{g}^*|\sin\theta}{\sigma^* \mathscr{B}^{*2}}, \tag{2.2.9}$$

which is on the order of 1 mm/s based on tables 2.1 and 2.2. The appropriate ϵ scale follows by considering $\mathscr{Q}^* = \mathscr{U}^* \mathscr{H}^*$, where $\mathscr{Q}^*$ is the dimensional liquid metal flux, from which we obtain

$$\epsilon = \frac{\sigma^* \mathscr{B}^{*2} \mathscr{Q}^*}{\rho^*\,|\boldsymbol{g}^*|\,\mathscr{L}^* \sin\theta}. \tag{2.2.10}$$

Dimensionless quantity	Definition	Description	Typical value
Aspect ratio	$\epsilon = \dfrac{\mathscr{H}^*}{\mathscr{L}^*}$	$\dfrac{\text{Film height}}{\text{Flow length}}$	$\lfloor 0.1,\ 1.0 \rceil \times 10^{-3}$
Reynolds number	$\mathrm{Re} = \dfrac{\mathscr{U}^*\mathscr{L}^*}{\nu^*}$	$\dfrac{\text{Inertia}}{\text{Viscosity}}$	$\lfloor 0.9,\ 1.7 \rceil \times 10^{3}$
Magnetic Reynolds number	$\mathrm{Rm} = \dfrac{\mathscr{U}^*\mathscr{L}^*}{\eta^*}$	$\dfrac{\text{EM induction}}{\text{EM diffusion}}$	$\lfloor 3.4,\ 5.0 \rceil \times 10^{-3}$
Hartmann number	$\mathrm{Ha} = \dfrac{\mathscr{B}^*\mathscr{H}^*\sqrt{\sigma^*}}{\sqrt{\rho^*\nu^*}}$	$\sqrt{\dfrac{\text{EM}}{\text{Viscosity}}}$	$\lfloor 0.8,\ 9.8 \rceil \times 10$
Froude number	$\mathrm{Fr} = \dfrac{\mathscr{U}^*}{\sqrt{\lvert \boldsymbol{g}^* \rvert \mathscr{L}^*}}$	$\sqrt{\dfrac{\text{Inertia}}{\text{Gravity}}}$	3.2×10^{-4}
Interaction parameter	$\mathrm{N} = \dfrac{\mathrm{Ha}^2}{\mathrm{Re}}$	$\dfrac{\text{EM}}{\text{Inertia}}$	$\lfloor 0.1,\ 5.7 \rceil$
Stokes number	$\mathrm{St} = \dfrac{\mathrm{Re}}{\mathrm{Fr}^2}$	$\dfrac{\text{Gravity}}{\text{Viscosity}}$	$\lfloor 0.9,\ 1.6 \rceil \times 10^{10}$
Bond number	$\mathrm{Bo} = \dfrac{\rho^*\,\lvert \boldsymbol{g}^* \rvert\,\mathscr{H}^{*2}\sin\theta}{\gamma^*}$	$\dfrac{\text{Gravity}}{\text{Surface tension}}$	$\lfloor 0.001,\ 1.0 \rceil \times 10^{-3}$
Peclét number	$\mathrm{Pe} = \dfrac{\mathscr{U}^*\mathscr{L}^*}{\kappa^*}$	$\dfrac{\text{Advection}}{\text{Conduction}}$	$\lfloor 3.6,\ 5.0 \rceil \times 10^{2}$

Table 2.4: Dimensionless quantities, where we have used the velocity scale (2.2.9)*, and values from tables 2.1 and 2.2.*

We note that the natural y^*-scaling in the region exterior to the divertor does not carry a factor of ϵ, that is, the magnetic potential varies on a vertical scale Y, where $Y = \epsilon y$. We now expand our applied potential in an asymptotic expansion in the small parameter ϵ, valid within the divertor where $Y = \epsilon y \ll 1$, to obtain

$$A^{\mathrm{a}}(x, Y) = A^{\mathrm{a}}(x, 0) + \epsilon y \frac{\partial A^{\mathrm{a}}}{\partial Y}(x, 0) + \frac{\epsilon^2 y^2}{2}\frac{\partial^2 A^{\mathrm{a}}}{\partial Y^2}(x, 0) + \cdots \tag{2.2.11a}$$

$$= A^{\mathrm{a}}_0(x) + \epsilon y B^{\mathrm{a}}_{x0}(x) + \frac{\epsilon^2 y^2}{2}\frac{\partial B^{\mathrm{a}}_x}{\partial Y}(x, 0) + \cdots \tag{2.2.11b}$$

where we denote the x-component of the applied field at $Y = 0$ by $B^{\mathrm{a}}_{x0}(x) = B^{\mathrm{a}}_x(x, 0)$, and the Y-component of the applied field at $Y = 0$ by $B^{\mathrm{a}}_{Y0}(x) = -\mathrm{d}A^{\mathrm{a}}_0/\mathrm{d}x$.

We now write down in detail the dimensionless poloidal system, (2.1.26–32), in this two-dimensional geometry, after neglecting terms of order $\epsilon^2\,\mathrm{Re}\,/\,\mathrm{Ha}^2$, $\epsilon^2\,\mathrm{Rm}$,

$\epsilon^2 \,\mathrm{Rm}\, \eta^*/\eta^{\mathrm{s}*}$, $\epsilon^2/\,\mathrm{Ha}^2$, ϵ^2, χ, χ^{s}, Rm or higher, while retaining all other effects and considering the dominant balance (2.2.8). For the moment we take $\chi/\,\mathrm{Rm}$ and $\chi^{\mathrm{s}}/\,\mathrm{Rm}$ to be $\mathcal{O}(1)$ as $\epsilon \to 0$.

In the vacuum regions above and below the divertor there is no induced current so the equations (2.1.26) governing the induced potential reduce to Laplace's equation

$$\frac{\partial^2 A^{\mathrm{i}-}}{\partial x^2} + \frac{\partial^2 A^{\mathrm{i}-}}{\partial Y^2} = 0, \quad \text{where } \ y < -h^{\mathrm{s}},\ Y < -\epsilon h^{\mathrm{s}}, \tag{2.2.12a}$$

$$\frac{\partial^2 A^{\mathrm{i}+}}{\partial x^2} + \frac{\partial^2 A^{\mathrm{i}+}}{\partial Y^2} = 0, \quad \text{where } \ y > h,\ Y > \epsilon h. \tag{2.2.12b}$$

In the substrate layer, $-h^{\mathrm{s}} < y < 0$, the leading-order equation (2.1.27) governing the induced potential takes the form

$$\frac{\partial^2 A^{\mathrm{is}}}{\partial y^2} = 0. \tag{2.2.13}$$

In the fluid layer, $0 < y < h$, the governing equations (2.1.28) are simplified to

$$\frac{\partial^2 A^{\mathrm{i}}}{\partial y^2} = -\epsilon u B^{\mathrm{a}}_{Y0}, \tag{2.2.14a}$$

$$\frac{\partial u}{\partial x} + \frac{\partial v}{\partial y} = 0, \tag{2.2.14b}$$

$$\frac{\partial p}{\partial x} = \frac{1}{\mathrm{Ha}^2}\frac{\partial^2 u}{\partial y^2} + 1 - u\left(B^{\mathrm{a}}_{Y0}\right)^2 + 2\epsilon u y \frac{\mathrm{d}B^{\mathrm{a}}_{x0}}{\mathrm{d}x} B^{\mathrm{a}}_{Y0} + \epsilon v B^{\mathrm{a}}_{x0} B^{\mathrm{a}}_{Y0}, \tag{2.2.14c}$$

$$\frac{\partial p}{\partial y} = -\epsilon \cot\theta + \epsilon u B^{\mathrm{a}}_{Y0}\left(B^{\mathrm{a}}_{x0} + \mathrm{Rm}\,\frac{\partial A^{\mathrm{i}}}{\partial y}\right). \tag{2.2.14d}$$

We use the fact that A^{a} satisfies Laplace's equation to expand the boundary conditions (2.1.29) at the substrate–vacuum interface up to $\mathcal{O}(\epsilon)$. We find that at $y = -h^{\mathrm{s}}$, $Y = -\epsilon h^{\mathrm{s}}$, the boundary conditions (2.1.29) are given by

$$A^{\mathrm{is}} = A^{\mathrm{i}-} - \epsilon h^{\mathrm{s}} \frac{\partial A^{\mathrm{i}-}}{\partial Y}, \tag{2.2.15a}$$

$$\frac{\partial A^{\mathrm{is}}}{\partial y} = \epsilon \frac{\partial A^{\mathrm{i}-}}{\partial Y} + \frac{\chi^{\mathrm{s}}}{\mathrm{Rm}}\left(B^{\mathrm{a}}_{x0} - \epsilon h^{\mathrm{s}} \frac{\partial B^{\mathrm{a}}_{Y0}}{\partial x}\right). \tag{2.2.15b}$$

At the liquid–substrate interface, $y = Y = 0$, the boundary conditions (2.1.30) are given by

$$A^{\mathrm{i}} = A^{\mathrm{is}}, \tag{2.2.16a}$$

$$\frac{\partial A^{\mathrm{i}}}{\partial y} = \frac{\partial A^{\mathrm{is}}}{\partial y} + \frac{\chi - \chi^{\mathrm{s}}}{\mathrm{Rm}} B^{\mathrm{a}}_{x0}, \tag{2.2.16b}$$

$$u = v = 0. \tag{2.2.16c}$$

At the liquid–vacuum free surface, we again use the fact that A^{a} satisfies Laplace's equation to deduce the boundary conditions up to $\mathcal{O}(\epsilon)$. We find that at $y = h$, $Y = \epsilon h$, the boundary conditions (2.1.31) are given by

$$A^{\mathrm{i}} = A^{\mathrm{i}+} + \epsilon h \frac{\partial A^{\mathrm{i}+}}{\partial Y}, \tag{2.2.17a}$$

$$\frac{\partial A^{\mathrm{i}}}{\partial y} = \epsilon \frac{\partial A^{\mathrm{i}+}}{\partial Y} + \frac{\chi}{\mathrm{Rm}} \left(B^{\mathrm{a}}_{x0} + \epsilon \frac{\partial}{\partial x} \left(h B^{\mathrm{a}}_{Y0} \right) \right), \tag{2.2.17b}$$

$$v = \frac{\partial h}{\partial t} + u \frac{\partial h}{\partial x}. \tag{2.2.17c}$$

It then follows that the stress balance conditions (2.1.31f) and (2.1.31g) at the free surface are given respectively by

$$p = -\frac{\epsilon^3}{\mathrm{Bo}} \frac{\partial^2 h}{\partial x^2} - \frac{\chi}{2\,\mathrm{Rm}} \left[\left(B^{\mathrm{a}}_{x0}\right)^2 + \left(B^{\mathrm{a}}_{Y0}\right)^2 + 2\epsilon h \left(B^{\mathrm{a}}_{x0} \frac{\partial B^{\mathrm{a}}_{x}}{\partial Y} + B^{\mathrm{a}}_{Y0} \frac{\partial B^{\mathrm{a}}_{Y}}{\partial Y} \right) \right], \tag{2.2.17d}$$

$$\frac{\partial u}{\partial y} = 0, \tag{2.2.17e}$$

where Bo is the Bond number defined in table 2.4.

While terms of $\mathcal{O}(\epsilon)$ in (2.2.12–17) are formally negligible in the limit as $\epsilon \to 0$ we have retained them, as we will find that a solvability condition at $\mathcal{O}(\epsilon)$ is needed to close the leading-order problem for the induced field.

2.2.3 The leading-order magnetic problem

We now solve system (2.2.12–17) asymptotically in the limit $\epsilon \to 0$, first for the induced field, and then for the flow, in the distinguished limit where Ha, ϵ^3/Bo, θ/ϵ, and h^{s} are $\mathcal{O}(1)$ as $\epsilon \to 0$. To this end, we expand the dependent variables in asymptotic expansions of the form

$$A^{\mathrm{i}} \sim A_0^{\mathrm{i}} + \epsilon A_1^{\mathrm{i}} + \epsilon^2 A_2^{\mathrm{i}} + \cdots \,, \tag{2.2.18}$$

and similarly for p and u. The induction equations (2.2.13) and (2.2.14), to leading-order in ϵ, become

$$\frac{\partial^2 A_0^{\mathrm{is}}}{\partial y^2} = 0, \quad \text{where} \quad -h^{\mathrm{s}} < y < 0, \tag{2.2.19a}$$
$$\frac{\partial^2 A_0^{\mathrm{i}}}{\partial y^2} = 0, \quad \text{where} \;\; 0 < y < h. \tag{2.2.19b}$$

We impose the boundary conditions: at the vacuum–substrate interface, $y = -h^{\mathrm{s}}$, $Y = 0$,

$$A_0^{\mathrm{is}} = A_0^{\mathrm{i}-}, \tag{2.2.20a}$$
$$\frac{\partial A_0^{\mathrm{is}}}{\partial y} = \frac{\chi^{\mathrm{s}}}{\mathrm{Rm}} B_{x0}^{\mathrm{a}}, \tag{2.2.20b}$$

at the liquid–substrate interface, $y = Y = 0$,

$$A_0^{\mathrm{i}} = A_0^{\mathrm{is}}, \tag{2.2.21a}$$
$$\frac{\partial A_0^{\mathrm{i}}}{\partial y} = \frac{\partial A_0^{\mathrm{is}}}{\partial y} + \frac{\chi - \chi^{\mathrm{s}}}{\mathrm{Rm}} B_{x0}^{\mathrm{a}}, \tag{2.2.21b}$$

and at the liquid–vacuum free surface, $y = h$, $Y = 0$,

$$A_0^{\mathrm{i}} = A_0^{\mathrm{i}+}, \tag{2.2.22a}$$
$$\frac{\partial A_0^{\mathrm{i}}}{\partial y} = \frac{\chi}{\mathrm{Rm}} B_{x0}^{\mathrm{a}}. \tag{2.2.22b}$$

The solution of (2.2.19–22) is given by

$$A_0^{\mathrm{is}} = A_0^{\mathrm{i}-}|_{Y=0} + (y + h^{\mathrm{s}}) \frac{\chi^{\mathrm{s}}}{\mathrm{Rm}} B_{x0}^{\mathrm{a}}, \quad \text{where} \quad -h^{\mathrm{s}} < y < 0, \tag{2.2.23a}$$
$$A_0^{\mathrm{i}} = A_0^{\mathrm{i}+}|_{Y=0} + (y - h) \frac{\chi}{\mathrm{Rm}} B_{x0}^{\mathrm{a}}, \quad \text{where} \;\; 0 < y < h. \tag{2.2.23b}$$

From (2.2.23) and (2.2.21a) it follows that

$$A_0^{\mathrm{i}+}|_{Y=0} - A_0^{\mathrm{i}-}|_{Y=0} = a(x,t), \tag{2.2.24a}$$

where

$$a(x,t) = \frac{h^{\mathrm{s}}\chi^{\mathrm{s}} + h\chi}{\mathrm{Rm}} B_{x0}^{\mathrm{a}}. \tag{2.2.24b}$$

The solution (2.2.23) determines how the induced potential varies with respect to y but not x. We will see in the toroidal case in § 2.3 that we can use the current continuity conditions (2.1.29a) and (2.1.31b) to determine the induced field at the upper and lower boundaries of the divertor. However, in the poloidal case these conditions are satisfied identically, and the problem is closed by a solvability condition at the next order, which we now derive.

The first-order induced potential satisfies

$$\frac{\partial^2 A_1^{\mathrm{is}}}{\partial y^2} = 0 \quad \text{where} \quad -h^{\mathrm{s}} < y < 0, \tag{2.2.25a}$$

$$\frac{\partial^2 A_1^{\mathrm{i}}}{\partial y^2} = -u_0 B_{Y0}^{\mathrm{a}} \quad \text{where} \quad 0 < y < h. \tag{2.2.25b}$$

At the substrate–vacuum interface we impose the boundary condition

$$\frac{\partial A_1^{\mathrm{is}}}{\partial y} = \frac{\partial A_0^{\mathrm{i}-}}{\partial Y} - \frac{\chi^{\mathrm{s}}}{\mathrm{Rm}} h^{\mathrm{s}} \frac{\partial B_{Y0}^{\mathrm{a}}}{\partial x} \quad \text{at} \quad y = -h^{\mathrm{s}},\ Y = 0, \tag{2.2.26}$$

at the liquid–substrate interface we require that

$$\frac{\partial A_1^{\mathrm{i}}}{\partial y} = \frac{\partial A_1^{\mathrm{is}}}{\partial y} \quad \text{at} \quad y = Y = 0, \tag{2.2.27}$$

and at the liquid–vacuum free surface we impose the boundary condition

$$\frac{\partial A_1^{\mathrm{i}}}{\partial y} = \frac{\partial A_0^{\mathrm{i}+}}{\partial Y} + \frac{\chi}{\mathrm{Rm}} \frac{\partial}{\partial x} \left(h B_{Y0}^{\mathrm{a}} \right), \quad \text{at} \quad y = h,\ Y = 0. \tag{2.2.28}$$

Integrating (2.2.25) we obtain

$$\left[\frac{\partial A_1^{\mathrm{i}}}{\partial y} \right]_{y=0}^{y=h} = -B_{Y0}^{\mathrm{a}}(x) \overline{Q}(x,t), \tag{2.2.29}$$

$$\left[\frac{\partial A_1^{\mathrm{is}}}{\partial y} \right]_{y=-h^{\mathrm{s}}}^{y=0} = 0, \tag{2.2.30}$$

where $\overline{Q}$ is the leading-order liquid metal flow rate, given by

$$\overline{Q}(x,t) = \int_0^{h(x,t)} u_0(x,y,t)\,\mathrm{d}y. \tag{2.2.31}$$

Upon enforcing the boundary conditions (2.2.26–28) we obtain the solvability condition

$$\left.\frac{\partial A_0^{\mathrm{i}+}}{\partial Y}\right|_{Y=0} - \left.\frac{\partial A_0^{\mathrm{i}-}}{\partial Y}\right|_{Y=0} = b(x,t), \tag{2.2.32a}$$

where

$$b(x,t) = -B^{\mathrm{a}}_{Y0}(x)\overline{Q}(x,t) - \frac{\partial}{\partial x}\left(\frac{\chi h(x,t) + \chi^{\mathrm{s}} h^{\mathrm{s}}}{\mathrm{Rm}} B^{\mathrm{a}}_{Y0}(x)\right). \tag{2.2.32b}$$

Now, in the vacuum region outside the divertor A_0^{i} solves Laplace's equation and satisfies the jump conditions (2.2.24) and (2.2.32) across the divertor. To solve this leading-order global problem we use the Plemelj formulae [2] as shown in appendix A.1, to give

$$\left.\frac{\partial A_0^{\mathrm{i}\pm}}{\partial x}\right|_{Y=0} = -\frac{1}{2\pi}\int_0^1 \frac{b(\xi,t)}{\xi - x}\,\mathrm{d}\xi \pm \frac{1}{2}\frac{\partial a}{\partial x}(x,t). \tag{2.2.33}$$

Finally, substituting (2.2.33) into (2.2.23) we obtain both components of the leading-order induced field within the divertor, namely

$$B^{\mathrm{is}}_{x0} = \frac{\partial A_0^{\mathrm{is}}}{\partial y} = \frac{h^{\mathrm{s}}\chi^{\mathrm{s}}}{\mathrm{Rm}} B^{\mathrm{a}}_{x0}, \tag{2.2.34a}$$

$$B^{\mathrm{i}}_{x0} = \frac{\partial A_0^{\mathrm{i}}}{\partial y} = \frac{h(x,t)\chi}{\mathrm{Rm}} B^{\mathrm{a}}_{x0}, \tag{2.2.34b}$$

$$B^{\mathrm{is}}_{y0} = -\frac{\partial A_0^{\mathrm{is}}}{\partial x} = \frac{1}{2\pi}\int_0^1 \frac{b(\xi,t)}{\xi - x}\,\mathrm{d}\xi - \frac{\partial}{\partial x}\left(\frac{(2y + h^{\mathrm{s}})\chi^{\mathrm{s}} - h(x,t)\chi}{2\,\mathrm{Rm}} B^{\mathrm{a}}_{x0}\right), \tag{2.2.34c}$$

$$B^{\mathrm{i}}_{y0} = -\frac{\partial A_0^{\mathrm{i}}}{\partial x} = \frac{1}{2\pi}\int_0^1 \frac{b(\xi,t)}{\xi - x}\,\mathrm{d}\xi - \frac{\partial}{\partial x}\left(\frac{h^{\mathrm{s}}\chi^{\mathrm{s}} + (2y - h(x,t))\chi}{2\,\mathrm{Rm}} B^{\mathrm{a}}_{x0}\right), \tag{2.2.34d}$$

where b is defined by (2.2.32b). The induced field varies in x through the applied field, and in both x and t through the free surface height h and the flow rate $\overline{Q}$.

The following decompositions are helpful when computing the induced field. By adding and subtracting $b(x,t)$ to the numerator of the integrand in (2.2.34), the principal-value integral may be re-expressed as

$$\fint_0^1 \frac{b(\xi,t)}{\xi - x}\,\mathrm{d}\xi = \int_0^1 \frac{b(\xi,t) - b(x,t)}{\xi - x}\,\mathrm{d}\xi + b(x,t)\log\left(\frac{1-x}{x}\right). \tag{2.2.35}$$

When $\xi \to x$, the integrand on the left-hand side of (2.2.35) diverges, whereas the integrand on the right-hand side approaches $\partial b/\partial x$, which allows for a more numerically stable computation. When computing the derivative of the principal-value integral with respect to x, the same tactic may be employed at higher order, as elucidated in the following calculation:

$$\frac{\partial}{\partial x}\left(\fint_0^1 \frac{b(\xi,t)}{\xi - x}\,\mathrm{d}\xi\right) = \fint_0^1 \frac{b(\xi,t)}{(\xi - x)^2}\,\mathrm{d}\xi \tag{2.2.36a}$$

$$= \int_0^1 \left[\frac{b(\xi,t) - b(x,t)}{(\xi - x)^2} - \frac{1}{\xi - x}\frac{\partial b}{\partial x}(x,t)\right]\mathrm{d}\xi + \frac{b(x,t)}{x(1-x)} + \frac{\partial b}{\partial x}(x,t)\log\left(\frac{1-x}{x}\right). \tag{2.2.36b}$$

Re-expressing the principal-value integral in this way exposes a logarithmic singularity in the induced field at the endpoints of the divertor $x = 0, 1$. This is a consequence of the fact that this model does not take into account how the flow enters or leaves the divertor region. We revisit this point in §2.2.5, where we show that more detailed modelling of the inlet and outlet regions regularises the endpoint singularities.

Finally, the above calculations may be extended to the case of a composite substrate comprising layers of different material, as shown in appendix A.2.1.

2.2.4 The leading-order flow problem

We now write down the leading-order flow equations, neglecting terms of orders ϵ in the momentum equations, but retaining the transverse gravitational term of order $\epsilon \cot\theta$. This simplification removes the effect of the induced (but not the applied) field on the flow.

In the fluid layer, $0 < y < h$, the leading-order governing equations are

$$\frac{\partial p_0}{\partial x} = \frac{1}{\mathrm{Ha}^2}\frac{\partial^2 u_0}{\partial y^2} + 1 - u_0\left(B^{\mathrm{a}}_{Y0}\right)^2, \tag{2.2.37a}$$

$$\frac{\partial p_0}{\partial y} = -\epsilon\cot\theta. \tag{2.2.37b}$$

At the liquid–substrate interface we have the no-slip condition

$$u_0 = 0, \quad \text{at } \ y = 0, \tag{2.2.38}$$

and at the liquid–vacuum free surface, $y = h$, we impose the dynamic boundary conditions

$$p_0 = -\frac{\epsilon^3}{\mathrm{Bo}}\frac{\partial^2 h}{\partial x^2} - \frac{\chi}{2\,\mathrm{Rm}}\left((B^{\mathrm{a}}_{x0})^2 + (B^{\mathrm{a}}_{Y0})^2\right), \tag{2.2.39a}$$

$$\frac{\partial u_0}{\partial y} = 0. \tag{2.2.39b}$$

Integrating (2.2.37b) and imposing (2.2.39a) gives the leading-order pressure

$$p_0 = \epsilon \cot\theta(h - y) - \frac{\epsilon^3}{\mathrm{Bo}}\frac{\partial^2 h}{\partial x^2} - \frac{\chi}{2\,\mathrm{Rm}}\left((B^{\mathrm{a}}_{x0})^2 + (B^{\mathrm{a}}_{Y0})^2\right). \tag{2.2.40}$$

We note that the magnetic contribution to the leading-order pressure is negative (assuming $\chi > 0$), and if strong enough, can cause negative pressures within the fluid that may lead to undesirable cavitation. This point is discussed further in §2.2.6.

Substituting (2.2.40) into (2.2.37a) gives an equation for u_0, namely

$$\frac{1}{\mathrm{Ha}^2}\frac{\partial^2 u_0}{\partial y^2} - u_0\left(B^{\mathrm{a}}_{Y0}\right)^2 + \varphi(x,t) = 0, \tag{2.2.41a}$$

where

$$\varphi(x,t) = 1 - \epsilon\cot\theta\frac{\partial h}{\partial x} + \frac{\epsilon^3}{\mathrm{Bo}}\frac{\partial^3 h}{\partial x^3} + \frac{\chi}{2\,\mathrm{Rm}}\frac{\mathrm{d}}{\mathrm{d}x}\left((B^{\mathrm{a}}_{x0})^2 + (B^{\mathrm{a}}_{Y0})^2\right). \tag{2.2.41b}$$

The successive terms in (2.2.41b) represent the driving forces for the flow, namely the components of gravity along and perpendicular to the substrate, surface tension, and the pressure due to the applied magnetic field.

Equation (2.2.41) along with boundary conditions (2.2.38) and (2.2.39b) admits the solution

$$u_0 = \frac{\varphi}{(B^{\mathrm{a}}_{Y0})^2}\left(1 - \frac{\cosh(\mathrm{Ha}(h-y)B^{\mathrm{a}}_{Y0})}{\cosh(\mathrm{Ha}\,hB^{\mathrm{a}}_{Y0})}\right). \tag{2.2.42}$$

With a strong magnetic field, $\mathrm{Ha} \gg 1$, we see that the horizontal velocity profile is approximately uniform outside the boundary layer at $y = 0$, typical of Hartmann

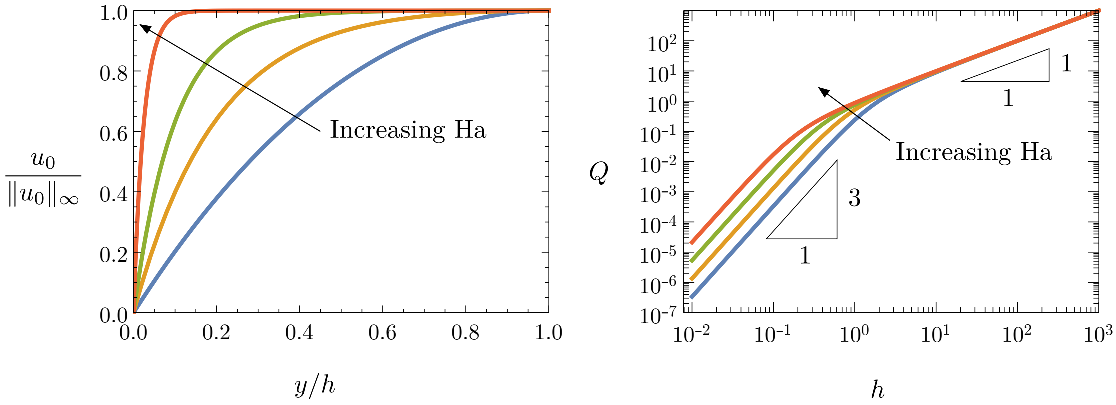

(a) $h = \varphi = B^{\mathrm{a}}_{Y0} = 1$, $\mathrm{Ha} \in \{1, 5, 10, 40\}$. *(b)* $B^{\mathrm{a}}_{Y0} = 1$, $\mathrm{Ha} \in \{1, 2, 4, 8\}$.

Figure 2.3: Hartmann flow profiles and flow rates. (a) Normalised horizontal velocity profiles with a constant applied poloidal field, given by (2.2.42). *(b) A log–log plot of flow rate as a function of fluid thickness h given by* (2.2.45).

flow, and is given by

$$u_0\big|_{\mathrm{Ha}\gg 1} \sim \frac{\varphi}{(B^{\mathrm{a}}_{Y0})^2}. \tag{2.2.43}$$

We note that the larger the y-component of the applied field, B^{a}_{Y0}, the slower the horizontal velocity, as the magnetic forces retard the flow. The standard Hartmann boundary layer adjacent to the substrate has width $\mathcal{O}(\mathrm{Ha}^{-1})$. On the other hand, from the full solution, (2.2.42), we also recover the classic parabolic viscous flow profile in the limit as the vertical component of the magnetic field vanishes

$$\lim_{B^{\mathrm{a}}_{Y0}\to 0} u_0 = \varphi\,\mathrm{Ha}^2\left(hy - \frac{y^2}{2}\right). \tag{2.2.44}$$

In figure 2.3(a) we plot flow profiles for a variety of field strengths and observe that the stronger the applied field the more uniform (and less parabolic) the velocity profile becomes.

The horizontal velocity (2.2.42) allows us to calculate the flow rate $\overline{Q} = \varphi Q$, where the flux function Q is given by

$$Q = \frac{1}{\varphi}\int_0^h u_0\,\mathrm{d}y = \frac{h}{(B^{\mathrm{a}}_{Y0})^2}\left(1 - \frac{\tanh(\mathrm{Ha}\,hB^{\mathrm{a}}_{Y0})}{\mathrm{Ha}\,hB^{\mathrm{a}}_{Y0}}\right). \tag{2.2.45}$$

It is noteworthy that for small h the flux function Q varies cubically with the liquid layer thickness, reducing to the classical hydrodynamical behaviour, whereas for large h the relationship is affine (see figure 2.3(b)).

From (2.2.2) and (2.2.45) we obtain the equation governing the evolution of the free surface, namely

$$\frac{\partial h}{\partial t} + \frac{\partial}{\partial x}\left[\frac{\varphi h}{(B^{\mathrm{a}}_{Y0})^2}\left(1 - \frac{\tanh(\mathrm{Ha}\, h B^{\mathrm{a}}_{Y0})}{\mathrm{Ha}\, h B^{\mathrm{a}}_{Y0}}\right)\right] = 0. \tag{2.2.46}$$

In the physically relevant limit in which $\epsilon \cot\theta$ and $\epsilon^3/\,\mathrm{Bo}$ are small, both B^{a}_{Y0} and φ are functions of x alone, so that equation (2.2.46) is a first-order hyperbolic partial differential equation of the form

$$\frac{\partial h}{\partial t} + \frac{\partial}{\partial x}\left(\varphi(x) Q(x,h)\right) = 0, \tag{2.2.47}$$

with

$$\varphi(x) = 1 + \frac{\chi}{2\,\mathrm{Rm}}\frac{\mathrm{d}}{\mathrm{d}x}\left((B^{\mathrm{a}}_{x0})^2 + (B^{\mathrm{a}}_{Y0})^2\right), \tag{2.2.48}$$

and Q defined by (2.2.45). The steady-state film thickness profile $h(x)$ is determined by the implicit equation

$$\varphi(x) Q(x,h) = 1. \tag{2.2.49}$$

In the exceptional case where the applied field is constant, then φ is constant, and the steady free-surface profile is also constant.

When the Hartmann number is large (see table 2.4), then the flux function (2.2.45) simplifies to

$$Q(x,h) \sim \frac{h}{(B^{\mathrm{a}}_{Y0}(x))^2} - \frac{1}{\mathrm{Ha}\,(B^{\mathrm{a}}_{Y0}(x))^3}, \tag{2.2.50}$$

up to exponentially small corrections. Therefore the steady film profile is given by

$$h(x) \sim \frac{(B^{\mathrm{a}}_{Y0}(x))^2}{\varphi(x)} + \frac{1}{\mathrm{Ha}\, B^{\mathrm{a}}_{Y0}(x)}, \tag{2.2.51}$$

and the film thickness scales with the square of the transverse applied field: where the applied field is stronger, the flow is slower, and thus the fluid height increases. However, the approximation (2.2.51) breaks down near any points where $B^{\mathrm{a}}_{Y0}(x)$ passes through zero. Indeed, when the applied field is equal to zero, the flux reverts

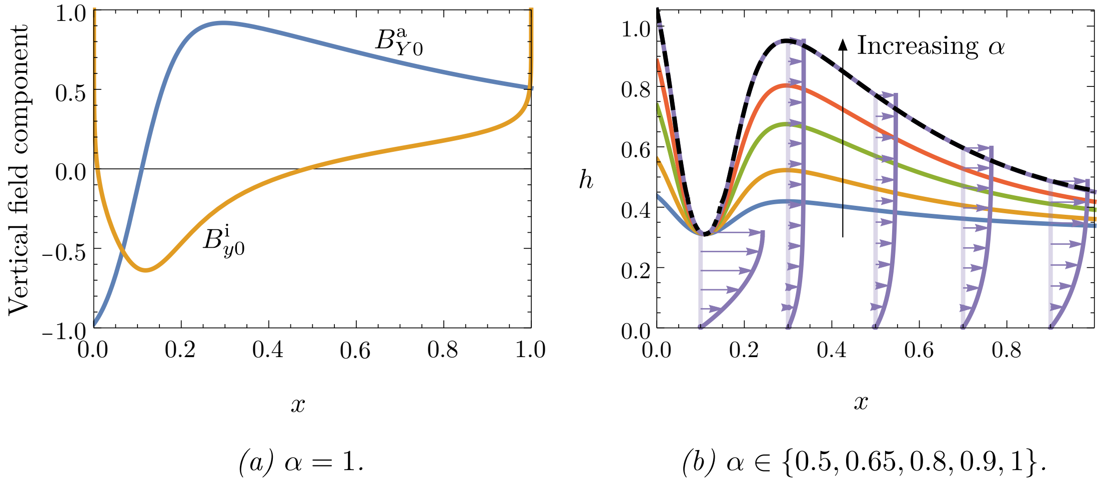

Figure 2.4: The base applied field is given by a sum of fundamental solutions of Laplace's equation:

$$A^{\mathrm{a}}(x,Y) = \frac{\alpha}{8}\sum_{i=1}^{2}\log\left((x-x_i)^2 + (Y-Y_i)^2\right),$$

for $(x_1, Y_1) = (0.2, 0.45)$ *and* $(x_2, Y_2) = (0.1, 0.15)$. *Other parameters used were* $\mathrm{Ha} = 10$, $\varphi = 1$, *and* $\chi = \chi^s = 0$. *(a) The* Y*-component of the applied magnetic field,* $B^{\mathrm{a}}_{Y0} = -\mathrm{d}A^{\mathrm{a}}/\mathrm{d}x|_{Y=0}$, *and the* y*-component of the associated induced field,* B^{i}_{y0}, *from* (2.2.34) *and* (2.2.35) *with* $\alpha = 1$. *(b) The steady-state fluid thicknesses given by* (2.2.49) *for different values of the applied field strength* α. *The dashed and dotted curves show the outer and inner asymptotic approximations, respectively given by* (2.2.55) *and* (2.2.61). *The outer solution is drawn in the region beyond* $x \in [x_0 - 0.4, x_0 + 0.4]$, *while the inner solution is drawn for* $\xi \in [-2, 2]$.

to the hydrodynamic limit

$$Q(x,h) \to \frac{\mathrm{Ha}^2\, h^3}{3} \quad \text{as} \quad B^{\mathrm{a}}_{Y0} \to 0, \tag{2.2.52}$$

which implies for the film thickness

$$h(x) \to \mathrm{Ha}^{-2/3}\left(\frac{3}{\varphi(x)}\right)^{1/3} \quad \text{as} \quad B^{\mathrm{a}}_{Y0} \to 0. \tag{2.2.53}$$

For large values of Ha, we therefore expect the film thickness to decrease markedly close to points where the transverse applied field changes sign, and ultimately to become insensitive to the applied field strength.

An applied field exhibiting a sign change has been used to compute steady-state induced field and free-surface profiles, as shown in figure 2.4. In figure 2.4(a) we plot the vertical components of both the applied and the induced field. Since we have set the magnetic susceptibility of the fluid to zero, $\chi = 0$, we see from (2.2.34) that the field does not vary with y, and we may plot it as solely a function of x. We observe the logarithmic singularity of the induced field manifest in the field diverging at the endpoints.

In figure 2.4(b) we show how the film thickness profile depends on variations in the applied field strength. As anticipated, the film varies significantly with x according to the strength of the local applied field, and the horizontal velocity profile transitions from parabolic to uniform moving from the region of weak field to strong field. The film thin dramatically near $x \approx 0.1$ where the applied field changes sign, attaining a minimum value of $3^{1/3}\,\mathrm{Ha}^{-2/3} \approx 0.31$ which is independent of the magnitude α of the applied field.

A matched asymptotic expansions approach further uncovers the spatial variation in film thickness both in regions of high field and close to sign change, exhibited in figure 2.4. The steady free surface is governed by equation (2.2.49). Fixing $\varphi = 1$, and at first considering $\mathrm{Ha}\, B^{\mathrm{a}}_{Y0}(x) \gg 1$ we expand Q via

$$Q \sim \frac{h}{(B^{\mathrm{a}}_{Y0})^2} - \frac{1}{\mathrm{Ha}\,|B^{\mathrm{a}}_{Y0}|^3}, \tag{2.2.54}$$

where the asymptotic expansion (2.2.54) is valid up to an exponentially small correction. Setting $Q = 1$ and rearranging, we find that the free surface is given by

$$h \sim (B^{\mathrm{a}}_{Y0})^2 + \frac{1}{\mathrm{Ha}\,|B^{\mathrm{a}}_{Y0}|}. \tag{2.2.55}$$

Approximation (2.2.55) breaks down in the vicinity of a sign change in B^{a}_{Y0}, where $\mathrm{Ha}\,|B^{\mathrm{a}}_{Y0}(x)| \lesssim 1$. Denoting the sign-change location by x_0, so $B^{\mathrm{a}}_{Y0}(x_0) = 0$, we employ the scalings

$$x = x_0 + \frac{X}{\mathrm{Ha}^{1/3}} \left| \frac{\mathrm{d}B^{\mathrm{a}}_{Y0}}{\mathrm{d}x}(x_0) \right|^{-1}, \quad h(x) = \frac{H(X)}{\mathrm{Ha}^{2/3}}, \quad B^{\mathrm{a}}_{Y0}(x) = \frac{b(X)}{\mathrm{Ha}^{1/3}}, \tag{2.2.56a–c}$$

and Taylor expand the applied field to give

$$b(X) = \pm X + \frac{X^2}{2\,\mathrm{Ha}^{1/3}} \frac{\mathrm{d}^2 B^{\mathrm{a}}_{Y0}}{\mathrm{d}x^2}(x_0) \left| \frac{\mathrm{d}B^{\mathrm{a}}_{Y0}}{\mathrm{d}x}(x_0) \right|^{-1} + \cdots, \tag{2.2.57}$$

where the sign of the first term matches the sign of the local field gradient. The flux then takes the form

$$Q = \frac{H}{b^2}\left(1 - \frac{\tan(Hb)}{Hb}\right), \tag{2.2.58}$$

allowing us to pose the steady equation $Q(H, X) = 1$ in terms of H, which takes the leading-order form

$$HX - \tanh(HX) \sim X^3, \tag{2.2.59}$$

subject to the matching conditions

$$H \sim X^2 + \frac{1}{|X|} \quad \text{as} \quad X \to -\infty. \tag{2.2.60}$$

The leading-order inner solution of (2.2.59) is given parametrically by

$$X = (\xi - \tanh\xi)^{1/3}, \qquad\qquad H = \frac{\xi}{(\xi - \tanh\xi)^{1/3}}. \tag{2.2.61a,b}$$

Writing $H \sim (\xi + 1 - 1)\,(\xi - \tanh\xi)^{-1/3} \sim (\xi+1)^{2/3} - (\xi - \tanh\xi)^{-1/3}$, we see that the matching conditions (2.2.60) are satisfied as $\xi \to -\infty$.

In figure 2.4(b), we plot the outer and inner solutions as black dashed and dotted curves, respectively, where we see that, for $\mathrm{Ha} = 10$, this matched expansion quantifies the free-surface thickness in the transition between high and low field. In particular, the inner approximation tells us that the minimum film thickness occurs at $X \sim 0$ and $H \sim 3^{1/3}$. By reversing the scalings (2.2.56) we infer that the minimum thickness occurs at the point $x = x_0$ where the applied field B^{a}_{Y0} is zero, and is given by $h(x_0) \sim 3^{1/3}/\,\mathrm{Ha}^{2/3}$, regardless of the form of the applied field.

When $\chi \neq 0$ the induced field exhibits y-dependence, as illustrated in figure 2.5(a) where $\chi = \mathrm{Rm}$. The sharply varying film thickness results in an induced field with rich structure: there are regions where the induced field is purely horizontal both near the sign change of the applied field $x \approx 0.1$ as well as near $x \approx 0.4$ in the vicinity of the substrate. The associated current is computed using

$$j = \partial B^{\mathrm{i}}_{x0}/\partial y - \partial B^{\mathrm{i}}_{y0}/\partial x, \tag{2.2.62}$$

which is plotted in figure 2.5(b). We observe in particular that large negative currents are induced near the minimum of the film thickness, where there is a large

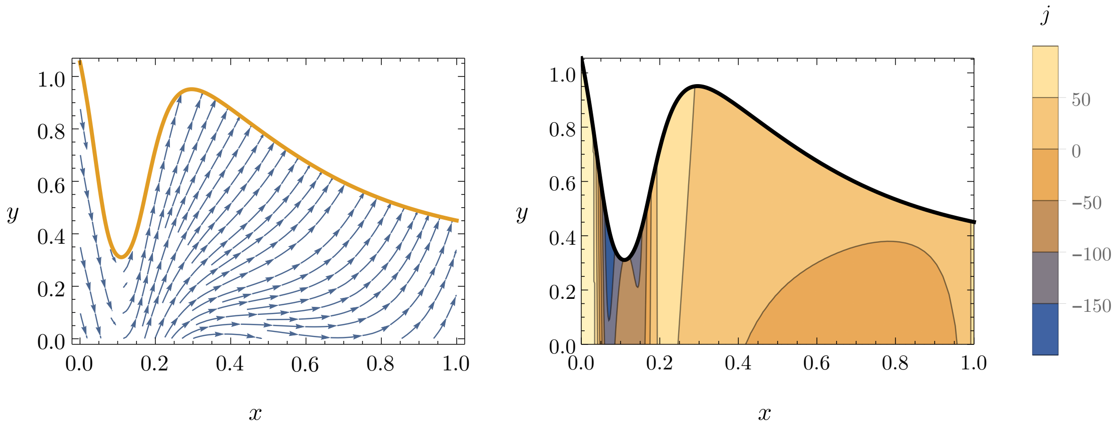

(a) Induced magnetic field $(B^{\mathrm{i}}_{x0}, B^{\mathrm{i}}_{y0})$. *(b) Induced current* j.

Figure 2.5: Induced fields (2.2.34) *and associated current magnitudes* (2.2.62) *with* $\mathrm{Ha} = 10$, $\varphi = \chi = \mathrm{Rm} = h^s = 1$, $\chi^s = 0$, *and the same applied field as in figure 2.4.*

curvature of free surface.

In summary, for a two-dimensional system with purely poloidal magnetic field the leading-order flow is strongly affected by a strong applied field but decouples from the induced field. In regions of high field, the flow is decelerated and made more uniform, and thus the film thickness is greater. The leading-order induced magnetic field depends on the flow, and can be determined via a non-local transform of the applied field, flow rate, and film height.

2.2.5 Regularising the logarithmic singularity

The solution for the induced magnetic field (2.2.34) exhibits a logarithmic singularity at the endpoints of the divertor, since b does not vanish there (due to the fact that $\overline{Q}$, h, and h^{s} do not vanish there, see (2.2.32b) and figure 2.4). However, we argue that this singularity is a remnant of the idealised model, and thus we do not expect it to have any physical manifestation. More specifically, we demonstrate that the singularity is the result of the model not considering the details of how the fluid inlet and outlet operate. To take these into account realistically is cumbersome, and would require detailed knowledge of the local geometry. Instead, we take an idealised approach that abstracts away the physical details of the inlet and outlet but still manages to regularise the singularity.

Consider an inlet channel of (dimensionless) width L through which we introduce the liquid metal with a net flow rate of 1, as illustrated in figure 2.6. For the sake

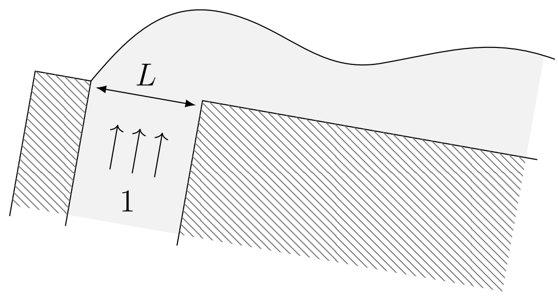

Figure 2.6: A schematic of the inlet of width L through which we pump liquid metal at a flow rate 1.

of simplicity, we consider the flow rate to be uniform across the width of the inlet and not varying with time. These assumptions may be relaxed if more information is available, but for the sake of demonstrating the suppression of the singularity this simple description will suffice. We model the outlet similarly, with a uniform net flow rate of -1. The thin-film equation (2.2.2) now includes a source term and takes the form

$$\frac{\partial h}{\partial t} + \frac{\partial \overline{Q}}{\partial x} = \begin{cases} 1/L, & 0 < x < L, \\ 0, & L < x < 1 - L, \\ -1/L, & 1 - L < x < 1. \end{cases} \tag{2.2.63}$$

The steady-state solution for the flow rate $\overline{Q}$ across the entire divertor therefore comprises three regions; an inlet zone, the main region, and an outlet zone: $\overline{Q}$ is constant in the main region, and tends linearly to zero in both the inlet and outlet zones. Moreover, h tends to zero in these end zones, and h^{s} is zero there. It then follows that the logarithmic singularity in the induced field is indeed suppressed.

Naturally, as we shrink the width of the inlet/outlet regions, $L \to 0$, the induced field given by (2.2.34) becomes increasingly singular, reflecting the fact that the origin of the logarithmic singularity is ignoring the fluid entering/exiting the system. If the size L of the inlet becomes comparable to ϵ, then a fully two-dimensional theory is needed to model the flow and induced field in this region.

2.2.6 Negative pressures

If pressure in the flow drops below the vapour pressure, the liquid lithium will be at risk of cavitation. Experiments show that cavitation is a source of concern for plasma-facing components [228]. The actual pressure required for the inception of

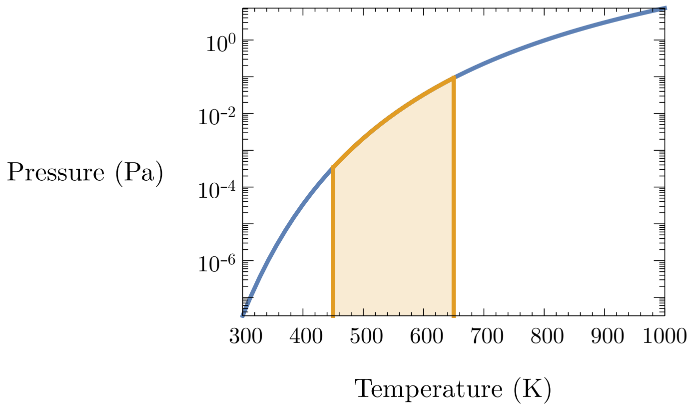

Figure 2.7: Vapour pressure of lithium from [78]*. A reasonable region of operating temperatures* $[450, 650]$ K *is highlighted.*

cavitation may differ from the vapour pressure, and be dependent on other factors, like contamination of the substance [21], however in the absence of reliable experimental data on the matter we focus on the vapour pressure. The vapour pressure for lithium in the operating temperature range of $[450, 650]$ K lies approximately in $[10^{-8}, 10^{-3}]$ Pa (see figure 2.7). The equivalent dimensionless range is obtained by dividing by a factor of $\sigma^* \mathscr{B}^{*2} \mathscr{U}^* \mathscr{L}^* \approx 10^3$ Pa (see (2.2.6e) as well as tables 2.1 and 2.2). We deduce that the dimensionless cavitation pressure is low, and so for our purposes it will suffice to analyse where the pressure in our system becomes negative.

The leading order pressure, (2.2.40), is given by

$$p_0 = \epsilon \cot\theta (h - y) - \frac{\epsilon^3}{\mathrm{Bo}} \frac{\partial^2 h}{\partial x^2} - \frac{\chi}{2\,\mathrm{Rm}} \left[(B^{\mathrm{a}}_{x0})^2 + (B^{\mathrm{a}}_{Y0})^2 \right]. \tag{2.2.64}$$

The lowest pressure is encountered at the free surface, $y = h$. If we neglect the contribution of surface tension, valid when $\epsilon^3/\,\mathrm{Bo} \ll 1$, (see table 2.4) or the surface is reasonably flat, then the surface pressure is given by the magnetic pressure term proportional to $-\chi/2\,\mathrm{Rm}$, which might be non-negligible (see table 2.2). This pressure term is caused by the difference in magnetic susceptibilities, and could be negated if the liquid metal used had a negative susceptibility, $\chi < 0$. The negative surface pressure persists to a significant depth of the layer when $\chi \tan\theta/(\epsilon\,\mathrm{Rm}) = \chi \eta^* \tan\theta/\mathscr{Q}^* \gtrsim \mathcal{O}(1)$, so the likelihood of cavitation may also be reduced by decreasing the inclination angle θ or increasing the flow rate $\mathscr{Q}^*$.

2.3 The Toroidal case

2.3.1 Axisymmetric geometry

In this section we consider a toroidal applied field, that is, a field that is perpendicular to the plane of the flow. For the sake of simplicity, it is tempting to consider a two-dimensional flow and a Cartesian geometry, as in the poloidal case in § 2.2. However, in the toroidal case and in a Cartesian frame, the requirement that the applied field be curl-free beyond the divertor implies that it is spatially uniform. It then follows that the magnetohydrodynamic effect on the flow vanishes, and the leading-order flow must be purely hydrodynamic. To see this, recall that, given the assumed symmetry of the geometry, both the induction equation (2.1.24) and the magnetic boundary conditions (2.1.25) are homogeneous in the poloidal directions. It follows that a purely toroidal applied field produces a purely toroidal induced field. The MHD forces on the flow, in (2.1.28e), take the form

$$\boldsymbol{j}^* \times \boldsymbol{B}^* = \frac{1}{\mu^*} \left(\boldsymbol{\nabla}^* \times \boldsymbol{B}^*\right) \times \boldsymbol{B}^* = \frac{1}{\mu^*}(\boldsymbol{B}^* \cdot \boldsymbol{\nabla}^*)\boldsymbol{B}^* - \frac{1}{2\mu^*}\boldsymbol{\nabla}^* \left(|\boldsymbol{B}^*|^2\right), \tag{2.3.1}$$

where the final equality comes from standard vector identities. For a toroidal applied field in a planar geometry, the first term on the right-hand side of (2.3.1) must vanish. The second term is a magnetic pressure, and may be adjoined to the hydrodynamic pressure in the absence of a free surface [169]. With a free surface, this term will affect the flow due to the free-surface pressure condition, however, it turns out that its contribution is exceedingly small (as both the applied field and the leading-order induced field are spatially uniform). Previous authors [56, 148] have encountered this difficulty and have merely proceeded assuming the applied field varies spatially, ignoring the spurious currents associated with such an assumption.

In this section, we instead consider an axisymmetric geometry with a conical divertor. In this scenario, we find that requiring the applied field to be curl-free implies that the field is inversely proportional to the radial distance from the axis of symmetry. The first term in (2.3.1) thus no longer vanishes, and the applied magnetic field imposes a nontrivial forcing to the fluid.

2.3.2 Coordinate system

We consider the axisymmetric geometry sketched in figure 2.8. The liquid metal flows on a conical substrate inclined at an angle θ to the horizontal, and is subject

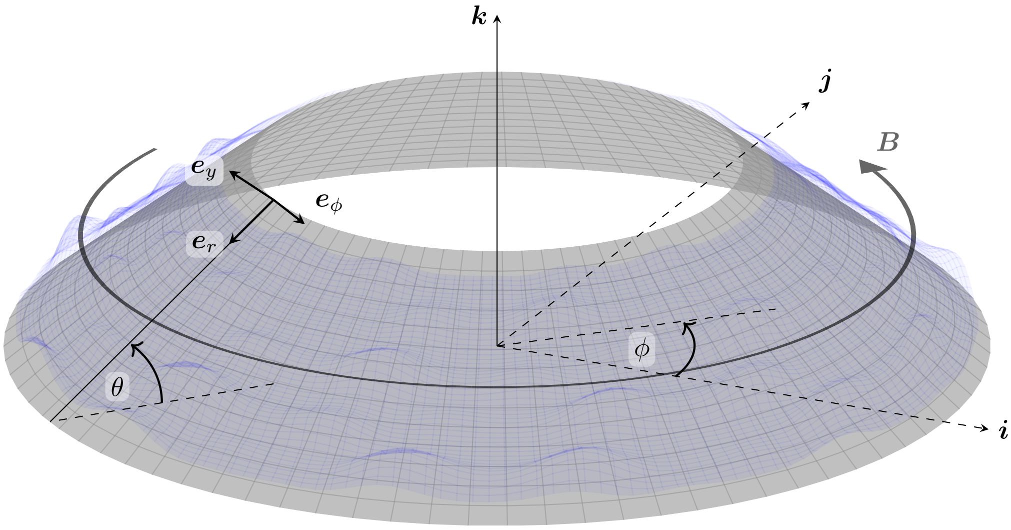

Figure 2.8: Schematic of the truncated conical divertor and free surface in the presence of a toroidal applied field $\boldsymbol{B}^*$. The Cartesian coordinate basis is $(\boldsymbol{i}, \boldsymbol{j}, \boldsymbol{k})$, and the local divertor coordinate basis is $(\boldsymbol{e}_r, \boldsymbol{e}_\phi, \boldsymbol{e}_y)$. The inclination angle of the divertor to the horizontal is θ. Dashed lines lie in the same horizontal plane.

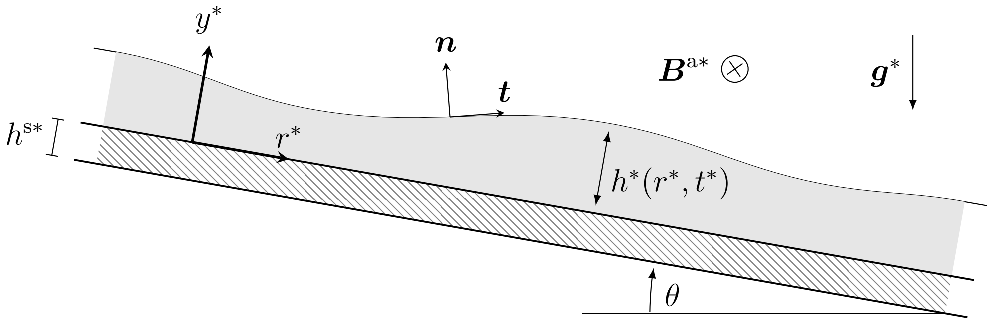

Figure 2.9: Schematic of the axisymmetric divertor configuration in the presence of a toroidal applied field.

to a magnetic field $\boldsymbol{B}^*$ which acts purely in the azimuthal direction. We define coordinates (r^*, y^*, ϕ) that lie parallel and normal to the substrate as follows:

$$\boldsymbol{r}^*(r^*, y^*, \phi) = (r^* \cos\theta + y^* \sin\theta)(\boldsymbol{i}\cos\phi + \boldsymbol{j}\sin\phi) + (y^*\cos\theta - r^*\sin\theta)\boldsymbol{k}, \quad (2.3.2)$$

where $(\boldsymbol{i}, \boldsymbol{j}, \boldsymbol{k})$ is the usual Cartesian coordinate basis. The coordinates (r^*, y^*, ϕ) are orthogonal, with scale factors given by

$$\left|\frac{\partial \boldsymbol{r}^*}{\partial r^*}\right| = 1, \qquad \left|\frac{\partial \boldsymbol{r}^*}{\partial y^*}\right| = 1, \qquad \left|\frac{\partial \boldsymbol{r}^*}{\partial \phi}\right| = R^*, \qquad (2.3.3\text{a–c})$$

where the distance from the central axis is denoted by

$$R^* = r^* \cos\theta + y^* \sin\theta > 0. \tag{2.3.4}$$

It is therefore straightforward to express the governing equations using the standard formulae for orthogonal curvilinear coordinates (for example, see chapter 2 in [212]).

We consider axisymmetric flow, with the velocity and pressure given by

$$\boldsymbol{u}^* = u^*(r^*, y^*, t^*)\boldsymbol{e}_r + v^*(r^*, y^*, t^*)\boldsymbol{e}_y, \qquad p^* = p^*(r^*, y^*, t^*), \tag{2.3.5a,b}$$

where the unit vectors in the coordinate system are denoted by $\boldsymbol{e}_r$, $\boldsymbol{e}_y$, and $\boldsymbol{e}_\phi$. We similarly assume that the free surface of the liquid is axisymmetric.

As noted in the beginning of this section, a purely toroidal applied field induces a purely toroidal field, and we therefore restrict our attention henceforth to magnetic fields of the form

$$\boldsymbol{B}^* = B^*(r^*, y^*, t^*)\boldsymbol{e}_\phi. \tag{2.3.6}$$

The corresponding two-dimensional configuration is sketched in figure 2.9. Next we spell out in detail how the governing equations and boundary conditions, (2.1.26–32), simplify in each region and on each interface in the problem.

2.3.3 Governing equations and boundary conditions

Vacuum

In $y^* < -h^{s*}$ and $y^* > h^*(r^*, t^*)$, we assume there is effectively free space, in which Maxwell's equations (2.1.26) are $\boldsymbol{\nabla}^* \cdot \boldsymbol{B}^* = 0$ and $\boldsymbol{\nabla}^* \times \boldsymbol{B}^* = \boldsymbol{0}$, which can only be satisfied by a magnetic field proportional to $1/R^*$, where R^* is defined by (2.3.4). We therefore set the external field to be

$$B^* = B^{a*}(r^*, y^*) = \frac{\mathscr{B}^* \mathscr{L}^*}{R^*} = \frac{\mathscr{B}^* \mathscr{L}^*}{r^* \cos\theta + y^* \sin\theta}, \tag{2.3.7}$$

where $\mathscr{L}^*$ is a length-scale and $\mathscr{B}^*$ is a parameter measuring the field strength; in principle $\mathscr{B}^*$ could be a function of time, but we will take it to be constant. The applied field B^{a*} is assumed to be given and, in practice, is generated by electromagnets some distance from the divertor.

Liquid

In $0 < y^* < h^*(r^*, t^*)$, we seek solutions with axisymmetric velocity and magnetic field given by (2.3.5a,b) and (2.3.6). It is also helpful to decompose the magnetic field according to

$$B^* = (1+\chi)\, B^{\mathrm{a}*} + B^{\mathrm{i}*}, \tag{2.3.8}$$

where $B^{\mathrm{a}*}$ is again the known applied field, given by (2.3.7), and χ is the magnetic susceptibility of the liquid. By substitution into (2.1.28c), we find that the induced field B^{i} in the liquid satisfies the equation

$$\begin{aligned}\frac{\partial B^{\mathrm{i}*}}{\partial t^*} - \eta^* \left[\frac{\partial}{\partial r^*}\left(\frac{1}{R^*}\frac{\partial}{\partial r^*}\left(R^* B^{\mathrm{i}*}\right)\right) + \frac{\partial}{\partial y^*}\left(\frac{1}{R^*}\frac{\partial}{\partial y^*}\left(R^* B^{\mathrm{i}*}\right)\right)\right] \\ = -R^* u^* \frac{\partial}{\partial r^*}\left[\frac{(1+\chi)B^{\mathrm{a}*} + B^{\mathrm{i}*}}{R^*}\right] - R^* v^* \frac{\partial}{\partial y^*}\left[\frac{(1+\chi)B^{\mathrm{a}*} + B^{\mathrm{i}*}}{R^*}\right],\end{aligned} \tag{2.3.9}$$

where η^* is the magnetic diffusivity of the liquid metal.

Next we write out the Navier–Stokes equations (2.1.28d) and (2.1.28e) with respect to our orthogonal coordinate system, namely

$$\frac{\partial}{\partial r^*}(R^* u^*) + \frac{\partial}{\partial y^*}(R^* v^*) = 0, \tag{2.3.10a}$$

$$\begin{aligned}\rho^*\left(\frac{\partial u^*}{\partial t^*} + u^*\frac{\partial u^*}{\partial r^*} + v^*\frac{\partial u^*}{\partial y^*}\right) = \frac{\rho^*\nu^*}{R^*}\left[\frac{\partial^2}{\partial r^{*2}}(R^* u^*) + \frac{\partial}{\partial y^*}\left(R^*\frac{\partial u^*}{\partial y^*} + v\frac{\partial R^*}{\partial r^*}\right)\right] \\ - \frac{\partial p^*}{\partial r^*} + \rho^*\,|\boldsymbol{g}^*|\sin\theta - \frac{(1+\chi)B^{\mathrm{a}*} + B^{\mathrm{i}*}}{(1+\chi)\mu_0^* R^*}\frac{\partial}{\partial r^*}\left(R^* B^{\mathrm{i}*}\right),\end{aligned} \tag{2.3.10b}$$

$$\begin{aligned}\rho^*\left(\frac{\partial v^*}{\partial t^*} + u^*\frac{\partial v^*}{\partial r^*} + v^*\frac{\partial v^*}{\partial y^*}\right) = \frac{\rho^*\nu^*}{R^*}\left[\frac{\partial^2}{\partial y^{*2}}(R^* v^*) + \frac{\partial}{\partial r^*}\left(R^*\frac{\partial v^*}{\partial r^*} + u^*\frac{\partial R^*}{\partial y^*}\right)\right] \\ - \frac{\partial p^*}{\partial y^*} - \rho^*\,|\boldsymbol{g}^*|\cos\theta - \frac{(1+\chi)B^{\mathrm{a}*} + B^{\mathrm{i}*}}{(1+\chi)\mu_0^* R^*}\frac{\partial}{\partial y^*}\left(R^* B^{\mathrm{i}*}\right).\end{aligned} \tag{2.3.10c}$$

Substrate

In $-h^{\mathrm{s}*} < y^* < 0$, we substitute for $\boldsymbol{B}^*$ from (2.3.6) and again decompose the toroidal magnetic flux component as follows:

$$B^* = (1+\chi^{\mathrm{s}})\, B^{\mathrm{a}*} + B^{\mathrm{is}*}, \tag{2.3.11}$$

where χ^{s} is the magnetic susceptibility of the substrate. It then follows from (2.1.27c) that the induced field $B^{\mathrm{is}*}$ in the substrate satisfies the equation

$$\frac{\partial B^{\mathrm{is}*}}{\partial t^*} = \eta^{\mathrm{s}*}\left[\frac{\partial}{\partial r^*}\left(\frac{1}{R^*}\frac{\partial}{\partial r^*}\left(R^* B^{\mathrm{is}*}\right)\right) + \frac{\partial}{\partial y^*}\left(\frac{1}{R^*}\frac{\partial}{\partial y^*}\left(R^* B^{\mathrm{is}*}\right)\right)\right]. \qquad (2.3.12)$$

Vacuum–fluid

Next we apply the boundary conditions (2.1.31) at the free surface $y^* = h^*(r^*, t^*)$ of the fluid. Given the axisymmetric geometry and purely toroidal magnetic field, the magnetic boundary condition (2.1.31c) is satisfied identically, while the conditions (2.1.31b) and (2.1.31d) are both equivalent to

$$\left[\frac{B^*}{\mu^*}\right]_-^+ = 0. \qquad (2.3.13)$$

Upon decomposing the magnetic field according to (2.3.8), we find that (2.3.13) reduces to the condition

$$B^{\mathrm{i}*} = 0 \quad \text{at} \quad y^* = h^*(r^*, t^*) \qquad (2.3.14)$$

on the induced field at the free surface. The electromagnetic jump condition (2.1.19b) provides an effective boundary condition for the electric field $\boldsymbol{E}^*$ in the vacuum above the liquid, should one wish to calculate it.

We note here in passing that the *ad hoc* approach adopted by [56] introduces spurious currents in the vacuum regions $y^* < -h^{\mathrm{s}*}$ and $y^* > h^*$, and gives rise to an irreconcilable inconsistency between the electromagnetic boundary conditions (2.1.31b) and (2.1.31d), except in the special case where the magnetic susceptibility of the fluid, χ, is zero.

In component form, the fluid dynamic boundary conditions (2.1.31e–g) at the free surface $y^* = h^*(r^*, t^*)$ read

$$v^* = \frac{\partial h^*}{\partial t^*} + u^* \frac{\partial h^*}{\partial r^*}. \tag{2.3.15a}$$

$$\left[1 - \left(\frac{\partial h^*}{\partial r^*}\right)^2\right] \left[\frac{\partial u^*}{\partial y^*} + \frac{\partial v^*}{\partial r^*}\right] + 2\frac{\partial h^*}{\partial r^*}\left[\frac{\partial v^*}{\partial y^*} - \frac{\partial u^*}{\partial r^*}\right] = 0, \tag{2.3.15b}$$

$$2\rho^* \nu^* \left[1 + \left(\frac{\partial h^*}{\partial r^*}\right)^2\right]^{-1} \left[\frac{\partial v^*}{\partial y^*} - \frac{\partial h^*}{\partial r^*}\left(\frac{\partial u^*}{\partial y^*} + \frac{\partial v^*}{\partial r^*}\right) + \left(\frac{\partial h^*}{\partial r^*}\right)^2 \frac{\partial u^*}{\partial r^*}\right] = p^* + \frac{\chi \left(B^{\mathrm{a}*}\right)^2}{2\mu_0^*} - \gamma^* \varkappa^*, \tag{2.3.15c}$$

where the free surface curvature is given by

$$\varkappa^* = -\left[1 + \left(\frac{\partial h^*}{\partial r^*}\right)^2\right]^{-3/2} \frac{\partial^2 h^*}{\partial r^{*2}} + \frac{1}{R^*}\left[1 + \left(\frac{\partial h^*}{\partial r^*}\right)^2\right]^{-1/2} \left(\sin\theta - \cos\theta \frac{\partial h^*}{\partial r^*}\right). \tag{2.3.15d}$$

Fluid–substrate

At $y^* = 0$, the induced field continuity condition in (2.1.31c) is again satisfied identically, and the remaining independent conditions for the magnetic field are

$$\frac{B^{\mathrm{is}*}}{1+\chi^{\mathrm{s}}} = \frac{B^{\mathrm{i}*}}{1+\chi}, \qquad \eta^{\mathrm{s}*}\frac{\partial}{\partial y^*}\left(R^* B^{\mathrm{is}*}\right) = \eta^* \frac{\partial}{\partial y^*}\left(R^* B^{\mathrm{i}*}\right), \tag{2.3.16a,b}$$

while the velocity satisfies the no-slip condition

$$u^* = v^* = 0. \tag{2.3.17}$$

Substrate–vacuum

Finally, at the boundary $y^* = -h^{\mathrm{s}*}$ between the substrate and the vacuum below, the boundary conditions (2.1.29) all collapse to

$$B^{\mathrm{is}*} = 0. \tag{2.3.18}$$

As before, the condition (2.1.19b) provides a boundary condition for the electric field in the space below the substrate, should one wish to solve for it.

2.3.4 The leading-order dimensionless model

We now non-dimensionalise the equations and boundary conditions and then exploit the sizes of the relevant dimensionless parameters to simplify the resulting model. With typical length- and thickness-scales for the film, $\mathscr{L}^*$ and $\mathscr{H}^*$, respectively, we assume that the aspect ratio $\epsilon = \mathscr{H}^*/\mathscr{L}^*$ is small. By balancing viscous stress with gravity in (2.3.10c), we infer a suitable velocity scale

$$\mathscr{U}^* = \frac{\mathscr{H}^{*2}\,|\boldsymbol{g}^*|\sin\theta}{\nu^*}. \tag{2.3.19}$$

The variables are then non-dimensionalised as follows:

$$\begin{aligned}
r^* &= \mathscr{L}^* r, & y^* &= \mathscr{H}^* y, && \text{(2.3.19a,b)}\\
u^* &= \mathscr{U}^* u, & v^* &= \epsilon\mathscr{U}^* v, && \text{(2.3.19c,d)}\\
p^* &= \rho^*\,|\boldsymbol{g}^*|\,\mathscr{L}^*\sin\theta\, p, & t^* &= (\mathscr{L}^*/\mathscr{U}^*)\, t, && \text{(2.3.19e,f)}\\
B^{\mathrm{i}*} &= \frac{2\epsilon^2(1+\chi)\mathscr{B}^*\mathscr{L}^*\mathscr{U}^*}{\eta^*\cos\theta}\, B^{\mathrm{i}}, & h^* &= \mathscr{H}^* h, && \text{(2.3.19g,h)}
\end{aligned}$$

For the moment, we neglect terms of order ϵ^2 and $\epsilon^2\,\mathrm{Rm}$ (both of which are certainly very small) to get a leading-order lubrication model.

The magnetic field in the substrate satisfies the leading-order version of (2.3.12), namely

$$\frac{\partial^2 B^{\mathrm{is}}}{\partial y^2} = 0, \tag{2.3.20}$$

while the boundary conditions (2.3.16) and (2.3.18) reduce to

$$B^{\mathrm{is}} = 0 \qquad \text{at} \;\; y = -h^{\mathrm{s}}, \tag{2.3.21a}$$

$$\frac{B^{\mathrm{is}}}{1+\chi^{\mathrm{s}}} = \frac{B^{\mathrm{i}}}{1+\chi}, \qquad \eta^{\mathrm{s}*}\frac{\partial B^{\mathrm{is}}}{\partial y} = \eta^*\frac{\partial B^{\mathrm{i}}}{\partial y} \qquad \text{at} \;\; y = 0, \tag{2.3.21b,c}$$

where the substrate thickness h^{s} has been normalised with the film thickness scaling $\mathscr{H}^*$. By eliminating B^{is}, we deduce that the magnetic field in the liquid satisfies the effective Robin boundary condition

$$\frac{\partial B^{\mathrm{i}}}{\partial y} = aB^{\mathrm{i}} \quad \text{at} \;\; y = 0, \tag{2.3.22}$$

where

$$a = \frac{\sigma^*}{h^{\mathrm{s}}\sigma^{\mathrm{s}*}}. \tag{2.3.23}$$

The dimensionless parameter a allows us to interpolate between the extreme cases of a perfectly insulating substrate ($a \to \infty$) and a perfectly conducting substrate ($a \to 0$). These calculations may be extended to consider the case of a composite substrate comprising several layers of different substrate material, as shown in appendix A.2.2.

When terms of order ϵ^2 and $\epsilon^2\,\mathrm{Rm}$ are neglected, the r-component (2.3.10b) of the momentum equation in the fluid layer reduces to

$$\epsilon^2\,\mathrm{Re}\left(\frac{\partial u}{\partial t}+u\frac{\partial u}{\partial r}+v\frac{\partial u}{\partial y}\right)=-\frac{\partial p}{\partial r}+1+\frac{\partial^2 u}{\partial y^2}-\frac{2\epsilon^2(1+\chi)^2\,\mathrm{Ha}^2}{\cos^2\theta}\frac{1}{r^2}\frac{\partial}{\partial r}\left(rB^{\mathrm{i}}\right). \tag{2.3.24a}$$

Similarly, neglecting terms of order ϵ^2, $\epsilon^4\,\mathrm{Re}$, and $\epsilon^2\,\mathrm{Rm}$ in the y-component (2.3.10c) of the momentum equation, we obtain

$$\frac{\partial p}{\partial y}=-\epsilon\cot\theta-\frac{2\epsilon^2(1+\chi)^2\,\mathrm{Ha}^2}{\cos^2\theta}\frac{1}{r}\frac{\partial B_i}{\partial y}. \tag{2.3.24b}$$

The normal stress boundary condition (2.3.15) reduces to

$$p=\frac{\epsilon^3}{\mathrm{Bo}}\varkappa-\frac{\chi(1+\chi)\,\mathrm{Ha}^2}{2\,\mathrm{Rm}\cos^2\theta}\frac{1}{r^2}\quad\text{at}\quad y=h(r,t), \tag{2.3.25a}$$

where

$$\varkappa=-\frac{\partial^2 h}{\partial r^2}+\frac{1}{r}\left(\frac{\tan\theta}{\epsilon}-\frac{\partial h}{\partial r}\right) \tag{2.3.25b}$$

is the dimensionless curvature of the free surface. The pressure within the fluid layer is thus found to be given by

$$p=\frac{\epsilon^3}{\mathrm{Bo}}\varkappa-\frac{\chi(1+\chi)\,\mathrm{Ha}^2}{2\,\mathrm{Rm}\cos^2\theta}\frac{1}{r^2}+\epsilon\cot\theta(h-y)-\frac{2\epsilon^2(1+\chi)^2\,\mathrm{Ha}^2}{\cos^2\theta}\frac{B^{\mathrm{i}}}{r}. \tag{2.3.25c}$$

As in the poloidal case, the magnetic contribution to the leading-order pressure is negative (assuming $\chi > 0$), and may contribute to negative pressures within the fluid giving rise to undesirable cavitation as discussed in §2.2.6.

In addition to a, we identify the other combinations of dimensionless parameters that appear in the model as follows:

$$
\begin{aligned}
&\text{reduced Reynolds number} && \overline{\mathrm{Re}} = \epsilon^2\,\mathrm{Re} && = \mathcal{O}\left(10^{-4}\right), && \text{(2.3.26a)}\\
&\text{reduced Hartmann number} && \lambda^2 = \frac{\epsilon(1+\chi)\,\mathrm{Ha}}{\cos\theta} && = \mathcal{O}\left(10^{-1}\right), && \text{(2.3.26b)}\\
&\text{magnetic stress parameter} && \beta = \frac{\chi(1+\chi)\,\mathrm{Ha}^2}{2\,\mathrm{Rm}\cos^2\theta} && = \mathcal{O}\left(10^{-2}\right), && \text{(2.3.26c)}\\
&\text{capillary parameter} && \Gamma = \frac{\epsilon^3}{\mathrm{Bo}} && = \mathcal{O}\left(10^{-7}\right), && \text{(2.3.26d)}\\
&\text{geometrical parameter} && \alpha = \epsilon\cot\theta && = \mathcal{O}\left(10^{-3}\right). && \text{(2.3.26e)}
\end{aligned}
$$

The smallness of each of these parameter groups implies that the effects of inertia, coupling between the magnetic field and the flow, magnetic stress effects at the free surface, surface tension, and transverse gravity are all likely to be rather weak. We note, however, that λ^2 and β are proportional to $\mathscr{B}^*$ and to $\mathscr{B}^{*2}$, respectively, and so might become important at slightly higher applied magnetic field strengths. Both surface tension and the transverse component of gravity can act as regularising influences, so we will retain them in the model for the moment but neglect all except the highest derivative term in the curvature $\varkappa$. As opposed to the poloidal case, here we have temporarily retained terms of order $\mathcal{O}(\overline{\mathrm{Re}})$. While we will neglect these terms in the leading-order solution, they will be reinstated for the subsequent linear stability analysis performed in §3.3.

In the limit where $\overline{\mathrm{Re}} \to 0$, our leading-order problem then reads

$$
\frac{\partial^2 B^{\mathrm{i}}}{\partial y^2} = -\frac{u}{r^2}, \tag{2.3.27a}
$$

$$
\frac{1}{r}\frac{\partial}{\partial r}(ru) + \frac{\partial v}{\partial y} = 0, \tag{2.3.27b}
$$

$$
-\frac{\partial^2 u}{\partial y^2} + 4\lambda^4\,\frac{B^{\mathrm{i}}}{r^2} = \varphi(r,t) := 1 - \alpha\frac{\partial h}{\partial r} - \frac{2\beta}{r^3} + \Gamma\,\frac{\partial^3 h}{\partial r^3}, \tag{2.3.27c}
$$

with boundary conditions

$$
u = v = \frac{\partial B^{\mathrm{i}}}{\partial y} - aB^{\mathrm{i}} = 0 \qquad \text{at} \quad y = 0, \tag{2.3.28a}
$$

$$
\frac{\partial u}{\partial y} = v - \frac{\partial h}{\partial t} - u\frac{\partial h}{\partial r} = B^{\mathrm{i}} = 0 \qquad \text{at} \quad y = h(r,t). \tag{2.3.28b}
$$

The four terms in the function $\varphi(r,t)$ defined in (2.3.27c) represent, respectively, the effects of gravity parallel and normal to the substrate, the magnetic contribution to the pressure, and surface tension. In particular, β measures the effect on the flow due to a nonzero magnetic susceptibility χ in the liquid. Although χ is usually very small, since β scales with $\mathscr{B}^{*2}$, this effect may still be significant when the applied field is sufficiently strong. We note also that (provided $\chi > 0$), the magnetic pressure contribution always acts in opposition to the gravitational body force, and could even drive flow up the sloping substrate at large enough values of β.

2.3.5 Leading-order solutions and the non-monotonic flux

The problem (2.3.27) and (2.3.28) can readily be solved for u, v and B^{i}. We normalise the problem by defining

$$u(r,y,t) = \frac{\varphi}{a^2\zeta^2}\,\mathcal{U}(Y;H,\zeta), \qquad B^{\mathrm{i}}(r,y,t) = \frac{\varphi}{a^4\zeta^4 r^2}\,\mathcal{B}(Y;H,\zeta), \tag{2.3.29a,b}$$

where

$$Y = \frac{y}{h}, \qquad H = \frac{\lambda h}{r}, \qquad \zeta = \frac{\lambda}{ar}. \tag{2.3.30a–c}$$

Then the governing equations (2.3.27) and boundary conditions (2.3.28) imply that $\mathcal{U}(Y)$ and $\mathcal{B}(Y)$ satisfy the problem

$$\frac{\mathrm{d}^2\mathcal{B}}{\mathrm{d}Y^2} + H^2\mathcal{U} = \frac{\mathrm{d}^2\mathcal{U}}{\mathrm{d}Y^2} - 4H^2\mathcal{B} + H^2 = 0, \tag{2.3.31a}$$

$$\mathcal{U}(0) = \frac{\mathrm{d}\mathcal{B}}{\mathrm{d}Y}(0) - \frac{H}{\zeta}\,\mathcal{B}(0) = \frac{\mathrm{d}\mathcal{U}}{\mathrm{d}Y}(1) = \mathcal{B}(1) = 0, \tag{2.3.31b}$$

explicit solutions of which are given in appendix A.3. In figure 2.10 we plot these scaled solutions versus Y for various values of the scaled thickness H and the scaled field strength ζ.

In figures 2.10(a) and 2.10(d) we observe that, for relatively small values of H, the normalised magnetic field and velocity both increase with increasing H; the induced field remains concave, with a global maximum in the interior of the film, and the velocity remains monotonic with respect to the vertical position y. This behaviour is consistent with the classical parabolic hydrodynamic flow profile, which is recovered in the limit $H \to 0$. For larger values of H, as shown in figure 2.10(b), the velocity becomes non-monotonic and increasingly oscillatory, and for sufficiently large H can even become negative within the film. Meanwhile, the induced field becomes approximately constant in the interior of the fluid, with magnetic forces

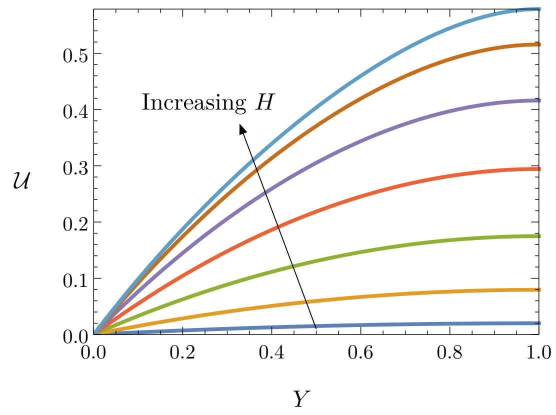

(a) $H \in \{0.2, 0.4, 0.6, 0.8, 1, 1.2, 1.4\}$.

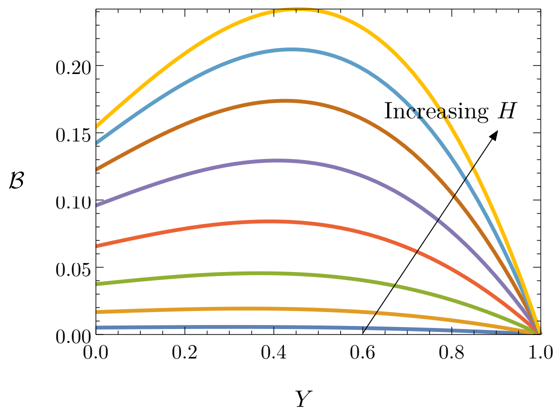

(d) $H \in \{0.5, 0.7, 0.9, 1.1, 1.3, 1.5, 1.7, 1.9\}$.

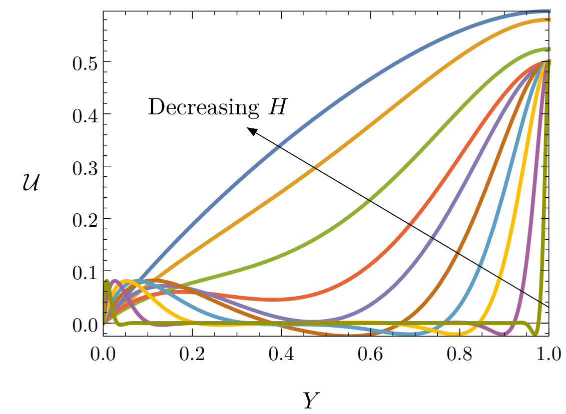

(b) $H \in \{1.5, 2.2, 3, 4, 5, 7, 10, 15, 30, 100\}$.

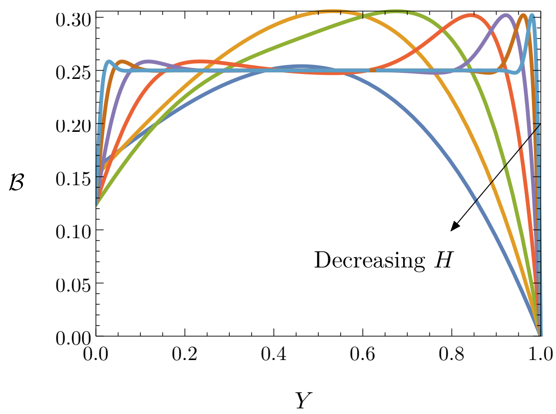

(e) $H \in \{2, 3, 5, 10, 20, 40, 80\}$.

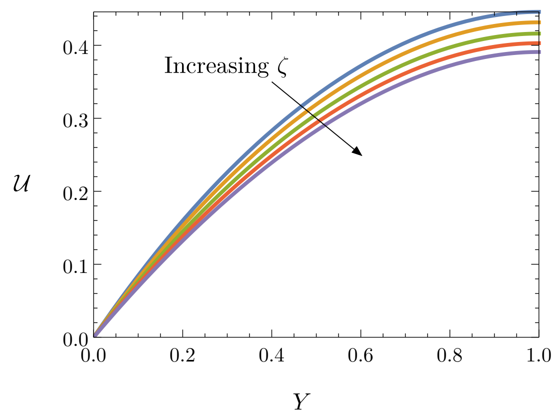

(c) $\zeta \in \{0, 0.3, 1, 3, \infty\}$.

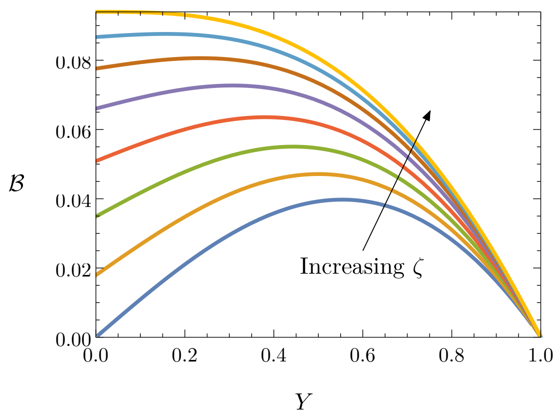

(f) $\zeta \in \{0, 0.2, 0.5, 1, 2, 4, 10, \infty\}$.

Figure 2.10: Scaled velocity $\mathcal{U}$ (a–c) and induced magnetic field $\mathcal{B}$ (d–f) plotted versus $Y = y/h$. In (a, b, d, e) we fix $\zeta = 1$ and vary H; in (c, f) we fix $H = 1$ and vary ζ.

balancing gravitational forces, while other effects manifest only in thin boundary layers, as shown in figure 2.10(e).

Figure 2.10(f) shows that the value of ζ has a pronounced effect on the induced field. This behaviour reflects the boundary condition (2.3.31b) that interpolates between a perfectly insulating substrate, with $\mathcal{B}(0) \to 0$ as $\zeta \to 0$, and a perfectly conducting substrate, with $\mathcal{B}'(0) \to 0$ as $\zeta \to \infty$. However, with $H = 1$, the magnitude of the induced field remains rather small, and figure 2.10(c) shows that it has little influence on the velocity profile.

Having solved for $u(r, y, t)$, we integrate the mass conservation equation (2.3.27b) and apply the kinematic boundary conditions at $y = 0$ and $y = h$ to obtain an evolution equation for the film thickness in the form

$$\frac{\partial h}{\partial t} + \frac{1}{r}\frac{\partial}{\partial r}(r\varphi Q) = 0, \tag{2.3.32}$$

where φ is given by equation (2.3.27c), and the flux function Q is defined by

$$Q(h; r) = \frac{1}{\varphi(r,t)} \int_0^{h(r,t)} u(r, y, t)\,\mathrm{d}y. \tag{2.3.33}$$

Again, we find that a suitably normalised version of Q may be expressed purely in terms of H and ζ, namely

$$a^3\zeta^3 Q = H \int_0^1 \mathcal{U}(Y)\,\mathrm{d}Y = F(H, \zeta), \tag{2.3.34}$$

say. By substituting for $\mathcal{U}(Y)$ from appendix A.3 and performing the integral, we find that F is given by

$$F(H, \zeta) = \frac{2\zeta\,(\sinh 2H - \sin 2H) + 3\cos 2H + 3\cosh 2H - 8\cos H \cosh H + 2}{4\big[\zeta(\cos 2H + \cosh 2H + 2) + \sin 2H + \sinh 2H\big]}. \tag{2.3.35}$$

For each fixed value of the parameter ζ, the scaled flux $F(H, \zeta)$ is a non-monotonic function of the scaled thickness H, as shown in figure 2.11(a). Note that the scaling factor $a\zeta = \lambda/r$ reflects the strength of the magnetic forces. As the film thickness tends to zero, viscous forces dominate magnetic effects, and the classical lubrication theory result is recovered, with

$$F(H, \zeta) \sim \frac{H^3}{3} \quad \text{as } H \to 0. \tag{2.3.36a}$$

However, as the film thickness increases, the magnetic stress takes over, and the

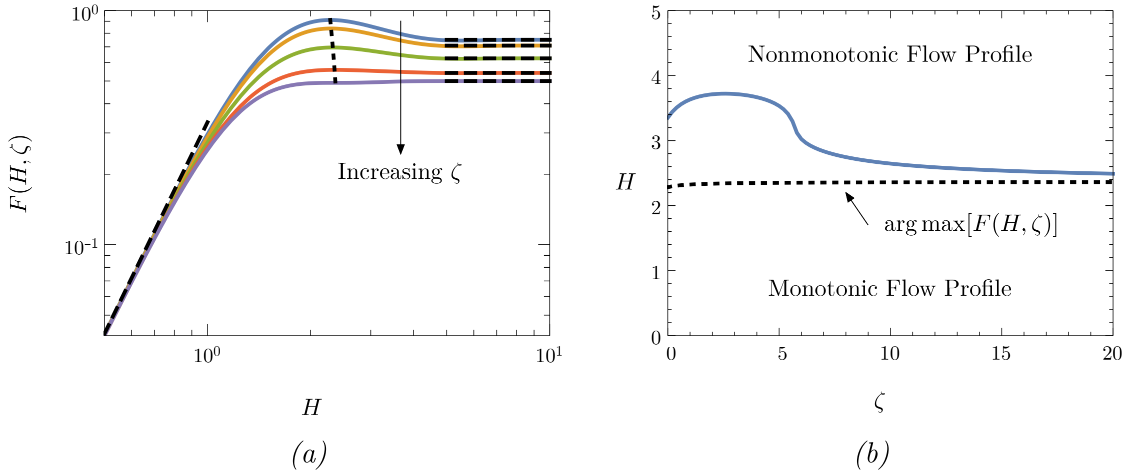

Figure 2.11: (a) The normalised flux function $F(H,\zeta)$, given by (2.3.35), plotted versus H with $\zeta \in \{0,\, 0.2,\, 1, 5,\, \infty\}$; the dashed curves show the asymptotic limits (2.3.36) and the dotted curve shows the locus of the maximum value of F, given implicitly by (2.3.38). (b) The (ζ, H) parameter space. The dotted black curve shows the maximising value H of the function $F(H,\zeta)$, defined implicitly as a function of ζ by (2.3.37). The solid blue curve shows the boundary between parameter values where the flow profile is monotonic or non-monotonic.

flux ultimately becomes independent of H, with

$$F(H,\zeta) \to \frac{1}{4}\left(2 + \frac{1}{1+\zeta}\right) \quad \text{as } H \to \infty. \tag{2.3.36b}$$

At intermediate values, $F(H,\zeta)$ is an oscillatory function of H. The first extremal value of H, corresponding to the global maximum in F, is given as a function of ζ by the implicit relation

$$\zeta = \frac{\cos 2H - 2\sin H \sinh H - 2\cos H \cosh H + 1}{2\cos H \sinh H + 2\sin H \cosh H}. \tag{2.3.37}$$

As shown by the dotted black curve in figure 2.11(b), as ζ ranges from 0 to ∞, the extremal value of H increases monotonically from H_0 to H_∞, where $H_0 \approx 2.284$ and $H_\infty \approx 2.365$ are the first positive zeros of the numerator and denominator, respectively, of the right-hand side of equation (2.3.37).

By substituting (2.3.37) into (2.3.35), we find that the maximum value of $F(H,\zeta)$ is given parametrically as a function of ζ by (2.3.37) and

$$\max F(H) = \frac{\sec H \sinh H + \tan H(\sec H \cosh H - 2)}{4}, \tag{2.3.38}$$

with $H \in (H_0, H_\infty)$. The relation (2.3.38) is plotted as a dotted curve in figure 2.11(a). To the left of this dotted curve, F is an increasing function of H but, as H increases past its extremal value, F starts to decrease again and then to oscillate. We will argue below in § 2.3.6 that only the increasing branch of F to the left of the dotted curve in figure 2.11(a) is relevant and, therefore, that no physical solutions exist in the region of (ζ, H) parameter space above the dotted curve in figure 2.11(b).

Figure 2.10(b) shows that the velocity profile becomes non-monotonic at larger values of H; indeed the oscillations in the flow profile become increasingly dramatic as H increases, and may even lead to flow reversal in the interior of the film. The solid blue curve in figure 2.11(b) shows the boundary between regions of the (ζ, H) parameter space where $u(y)$ is monotonic or non-monotonic. We note that non-monotonic solutions occur only for value of (ζ, H) above the black dotted curve in figure 2.11(b), showing the value of H that maximises F. We will thus contend in the next section that, although similar oscillatory flow profiles have been reported in the literature [56], they are unphysical and could never be observed in practice.

2.3.6 Steady states

We begin by letting all of the small parameters α, β and Γ tend to zero so that $\varphi(r,t) \equiv 1$. We also consider the divertor to occupy the dimensionless interval $r \in [1, 2]$. Steady solutions $h_0(r)$ of (2.3.32) are then given by

$$Q\big(h_0(r); r\big) = \frac{q}{r}, \tag{2.3.39}$$

where the constant q is set by specifying the inlet flux: $Q|_{r=1} = q$.

Differentiation of (2.3.39) with respect to r leads to

$$\frac{\mathrm{d}h_0}{\mathrm{d}r} = -\left(\frac{\partial Q}{\partial r} + \frac{q}{r^2}\right) \Big/ \frac{\partial Q}{\partial h}. \tag{2.3.40}$$

By differentiating (2.3.35), we find that

$$-r\frac{\mathrm{d}}{\mathrm{d}r}\left[\log\left(r^{1/3}h_0(r)\right)\right] = -\frac{4}{3} + \frac{4F - \zeta\partial F/\partial\zeta}{H\partial F/\partial H}, \tag{2.3.41}$$

where $F(H, \zeta)$ is the function defined in (2.3.35). This expression is uniformly positive (see figure 2.12), and it follows that $h_0(r)$ is a monotonic decreasing function which is bounded above by $h_0(1)/r^{1/3}$. However, as the imposed flux q increases,

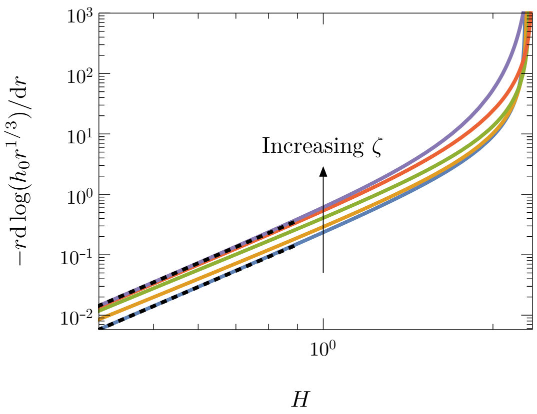

Figure 2.12: The normalised r-derivative of the steady state solution $h_0(r)$, defined by (2.3.41), plotted versus H with $\zeta \in \{0,\ 0.2,\ 1,\ 5,\ \infty\}$. The black dotted lines show the asymptotic behaviour as $H \to 0$, namely $71H^4/315$ ($\zeta = 0$), $176H^4/315$ ($\zeta > 0$).

so too does the film thickness at the inlet, eventually approaching the maximum of Q, where $\partial Q/\partial h = 0$, so that the denominator of the (2.3.40) approaches zero and the free surface forms a gradient singularity.

Solutions of (2.3.39) for $h_0(r)$ with various values of the parameters λ, a and q are plotted in figure 2.13. In figure 2.13(a) we observe that increasing the normalised field strength λ causes higher free surfaces due to increased magnetic drag on the flow. Figure 2.13(b) demonstrates that increasing the conductivity of the substrate (decreasing a) likewise decreases the flow velocity and thus increases the film thickness. Finally, in figure 2.13(c) we show the effects of increasing the flux, which acts to increase the film thickness globally. Since both H and ζ tend to zero, the viscous dominated behaviour (2.3.36a) applies in the limit as $r \to \infty$, and thus (2.3.39) implies that

$$h_0(r) \sim \left(\frac{3q}{r}\right)^{1/3} \quad \text{as } r \to \infty. \tag{2.3.42}$$

This limit is plotted as the black dotted curves in figures 2.13(a) to 2.13(c). In each of figures 2.13(a) and 2.13(b) the value of the flux q is held constant, as a consequence of which the free surface profiles all converge as $r \to \infty$.

Crucially, each of the solutions plotted in figures 2.13(a) to 2.13(c) exhibits a critical value of λ, a, and q, respectively, at which a singularity forms in the free surface, associated with $\partial Q/\partial h$ tending to zero at the inlet $r = 1$. Beyond each of these critical values, no steady free surface profile exists along the full extent of the divertor. The origin of the free-surface singularity may also be understood by considering the time-dependent problem (2.3.32). When $\varphi \equiv 1$, (2.3.32) is a first-

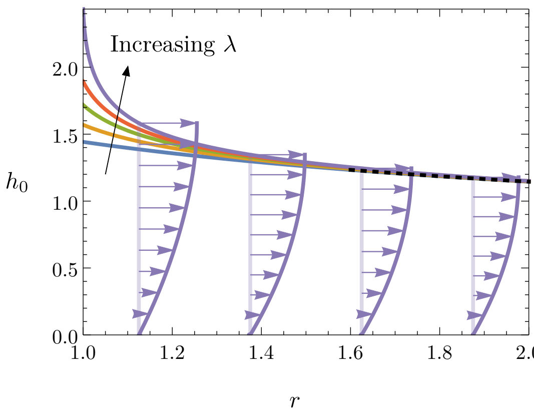

(a) $a = q = 1$, $\lambda \in \{0.01, 0.7, 0.8, 0.85, 0.89\}$.

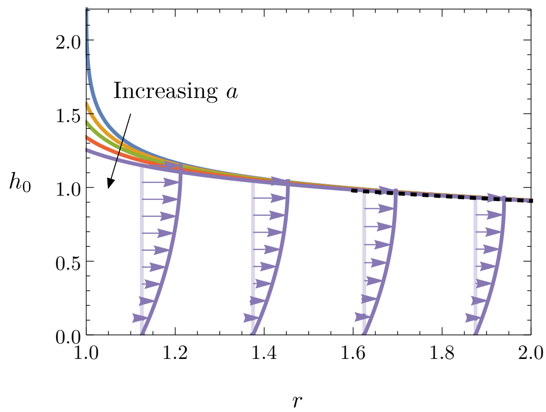

(b) $\lambda = 2q = 1, a \in \{0.023, 0.2, 0.5, 1.5, 100\}$.

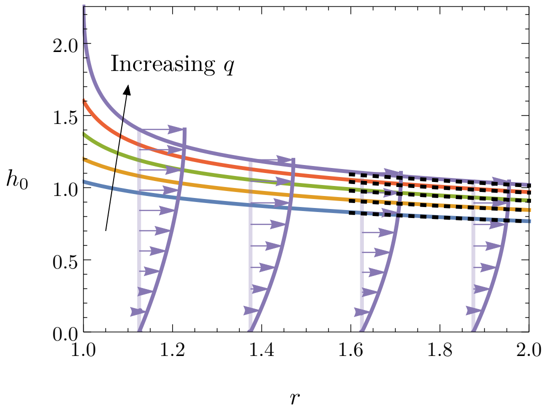

(c) $a = \lambda = 1$, $q \in \{0.3, 0.4, 0.5, 0.6, 0.695\}$.

Figure 2.13: Steady free-surface solutions of (2.3.39) *with the large-r limit* (2.3.42) *overlaid as black dotted curves, and the corresponding velocity profiles.*

order nonlinear hyperbolic PDE, with characteristics satisfying $\mathrm{d}r/\mathrm{d}t = \partial Q/\partial h$. As the value of $\partial Q/\partial h$ at $r = 1$ changes sign, the characteristics cease to point into the domain, and it becomes impossible to specify the flux at the inlet.

Since, as shown in figure 2.11(a), Q is an oscillatory function of h, there may be further regions of parameter space in which $\partial Q/\partial h$ becomes positive again, but we now argue that such branches cannot be physical. As shown above, $h_0(r)$ is a monotonic decreasing function, and it follows that, as r increases, a singular point where $\partial Q/\partial h$ tends to zero is necessarily encountered within a finite (and in practice very small) extent, so there still cannot exist steady solutions for an arbitrarily long divertor.

Therefore, when $\varphi \equiv 1$, smooth steady profiles only exist in the "subcritical" region of parameter space below the dotted black curve in figure 2.11(b). This

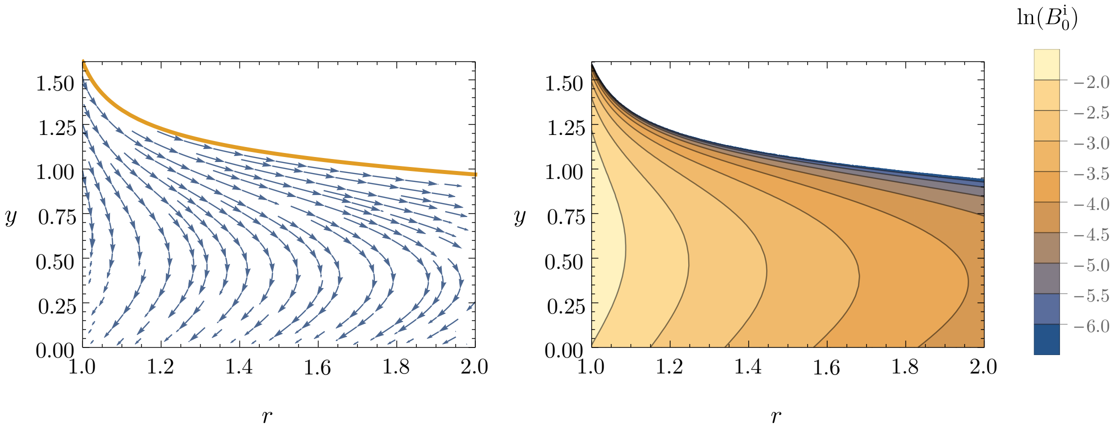

(a) Induced current $\boldsymbol{j}$. *(b) Induced magnetic field* B_0^{i}.

Figure 2.14: The induced current (2.3.43) *associated with the induced magnetic field* (2.3.29) *with flux* $q = 0.6$ *and* $a = \lambda = \varphi = 1$.

constraint places a strict bound on the value of Q (or, equivalently, h) imposed at the inlet. Importantly, figure 2.11(b) demonstrates that the non-monotonic velocity profiles seen, for example, in figure 2.10(b) occur for supercritical parameter values corresponding to unphysical steady state solutions, and we therefore do not expect to observe such exotic profiles in the wild.

Finally, we illustrate features of the induced magnetic field and associated current within the fluid layer in figure 2.14, where the current is computed via

$$\boldsymbol{j} = \boldsymbol{\nabla} \times (B_0^{\mathrm{i}} \boldsymbol{e}_\phi) = \frac{1}{r}\frac{\partial}{\partial r}\left(r B_0^{\mathrm{i}}\right) \boldsymbol{e}_r - \frac{\partial B_0^{\mathrm{i}}}{\partial y} \boldsymbol{e}_y. \tag{2.3.43}$$

In figure 2.14(a) we observe that the current lines exhibit significant curvature resulting from a balance between the downstream flow driving a vertical current, and the current continuity boundary conditions with the vacuum and the substrate. The induced field in figure 2.14(b) also reflects this balance, and demonstrates the downstream decay of the field as the applied field weakens.

2.4 Summary

In this chapter, we derive the equations and boundary conditions governing the fully-developed flow of a liquid metal in the presence of an applied magnetic field. We then consider two-dimensional flow and posed two canonical orientations of the applied field: the poloidal case, where the field lies exclusively in the plane parallel to the flow, and the toroidal case, where the applied field is orthogonal to the flow.

In the poloidal case, the leading-order flow decouples from the induced field and, as is classical of Hartmann flow, adopts an approximately uniform, decelerated profile for high field ($\mathrm{Ha} \gg 1$). The leading-order induced field depends non-locally on the flow and film height. The induced field exhibits logarithmic singularities at the flow endpoints, which may be suppressed by appropriately modelling the way the fluid enters and exits the domain.

In the toroidal case, we find that the influence of the magnetic field is weaker: it significantly effects the flow if $\epsilon\,\mathrm{Ha} = \mathcal{O}(1)$, compared with the poloidal case where we require $\mathrm{Ha} = \mathcal{O}(1)$. When the field does influence the flow, it exerts an MHD drag to decelerate the flow. In the high-field limit, the bulk adopts a uniform profile as it decelerates to zero, and all variation is relegated to boundary layers. Unlike Hartmann layers, the fluid flow in these layers remains of order unity, and may exhibit exotic profiles including backflow. Furthermore, we find that the leading-order fluid flow rate is a non-monotonic bounded function of the film height, and this can lead to singularities in the free surface profile. We argue that the exotic flow profiles belong to a region of parameter space where the free surface is singular, and thus do not expect to observe these in practice.

Given these leading-order canonical solutions, we are now equipped with a base state about which we will perturb in chapter 3 to analyse the stability of the thin film to unsteady perturbations. In subsequent chapters we will extend the model to include interactions between the fluid film and the core plasma beyond the divertor.

Chapter 3

Stability Analyses

The fluid film covering the solid divertor substrate must be steadily maintained to guarantee successful divertor function. A dry-out event could leave the substrate exposed and vulnerable to thermal damage, while large free-surface deflections make the fluid vulnerable to sputtering. Sputtering can result in fluid loss and impurities reaching the core plasma. It is therefore desirable to maintain as level and steady a free surface as possible.

In chapter 2 we derive and solve the leading-order equations governing the fluid flow and electromagnetic fields in the poloidal and toroidal cases. In each case, this provides an evolution equation governing the height h of the free surface, and steady state solutions of these thin-film equations are explored. In this chapter, we analyse the stability, to unsteady perturbations, of the steady thin film solutions presented previously.

The chapter is organised as follows. In §§ 3.1 and 3.2 we neglect the higher-order contributions of surface tension and transverse gravity, and study unsteady solutions of the resulting thin film equations in the presence of both poloidal and toroidal applied fields, respectively. In particular, we highlight nonlinear effects and their suppression in the poloidal case. In § 3.3 we consider the linear stability when the higher-order terms are restored. While the poloidal case is well studied, there remain significant gaps in the literature on the toroidal problem. We perform a detailed linear stability analysis in which the effect of inertia is reinstated in the perturbation. Finally, we summarise our findings in § 3.4.

3.1 Unsteady Poloidal problem

3.1.1 Model problem

We recall from the poloidal solution (2.2.46) that the film thickness $h(x,t)$ is governed by the equation

$$\frac{\partial h}{\partial t} + \frac{\partial}{\partial x}\left[\varphi\left(x, \frac{\partial h}{\partial x}, \frac{\partial^3 h}{\partial x^3}\right) Q\,(x,h)\right] = 0. \tag{3.1.1}$$

where the flow rate φQ comprises the flux function

$$Q = \frac{h}{(B^{\mathrm{a}}_{Y0})^2}\left(1 - \frac{\tanh(\mathrm{Ha}\, h B^{\mathrm{a}}_{Y0})}{\mathrm{Ha}\, h B^{\mathrm{a}}_{Y0}}\right), \tag{3.1.2}$$

and the higher-order factor

$$\varphi = 1 - \epsilon \cot\theta \frac{\partial h}{\partial x} + \frac{\epsilon^3}{\mathrm{Bo}}\frac{\partial^3 h}{\partial x^3} + \frac{\chi}{2\,\mathrm{Rm}}\frac{\mathrm{d}}{\mathrm{d}x}\left((B^{\mathrm{a}}_{x0})^2 + (B^{\mathrm{a}}_{Y0})^2\right). \tag{3.1.3}$$

In this section we neglect the higher-order effects of transverse gravity and surface tension, as well as the contribution of magnetic pressure, respectively the second, third, and fourth terms on the right-hand side of (3.1.3), and so set $\varphi = 1$. This approximation is relevant in the limit where $\chi/\,\mathrm{Rm} = \mathcal{O}(\epsilon)$, and either $\epsilon \cot\theta$ and $\epsilon^3/\,\mathrm{Bo}$ are also $\mathcal{O}(\epsilon)$, or the free surface is sufficiently flat, so that $\partial h/\partial x$ and $\partial^3 h/\partial x^3$ are small. We will reinstate the higher-order effects in the stability analysis in §3.3, and explore them further still in chapter 5.

It is worth addressing an important nuance when these assumptions do not hold. A steady solution to (3.1.4) is one in which the flow rate φQ is constant, and can only exist if φ does not change sign within the divertor (otherwise the flow rate must be zero everywhere). If assumptions guaranteeing that φ is of one sign do not hold, then the applied field and divertor need to be designed in such a way that φ does not change sign, even temporarily. A sign change in φ acts to induce rupture (or flooding) in the thin film at the location of the sign change, as the surface forces act to push the liquid in opposite directions away from (or towards) the zero.

With $\varphi = 1$, we can write the thin-film equation (3.1.1) as

$$\frac{\partial h}{\partial t} + \frac{\partial Q}{\partial h}\frac{\partial h}{\partial x} = -\frac{\partial Q}{\partial x}. \tag{3.1.4}$$

As in chapter 2, we find the steady free-surface profile $h_0(x)$ by solving the steady-state equation

$$Q(h_0(x), x) = 1. \tag{3.1.5}$$

In this section we analyse a model unsteady problem in which a time-dependent thickness $h_{\mathrm{bc}}(t)$ is imposed at the inlet $x = 0$. We therefore consider the solution of the PDE (3.1.4) subject to the boundary condition

$$h(0, t) = h_{\mathrm{bc}}(t). \tag{3.1.6}$$

3.1.2 Linear stability analysis

We begin by considering the fully developed response of the film to small-amplitude sinusoidal perturbations. We therefore set

$$h_{\mathrm{bc}}(t) = h_0(0) + \delta\, \mathrm{e}^{\mathrm{i}\omega t}, \tag{3.1.7}$$

where ω is a prescribed perturbation frequency and $\delta \ll 1$, and seek solutions of (3.1.4) of the form

$$h = h_0(x) + \delta h_1(x)\, \mathrm{e}^{\mathrm{i}\omega t}. \tag{3.1.8}$$

A solution of the form (3.1.8) represents a fully developed perturbation to the boundary-value problem (3.1.4) and (3.1.6) that is independent of initial conditions.

Substituting (3.1.8) into (3.1.4) and neglecting terms of $\mathcal{O}(\delta^2)$, we obtain the equation

$$\frac{\mathrm{d}h_1}{\mathrm{d}x} \Big/ h_1 = -\left(\mathrm{i}\omega + \frac{\mathrm{d}}{\mathrm{d}x}\left(\frac{\partial Q}{\partial h}\right)\right) \Big/ \frac{\partial Q}{\partial h}, \tag{3.1.9}$$

where derivatives of Q are evaluated at $(x, h_0(x))$. Equation (3.1.9) can then be integrated subject to $h_1(0) = 1$ to give

$$h_1(x) = \left.\frac{\partial Q}{\partial h}\right|_{x=0} \left(\frac{\partial Q}{\partial h}\right)^{-1} \exp\left(-\mathrm{i}\omega \int_0^x \left(\frac{\partial Q}{\partial h}\right)^{-1} \mathrm{d}x\right). \tag{3.1.10}$$

The perturbation in (3.1.10) evidently comprises a spatially-dependent amplitude function

$$|h_1(x)| = \left|\frac{\partial Q}{\partial h}(h_0(0), 0) \Big/ \frac{\partial Q}{\partial h}(h_0(x), x)\right|, \tag{3.1.11}$$

multiplied by an exponential oscillatory term which captures all the ω-dependence and has modulus 1.

To explore the behaviour of the perturbation amplitude (3.1.11), note that

$$\frac{\partial Q}{\partial h} = \left(\frac{\tanh(\mathrm{Ha}\, h B^{\mathrm{a}}_{Y0})}{B^{\mathrm{a}}_{Y0}}\right)^2. \tag{3.1.12}$$

Substituting (3.1.12) into (3.1.11) we find that the amplitude satisfies

$$|h_1| \leq \left(\frac{\tanh(\mathrm{Ha}\, h_0(0) B^{\mathrm{a}}_{Y0}(0))}{B^{\mathrm{a}}_{Y0}(0)} \max_x \frac{B^{\mathrm{a}}_{Y0}(x)}{\tanh(\mathrm{Ha}\, h_0(x) B^{\mathrm{a}}_{Y0}(x))}\right)^2, \tag{3.1.13}$$

which must be finite over any finite divertor as the function $x/\tanh(x)$ is bounded on any compact domain. When $\mathrm{Ha} \gg 1$, we expect the tanh terms to be approximately 1 (away from any zeros of B^{a}_{Y0}), and thus $|h_1| \lesssim (\max_x B^{\mathrm{a}}_{Y0}(x)/B^{\mathrm{a}}_{Y0}(0))^2$. This highlights the fact that perturbations may grow with increasing x, but only to the extent that the field grows to exceed its inlet value. As observed in §2.2.4, a stronger field results in slower fluid flow and thus a higher free surface. This mechanism affects perturbations analogously, and so locations downstream of the inlet with higher field will see enlarged perturbations. In particular, note that for a constant field the steady free surface h_0 is constant, and it follows that the perturbation amplitude is constant $h_1 = 1$.

To recap, we find that the thin film is stable to time-harmonic perturbations, in the sense that these perturbations may only grow to a limited extent as they are advected downstream. In the next section we compare with numerical solutions of the fully nonlinear problem.

3.1.3 Numerical solution

In this section we describe a numerical method to solve (3.1.4) by a method-of-lines approach, where the spatial domain is discretised using the Kurganov–Tadmor high-resolution central scheme [104] (we use a superbee limiter [171] instead of the minmod limiter originally proposed as this is parameter-free and results in less dissipation). The time stepping is done with Matlab's `ode15s`. The advantage of such a numerical scheme is that the system need not be first-order, allowing higher h-derivatives to be included in φ. The scheme captures shocks sharply with little dissipation and is total-variation-diminishing so does not introduce large spurious oscillations.

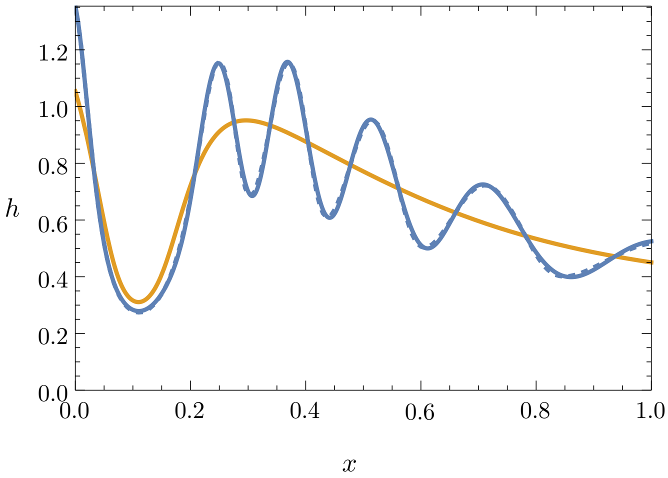

Figure 3.1: Free surface profiles. The orange curve shows the steady solution $h_0(x)$ of equation (3.1.5). The blue curves show snapshots of unsteady perturbations: the solid blue curve is the linearised perturbation, given by the real part of (3.1.10), while the dotted blue curve is the numerical solution of the full system (3.1.4) where the boundary condition imposed is (3.1.14). In both cases $\mathrm{Ha} = 10$, $\omega = 60$, $\delta = 0.3$, and $t = 10\pi$. The applied field used is the same as in figure 2.4(a).

We now compare the linear perturbations predicted by (3.1.10) to perturbations of the full nonlinear system, imposing the sinusoidal boundary condition

$$h_{\mathrm{bc}}(t) = h_0(0) + \delta \cos(\omega t). \tag{3.1.14}$$

As we see in figure 3.1, the linear perturbations are remarkably accurate in capturing the behaviour of the nonlinear solution. The reason for this is that when $\mathrm{Ha} \gg 1$ the term $\partial Q/\partial h$ depends only weakly on h and thus the linearisation neglects only exponentially small effects. Thus all characteristics are approximately parallel, regardless of the fluid height, and any fluid profile is advected downstream identically, with no leading-order dispersion or wave-steepening as we would expect in a classical hydrodynamic system, where $\partial Q/\partial h$ depends strongly on h. This insight will be exploited below in § 3.1.6 to construct a leading-order asymptotic solution in the limit $\mathrm{Ha} \to \infty$ using matched asymptotic expansions.

3.1.4 Exact solution for an affine applied field

Insight into the generic behaviour may be obtained by solving (3.1.4) explicitly in a simple representative case. The characteristic equations satisfied along a characteristic are

$$\frac{\mathrm{d}x}{\mathrm{d}t} = \frac{\partial Q}{\partial h}, \qquad \frac{\mathrm{d}h}{\mathrm{d}t} = -\frac{\partial Q}{\partial x}. \tag{3.1.15a,b}$$

From (3.1.4) and (3.1.15) we find that

$$\frac{\mathrm{d}}{\mathrm{d}t}\left(Q(h(x,t),x)\right) = 0, \tag{3.1.16}$$

and thus Q is constant along characteristics. Similarly, we find that hB^{a}_{Y0} evolves along characteristics such that it satisfies

$$\frac{\mathrm{d}}{\mathrm{d}t}\left(h(x,t)B^{\mathrm{a}}_{Y0}(x)\right) = 3Q\frac{\mathrm{d}B^{\mathrm{a}}_{Y0}}{\mathrm{d}x}. \tag{3.1.17}$$

Since Q is constant along characteristics, we have $Q(h(x,t),x) = Q(h_0(\xi),\xi) \equiv 1$ on a characteristic leaving $t = 0$ at $x = \xi > 0$. It follows that $h(x,t) \equiv h_0(x)$ ahead of the characteristic through $(x,t) = (0,0)$. We therefore focus on the behaviour behind this leading characteristic, and consider the solution of (3.1.4) and (3.1.6) on a characteristic leaving $x = 0$ at time $t = \tau > 0$. The corresponding initial conditions for (3.1.4) and (3.1.6) are

$$x = 0, \quad h = h_{\mathrm{bc}}(\tau) \quad \text{at} \quad t = \tau. \tag{3.1.18}$$

To make further analytical progress we look for a simple form for the right-hand side of (3.1.17). To this end we assume that the vertical component of the applied field is affine, namely $B^{\mathrm{a}}_{Y0} = ax + b$. From (3.1.16) and (3.1.17) it follows that

$$Q(h,x) = Q(h_{\mathrm{bc}}(\tau,0),0), \qquad hB^{\mathrm{a}}_{Y0}(x) = b\,h_{\mathrm{bc}}(\tau) + 3Qa(t-\tau). \tag{3.1.19a,b}$$

Writing

$$Q = h^3\,\mathrm{Ha}^2\,F(\mathrm{Ha}\,hB^{\mathrm{a}}_{Y0}), \tag{3.1.20a}$$

where

$$F(x) = \frac{1}{x^2}\left(1 - \frac{\tanh(x)}{x}\right), \tag{3.1.20b}$$

and using (3.1.19), we can solve for h and x in terms of t and τ, namely

$$h(t,\tau) = h_{\mathrm{bc}}(\tau)\left[\frac{F(\mathrm{Ha}\,b\,h_{\mathrm{bc}}(\tau))}{F\left(\mathrm{Ha}\,b\,h_{\mathrm{bc}}(\tau) + 3\,\mathrm{Ha}^3\,a(t-\tau)h_{\mathrm{bc}}(\tau)^3 F(\mathrm{Ha}\,b\,h_{\mathrm{bc}}(\tau))\right)}\right]^{1/3}, \tag{3.1.21}$$

and

$$x(t,\tau) = \frac{b}{a}\left(\frac{h_{\mathrm{bc}}(\tau)}{h(t,\tau)} - 1\right) + \frac{3\,\mathrm{Ha}^2(t-\tau)h_{\mathrm{bc}}(\tau)^3 F(\mathrm{Ha}\,b\,h_{\mathrm{bc}}(\tau))}{h(t,\tau)}. \tag{3.1.22}$$

To recap, when $\varphi = 1$ and the vertical component of the applied field is affine, we have found parametric expressions (3.1.21) and (3.1.22) for the free-surface height h and characteristics (x,t), respectively. These formulae are useful for testing numerical solutions for more general φ and applied fields. We will also find in § 3.1.6 that the exact solution (3.1.21) and (3.1.22) provides the basis for the asymptotic solution of the problem in the limit $\mathrm{Ha} \to \infty$.

3.1.5 Shock formation in a uniform field

The solution for the case of a uniform applied field may be obtained by taking the limit $a \to 0$ in (3.1.21) and (3.1.22), resulting in

$$h = h_{\mathrm{bc}}(\tau), \tag{3.1.23a}$$

$$x = \mathrm{Ha}^2(t-\tau)h_{\mathrm{bc}}(\tau)^2\left[3F(\mathrm{Ha}\,b\,h_{\mathrm{bc}}(\tau)) + \mathrm{Ha}\,b\,h_{\mathrm{bc}}(\tau)F'(\mathrm{Ha}\,b\,h_{\mathrm{bc}}(\tau))\right], \tag{3.1.23b}$$

where F is the function defined in (3.1.20b). As pointed out in § 3.1.3, it appears to be difficult to form shocks in our system, because the flux function Q varies approximately linearly with h. In this simple case, one can find an explicit criterion for a shock to form.

A shock forms when characteristics begin to overlap, occurring when $\partial x/\partial\tau = 0$. By differentiating (3.1.23b) with respect to τ, we find that this corresponds to values of x satisfying

$$\frac{x}{\mathrm{Ha}^2\,h_{\mathrm{bc}}(\tau)^3}\frac{\mathrm{d}h_{\mathrm{bc}}}{\mathrm{d}t}(\tau) = \frac{1}{2}\,f(\mathrm{Ha}\,b\,h_{\mathrm{bc}}(\tau)), \tag{3.1.24}$$

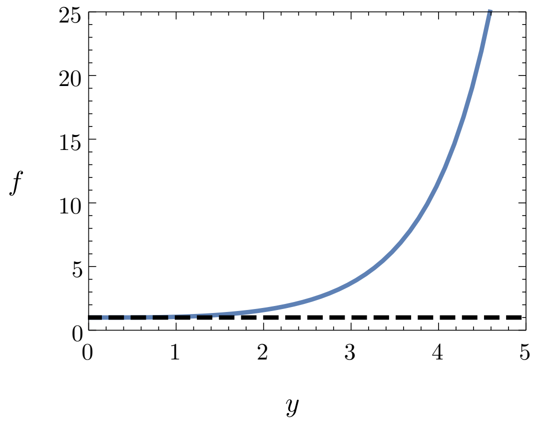

Figure 3.2: MHD suppression factor $f(y)$ defined in (3.1.25) *as a solid curve and the black dashed line marking $f = 1$.*

where

$$f(y) = \frac{2\left[yF'(y) + 3F(y)\right]^2}{y^2F''(y) + 6yF'(y) + 6F(y)} = \frac{\sinh^3 y}{y^3 \cosh y}. \tag{3.1.25}$$

As shown in figure 3.2, $f(y)$ is a positive even function which satisfies $f(0) = 1$ and increases exponentially for positive y. We deduce that shocks can only form for positive $\mathrm{d}h_{\mathrm{bc}}/\mathrm{d}t$ (when $\mathrm{d}h_{\mathrm{bc}}/\mathrm{d}t < 0$ the characteristics are rarefied), and that a shock will form within the domain $x \in (0, 1)$ of the divertor if and only if the inlet thickness h_{bc} satisfies

$$\frac{1}{\mathrm{Ha}^2 (h_{\mathrm{bc}})^3} \frac{\mathrm{d}h_{\mathrm{bc}}}{\mathrm{d}t} > \frac{1}{2} f(\mathrm{Ha}\, b\, h_{\mathrm{bc}}). \tag{3.1.26}$$

The function f therefore represents the extent to which the MHD forces suppress shock formation; the larger the value of f, the more shocks are suppressed. Purely hydrodynamical flow is recovered in the limit $b \to 0$, in which case the suppression factor is $f(y) \to 1$ as $y \to 0$. Since f is monotonically increasing for $y > 0$ (see figure 3.2) we conclude that increasing the applied field always acts to suppress shock formation. In fact, when $y \gg 1$ we find that $f \sim \mathrm{e}^{2y}/4y^3$, and the suppression is overwhelmingly effective. In our application where we expect $\mathrm{Ha} \geq 10$, and taking $h_{\mathrm{bc}} = b = 1$, we obtain a large suppression factor of $f(10) > 10^5$, indicating that, for an $\mathcal{O}(1)$ constant magnetic field, a shock could form only for extremely small or rapidly varying film thickness. We will see below in § 3.1.6 that the picture is somewhat different when the applied field changes sign somewhere along the divertor.

3.1.6 Matched asymptotic solutions for a general applied field

In this section, we extend the above analysis to describe an arbitrary field, in particular one that changes sign at some location $x_0 \in (0, 1)$ along the divertor. The complicated form of the flux function Q means that the solution by the method of characteristics is unwieldy in general. Instead, we exploit the largeness of the Hartmann number Ha to analyse the problem using matched asymptotic expansions. Our approach is to split the domain into three regions. In the outer regions $0 < x < x_0$ and $x_0 < x < 1$, the applied field B^{a}_{Y0} is nonzero, and, in the limit $\mathrm{Ha} \to \infty$, the flux Q becomes a linear function of h, as pointed out in §3.1.3. To leading order, the film thickness h in these regions therefore satisfies a first-order linear hyperbolic PDE, which can be readily solved analytically. However, the limit $\mathrm{Ha} \to \infty$ is nonuniform when the applied field B^{a}_{Y0} passes through zero, implying that there is a boundary layer in the vicinity of $x = x_0$, where $B^{\mathrm{a}}_{Y0} = 0$. In this inner layer, the film thickness satisfies a fully nonlinear PDE but, since the applied field is approximately a linear function of the position, the inner problem may be integrated as in §3.1.5. By matching the inner and outer solutions, we obtain effective coupling conditions between the flux entering the inner layer from $x < x_0$ and the flux propagating into $x > x_0$, thereby closing the solution of the outer problem.

The overall outcome of our analysis is that the effects of nonlinearity, manifesting as wave dispersion, steepening and rarefaction, are localised near zeros of the applied field. They are captured by a single functional equation which governs the modulation of the film thickness along a characteristics as it passes through the inner layer. Analysis of this functional equation provides a criterion for shock formation in the inner layer.

Outer solution

Consider a characteristic leaving the inlet $x = 0$ at time $t = \tau$, along which the characteristic equations (3.1.15) are satisfied. In the outer regions where $\mathrm{Ha}\, B^{\mathrm{a}}_{Y0} h \gg 1$, the flux function Q given in (3.1.2), in the limit of $\mathrm{Ha} \gg 1$ is approximated up to exponentially small terms by

$$Q(h, x) \sim \frac{h}{(B^{\mathrm{a}}_{Y0}(x))^2} - \frac{1}{\mathrm{Ha}\, |B^{\mathrm{a}}_{Y0}(x)|^3}. \tag{3.1.27}$$

From equation (3.1.16) we know that Q is constant along characteristics, and therefore $Q(h,x) = Q(h_{\rm bc}(\tau),0)$, from which it follows that

$$h \sim \frac{h_{\rm bc}(\tau)(B^{\rm a}_{Y0}(x))^2}{(B^{\rm a}_{Y0}(0))^2} + \frac{1}{\mathrm{Ha}\,|B^{\rm a}_{Y0}(x)|} - \frac{(B^{\rm a}_{Y0}(x))^2}{\mathrm{Ha}(B^{\rm a}_{Y0}(0))^3}. \tag{3.1.28}$$

From (3.1.15) we find that the characteristics have slope $\mathrm{d}t/\mathrm{d}x = (\partial Q/\partial h)^{-1}$, and therefore

$$t \sim \tau + \int_0^x \left(B^{\rm a}_{Y0}(z)\right)^2 \,\mathrm{d}z. \tag{3.1.29}$$

The film thickness in the outer region $x < x_0$ is then found to be given explicitly by

$$h(x,t) \sim \frac{(B^{\rm a}_{Y0}(x))^2}{(B^{\rm a}_{Y0}(0))^2}\, h_{\rm bc}\left(t - \int_0^x \left(B^{\rm a}_{Y0}(z)\right)^2 \,\mathrm{d}z\right) + \frac{1}{\mathrm{Ha}\,|B^{\rm a}_{Y0}(x)|} - \frac{(B^{\rm a}_{Y0}(x))^2}{\mathrm{Ha}(B^{\rm a}_{Y0}(0))^3}. \tag{3.1.30}$$

Inner region

Let us now assume that the applied field undergoes a sign change at $x = x_0$. In the vicinity of x_0 where $\mathrm{Ha}\,|B^{\rm a}_{Y0}(x)| \lesssim 1$, we rescale the inner problem just as in the steady case via the scalings (2.2.56), along with an inner time variable T defined by

$$t = \tau + \int_0^{x_0} \left(B^{\rm a}_{Y0}(z)\right)^2 \,\mathrm{d}z + \frac{T}{\mathrm{Ha}}\left|\frac{\mathrm{d}B^{\rm a}_{Y0}}{\mathrm{d}x}(x_0)\right|^{-1}, \tag{3.1.31}$$

and introduce the scaled flux function

$$\psi(z) = \frac{1}{(B^{\rm a}_{Y0}(0))^2}\, h_{\rm bc}\left(\tau + \frac{z}{\mathrm{Ha}}\left|\frac{\mathrm{d}B^{\rm a}_{Y0}}{\mathrm{d}x}(x_0)\right|^{-1}\right). \tag{3.1.32}$$

The characteristic equations (3.1.15) then take the scaled form

$$\frac{\mathrm{d}X}{\mathrm{d}T} = \frac{\partial Q}{\partial H}, \qquad\qquad \frac{\mathrm{d}H}{\mathrm{d}T} = -\frac{\partial Q}{\partial X}, \tag{3.1.33a,b}$$

where

$$Q = \frac{H}{X^2}\left(1 - \frac{\tanh(HX)}{HX}\right) + \mathcal{O}(\mathrm{Ha}^{-1/3}). \tag{3.1.34}$$

By writing the outer solution (3.1.30) in inner variables at leading-order, we obtain the matching conditions

$$H \sim X^2\psi\left(T - \frac{X^3}{3}\right) + \frac{1}{|X|}, \quad \text{as} \quad X \to -\infty. \tag{3.1.35}$$

We find from equations (3.1.33) that along characteristics

$$\frac{\mathrm{d}Q}{\mathrm{d}T} = 0, \qquad\qquad \frac{\mathrm{d}}{\mathrm{d}T}(HX) = 3Q, \tag{3.1.36a,b}$$

from which it follows that Q is constant along characteristics in the inner region (and in fact is constant along characteristics everywhere). Equation (3.1.36b) is integrable in the same way as (3.1.17), because the applied field is approximately linear in the inner region, and leads to

$$T - \frac{1 + HX}{3Q(c)} = c, \tag{3.1.37}$$

where c is constant along each characteristic. Matching according to (3.1.35) we find that $Q(c) \sim \psi(c)$ so the flux in the inner region is set by the inlet boundary condition on the given characteristic, and therefore

$$T = c + \frac{1 + HX}{3\psi(c)}, \qquad\qquad \frac{HX - \tanh(HX)}{X^3} = \psi(c). \tag{3.1.38a,b}$$

The formulation (3.1.38) allows us to write down the inner solution $H(X, T)$ parametrically via

$$X = \frac{\left[3\psi(c)(T-c) - 1 - \tanh(3\psi(c)(T-c) - 1)\right]^{1/3}}{\left[\psi(c)\right]^{1/3}}, \tag{3.1.39a}$$

$$H = \frac{\left[3\psi(c)(T-c) - 1\right]\left[\psi(c)\right]^{1/3}}{\left[3\psi(c)(T-c) - 1 - \tanh(3\psi(c)(T-c) - 1)\right]^{1/3}}. \tag{3.1.39b}$$

Matching

We now proceed to match the outer region $x > x_0$ downstream of the inner region with this inner solution (3.1.39). We consider the characteristic leaving the vicinity of the field sign change at time $t = \xi$, where

$$\int_{x_0}^{x} \left(B^{\mathrm{a}}_{Y0}(z)\right)^2 \,\mathrm{d}z = t - \xi. \tag{3.1.40}$$

From (3.1.27) we know that the film thickness in this region takes the form

$$h = \left(B^{\mathrm{a}}_{Y0}(x)\right)^2 \tilde{Q}(\xi) + \frac{1}{\mathrm{Ha}\,|B^{\mathrm{a}}_{Y0}(x)|}, \tag{3.1.41}$$

where the modified flux function $\tilde{Q}$ is to be determined by matching to the inner solution. To this end, we write (3.1.40) in inner variables, to find that

$$\begin{aligned}\frac{X^3}{3\,\mathrm{Ha}}\left|\frac{\mathrm{d}B^{\mathrm{a}}_{Y0}}{\mathrm{d}x}(x_0)\right|^{-1} &\sim \int_{x_0}^{x} \left(B^{\mathrm{a}}_{Y0}(z)\right)^2\,\mathrm{d}z \\ &= t-\xi = \tau + \int_0^{x_0} \left(B^{\mathrm{a}}_{Y0}(z)\right)^2\,\mathrm{d}z + \frac{T}{\mathrm{Ha}}\left|\frac{\mathrm{d}B^{\mathrm{a}}_{Y0}}{\mathrm{d}x}(x_0)\right|^{-1} - \xi.\end{aligned} \tag{3.1.42}$$

To facilitate matching, we define the inner time variable σ so that

$$\xi = \tau + \int_0^{x_0} \left(B^{\mathrm{a}}_{Y0}(z)\right)^2 \mathrm{d}z + \frac{\sigma}{\mathrm{Ha}}\left|\frac{\mathrm{d}B^{\mathrm{a}}_{Y0}}{\mathrm{d}x}(x_0)\right|^{-1}. \tag{3.1.43}$$

Writing the outer solution (3.1.30) in inner variables at leading-order, we then obtain the matching condition

$$\sigma \sim T - \frac{X^3}{3}, \qquad H \sim X^2\widehat{Q}(\sigma) + \frac{1}{X}, \qquad \text{as } X \to \infty, \tag{3.1.44}$$

where $\widehat{Q}(\sigma) = \tilde{Q}(\xi)$.

We find from (3.1.39) that the limit $X \to \infty$ is obtained in the inner solution by letting $c \to -\infty$, whereby

$$X \sim \frac{[3\psi(c)(T-c)-2]^{1/3}}{[\psi(c)]^{1/3}}, \qquad H \sim \frac{[3\psi(c)(T-c)-1]\,[\psi(c)]^{1/3}}{[3\psi(c)(T-c)-2]^{1/3}}, \tag{3.1.45a,b}$$

from which it follows from (3.1.44) that

$$\sigma \sim T - \frac{X^3}{3} \sim c + \frac{2}{3\psi(c)}, \tag{3.1.46}$$

and thus from (3.1.38) that

$$\widehat{Q}(\sigma) \sim \frac{HX-1}{X^3} \sim \psi(c). \tag{3.1.47}$$

The leading-order flux function in the downstream outer region is thus given parametrically by

$$\sigma = c + \frac{2}{3\psi(c)}, \qquad \widehat{Q}(\sigma) = \psi(c), \tag{3.1.48}$$

or, equivalently, by the functional equation

$$\widehat{Q}\left(c + \frac{2}{3\psi(c)}\right) = \psi(c). \tag{3.1.49}$$

We recall that the function ψ, defined by (3.1.32), describes the flux passing into the inner layer from the upstream region $x < x_0$, while $\widehat{Q}(\sigma) = \tilde{Q}(\xi)$ describes the flux passing from the inner later into the downstream region $x > x_0$. If equation (3.1.49) can be solved for $\widehat{Q}$, then the film thickness in $x > x_0$ is given by (3.1.41), and the leading-order solution is then fully determined everywhere. The second term in the argument of $\widehat{Q}$ expresses the modulation of the flux induced by the nonlinear flow in the inner region. This modulation allows for shocks to form, as we will discuss later.

Comparison with numerics

We demonstrate the accuracy of the asymptotic solution by comparing it to numerical solutions of the characteristic equations (3.1.15). To compute $h(x,t)$ we shoot for the value τ such that the characteristic emanating from $(0,\tau)$ goes through the point (x,t). Having found τ and integrated the characteristic equations (3.1.15), the value for $h(x,t)$ is known. For a complete profile at time t, a spatial discretisation is performed, and each spatial node x_i is used in sequence. Continuation — using the value τ_{i-1} corresponding to (x_{i-1},t) as the initial guess for τ_i — provides fast convergence.

The main advantage of this approach is that, unlike discretisations for general conservation equations, there is no dissipation as is inevitably introduced in other numerical schemes. A restriction of this approach is that it assumes that such a characteristic exists and is unique, which only holds when the Cauchy data is smooth and there are no shocks. Later on we show that this restriction remains surprisingly weak in the poloidal case.

In the matched asymptotics case the characteristics are visualised as follows. For each characteristic, the inner and outer solutions are stitched together continuously at some chosen points $x_0 \pm \Delta$, with $\mathrm{Ha}^{-1} \ll \Delta \ll 1$. This allows us to determine the value of c on each characteristic from (3.1.39a) using the known X and T values.

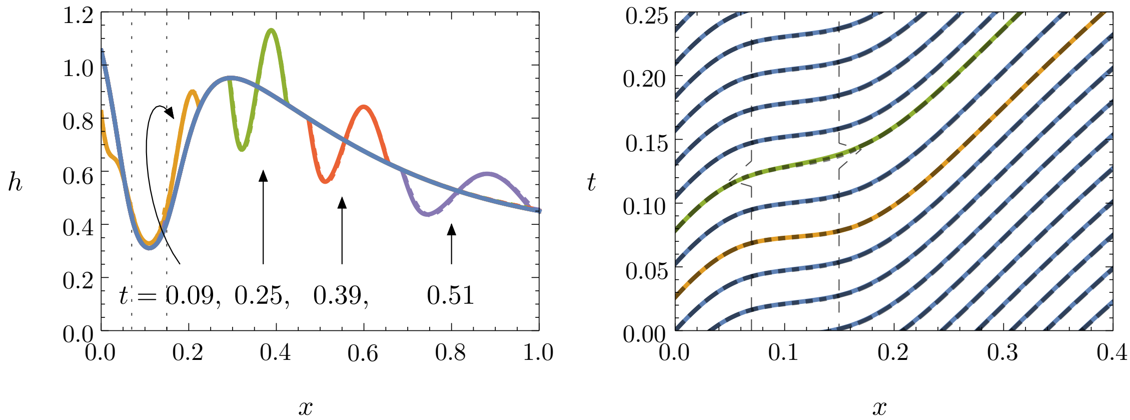

(a) $\delta = 0.3$. *(b) $\delta = 0.5$.*

Figure 3.3: (a) Snapshots of the free surface governed by (3.1.4) *at various times t (distinguished by curve colour) subject to the inlet boundary condition* (3.1.50) *solved via method of characteristics by directly integrating* (3.1.15) *(solid curves), and by the matched asymptotic solution (dotted curves). The applied field is that used in figure 2.4(a). The initial condition (blue curve) is the steady state (as in figure 2.4(b)). The inner region is illustrated by the dotted lines. (b) Characteristics of equation* (3.1.4) *subject to steady initial conditions and the inlet boundary condition* (3.1.50)*. The characteristics associated with the perturbation peak (orange curve) and trough (green curve) are highlighted. Solid curves are obtained by directly integrating* (3.1.15)*, while the broken black curves are the matched asymptotic solution, where inner and outer solutions are joined at the dashed lines.*

To display key solution features, a useful inlet boundary condition to impose is one period of a sin perturbation

$$h_{\mathrm{bc}}(t) = h_0(0) + \delta \sin(60t)\Pi(2\pi - 60t), \tag{3.1.50}$$

where h_0 is the steady state solution and Π the Heaviside step function. In figure 3.3(a) we show snapshots of time-dependent solutions of equation (3.1.4) subject to (3.1.50) with $\delta = 0.3$. Dotted vertical lines illustrate the position of the inner region. We find excellent agreement between the direct numerical (solid curves) and asymptotic solutions (dashed curves, difficult to distinguish as they nearly perfectly coincide). In the vicinity of the applied field sign change, $x \approx 0.1$, the oscillations alter the free surface only a small amount, while beyond this region they manifest more significantly, although spread over a smaller extent of the divertor (due to conservation of mass). This is the time-dependent manifestation of the observation made in the steady case: in a stronger applied field, the flow is decelerated and the film is thicker.

In figure 3.3(b) we show the characteristics corresponding to solutions of equation (3.1.4) subject to boundary condition (3.1.50) with $\delta = 0.5$ to obtain more visible deflection in the perturbed characteristics. The peak (orange curve) and trough (green curve) of the perturbation are highlighted. The broken black curves show the matched asymptotic approximation computed by joining the inner and outer solutions at the vertical dashed lines. To obtain good agreement for the characteristic associated with the perturbation trough, the stitching point needed to be altered by increasing Δ to ensure that the magnitude $\mathrm{Ha}\, B^{\mathrm{a}}_{Y0} h$ is sufficiently small. As expected, the perturbed characteristics deviate from their neighbours: the peak moves slightly faster, and thus its associated characteristic is shifted slightly down upon emerging from the inner region, while the trough moves slightly slower and upon emerging from the inner region is shifted up.

The deviation of the characteristics as they pass through the inner region results in the modulation of the flux described by the functional equation (3.1.49): the oscillations emerging into $x > x_0$ are slightly modified compared to those entering from $x < x_0$. This modulation is manifested in figure 3.3(b) in the non-uniform spacing of the characteristics in $x > x_0$. In the next section we examine the circumstances under which shocks can form in the inner region.

Shock formation

As mentioned above, no shocks can form in the outer region as the characteristics are parallel curves (up to exponentially small corrections). A shock forms in the inner region if and only if $\partial X/\partial c = 0$. From (3.1.39), and defining $z(c) = 1 - 3\psi(c)(T - c)$, the criterion may be written as

$$\frac{\psi'(c)}{(\psi(c))^2} = g(z) := \frac{3\tanh^2(z)}{(1-z)\tanh^2(z) - \tanh(z) + z}, \tag{3.1.51}$$

where the prime denotes differentiation with respect to the argument. The function $g(z)$ is continuous and monotonic, increasing unboundedly as $z \to \infty$, while $g(z) \to 3/2$ as $z \to -\infty$, as illustrated in figure 3.4. Therefore there will be a shock in the inner region if and only if

$$\frac{\psi'(c)}{(\psi(c))^2} > \frac{3}{2}, \tag{3.1.52}$$

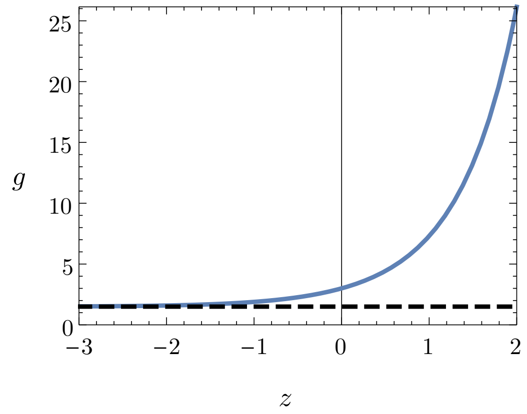

Figure 3.4: Shock criterion function $g(z)$ defined in (3.1.51) *as a solid curve and the dashed line marking $g = 3/2$.*

which from (3.1.32) may be written as

$$\frac{1}{\mathrm{Ha}(h_{\mathrm{bc}})^2}\frac{\mathrm{d}h_{\mathrm{bc}}}{\mathrm{d}t} \gtrsim \frac{3}{2(B^{\mathrm{a}}_{Y0}(0))^2}\left|\frac{\mathrm{d}B^{\mathrm{a}}_{Y0}}{\mathrm{d}x}(x_0)\right|. \tag{3.1.53}$$

Since $\mathrm{Ha} \gg 1$, we see from (3.1.53) that a shock can only form if the inlet film thickness becomes sufficiently thin or varies sufficiently rapidly. We note from (3.1.48) that the flux function $\widehat{Q}$ becomes multivalued if $\mathrm{d}\sigma/\mathrm{d}c = 0$, which is equivalent to the criterion (3.1.52), and is to be expected if a shock forms in the inner region.

For the purpose of illustration, we provide an example. From definition (3.1.32) we find that the familiar sinusoidal inlet condition (3.1.14) corresponds (up to a time-translation) to

$$\psi(c) = k(1 + a\cos(\Omega c)), \tag{3.1.54}$$

where

$$k = \frac{h_0(0)}{B^{\mathrm{a}}_{Y0}(0)^2}, \qquad a = \frac{\delta}{h_0(0)}, \qquad \Omega = \frac{\omega}{\mathrm{Ha}}\left|\frac{\mathrm{d}B^{\mathrm{a}}_{Y0}}{\mathrm{d}x}(x_0)\right|^{-1}. \tag{3.1.55a–c}$$

The criterion (3.1.52) predicts that a shock forms if

$$\frac{a\,\Omega\sin(\Omega\, c)}{k(1 + a\cos(\Omega\, c))^2} + \frac{3}{2} < 0 \tag{3.1.56}$$

for some c. The critical parameter values, bounding the region in parameter space

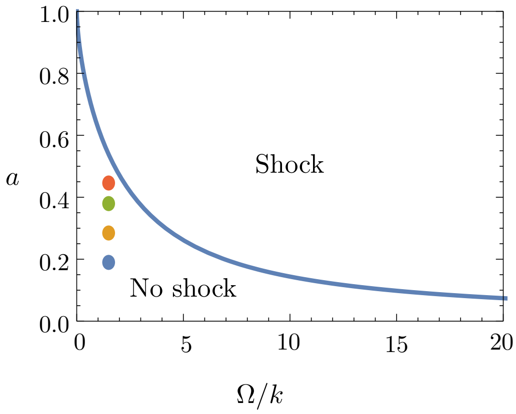

(a)

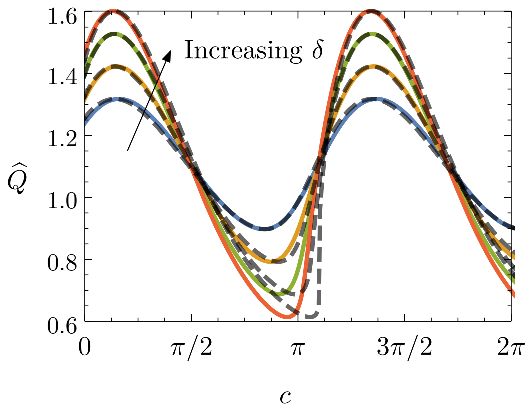

(b)

Figure 3.5: (a) Critical parameters determining whether a shock forms for the flux function (3.1.54). *The dots correspond to the parameter values of curves of matching colour in (b). (b) Flux function* $\widehat{Q}$ *given by* (3.1.48), *where* ψ *is given in* (3.1.54) *and* (3.1.55) *for* $\omega = 200$ *and* $\delta \in \{0.2, 0.3, 0.4, 0.47\}$, *displayed as solid curves. The black dashed curves show scaled fluxes obtained via numerical solution of the characteristic equations* (3.1.15) *where* $\mathrm{Ha} = 10$, $q = 1$, *and* $x_1 = 2.5$. *The applied field is that used in figure 2.4(a).*

where shocks form, may be found by equating the left-hand side of (3.1.56) and its derivative to zero. They are given parametrically by

$$\frac{\Omega}{k} = \frac{6\tan^3(\tilde{c})}{2\tan^2(\tilde{c}) + 1}, \qquad a = \frac{2\cos(\tilde{c})}{\cos(2\tilde{c}) - 3}, \qquad (3.1.57\text{a,b})$$

where $\tilde{c} = \Omega\, c \in (\pi, 3\pi/2)$. The critical curve in $(a, \Omega/k)$-parameter space is shown in figure 3.5(a). The representation in figure 3.5(a) demonstrates our earlier observation: shocks may form when the inlet film thickness is sufficiently small or oscillating sufficiently rapidly, that is, sufficiently large a or Ω, respectively.

We compare this formulation to numerical simulations in figure 3.5(b), where we plot $\widehat{Q}(c)$ from (3.1.49) for various values of δ, displayed as solid curves, overlayed by scaled fluxes obtained by solution of the characteristic equations (3.1.15), displayed as black dashed curves. The scaled fluxes are obtained by computing the flux Q at some fixed location x_1 (sufficiently far downstream of the sign change so as to have undergone the low-field modulation) for a series of times t. Having found the characteristic emanating from $(0, \tau)$ that passes through (x_1, t), the scaled flux curve passes (up to a translation) through the point

$$(c,\, \widehat{Q}) = \left(\tau \,\mathrm{Ha} \left| \frac{\mathrm{d}B^{\mathrm{a}}_{Y0}}{\mathrm{d}x}(x_0) \right|,\; \frac{h_{\mathrm{bc}}(\tau)}{B^{\mathrm{a}}_{Y0}(0)^2} \right). \tag{3.1.58}$$

The first-order term of magnitude $\mathcal{O}(1/\,\mathrm{Ha})$ is neglected to align the leading-order approximation with the numerical calculation.

We see in figure 3.5(b) that, as δ is increased, the amplitudes of the fluctuations in the flux function increase, as does the distortion at its minimum. As δ approaches its critical value $\widehat{Q}$ becomes more singular, ultimately forming a shock and becoming multivalued for $\delta > 0.5675$.

The numerical results align closely with the approximation for large $\widehat{Q}$, while for smaller $\widehat{Q}$, and thus smaller $\mathrm{Ha}\, h$, a slight discrepancy emerges with the full nonlinear system being nearer the criticality. We deduce that, when the oscillation amplitude δ is sufficiently large so as to cause $\mathrm{Ha}\, h$ to no longer be large, the asymptotic approximation slightly underestimates the full effects of nonlinearity.

Finally, let us compare the shock formation condition (3.1.53) with the condition (3.1.26) obtained previously. For a uniform magnetic field, (3.1.26) indicates exponetially strong suppression of shocks, reflecting the exponentially small effect of the nonlinearity when $\mathrm{Ha} \gg 1$. We can expect the same to be true for any applied magnetic field that is everywhere bounded away from zero. However, the analysis of this section shows how nonlinear effects do come into play in a neighbourhood of any root of the applied magnetic field. The criterion (3.1.53) shows that shocks are still suppressed when $\mathrm{Ha} \gg 1$, in the sense that they can only form for film thicknesses that are sufficiently small or varying sufficiently rapidly, but the suppression factor is proportional to Ha, rather than being exponentially large. Since Ha typically is of order 10, and the normal component of the applied field may change sign near the strike point on the divertor, it is quite conceivable that regimes where nonlinearity plays an important role could be encountered in practice.

3.1.7 Summary

We consider the stability of the thin film in the poloidal case neglecting higher-order effects and magnetic pressures, finding it stable to inlet perturbations. We find analytical solutions when the applied field is affine, and demonstrate two numerical methods for more general fields. We find that the behaviour is well captured by a linear approximation, owing to the fact that the nonlinearities are exponentially small in the typical high-field case. One fascinating implication of this feature is that the MHD effects strongly suppress the formation of shocks and rarefactions. When the vertical component of the applied field undergoes a sign change, the nonlinearities manifest in the vicinity of the sign change and the exponential shock suppression is weakened. We use matched asymptotic expansions to derive a functional equation that captures the nonlinear distortion of waves as they pass through the sign change, and thus derive a universal criterion on the inlet film thickness for the formation of shocks.

3.2 Unsteady Toroidal problem

3.2.1 Linear stability analysis

In this section we consider unsteady solutions of the thin-film equation for the toroidal case (2.3.32), which we rewrite here:

$$\frac{\partial h}{\partial t} + \frac{1}{r}\frac{\partial}{\partial r}(r\varphi Q) = 0. \tag{3.2.1}$$

Here φ is given in (2.3.27c) in the form

$$\varphi(r,t) = 1 - \alpha\frac{\partial h}{\partial r} - \frac{2\beta}{r^3} + \Gamma\frac{\partial^3 h}{\partial r^3} \tag{3.2.2}$$

and the flux function Q is given by (2.3.35) as

$$Q = \frac{r^3}{\lambda^3}F\left(\frac{\lambda h}{r}, \frac{\lambda}{ar}\right), \tag{3.2.3}$$

where F is defined by (2.3.35), and α, β, Γ, λ, and a are parameters. As in the poloidal case, we assume in the first instance that $\varphi = 1$, neglecting the higher-order effects of transverse gravity and surface tension, as well as the magnetic stresses. We solve the resulting nonlinear hyperbolic equation numerically using the Kurganov–Tadmor scheme [104] with the parameter-free Superbee limiter [171]. For the purposes of illustration, we initiate the simulation at the steady state film profile, $h(r,0) = h_0(r)$ with specified flux q, and, as in (3.1.50), subsequently perturb

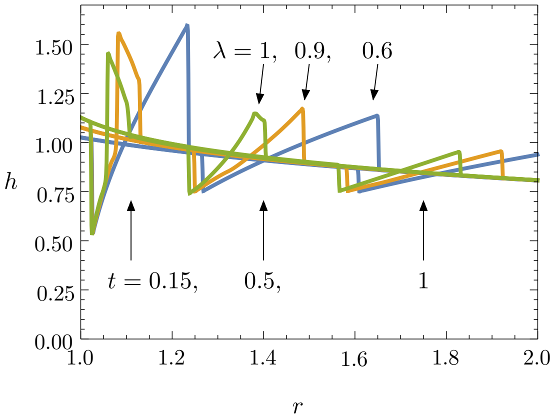

(a) $a = 1$.

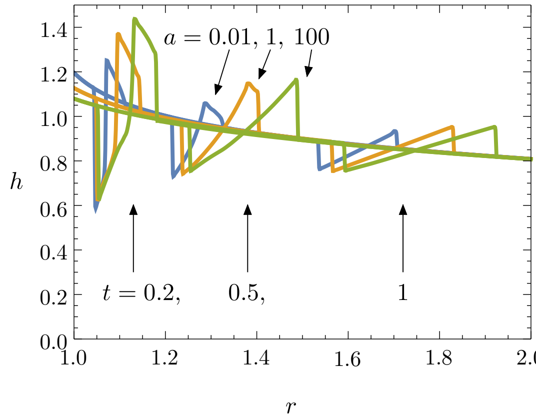

(b) $\lambda = 1$.

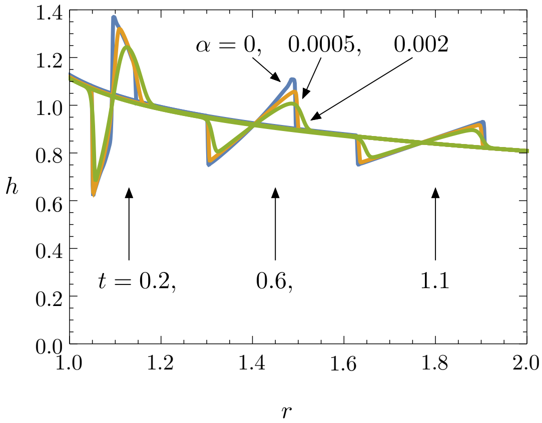

(c) $a = \lambda = 1$.

Figure 3.6: Snapshots of numerical simulations for the film thickness $h(r,t)$*, satisfying* (3.2.1)*, at the indicated times, with the time-dependent inlet flux given by* (3.2.4) *for steady flux* $q = 0.35$ *and* $A = 1.1$.

the inlet film height by one period of a sinusoid by applying the boundary condition

$$h(1,t) = h_0(r) + A\sin(60t)\Pi(2\pi - 60t), \tag{3.2.4}$$

where Π is the Heaviside function. The values of q and A are chosen to ensure that the criticality bound described in §2.3.5 is never exceeded, and the hyperbolic evolution problem thus remains well posed for all time.

In figures 3.6(a) and 3.6(b) we plot the computed free surface profiles at various times and for various values of λ, and a. We observe that, despite the smooth profile of the inlet perturbation, the free surface develops a sawtooth appearance, due to wave steepening that results in the formation of shocks and rarefactions, typical of nonlinear wave propagation. We also observe that either a higher field strength (larger λ) or a more conducting substrate (smaller a) slows the propagation of the disturbance (in particular at the higher free-surface heights), but does not necessarily lead to the disturbance magnitude being damped. This is consistent with our observations for the steady case where these two effects both lead to a higher free surface due to increased drag.

Finally, in figure 3.6(c), we relax the assumption that $\varphi \equiv 1$ to demonstrate how the sharp sawtooth is regularised by small contributions of the higher-order effects; here we reintroduce transverse gravity, by using small but nonzero values of the parameter α, while still neglecting surface tension. When introducing higher-order derivatives, we must impose the correct number of associated boundary conditions for the problem to be well posed. In the simulations shown in figure 3.6(c), we impose the flux condition (3.2.4) at the inlet and a passive zero-derivative boundary condition $\partial h/\partial r = 0$ at the outlet $r = 2$. The results show that more diffusion (larger α) does not change the propagation speed but smooths the slope discontinuities and somewhat damps the perturbation magnitude.

The simulations plotted in figure 3.6 display no growth of the perturbations as they propagate downstream, suggesting that the steady state free-surface profile is stable. We now investigate this behaviour analytically by looking at the linear stability of the system, just as in the poloidal case in §3.1.2. Let us suppose that the inlet thickness is subject to small-amplitude time-harmonic fluctuations, so that, at $r = 1$,

$$h(1,t) = h_0(1) + \delta \mathrm{e}^{-\mathrm{i}\omega t}, \tag{3.2.5}$$

where the frequency ω is specified and $0 < \delta \ll 1$. Since the coefficients of h vary in space in the governing equation (3.2.1), we consider perturbations to the free-surface profile of the form

$$h(r,t) = h_0(r) + \delta h_1(r) \mathrm{e}^{-\mathrm{i}\omega t}. \tag{3.2.6}$$

Substituting (3.2.6) into (3.2.1) and neglecting terms of $\mathcal{O}(\delta^2)$, we obtain the equation

$$\frac{1}{h_1}\frac{\mathrm{d}h_1}{\mathrm{d}r} = -\left(\frac{\partial Q}{\partial h}\right)^{-1}\left[-i\omega + \frac{1}{r}\frac{\mathrm{d}}{\mathrm{d}r}\left(r\frac{\partial Q}{\partial h}\right)\right], \tag{3.2.7a}$$

where derivatives of Q are evaluated at $(h_0(r); r)$, and h_1 is subject to the boundary condition

$$h_1(1) = 1. \tag{3.2.7b}$$

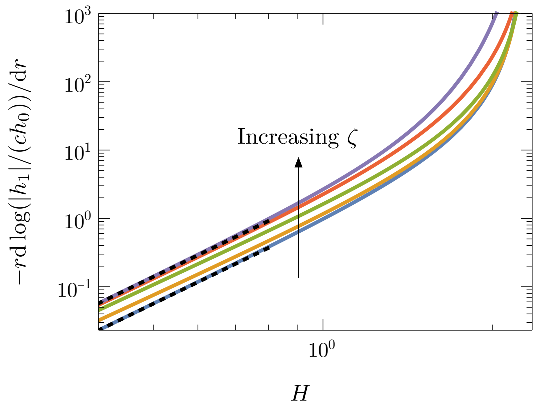

Figure 3.7: The right-hand side of (3.2.10) *plotted versus* H *with* $\zeta \in \{0,\ 0.2,\ 1,\ 5,\ \infty\}$. *The black dotted lines show the asymptotic behaviour as* $H \to 0$, *namely* $284H^4/315$ $(\zeta = 0)$, $704H^4/315$ $(\zeta > 0)$.

The solution of the problem (3.2.7) may be expressed in the form

$$h_1(r) = c\left(r\frac{\partial Q}{\partial h}(h_0(r); r)\right)^{-1} \exp\left(i\omega\int_1^r \left(\frac{\partial Q}{\partial h}(h_0(s); s)\right)^{-1} \mathrm{d}s\right), \tag{3.2.8}$$

where $c = \partial Q/\partial h$ evaluated at $(h_0(1); 1)$. The perturbation in (3.2.8) evidently comprises a spatially-dependent amplitude function

$$\left|\frac{h_1(r)}{c}\right| = \left(r\frac{\partial Q}{\partial h}(h_0(r); r)\right)^{-1}, \tag{3.2.9}$$

multiplied by an exponential oscillatory term which captures all the ω-dependence and has modulus 1. To explore the behaviour of the perturbation amplitude (3.2.9), we compute

$$-r\frac{\mathrm{d}}{\mathrm{d}r}\log\left(\frac{|h_1|}{ch_0}\right) = H\frac{\partial}{\partial H}\left(\frac{4F - \zeta\partial F/\partial\zeta}{H\partial F/\partial H}\right), \tag{3.2.10}$$

where F is again the expression given in (2.3.35). The expression on the right-hand side of (3.2.10) is a positive increasing function of H, which tends to infinity as H approaches the critical maximal value where $\partial Q/\partial h = 0$ (see figure 3.7). We deduce that, as r increases, the perturbation amplitude $|h_1(r)|$ decreases monotonically relative to the leading-order film thickness $h_0(r)$, and therefore respects the upper bounds

$$|h_1(r)| \leq \frac{|h_1(1)|}{h_0(1)}\, h_0(r) \leq \frac{|h_1(1)|}{r^{1/3}}. \tag{3.2.11}$$

The linear analysis is compared with numerical solutions of the hyperbolic PDE (3.2.1) in figure 3.8. The linear perturbations accurately capture the be-

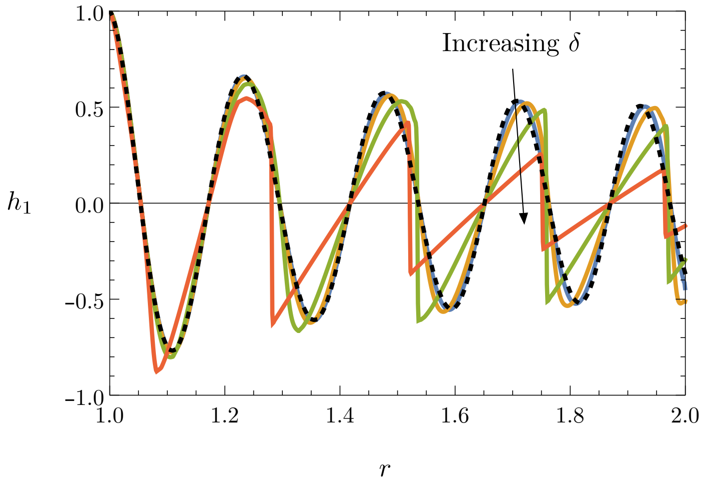

Figure 3.8: Snapshots of nonlinear perturbations to the steady free surface with steady flux $q = 0.35$ *and* $a = \lambda = 1$. *The perturbed solution* $h(r, t)$ *satisfies* (3.2.1) *with the boundary condition* $h(1, t) = h_0(1) + \delta \sin(\omega t)$, *where* $\omega = 20$ *and* $\delta \in \{0.01, 0.03, 0.1, 0.3\}$. *The perturbation* h_1 *is then computed via* $h_1(r) = (h(r, t) - h_0(r))/\delta$ *and plotted at time* $t = (2\pi/\omega)\lceil 3\omega/2\pi \rceil + \pi/2\omega$. *The dashed curve is the perturbation given by the linear theory in* (3.2.8).

haviour of nonlinear solutions for small perturbation magnitudes δ, while for larger perturbations the nonlinearities increasingly dominate the dynamics, leading to wave steepening and shock formation. This is in contrast with the poloidal case from § 3.1, where the nonlinearities are suppressed for high-field, and thus only negligible wave-steepening is observed. We observe in figure 3.8 that, despite the nonlinear effects, the amplitude of the perturbations continues to decay as they propagate downstream; indeed the amplitude decays more rapidly as δ increases, due to dissipation by the shocks.

The analysis of this section appears to show that there is no possibility of the steady base state suffering a linear instability. However, our governing thin-film equation (3.2.1) was derived by setting $\overline{\mathrm{Re}} = 0$ and thus assuming that inertia effects are uniformly negligible. In the next section, we perform a more detailed stability analysis that relaxes this assumption.

3.3 High-frequency stability analysis of the toroidal case

3.3.1 Background

While the stability of the poloidal case appears to be well studied for both pipe flows [100, 141, 142, 208] and free-surface flows [63] (see also references in [63]), stability analysis of the solutions in the toroidal case appear to be understudied in the literature. We present a brief review of related studies and then explain how the rest of this chapter contributes to the literature.

The stability of flow subject to co-planar perturbations of a parallel applied magnetic field is considered in [133]. Stuart [190] extends the stability analysis to include perturbations to the velocity field and thus finds the critical Reynolds number of the flow for the onset of linear instability. In [40] the same perturbation equations are considered, about different base velocity profiles corresponding to half-jets and jets. In [221], Stuart's derivation of [190] is extended to include a toroidal component of the applied magnetic field (parallel to the substrate but perpendicular to the flow). It is found in [221] and [189] that, in the purely toroidal case, linearised perturbations are unaffected by the magnetic field, and the critical Reynolds number is thus the same as for pure hydrodynamic flow. In [65] and [210] numerical analyses of Stuart's eigenvalue problem are performed for both two- and three-dimensional disturbances. In [49] a similar numerical analysis is performed for a co-planar field with a toroidal component as well as heating from below, and sufficient conditions for nonlinear stability are discussed. The nonlinear stability of a shear flow subject to a co-planar field with a toroidal component is also examined in [223].

All of the above work considers a parabolic flow profile with no free surface in the presence of a constant applied field, but plasma-facing components must have exposed free surfaces. A somewhat similar problem to ours is studied in [56], namely the linear stability of a steady free-surface flow in the presence of a linearly varying applied magnetic field. We now briefly outline the approach and results in [56], before explaining how the work in this chapter extends and improves upon them.

The model in [56] is based on a planar geometry, and a transverse magnetic field is imposed that varies linearly with position. The intention is to approximate the true inverse radial variation of magnetic field in an axisymmetric geometry, but the authors acknowledge that their linearly varying field is not curl-free and thus introduces spurious unphysical currents outside the liquid metal. The idealised two-dimensional geometry permits the existence of a fully developed unidirectional flow, with the liquid velocity and the induced magnetic field both uniform in the direction of motion. At small values of the Hartmann number, viscous effects dominate, and the fully-developed velocity reduces to a quadratic profile characteristic of purely hydrodynamic flow. However, as the Hartmann number increases, magnetic effects become increasingly important, and the velocity profile starts to exhibit oscillations of increasing amplitude. A linear stability analysis is performed by perturbing the unidirectional base state and simplifying the resulting linearised problem through various *ad hoc* approximations. The solutions thus obtained suggest that, when the Reynolds number is sufficiently large, the flow exhibits a long-wave instability analogous to the hydrodynamic instability identified by Yih [225].

In §2.3, a genuinely axisymmetric geometry is considered, with a toroidal magnetic field that satisfies Maxwell's equations both inside and outside the flowing liquid metal. For non-zero Reynolds number there is no fully-developed unidirectional flow in an axisymmetric geometry, and on the face of it a linear stability analysis analogous to that in [56] is not possible. Instead, we perform a multiple-scales stability analysis of high-frequency disturbances in which inertial effects may be significant despite the assumed smallness of the reduced Reynolds number. This approach results in an Orr–Summerfeld-type problem analogous to that obtained in [56], which we solve both asymptotically and numerically without introducing any artificial approximations. We find that the coupling between the magnetic induction and the flow may have a profound effect on the stability; in particular, there are regions of parameter space where the long-wave hydrodynamic instability identified in [225] is suppressed, resulting in a dramatic increase in the critical Reynolds number beyond which the base flow is unstable.

3.3.2 Synopsis

We start by outlining the derivations and analysis to follow, to guide the reader through the technical details. In §3.3.3 we perform a multiple-scales perturbation analysis of the underlying equations (2.3.27) and (2.3.28) to produce a linearised system governing small perturbations that act over sufficiently small space- and time-scales for inertial effects to become important. We seek separable solutions in the form of harmonic waves propagating in the r-direction, and thus ultimately obtain a generalised eigenvalue problem that, in principle, determines the linearised wave-speed c as a function of the wave-number k. This eigenvalue problem is normalised in §3.3.4 to reduce the number of independent parameters in the problem. Our focus then is on studying how the normalised wave-speed $\mathfrak{c}$ depends on the normalised wave-number κ. In particular, we want to determine whether the imaginary part of $\mathfrak{c}$ is positive for any $\kappa \in (0, \infty)$, in which case the base state is linearly unstable. To this end, we analyse in detail the limiting behaviours as $\kappa \to 0$ and as $\kappa \to \infty$ in §§3.3.5 and 3.3.6, respectively.

In the small-κ limit, we find that there are two families of solution branches: §3.3.5.1 concerns the *bounded* branch, on which $\mathfrak{c}$ tends to a constant, while §3.3.5.2 concerns the *divergent* branches, on which $\mathfrak{c}$ tends to infinity as $\kappa \to 0$. Our analysis reveals the set of parameter values for which the steady base state is stable in the limit $\kappa \to 0$, corresponding to arbitrarily long waves, thus generalising the hydrodynamic stability analysis of [225]. The corresponding large-κ analysis in § 3.3.6 establishes that, for all parameter values, $\mathrm{Im}[\mathfrak{c}]$ is ultimately negative in the limit as $\kappa \to \infty$, and thus that the base state is stable to perturbations with arbitrarily small wave-length.

A numerical approach to determine $\mathfrak{c}$ for any value of κ is described in § 3.3.7. We find that the different solution branches identified in § 3.3.5 may intersect and switch places, and it is therefore necessary to track all relevant branches carefully as κ is varied. For certain parameter values, although the problem is predicted to be stable in the limits as $\kappa \to 0$ and as $\kappa \to \infty$, the sign of $\mathrm{Im}[\kappa]$ may change at intermediate values of κ and thus render the problem unstable to finite-wavelength perturbations.

Finally, in § 3.3.8 we summarise the results of the stability analysis and explain their real-world relevance. In particular, we show how the critical Reynolds number, below which the steady base flow is stable, varies with the physical parameters in the problem.

3.3.3 Multiple-scales perturbation

Here we consider the stability of high-frequency disturbances on time- and length-scales that are small enough for inertia effects to become significant, despite the smallness of $\overline{\mathrm{Re}}$. With the inertia terms reinstated, the thin-film problem (2.3.27) and (2.3.28) becomes

$$\frac{\partial^2 B^{\mathrm{i}}}{\partial y^2} + \frac{u}{r^2} = 0, \tag{3.3.1a}$$

$$\frac{1}{r}\frac{\partial}{\partial r}(ru) + \frac{\partial v}{\partial y} = 0, \tag{3.3.1b}$$

$$\overline{\mathrm{Re}}\left(\frac{\partial u}{\partial t} + u\frac{\partial u}{\partial r} + v\frac{\partial u}{\partial y}\right) - \frac{\partial^2 u}{\partial y^2} + 4\lambda^4\frac{B^{\mathrm{i}}}{r^2} = \varphi(r,t), \tag{3.3.1c}$$

with boundary conditions

$$u = v = \frac{\partial B^{\mathrm{i}}}{\partial y} - aB^{\mathrm{i}} = 0 \qquad \text{at} \quad y = 0, \tag{3.3.2a}$$

$$\frac{\partial u}{\partial y} = v - \frac{\partial h}{\partial t} - u\frac{\partial h}{\partial r} = B^{\mathrm{i}} = 0 \qquad \text{at} \quad y = h(r,t). \tag{3.3.2b}$$

We proceed asymptotically in the limit as $\overline{\mathrm{Re}} \to 0$ by considering a multiple-scales perturbation about the steady base flow, writing

$$u = \tilde{u}(r,y) + \delta\,\overline{\mathrm{Re}}\,\hat{u}\left(\hat{r},r,y,\hat{t}\right), \tag{3.3.3a}$$

$$B^{\mathrm{i}} = \tilde{B}(r,y) + \delta\,\overline{\mathrm{Re}}\,\hat{B}\left(\hat{r},r,y,\hat{t}\right), \tag{3.3.3b}$$

$$v = \tilde{v}(r,y) + \delta\,\hat{v}\left(\hat{r},r,y,\hat{t}\right), \tag{3.3.3c}$$

$$h = \tilde{h}(r) + \delta\,\overline{\mathrm{Re}}\,\hat{h}\left(\hat{r},r,\hat{t}\right), \tag{3.3.3d}$$

where

$$\hat{r} = \frac{r}{\overline{\mathrm{Re}}}, \qquad\qquad \hat{t} = \frac{t}{\overline{\mathrm{Re}}} \tag{3.3.4a,b}$$

are fast length- and time-variables, and $\delta \ll 1$ is a small parameter. The first terms on the right-hand sides of decompositions (3.3.3) denote the steady base flow, which may be determined asymptotically with the expansion

$$\tilde{u}(r,y) \sim \tilde{u}_0(r,y) + \overline{\mathrm{Re}}\,\tilde{u}_1(r,y) + \cdots, \tag{3.3.5a}$$

$$\tilde{B}(r,y) \sim \tilde{B}_0(r,y) + \overline{\mathrm{Re}}\,\tilde{B}_1(r,y) + \cdots, \tag{3.3.5b}$$

$$\tilde{v}(r,y) \sim \tilde{v}_0(r,y) + \overline{\mathrm{Re}}\,\tilde{v}_1(r,y) + \cdots, \tag{3.3.5c}$$

$$\tilde{h}(r) \sim \tilde{h}_0(r) + \overline{\mathrm{Re}}\,\tilde{h}_1(r) + \cdots. \tag{3.3.5d}$$

Similarly, the perturbative terms of $\mathcal{O}(\delta)$ may be expanded via

$$\hat{u}\left(\hat{r},r,y,\hat{t}\right) \sim \hat{u}_0\left(\hat{r},r,y,\hat{t}\right) + \overline{\mathrm{Re}}\,\hat{u}_1\left(\hat{r},r,y,\hat{t}\right) + \cdots\,, \tag{3.3.6a}$$

$$\hat{B}\left(\hat{r},r,y,\hat{t}\right) \sim \hat{B}_0\left(\hat{r},r,y,\hat{t}\right) + \overline{\mathrm{Re}}\,\hat{B}_1\left(\hat{r},r,y,\hat{t}\right) + \cdots\,, \tag{3.3.6b}$$

$$\hat{v}\left(\hat{r},r,y,\hat{t}\right) \sim \hat{v}_0\left(\hat{r},r,y,\hat{t}\right) + \overline{\mathrm{Re}}\,\hat{v}_1\left(\hat{r},r,y,\hat{t}\right) + \cdots\,, \tag{3.3.6c}$$

$$\hat{h}\left(\hat{r},r,\hat{t}\right) \sim \hat{h}_0\left(\hat{r},r,\hat{t}\right) + \overline{\mathrm{Re}}\,\hat{h}_1\left(\hat{r},r,\hat{t}\right) + \cdots\,. \tag{3.3.6d}$$

To proceed, we have to decide how to decompose the pressure gradient term φ in powers of $\overline{\mathrm{Re}}$. Bearing in mind the relative typical sizes of the parameters α, β, Γ and $\overline{\mathrm{Re}}$ given in (2.3.26), and aiming to include transverse gravity and surface tension in the perturbation dynamics, we consider the case where $\alpha = \mathcal{O}\left(\overline{\mathrm{Re}}\right)$, $\beta = \mathcal{O}(1)$, and $\Gamma = \mathcal{O}\left(\overline{\mathrm{Re}}^3\right)$ as $\overline{\mathrm{Re}} \to 0$, and so define the $\mathcal{O}(1)$ quantities

$$\varphi_0 = 1 - \frac{2\beta}{r^3}, \qquad \hat{\alpha} = \frac{\alpha}{\overline{\mathrm{Re}}}, \qquad \hat{\Gamma} = \frac{\Gamma}{\overline{\mathrm{Re}}^3}. \tag{3.3.7a,b,c}$$

Substituting (3.3.3), (3.3.5) and (3.3.6) into equations (3.3.1) and (3.3.2), we find that the leading-order base terms $\tilde{u}_0(r,y)$, $\tilde{v}_0(r,y)$, $\tilde{B}_0(r,y)$ and $\tilde{h}_0(r)$ refer to solutions of the leading-order (inertia-free) model, as constructed in § 2.3.5. Next, linearising with respect to δ, we find that, to leading order in $\overline{\mathrm{Re}}$, the multiple-scales perturbation satisfies

$$\frac{\partial^2 \hat{B}_0}{\partial y^2} + \frac{\hat{u}_0}{r^2} = \frac{\partial \hat{u}_0}{\partial \hat{r}} + \frac{\partial \hat{v}_0}{\partial y} = 0, \tag{3.3.8a}$$

$$\frac{\partial \hat{u}_0}{\partial \hat{t}} + \tilde{u}_0\frac{\partial \hat{u}_0}{\partial \hat{r}} + \frac{\partial \tilde{u}_0}{\partial y}\hat{v}_0 - \frac{\partial^2 \hat{u}_0}{\partial y^2} + 4\lambda^4\,\frac{\hat{B}_0}{r^2} + \hat{\alpha}\frac{\partial \hat{h}_0}{\partial \hat{r}} - \hat{\Gamma}\frac{\partial^3 \hat{h}_0}{\partial \hat{r}^3} = 0, \tag{3.3.8b}$$

and boundary conditions

$$\hat{u}_0 = \hat{v}_0 = \frac{\partial \hat{B}_0}{\partial y} - a\hat{B}_0 = 0 \quad \text{at} \quad y = 0, \tag{3.3.9a}$$

$$\frac{\partial \hat{u}_0}{\partial y} + \frac{\partial^2 \tilde{u}_0}{\partial y^2}\,\hat{h}_0 = \hat{B}_0 + \frac{\partial \tilde{B}_0}{\partial y}\,\hat{h}_0 = \hat{v}_0 - \frac{\partial \hat{h}_0}{\partial \hat{t}} - \tilde{u}_0\frac{\partial \hat{h}_0}{\partial \hat{r}} = 0 \quad \text{at} \quad y = \tilde{h}_0(r). \tag{3.3.9b}$$

The problem (3.3.8) and (3.3.9) is linear and autonomous in $\hat{t}$ and $\hat{r}$, and depends only parametrically on r. We therefore suppress the dependence on r, for the moment, and seek separable harmonic solutions of wave-number k and wave-speed

c, that is (recycling notation),

$$\hat{u}_0 = \hat{u}(y)\mathrm{e}^{\mathrm{i}k\left(\hat{r}-c\hat{t}\right)}, \qquad \hat{v}_0 = \hat{v}(y)\mathrm{e}^{\mathrm{i}k\left(\hat{r}-c\hat{t}\right)}, \tag{3.3.10a,b}$$

$$\hat{B}_0 = \hat{B}(y)\mathrm{e}^{\mathrm{i}k\left(\hat{r}-c\hat{t}\right)}, \qquad \hat{h}_0 = \hat{h}\mathrm{e}^{\mathrm{i}k\left(\hat{r}-c\hat{t}\right)}, \tag{3.3.10c,d}$$

which results in the ODE problem

$$\frac{\mathrm{d}^2\hat{B}}{\mathrm{d}y^2} + \frac{\hat{u}}{r^2} = \frac{\mathrm{d}\hat{v}}{\mathrm{d}y} + \mathrm{i}k\hat{u} = 0, \tag{3.3.11a}$$

$$\mathrm{i}k\left(\tilde{u}_0 - c\right)\hat{u} + \frac{\mathrm{d}\tilde{u}_0}{\mathrm{d}y}\,\hat{v} - \frac{\mathrm{d}^2\hat{u}}{\mathrm{d}y^2} + \frac{4\lambda^4}{r^2}\,\hat{B} + \mathrm{i}k\left(\hat{\alpha} + \hat{\Gamma}k^2\right)\hat{h} = 0, \tag{3.3.11b}$$

with boundary conditions

$$\hat{u} = \hat{v} = \frac{\mathrm{d}\hat{B}}{\mathrm{d}y} - a\hat{B} = 0 \qquad \text{at} \quad y = 0, \tag{3.3.12a}$$

$$\frac{\mathrm{d}\hat{u}}{\mathrm{d}y} - \varphi_0\hat{h} = \hat{B} + \frac{\mathrm{d}\tilde{B}_0}{\mathrm{d}y}\,\hat{h} = \hat{v} - \mathrm{i}k\left(\tilde{u}_0 - c\right)\hat{h} = 0 \qquad \text{at} \quad y = \tilde{h}_0. \tag{3.3.12b}$$

The system (3.3.11) and (3.3.12) is similar to the linearised problem derived by [56], except that (i) our geometry is axisymmetric, not two-dimensional; (ii) we have included conductivity in the substrate; (iii) we do not artificially ignore the perturbation $\hat{B}$ to the magnetic field.

We can eliminate $\hat{u}$ and $\hat{B}$ from (3.3.11) and thus obtain a single ODE for $\hat{v}(y)$, namely

$$\frac{\mathrm{d}^4\hat{v}}{\mathrm{d}y^4} + \mathrm{i}k(c - \tilde{u}_0)\frac{\mathrm{d}^2\hat{v}}{\mathrm{d}y^2} + \left(\frac{4\lambda^4}{r^4} + \mathrm{i}k\frac{\mathrm{d}^2\tilde{u}_0}{\mathrm{d}y^2}\right)\hat{v} + \frac{4\mathrm{i}ka\lambda^4}{r^2}\,\hat{B}(0) = 0, \tag{3.3.13}$$

which is subject to

$$\hat{v} = \frac{\mathrm{d}\hat{v}}{\mathrm{d}y} = \frac{\mathrm{d}^3\hat{v}}{\mathrm{d}y^3} - k^2\left(\hat{\alpha} + \hat{\Gamma}k^2\right)\hat{h} + \frac{4\mathrm{i}k\lambda^4\hat{B}(0)}{r^2} = 0 \qquad \text{at} \quad y = 0, \tag{3.3.14a}$$

$$\begin{aligned} \hat{v} - \mathrm{i}k\left(\tilde{u}_0 - c\right)\hat{h} &= \frac{\mathrm{d}^2\hat{v}}{\mathrm{d}y^2} + \mathrm{i}k\varphi_0\hat{h} \\ = \frac{\mathrm{d}^3\hat{v}}{\mathrm{d}y^3} - \mathrm{i}k\left(\tilde{u}_0 - c\right)\frac{\mathrm{d}\hat{v}}{\mathrm{d}y} &- \left(k^2\left(\hat{\alpha} + \hat{\Gamma}k^2\right) + \frac{4\mathrm{i}k\lambda^4}{r^2}\,\frac{\mathrm{d}\tilde{B}_0}{\mathrm{d}y}\right)\hat{h} = 0 \qquad \text{at} \quad y = \tilde{h}_0. \end{aligned} \tag{3.3.14b}$$

3.3.4 Normalised problem

We normalise the leading-order solutions $\tilde{u}_0$ and $\tilde{B}_0$ using (2.3.29) and (2.3.30) as in §2.3.5, and similarly scale the first-order problem as follows:

$$\hat{v}(y) = -\frac{4\mathrm{i}ka\lambda^4\tilde{h}_0^4\hat{B}(0)}{r^2}\,\mathcal{V}(Y), \qquad k = \frac{\lambda^2}{\varphi_0 r^2\tilde{h}_0^2}\,\kappa, \qquad \hat{\alpha} = \varphi_0^2\tilde{h}_0^3\tilde{\alpha}, \tag{3.3.15a–c}$$

$$\hat{h} = \frac{4a\lambda^2H^4\hat{B}(0)}{\varphi_0}\,\mathcal{H}, \qquad c = \frac{\varphi_0}{a^2\zeta^2}\,\mathfrak{c}, \qquad \hat{\Gamma} = \varphi_0^4\tilde{h}_0^{11}\tilde{\Gamma}. \tag{3.3.15d–f}$$

We thus obtain the normalised equation

$$\frac{\mathrm{d}^4\mathcal{V}}{\mathrm{d}Y^4} + \mathrm{i}\kappa(\mathfrak{c}-\mathcal{U})\frac{\mathrm{d}^2\mathcal{V}}{\mathrm{d}Y^2} + \left(4H^4 + \mathrm{i}\kappa\frac{\mathrm{d}^2\mathcal{U}}{\mathrm{d}Y^2}\right)\mathcal{V} = 1, \tag{3.3.16}$$

which is analogous to equation (4.2) in [190], albeit with a different form of the base flow $\mathcal{U}(Y)$ and also with different boundary conditions, namely

$$\mathcal{V}(0) = \frac{\mathrm{d}\mathcal{V}}{\mathrm{d}Y}(0) = \frac{\mathrm{d}^2\mathcal{V}}{\mathrm{d}Y^2}(1) - \frac{H^2}{\mathfrak{c}-\mathcal{U}(1)}\,\mathcal{V}(1) = 0, \tag{3.3.17a}$$

$$\frac{\mathrm{d}^3\mathcal{V}}{\mathrm{d}Y^3}(0) - \frac{\mathrm{i}H^4\kappa\left(\tilde{\alpha} + H^4\tilde{\Gamma}\kappa^2\right)}{\mathfrak{c}-\mathcal{U}(1)}\,\mathcal{V}(1) = \frac{\zeta}{H}. \tag{3.3.17b}$$

In principle, the four boundary conditions (3.3.17) are sufficient to solve the ODE (3.3.16) for $\mathcal{V}(Y)$, with the solution depending parametrically on the normalised wave-number κ and wave-speed $\mathfrak{c}$, as well as on the parameters H, ζ, $\tilde{\alpha}$, and $\tilde{\Gamma}$. The remaining boundary condition

$$\frac{\mathrm{d}^3\mathcal{V}}{\mathrm{d}Y^3}(1) + \mathrm{i}\kappa\left(\mathfrak{c}-\mathcal{U}(1)\right)\frac{\mathrm{d}\mathcal{V}}{\mathrm{d}Y}(1) = \left(\mathrm{i}H^2\kappa\left(\tilde{\alpha} + H^4\tilde{\Gamma}\kappa^2\right) - 4\frac{\mathrm{d}\mathcal{B}}{\mathrm{d}Y}(1)\right)\frac{\mathrm{d}^2\mathcal{V}}{\mathrm{d}Y^2}(1) \tag{3.3.18}$$

thus effectively provides an algebraic dispersion relation between $\mathfrak{c}$ and κ. The temporal stability of the base state then depends on the imaginary part of $\mathfrak{c}$: if $\mathrm{Im}[\kappa\mathfrak{c}]$ is positive for any real value of κ, then the base state is linearly unstable; otherwise it is linearly stable. Since the problem (3.3.16–18) is invariant under the transformation $\{V,\kappa,c\} \mapsto \{\overline{V},-\kappa,\overline{c}\}$ (where the bar denotes complex conjugation), in practice we can restrict our attention to positive values of κ.

For any given values of the parameters H, ζ, $\tilde{\alpha}$, $\tilde{\Gamma}$, and the normalised wave-number κ, the generalised eigenvalue problem (3.3.16–18) gives an infinite set of possible values for the wave-speed $\mathfrak{c}$, and we are interested in the one with the largest imaginary part. Numerical solution of the problem is discussed below in § 3.3.7, but first, to guide and validate the numerics, we examine the asymptotic limits as the wave-number tends to zero or to infinity.

3.3.5 Small wave-number limit

3.3.5.1 Bounded branch

We follow the approach of [225] to analyse the dispersion relation in the limit as $\kappa \to 0$. We find that limiting solutions of (3.3.16–18) fall into two possible classes: one in which $\mathfrak{c}$ is bounded and one in which $\mathfrak{c}$ scales with $1/\kappa$ as $\kappa \to 0$. We begin by analysing the former case. Since the first-order coefficients of κ in the system (3.3.16–18) are pure imaginary, we seek solutions for $\mathcal{V}$ and $\mathfrak{c}$ as asymptotic expansions of the form

$$\mathcal{V}(Y) \sim \mathcal{V}_0(Y) + \mathrm{i}\kappa\mathcal{V}_1(Y) + \cdots, \qquad \mathfrak{c} \sim \mathfrak{c}_0 + \mathrm{i}\kappa\mathfrak{c}_1 + \cdots, \tag{3.3.19a,b}$$

where $\mathfrak{c}_0$ and $\mathfrak{c}_1$ are real. The steady base state is then stable or unstable, in the limit $\kappa \to 0$, depending on whether $\mathfrak{c}_1$ is negative or positive, respectively.

At leading order, we obtain the problem

$$\frac{\mathrm{d}^4\mathcal{V}_0}{\mathrm{d}Y^4} + 4H^4\mathcal{V}_0 = 1, \tag{3.3.20}$$

subject to

$$\mathcal{V}_0(0) = \frac{\mathrm{d}\mathcal{V}_0}{\mathrm{d}Y}(0) = \frac{\mathrm{d}^3\mathcal{V}_0}{\mathrm{d}Y^3}(0) - \frac{\zeta}{H} = \frac{\mathrm{d}^3\mathcal{V}_0}{\mathrm{d}Y^3}(1) + 4\frac{\mathrm{d}\mathcal{B}}{\mathrm{d}Y}(1)\frac{\mathrm{d}^2\mathcal{V}_0}{\mathrm{d}Y^2}(1) = 0, \tag{3.3.21}$$

and the leading-order wave-speed is then found from

$$\mathfrak{c}_0 = \mathcal{U}(1) + H^2\mathcal{V}_0(1) \Big/ \frac{\mathrm{d}^2\mathcal{V}_0}{\mathrm{d}Y^2}(1). \tag{3.3.22}$$

The solution of the boundary-value problem (3.3.20) and (3.3.21) may be written in the form

$$\mathcal{V}_0(Y) = -\frac{\zeta}{H^4\dfrac{\partial}{\partial H}\left[\dfrac{1}{H^2}\dfrac{\partial^3\Psi}{\partial Y^3}(0;H)\right]}\left[\Psi(Y;H) + H\frac{\partial\Psi}{\partial H}(Y;H) - Y\frac{\partial\Psi}{\partial Y}(Y;H)\right], \tag{3.3.23}$$

where Ψ is the leading-order stream-function, defined by

$$\Psi(Y;H) = \int_0^Y \mathcal{U}\left(\bar{Y}\right)\,\mathrm{d}\bar{Y}. \tag{3.3.24}$$

By substituting (3.3.23) into (3.3.22), we find that the leading-order wave-speed is given by

$$\mathfrak{c}_0 = \frac{\partial F}{\partial H}, \tag{3.3.25}$$

where $F(H,\zeta) = H\Psi(1;H)$ is equivalent to the normalised flux defined in (2.3.35). Thus the leading-order wave-speed is just the characteristic wave-speed of the underlying hyperbolic equation (3.3.22), a result that is also consistent with the simple linearised solution (3.2.8). The resulting behaviour of $\mathfrak{c}_0$ as a function of H for varying ζ is plotted in figure 3.9(a). Notably, the wave-speed is positive for physically relevant values of H, but tends to zero as H approaches the critical value where $\partial Q/\partial H = 0$.

The first-order problem reads

$$\frac{\mathrm{d}^4\mathcal{V}_1}{\mathrm{d}Y^4} + 4H^4\mathcal{V}_1 = -\left(\mathfrak{c}_0 - \mathcal{U}\right)\frac{\mathrm{d}^2\mathcal{V}_0}{\mathrm{d}Y^2} - \mathcal{V}_0\frac{\mathrm{d}^2\mathcal{U}}{\mathrm{d}Y^2}, \tag{3.3.26}$$

subject to

$$\mathcal{V}_1(0) = \frac{\mathrm{d}\mathcal{V}_1}{\mathrm{d}Y}(0) = \frac{\mathrm{d}^3\mathcal{V}_1}{\mathrm{d}Y^3}(0) - \frac{H^4\tilde{\alpha}\mathcal{V}_0(1)}{\mathfrak{c}_0 - \mathcal{U}(1)} = 0, \tag{3.3.27a}$$

$$\frac{\mathrm{d}^3\mathcal{V}_1}{\mathrm{d}Y^3}(1) + 4\frac{\mathrm{d}\mathcal{B}}{\mathrm{d}Y}(1)\frac{\mathrm{d}^2\mathcal{V}_1}{\mathrm{d}Y^2}(1) = H^2\tilde{\alpha}\,\frac{\mathrm{d}^2\mathcal{V}_0}{\mathrm{d}Y^2}(1) - \left(\mathfrak{c}_0 - \mathcal{U}(1)\right)\frac{\mathrm{d}\mathcal{V}_0}{\mathrm{d}Y}(1), \tag{3.3.27b}$$

and the first correction to the wave-speed is then given by

$$\mathfrak{c}_1 = \left(H^2\mathcal{V}_1(1) - \big(\mathfrak{c}_0 - \mathcal{U}(1)\big)\frac{\mathrm{d}^2\mathcal{V}_1}{\mathrm{d}Y^2}(1)\right)\Big/\frac{\mathrm{d}^2\mathcal{V}_0}{\mathrm{d}Y^2}(1). \tag{3.3.28}$$

It may be observed that the solutions for $\mathcal{V}_1$ and $\mathfrak{c}_1$ can only vary affinely with the stabilising gravitational parameter $\tilde{\alpha}$, i.e. we can write

$$\mathcal{V}_1(Y) \equiv \mathcal{V}_{1,0}(Y) + \tilde{\alpha}\mathcal{V}_{1,\alpha}(Y), \qquad \mathfrak{c}_1 \equiv \mathfrak{c}_{1,0} + \tilde{\alpha}\mathfrak{c}_{1,\alpha}, \tag{3.3.29a,b}$$

and the coefficients $\mathfrak{c}_{1,0}$ and $\mathfrak{c}_{1,\alpha}$ may thus be solved for independently. The terms

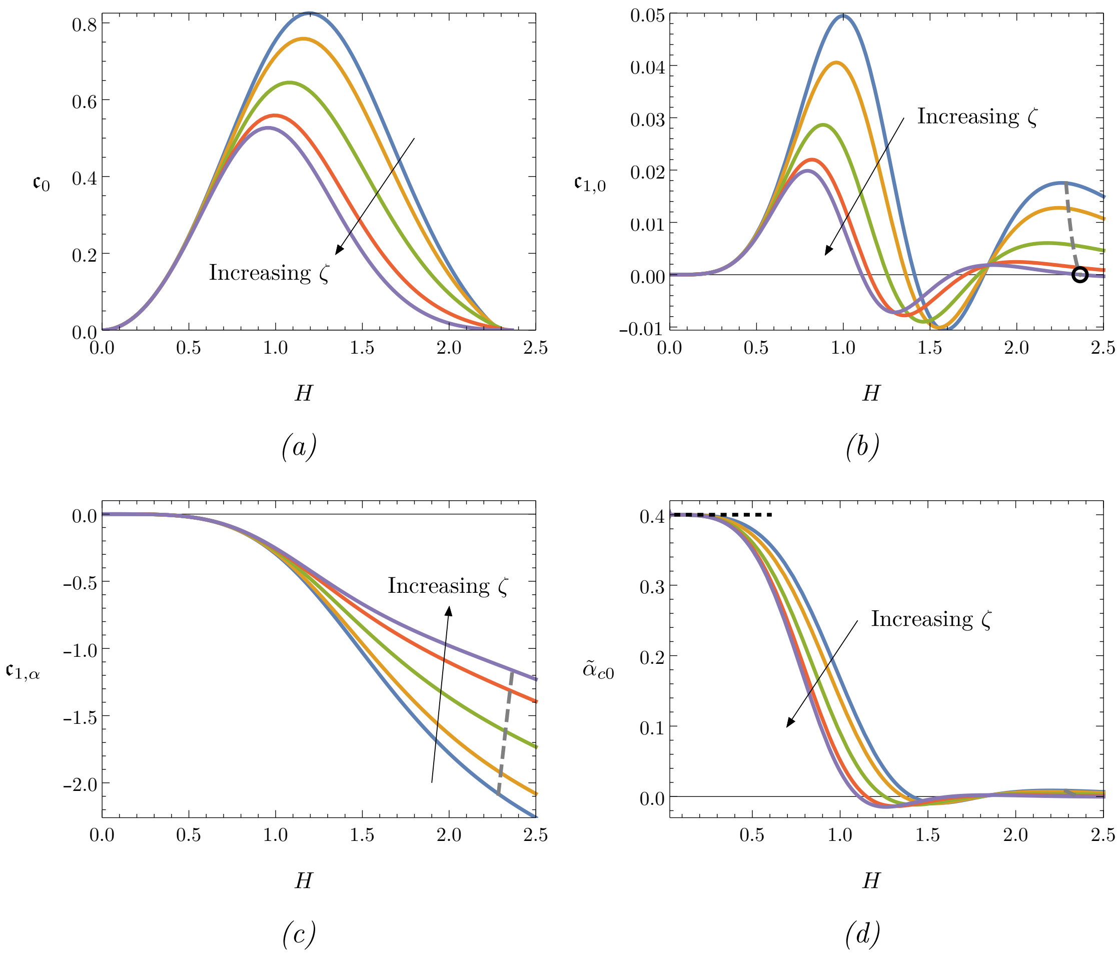

Figure 3.9: (a) The leading-order wave-speed $\mathfrak{c}_0$; (b) the first-order wave-speed $\mathfrak{c}_{1,0}$ evaluated at $\tilde{\alpha} = 0$; (c) the coefficient $\mathfrak{c}_{1,\alpha}$ in the first-order wave-speed $\mathfrak{c}_1$; (d) the critical value of $\tilde{\alpha}$ for stability of long waves. All are plotted versus H for $\zeta \in \{0, 0.2, 1, 5, \infty\}$, with a grey dashed curve bounding the range of parameters where physical steady solutions exist. In (b), the black circle indicates the $\zeta \to \infty$ curve crossing the horizontal axis at the critical value of H. In (d), the black dotted curve shows the asymptotic behaviour $\tilde{\alpha}_{c0} \to 2/5$ as $H \to 0$.

proportional to $\tilde{\alpha}$ are relatively straightforward to evaluate, in the forms

$$\mathcal{V}_{1,\alpha}(Y) = \frac{1}{4H^2 \partial \mathcal{B}(0)/\partial H} \left[4H^3 \mathcal{B}(0) \mathcal{V}_0(Y) - \zeta \Psi(Y) \right] \tag{3.3.30a}$$

$$\mathfrak{c}_{1,\alpha} = -HF(H, \zeta), \tag{3.3.30b}$$

where F is again the function defined by (2.3.35). Explicit solutions can also be found for $\mathcal{V}_{1,0}$ and $\mathfrak{c}_{1,0}$, but they are too long-winded to reproduce here. The solutions for $\mathfrak{c}_{1,0}$ and $\mathfrak{c}_{1,\alpha}$ are plotted versus H for various values of ζ in figures 3.9(b) and 3.9(c).

The coefficient $\mathfrak{c}_{1,0}$ may be positive or negative for physically relevant values of ζ and H. We note for future reference that, in the limit $\zeta \to \infty$, one can express $\mathfrak{c}_{1,0}$ in the form

$$\mathfrak{c}_{1,0} = \big[\cos(H)\sinh(H) + \sin(H)\cosh(H)\big]G(H), \tag{3.3.31}$$

where the function $G(H)$ is finite for all H. We recall from § 2.3.5 that the term in square brackets in (3.3.31) is zero when $\zeta \to \infty$ and H is at its critical value where $\partial Q/\partial H = 0$. It follows that, when $\zeta \to \infty$, corresponding to a perfectly conducting substrate, $\mathfrak{c}_{1,0}$ is zero precisely at the critical value of H. This behaviour is highlighted by the black circle in figure 3.9(b): the curve corresponding to $\zeta \to \infty$ crosses the horizontal axis precisely when it intersects the grey dashed curve which marks the critical value of H.

The coefficient $\mathfrak{c}_{1,\alpha}$ is always negative, as we would expect since transverse gravity always has a stabilising effect. Therefore, the steady base state is stable if $\tilde{\alpha}$ is sufficiently large, specifically if it exceeds a critical value $\tilde{\alpha}_{c0} = -\mathfrak{c}_{1,0}/\mathfrak{c}_{1,\alpha}$, which is plotted in figure 3.9(d). Intriguingly, we see that there is a range of parameter values for which $\tilde{\alpha}_{c0}$ is negative, and therefore for which the base state is stable to long-wave perturbations regardless of the value of $\tilde{\alpha}$. It thus appears that magnetic effects may be sufficient to stabilise long waves even when there is no transverse component of gravity, in contrast with the results of [225], which are recovered in the hydrodynamic limit $H \to 0$. However, we will see below in § 3.3.7 that the picture changes when all values of κ are considered, and not just the limit $\kappa \to 0$.

3.3.5.2 Divergent solutions

Here we analyse the second class of solutions to the problem (3.3.16–18), in which $\mathfrak{c}$ diverges as $\kappa \to 0$, by posing the asymptotic expansions

$$\mathcal{V}(Y) \sim \mathcal{V}_0(Y) + \mathrm{i}\kappa\mathcal{V}_1(Y) + \cdots, \qquad \mathfrak{c} \sim -\frac{\mathrm{i}\mathfrak{c}_{-1}}{\kappa} + \cdots. \tag{3.3.32a,b}$$

This ansatz corresponds to perturbations proportional to $\mathrm{e}^{-\mathfrak{c}_{-1}t}$, so that $\mathfrak{c}_{-1}$ represents the limiting linear decay rate as $\kappa \to 0$. The leading-order problem then takes the form

$$\frac{\mathrm{d}^4\mathcal{V}_0}{\mathrm{d}Y^4} + \mathfrak{c}_{-1}\frac{\mathrm{d}^2\mathcal{V}_0}{\mathrm{d}Y^2} + 4H^4\mathcal{V}_0 = 1, \tag{3.3.33}$$

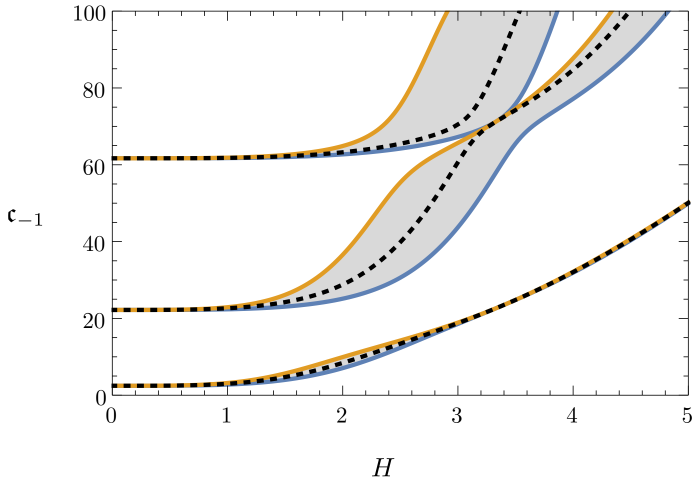

Figure 3.10: Limiting linear decay rate $\mathfrak{c}_{-1}$ versus normalised film thickness H. The grey shaded regions indicate parameter values for which (3.3.35) *gives positive values of ζ, bounded below by the solid blue curves where $\zeta = 0$ and above by the solid orange curves where $\zeta \to \infty$. The black dotted curves show contours where $\zeta = 1$.*

subject to the boundary conditions

$$\mathcal{V}_0(0) = \frac{\mathrm{d}\mathcal{V}_0}{\mathrm{d}Y}(0) = \frac{\mathrm{d}^2\mathcal{V}_0}{\mathrm{d}Y^2}(1) = \frac{\mathrm{d}^3\mathcal{V}_0}{\mathrm{d}Y^3}(0) - \frac{\zeta}{H} = \frac{\mathrm{d}^3\mathcal{V}_0}{\mathrm{d}Y^3}(1) + \mathfrak{c}_{-1}\frac{\mathrm{d}\mathcal{V}_0}{\mathrm{d}Y}(1) = 0. \quad (3.3.34)$$

By solving the constant-coefficients equation (3.3.33) and applying the five boundary conditions in (3.3.34), we obtain a functional relation between the leading-order wave-speed $\mathfrak{c}_{-1}$ and the parameters H and ζ, which may be expressed in the form

$$\zeta = \frac{\left(\mathfrak{c}_{-1} + 2H^2\right)\left(\mathfrak{c}_{-1} - 4H^2\right)\Delta_+ \sin\Delta_+ - \left(\mathfrak{c}_{-1} + 4H^2\right)\left(\mathfrak{c}_{-1} - 2H^2\right)\Delta_- \sin\Delta_-}{2H\left[16H^4 - \left(\mathfrak{c}_{-1} + 2H^2\right)\left(\mathfrak{c}_{-1} - 4H^2\right)\cos\Delta_+ - \left(\mathfrak{c}_{-1} + 4H^2\right)\left(\mathfrak{c}_{-1} - 2H^2\right)\cos\Delta_-\right]}, \quad (3.3.35a)$$

where we have introduced the shorthand

$$\Delta_\pm = \sqrt{\mathfrak{c}_{-1} \pm 4H^2}. \quad (3.3.35b)$$

There are three cases to consider: if $\mathfrak{c}_{-1} \geq 4H^2$, then Δ_+ and Δ_- are both real; if $-4H^2 \leq \mathfrak{c}_{-1} < 4H^2$, then Δ_- becomes pure imaginary; and if $\mathfrak{c}_{-1} < -4H^2$, then both Δ_+ and Δ_- are pure imaginary. However, it may be shown that (3.3.35) returns non-negative values of ζ only when $\mathfrak{c}_{-1} > 0$, so the final case can be discarded. In figure 3.10, the blue and orange solid curves show $(H, \mathfrak{c}_{-1})$ parameter values where the numerator and the denominator of (3.3.35) are zero, respectively.

These curves bound the shaded grey regions corresponding to positive values of ζ, and the particular contours with $\zeta = 1$ are picked out as black dotted curves. We conclude that, for any positive values of ζ and H, (3.3.35) admits a countably infinite spectrum of solutions for $\mathfrak{c}_{-1}$. The nth branch emerges from $\mathfrak{c}_{-1} \to (n+1/2)^2\pi^2$ as $H \to 0$, with $n = 0, 1, 2, \ldots$, and indeed every branch satisfies $\mathfrak{c}_{-1} > \pi^2/4$. It follows that our system has an infinite set of solution branches where the wave-speed diverges like $1/\kappa$ as $\kappa \to 0$, but that each of them has positive decay rate and so is exponentially damped.

3.3.6 Large wave-number limit

It is clear that surface tension, characterised by the parameter $\tilde{\Gamma}$, must ultimately dominate and stabilise the problem if the wave-number κ is sufficiently large. However, we are interested in the "worst-case scenario" where surface tension is negligible, and the question of whether the problem is stable even in its absence. To corroborate the numerical results presented below, we now consider the asymptotic limit as $\kappa \to \infty$ with $\tilde{\Gamma}$ set to zero. Before proceeding with the asymptotic analysis, we first note that integration of equation (3.3.16) with respect to Y and application of the boundary conditions (3.3.17) leads to the identity

$$4H^4 \int_0^1 \mathcal{V}(Y)\,\mathrm{d}Y - \frac{4H^2\mathcal{B}'(0)\mathcal{V}(1)}{c - \mathcal{U}(1)} = 1 + \frac{\zeta}{H}. \tag{3.3.36}$$

We seek an outer solution for $\mathcal{V}$ by taking the limit $\kappa \to \infty$ in equation (3.3.16), resulting in

$$(\mathfrak{c} - \mathcal{U})\frac{\mathrm{d}^2\mathcal{V}}{\mathrm{d}Y^2} + \frac{\mathrm{d}^2\mathcal{U}}{\mathrm{d}Y^2}\mathcal{V} = \mathcal{O}\left(\kappa^{-1}\right). \tag{3.3.37}$$

Evidently the order of equation (3.3.16) has been reduced by two, so this is a singular perturbation. However, the boundary conditions (3.3.17) and (3.3.18) at $Y = 1$ may be expressed in the forms

$$\left[c - \mathcal{U}(1)\right]\frac{\mathrm{d}^2\mathcal{V}}{\mathrm{d}Y^2}(1) - H^2\mathcal{V}(1) = 0, \tag{3.3.38a}$$

$$\left[c - \mathcal{U}(1)\right]\frac{\mathrm{d}\mathcal{V}}{\mathrm{d}Y}(1) - H^2\tilde{\alpha}\frac{\mathrm{d}^2\mathcal{V}}{\mathrm{d}Y^2}(1) = \mathcal{O}\left(\kappa^{-1}\right), \tag{3.3.38b}$$

$$\left[c - \mathcal{U}(1)\right]^2\frac{\mathrm{d}\mathcal{V}}{\mathrm{d}Y}(1) - H^4\tilde{\alpha}\mathcal{V}(1) = \mathcal{O}\left(\kappa^{-1}\right), \tag{3.3.38c}$$

and, recalling that $\mathcal{U}''(1) = -H^2$, we find that two of the three conditions in (3.3.38) are satisfied identically by solutions of the outer problem (3.3.37) up to $\mathcal{O}\left(\kappa^{-1}\right)$.

As a consequence of this redundancy, there is no boundary layer at $Y=1$, and we apply (3.3.38) directly to the outer problem (3.3.37).

Now we substitute the asymptotic expansions

$$\mathcal{V}(Y) \sim \mathcal{V}_\infty(Y) + \kappa^{-1/2}\mathcal{V}_{\infty 1}(Y) + \cdots, \qquad \mathfrak{c} \sim \mathfrak{c}_\infty + \kappa^{-1/2}\mathfrak{c}_{\infty 1} + \cdots \tag{3.3.39a,b}$$

into equation (3.3.37). The leading-order equation may be integrated once to give

$$(\mathfrak{c}_\infty - \mathcal{U})\frac{\mathrm{d}\mathcal{V}_\infty}{\mathrm{d}Y} + \frac{\mathrm{d}\mathcal{U}}{\mathrm{d}Y}\mathcal{V}_\infty = A_1, \tag{3.3.40}$$

where A_1 is an integration constant. As we will see below, matching with the boundary layer at $Y=0$ requires $\mathcal{V}_\infty(0)$ to be zero. Following one further integration with respect to Y, we thus find the leading-order outer solution in the form

$$\mathcal{V}_\infty(Y) = A_1\big[\mathfrak{c}_\infty - \mathcal{U}(Y)\big]\int_0^Y \frac{\mathrm{d}\eta}{\big[\mathfrak{c}_\infty - \mathcal{U}(\eta)\big]^2}. \tag{3.3.41}$$

Using the leading-order solution (3.3.41), we find that (as anticipated) (3.3.38) collapses to a single relation

$$A_1 = \frac{H^4\tilde{\alpha}\mathcal{V}_\infty(1)}{\mathfrak{c}_\infty - \mathcal{U}(1)} = H^4\tilde{\alpha}A_1\int_0^1 \frac{\mathrm{d}Y}{\big[\mathfrak{c}_\infty - \mathcal{U}(Y)\big]^2}. \tag{3.3.42}$$

For non-trivial solutions, we must therefore have

$$H^4\tilde{\alpha}\int_0^1 \frac{\mathrm{d}Y}{\big[\mathfrak{c}_\infty - \mathcal{U}(Y)\big]^2} = 1, \tag{3.3.43}$$

which determines the leading-order wave-speed $\mathfrak{c}_\infty$ as $\kappa \to \infty$, as a function of $\tilde{\alpha}$, H and ζ. The amplitude A_1 remains undetermined by equation (3.3.42) but may in principle be found by substituting (3.3.41) into the identity (3.3.36).

Equation (3.3.43) admits real roots for the limiting wave-speed $\mathfrak{c}_\infty$. To determine the stability, we must therefore proceed to $\mathcal{O}\left(\kappa^{-1/2}\right)$ in (3.3.37), obtaining

$$\mathfrak{c}_{\infty 1}\frac{\mathrm{d}\mathcal{V}_\infty}{\mathrm{d}Y} + (\mathfrak{c}_\infty - \mathcal{U})\frac{\mathrm{d}\mathcal{V}_{\infty 1}}{\mathrm{d}Y} + \frac{\mathrm{d}\mathcal{U}}{\mathrm{d}Y}\mathcal{V}_{\infty 1} = A_2, \tag{3.3.44}$$

where A_2 is another integration constant. By integrating once more with respect to Y, we find that the first correction to the outer solution takes the form

$$\frac{\mathcal{V}_{\infty 1}(Y)}{\mathfrak{c}_\infty - \mathcal{U}(Y)} = \frac{\mathcal{V}_{\infty 1}(0)}{\mathfrak{c}_\infty} + \frac{\mathfrak{c}_{\infty 1}\mathcal{V}_\infty(Y)}{\left[\mathfrak{c}_\infty - \mathcal{U}(Y)\right]^2} + A_2 \int_0^Y \frac{\mathrm{d}\eta}{\left[\mathfrak{c}_\infty - \mathcal{U}(\eta)\right]^2} - 2\mathfrak{c}_{\infty 1} A_1 \int_0^Y \frac{\mathrm{d}\eta}{\left[\mathfrak{c}_\infty - \mathcal{U}(\eta)\right]^3}, \quad (3.3.45)$$

where $\mathcal{V}_{\infty 1}(0)$ remains to be determined through asymptotic matching with the boundary layer at $Y = 0$.

To this end, we perform the scalings

$$Y = \kappa^{-1/2}\hat{Y}, \qquad \mathcal{V}(Y) = \kappa^{-1/2}\hat{\mathcal{V}}\big(\hat{Y}\big), \quad (3.3.46\text{a,b})$$

transforming the governing equation (3.3.16) into

$$\frac{\mathrm{d}^4\hat{\mathcal{V}}}{\mathrm{d}\hat{Y}^4} + \mathrm{i}\mathfrak{c}_\infty \frac{\mathrm{d}^2\hat{\mathcal{V}}}{\mathrm{d}\hat{Y}^2} = \mathcal{O}\left(\kappa^{-1/2}\right), \quad (3.3.47)$$

subject to

$$\hat{\mathcal{V}} = \frac{\mathrm{d}\hat{\mathcal{V}}}{\mathrm{d}\hat{Y}} = 0 \quad \text{at } \hat{Y} = 0. \quad (3.3.48)$$

By matching with the leading-order outer solution (3.3.41) (and verifying *a posteriori* our supposition that $\mathcal{V}_\infty(0) = 0$), we obtain the leading-order inner solution

$$\hat{\mathcal{V}}\big(\hat{Y}\big) \sim \frac{A_1}{\mathfrak{c}_\infty}\left[\hat{Y} - \frac{(1 \pm \mathrm{i})}{\sqrt{2|\mathfrak{c}_\infty|}}\left(1 - \mathrm{e}^{-(1\mp\mathrm{i})\hat{Y}\sqrt{|\mathfrak{c}_\infty|/2}}\right)\right], \quad (3.3.49)$$

where $\mathfrak{c}_\infty = \pm|\mathfrak{c}_\infty|$. By expanding (3.3.49) as $\hat{Y} \to \infty$, we obtain the matching condition

$$\mathcal{V}_{\infty 1}(0) = -\frac{(\mathrm{i} \pm 1)A_1}{\sqrt{2}\,|\mathfrak{c}_\infty|^{3/2}}. \quad (3.3.50)$$

Again at $\mathcal{O}\left(\kappa^{-1/2}\right)$, the three boundary conditions (3.3.38) at $Y = 1$ collapse to a single relation, namely

$$\mathfrak{c}_{\infty 1}A_1 + \left[\mathfrak{c}_\infty - \mathcal{U}(1)\right]A_2 = H^4\tilde{\alpha}\mathcal{V}_{\infty 1}(1). \quad (3.3.51)$$

The right-hand side of equation (3.3.51) is evaluated using the $\mathcal{O}\left(\kappa^{-1/2}\right)$ outer solution (3.3.45). Again we find that the amplitude A_2 drops out (although it could in principle be calculated using (3.3.36)), and we obtain the following expression

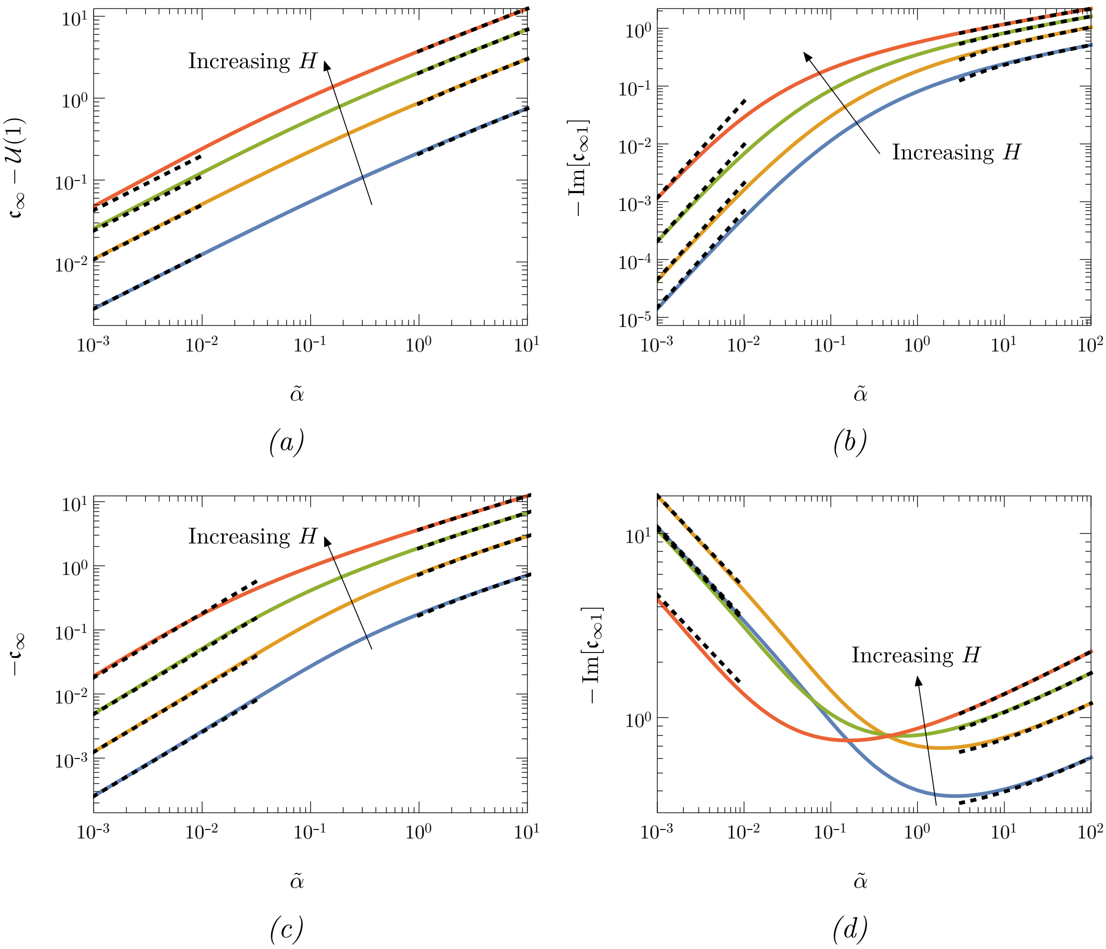

Figure 3.11: The leading-order (a, c) and first-order (b, d) wave-speeds in the short wave-length limit $\kappa \to \infty$ plotted versus the gravitational parameter $\tilde{\alpha}$ with $\zeta = 1$ and $H \in \{0.5, 1, 1.5, 2\}$, for the positive (a, b) and negative (c, d) roots of (3.3.43)*. The dotted lines show the asymptotic limits* (3.3.53) *and* (3.3.54)*.*

for the first-order wave-speed

$$\mathfrak{c}_{\infty 1} = -\frac{(\mathrm{i} \pm 1)}{2^{3/2}|\mathfrak{c}_\infty|^{5/2}} \Bigg/ \int_0^1 \frac{\mathrm{d}Y}{\left|\mathfrak{c}_\infty - \mathcal{U}(Y)\right|^3}. \tag{3.3.52}$$

In summary, solution of the nonlinear algebraic equations (3.3.43) and (3.3.52) determines $\mathfrak{c}_\infty$ and $\mathfrak{c}_{\infty 1}$ as functions of $\tilde{\alpha}$, H and ζ.

For given positive values of H, ζ and $\tilde{\alpha}$, equation (3.3.43) admits two possible real roots for $\mathfrak{c}_\infty$: one positive, with $\mathfrak{c}_\infty > \mathcal{U}(1)$, and one negative. The first correction to each solution is then found by substituting $\mathfrak{c}_\infty$ into equation (3.3.52). For the positive root, we plot $\mathfrak{c}_\infty - \mathcal{U}(1)$ and $-\operatorname{Im}[\mathfrak{c}_{\infty 1}]$ versus $\tilde{\alpha}$ with $\zeta = 1$ and various values of H in figures 3.11(a) and 3.11(b), respectively. The dotted lines show the asymptotic limits

$$\mathfrak{c}_\infty \sim \mathcal{U}(1) + \frac{H^2}{2}\left(\pi\tilde{\alpha}\right)^{2/3}, \qquad \text{as} \quad \tilde{\alpha} \to 0, \tag{3.3.53a}$$

$$\mathfrak{c}_{\infty 1} \sim -\frac{(\mathrm{i}+1)\pi^{2/3}H^6}{3\sqrt{2}\,\mathcal{U}(1)^{5/2}}\,\tilde{\alpha}^{5/3} \qquad \text{as} \quad \tilde{\alpha} \to 0, \tag{3.3.53b}$$

$$\mathfrak{c}_\infty \sim H^2\sqrt{\tilde{\alpha}} + \frac{F(H,\zeta)}{H}, \qquad \text{as} \quad \tilde{\alpha} \to \infty, \tag{3.3.53c}$$

$$\mathfrak{c}_{\infty 1} \sim -\frac{(\mathrm{i}+1)H}{2^{3/2}}\left[\tilde{\alpha}^{1/4} - \frac{5F(H,\zeta)}{2H^3}\,\tilde{\alpha}^{-1/4}\right] \qquad \text{as} \quad \tilde{\alpha} \to \infty, \tag{3.3.53d}$$

derived in appendix A.4. Evidently, the leading-order wave-speed increases monotonically from $\mathcal{U}(1)$ to $+\infty$ as $\tilde{\alpha}$ increases. Meanwhile, the correction $\mathfrak{c}_{\infty 1}$ always has negative imaginary part, although it tends to zero as $\tilde{\alpha} \to 0$.

In figures 3.11(c) and 3.11(d), with the same values of ζ and H, we plot $-\mathfrak{c}_\infty$ and $-\operatorname{Im}[\mathfrak{c}_{\infty 1}]$ versus $\tilde{\alpha}$ for the negative root of equation (3.3.43). The dotted lines show the asymptotic limits

$$\mathfrak{c}_\infty \sim -\frac{H^4}{\mathcal{U}'(0)}\,\tilde{\alpha}, \qquad \text{as} \quad \tilde{\alpha} \to 0, \tag{3.3.54a}$$

$$\mathfrak{c}_{\infty 1} \sim -\frac{(\mathrm{i}-1)\,\mathcal{U}'(0)^{3/2}}{H^2\sqrt{2\tilde{\alpha}}} \qquad \text{as} \quad \tilde{\alpha} \to 0, \tag{3.3.54b}$$

$$\mathfrak{c}_\infty \sim -H^2\sqrt{\tilde{\alpha}} + \frac{F(H,\zeta)}{H}, \qquad \text{as} \quad \tilde{\alpha} \to \infty, \tag{3.3.54c}$$

$$\mathfrak{c}_{\infty 1} \sim -\frac{(\mathrm{i}-1)H}{2^{3/2}}\left[\tilde{\alpha}^{1/4} + \frac{5F(H,\zeta)}{2H^3}\,\tilde{\alpha}^{-1/4}\right] \qquad \text{as} \quad \tilde{\alpha} \to \infty, \tag{3.3.54d}$$

calculated in appendix A.4. This time we see that $\mathfrak{c}_\infty$ decreases from 0 to $-\infty$ as $\tilde{\alpha}$ increases. The imaginary part of the first correction $\mathfrak{c}_{\infty 1}$ has a rather complicated dependence on ζ and H, but always remains negative, tending to $-\infty$ both as $\tilde{\alpha} \to 0$ and as $\tilde{\alpha} \to \infty$.

For each of the roots depicted in figure 3.11, the limiting wave-speed $\mathfrak{c}_\infty$ as $\kappa \to \infty$ is purely real, and the first correction $\mathfrak{c}_{\infty 1}$ always has negative imaginary part. We conclude that the base state is indeed stable to large wave-number disturbances. However, figure 3.11(b) shows that, for the positive root $\mathfrak{c}_\infty$, the magnitude of $\mathfrak{c}_{\infty 1}$ tends to zero as $\tilde{\alpha} \to 0$, and consequently we will find that increasingly large values of the wave-number κ are required for the behaviour (3.3.39) to emerge when $\tilde{\alpha}$ is small.

3.3.7 Numerical solution for arbitrary wave-number

We now pursue numerical solutions of the problem (3.3.16–18) for arbitrary values of the wave-number κ. Let us introduce the fourth-order differential operator $\mathcal{L}$, defined by writing equation (3.3.16) as $\mathcal{L}[\mathcal{V}] = 1$. Then for any given κ we consider the particular solutions $\mathcal{V}^1$, $\mathcal{V}^2$, and $\mathcal{V}^3$ satisfying

$$\mathcal{L}[\mathcal{V}^1] = 1, \qquad \mathcal{V}^1(0) = \frac{\mathrm{d}\mathcal{V}^1}{\mathrm{d}Y}(0) = \frac{\mathrm{d}^2\mathcal{V}^1}{\mathrm{d}Y^2}(0) = \frac{\mathrm{d}^3\mathcal{V}^1}{\mathrm{d}Y^3}(0) = 0, \tag{3.3.55a}$$

$$\mathcal{L}[\mathcal{V}^2] = 0, \qquad \mathcal{V}^2(0) = \frac{\mathrm{d}\mathcal{V}^2}{\mathrm{d}Y}(0) = \frac{\mathrm{d}^2\mathcal{V}^2}{\mathrm{d}Y^2}(0) = 0, \quad \frac{\mathrm{d}^3\mathcal{V}^2}{\mathrm{d}Y^3}(0) = 1, \tag{3.3.55b}$$

$$\mathcal{L}[\mathcal{V}^3] = 0, \qquad \mathcal{V}^3(0) = \frac{\mathrm{d}\mathcal{V}^3}{\mathrm{d}Y}(0) = \frac{\mathrm{d}^3\mathcal{V}^3}{\mathrm{d}Y^3}(0) = 0, \quad \frac{\mathrm{d}^2\mathcal{V}^3}{\mathrm{d}Y^2}(0) = 1. \tag{3.3.55c}$$

Note that the operator $\mathcal{L}$ depends on κ, which we take as given, and on $\mathfrak{c}$, which at this stage we guess, say $\mathfrak{c}(\kappa) = c_1$. Given the values of κ and c_1, it is straightforward to solve the initial-value problems (3.3.55) for the particular solutions $\mathcal{V}^j$. Any combination of the form $\mathcal{V} = \mathcal{V}^1 + c_2\mathcal{V}^2 + c_3\mathcal{V}^3$ then solves the original equation (3.3.16), and the boundary conditions (3.3.17) can be satisfied by an appropriate choice of the constants c_2 and c_3. The remaining auxiliary boundary condition (3.3.18) is then the residual we seek to bring to zero, and thus this procedure reduces to a complex root-finding process for c_1.

For each set of parameters $\{H, \zeta, \tilde{\alpha}, \tilde{\Gamma}\}$ and each value of the wave-number κ, we are interested in the root for $\mathfrak{c}$ with the largest imaginary part, corresponding to the most unstable perturbation mode. The analysis from § 3.3.5 is used to initialise the root-finding at small values of κ, and continuation is then used to track individual branches of $\mathfrak{c}(\kappa)$ over a range of values of κ. However, we will see that the values of $\mathrm{Im}[\mathfrak{c}]$ on different solution branches may cross as κ is varied. We therefore also discover distinct branches using deflation [50]: having found one root of our residual function, say $\mathfrak{c}(\kappa) = c_1$, we next seek a root of the deflated residual, given by multiplying the residual function by $(1 + |\mathfrak{c}(\kappa) - c_1|^{-2})$.

We first verify that the results of the numerical procedure outlined above are consistent with the asymptotic predictions from §§3.3.5 and 3.3.6. In figure 3.12(a), we show numerically computed solutions for $\mathrm{Re}[\mathfrak{c}]$ and $\mathrm{Im}[\mathfrak{c}]$ on the bounded branch of the dispersion relation for $\mathfrak{c}(\kappa)$, with the parameters $H = \zeta = 1$ and $\tilde{\Gamma} = 0$ held fixed while the value of $\tilde{\alpha}$ is varied. The black dotted lines demonstrate that $\mathrm{Re}[\mathfrak{c}]$ approaches the value predicted by (3.3.25) and $\mathrm{Im}[\mathfrak{c}]$ tends to zero, with limiting gradient as predicted by (3.3.28).

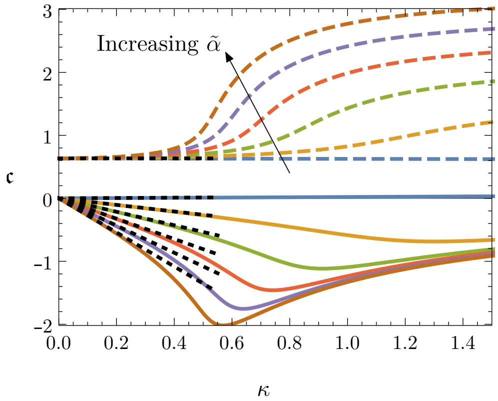

(a) $\tilde{\Gamma} = 0$, $\tilde{\alpha} \in \{0, 2, 4, 6, 8, 10\}$.

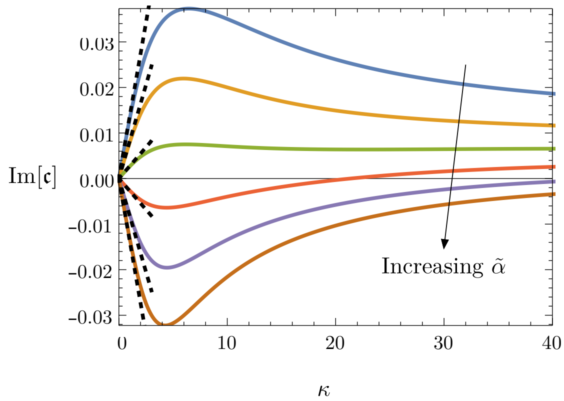

(b) $\tilde{\Gamma} = 0$, $\tilde{\alpha} \in \{0.04, 0.06, 0.08, 0.1, 0.12, 0.14\}$.

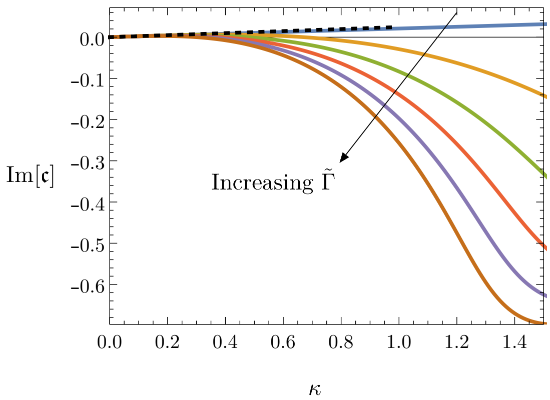

(c) $\tilde{\alpha} = 0$, $\tilde{\Gamma} \in \{0, 0.2, 0.4, 0.6, 0.8, 1\}$.

Figure 3.12: The bounded branch of $\mathfrak{c}$ *plotted versus* κ*, computed numerically by solution of (3.3.16–18) with* $H = \zeta = 1$*. In (a), solid curves show* Im[$\mathfrak{c}$]*, dashed curves show* Re[$\mathfrak{c}$]*. The black dotted curves show the small-*κ *asymptotic behaviour predicted by* (3.3.25) *and* (3.3.28).

In figure 3.12(b) we explore in more detail the behaviour for small values of $\tilde{\alpha}$ close to the critical value $\tilde{\alpha}_{c0} \approx 0.09$ when $H = \zeta = 1$ (see figure 3.9(d)). As predicted, the gradient of Im[$\mathfrak{c}(\kappa)$] at $\kappa = 0$ becomes negative, and long waves are thus stabilised, when $\tilde{\alpha} > \tilde{\alpha}_{c0}$. However, we observe that there is a range of values of $\tilde{\alpha}$ such that Im[$\mathfrak{c}$] is negative as $\kappa \to 0$ but changes sign as κ increases. From § 3.3.6, we know that Im[$\mathfrak{c}$] must ultimately become negative again at sufficiently large κ but, nevertheless, there is a range of intermediate values of κ for which Im[$\mathfrak{c}$] > 0. For such parameter values, the problem is unstable although the small-κ asymptotic analysis from § 3.3.5.1 predicts otherwise, and the critical value $\tilde{\alpha}_c$ is therefore larger than the small-κ value $\tilde{\alpha}_{c0}$. We will show below how figure 3.9(d) is modified when all wave-numbers κ are taken into account, and not just the limit

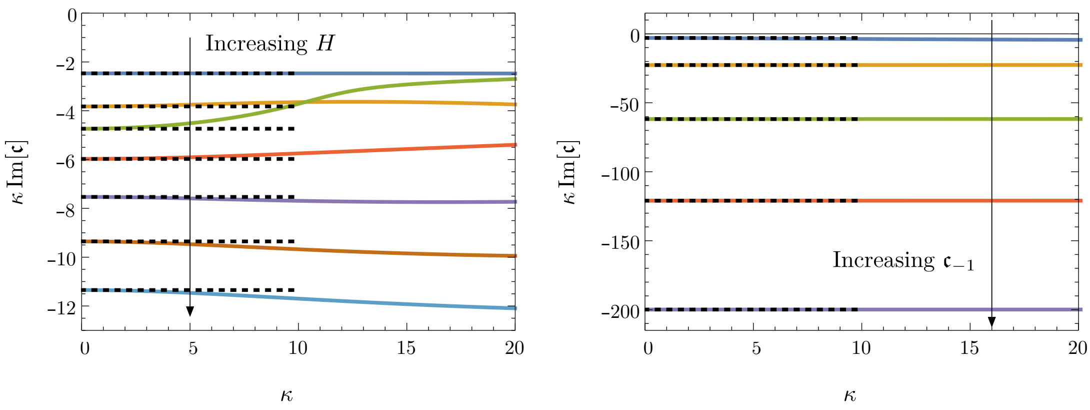

(a) $H \in \{0.1, 1.3, 1.5, 1.7, 1.9, 2.1, 2.3\}$*.*

(b) $H = 1$*, multiple branches.*

Figure 3.13: The linear growth rate, $\kappa\,\mathrm{Im}[\mathfrak{c}]$*, plotted versus* κ *for the divergent solution branches, computed numerically by solution of (3.3.16–18) with* $\tilde{\alpha} = \tilde{\Gamma} = 0$ *and* $\zeta = 1$*. (a) The divergent branch with minimal* $\mathfrak{c}_{-1}$ *and varying* H*. (b) The first five divergent branches with* $H = 1$*. The black dotted lines show the small-*κ *asymptotic behaviour predicted by* (3.3.35)*.*

as $\kappa \to 0$.

Figure 3.12(c) illustrates the stabilising influence of surface tension, measured by the parameter $\tilde{\Gamma}$. Increasing the value of $\tilde{\Gamma}$ rapidly damps high wave-numbers, as expected, but does not affect the behaviour as $\kappa \to 0$: only transverse gravity is able to counteract the long-wave instability.

In figure 3.13 we explore the behaviour of the divergent branches as $\kappa \to 0$. In figure 3.13(a) we plot the linear growth rate $\kappa\,\mathrm{Im}[\mathfrak{c}(\kappa)]$ versus κ for the first divergent branch (i.e. with smallest value of $\mathfrak{c}_{-1}$) with a variety of H values, while, in figure 3.13(b), we fix $H = 1$ and plot the first five divergent branches. In all cases, we observe excellent agreement with the small-κ asymptotic approximations given by (3.3.35) (shown as black dotted lines), over a surprisingly wide range of values of κ.

In figure 3.14, we show the behaviours of $\mathrm{Re}[\mathfrak{c}]$ and $\mathrm{Im}[\mathfrak{c}]$ at large values of κ, with $H = 1$, $\zeta = 1$, $\tilde{\Gamma} = 0$ and various values of $\tilde{\alpha}$. The large-κ predictions given by (3.3.43) and (3.3.52) are shown as black dashed curves. Figures 3.14(a) and 3.14(d) demonstrate that the values of $\mathrm{Re}[\mathfrak{c}]$ on the bounded and divergent branches approach the positive and negative roots $\mathfrak{c}_\infty$ of equation (3.3.43), respectively. Figures 3.14(b) and 3.14(e) show the corresponding values of $\mathrm{Im}[\mathfrak{c}]$, which appear to tend slowly towards the predicted behaviour $\mathrm{Im}[\mathfrak{c}_{\infty 1}]\kappa^{-1/2}$, with $\mathfrak{c}_{\infty 1}$ given by equation (3.3.52). Figures 3.14(c) and 3.14(f) demonstrate that the numerical

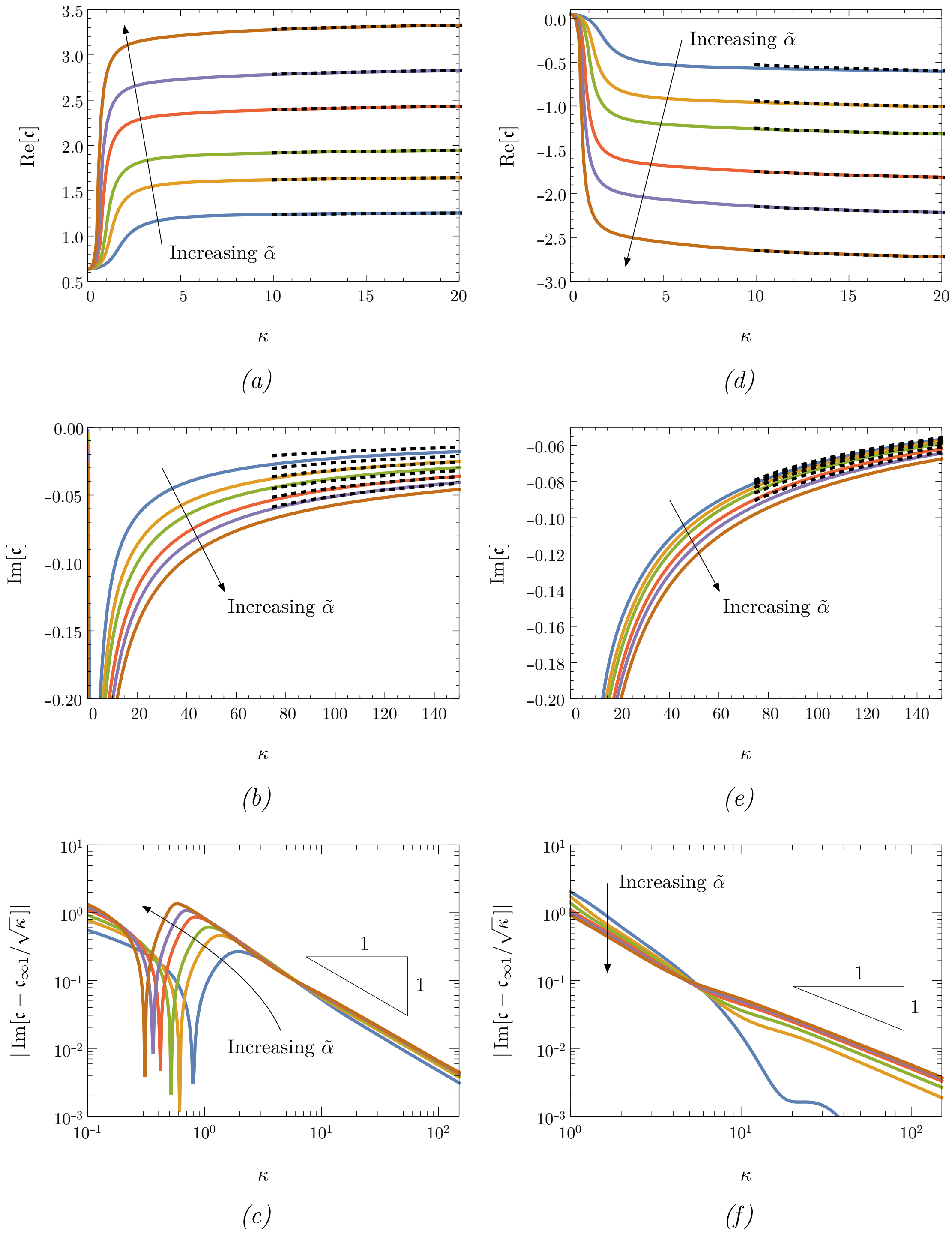

Figure 3.14: Numerically computed dispersion relation between $\mathfrak{c}$ and κ, with $H = \zeta = 1$, $\tilde{\Gamma} = 0$ and $\tilde{\alpha} \in \{1, 2, 3, 5, 7, 10\}$. (a–c) show the bounded branch, while (d–f) show the first divergent branch. The large-κ predictions given by (3.3.43) *and* (3.3.52) *are shown as black dashed curves. In (c) and (f) we confirm that the errors in (b) and (e), respectively, scale with $1/\kappa$ as $\kappa \to \infty$.*

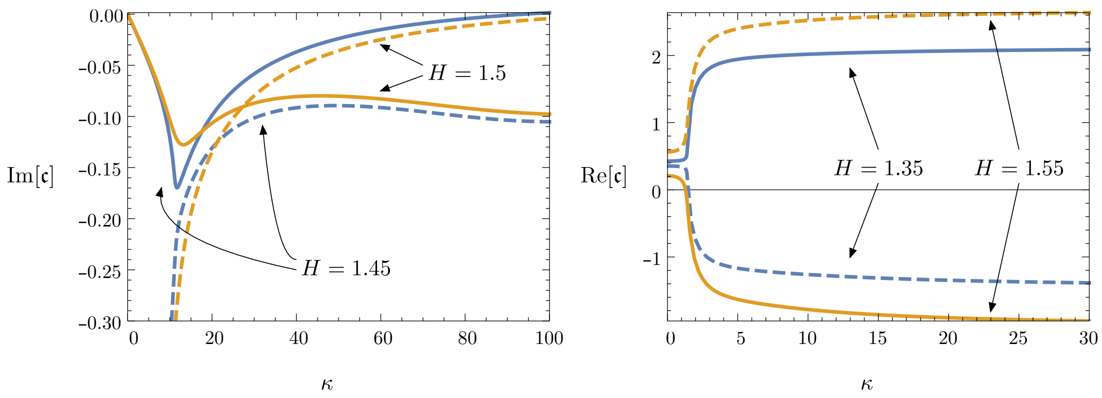

(a) $\tilde{\alpha} = 0$, $H \in \{1.45, 1.5\}$. *(b)* $\tilde{\alpha} = 1$, $H \in \{1.35, 1.55\}$.

Figure 3.15: Numerically computed dispersion relations computed with $\tilde{\Gamma} = 0$, $\zeta = 1$, and various values of H and $\tilde{\alpha}$. Branches bounded as $\kappa \to 0$ are plotted as solid curves, while the divergent branches appear as dashed curves. In both cases, we observe a bifurcation whereby the behaviours for large κ interchange between the bounded branch and the first divergent branch.

and asymptotic results do indeed converge, with the discrepancy between them scaling with $1/\kappa$ as $\kappa \to \infty$. As shown in § 3.3.6, the coefficient $\mathfrak{c}_{\infty 1}$ of $\kappa^{-1/2}$ in the large-κ asymptotic expansion of $\mathfrak{c}$ may be rather small when $\tilde{\alpha}$ is small, while figures 3.14(c) and 3.14(f) suggest that the coefficient of κ^{-1} is relatively insensitive to the value of $\tilde{\alpha}$. It follows that increasingly large values of κ need to be used to observe the predicted $\kappa^{-1/2}$ behaviour of $\mathrm{Im}[\mathfrak{c}]$ when $\tilde{\alpha}$ is small. This is even more the case for the higher divergent solution branches, on which, as seen in figure 3.13(b) and explained in § 3.3.5.2, the coefficient $\mathfrak{c}_{-1}$ can be tens or hundreds of times larger than the minimal value, requiring κ to be hundreds or thousands of times larger for the solution to converge to the large-κ regime.

Having verified that our numerical results reproduce the asymptotic predictions for the various solution branches as $\kappa \to 0$ and as $\kappa \to \infty$, we are ready to investigate numerically how these branches are connected via intermediate κ. For example, in figure 3.14 the branches with $\mathfrak{c}_\infty > \mathcal{U}(1)$ as $\kappa \to \infty$ all correspond to branches with bounded imaginary part as $\kappa \to 0$, while the branches with $\mathfrak{c}_\infty < 0$ as $\kappa \to \infty$ all correspond to branches with divergent imaginary part as $\kappa \to 0$. However, this is not always the case: figure 3.15 illustrates a bifurcation that occurs whereby the bounded and divergent solution branches exchange their tails at an intermediate value of κ.

Consider the blue solid curve in figure 3.15(a), showing the bounded branch

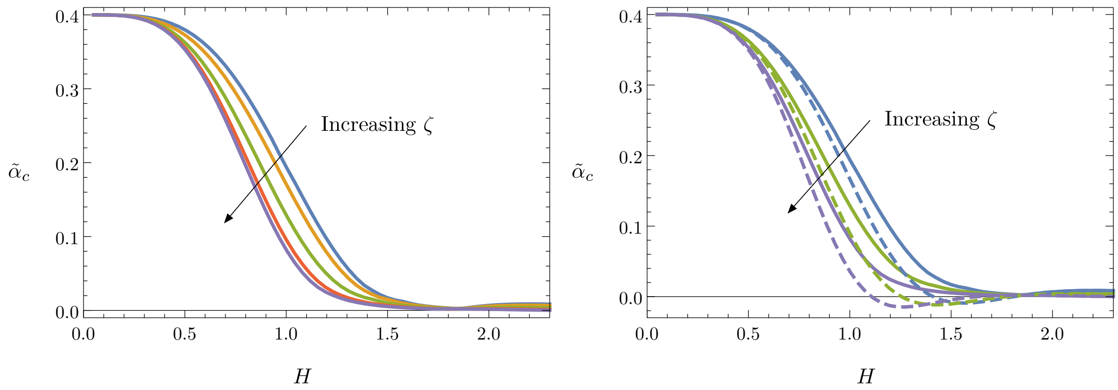

(a) *(b)*

Figure 3.16: The critical value $\tilde{\alpha}_c$ of the gravitational parameter $\tilde{\alpha}$ for stability of the base state to all wave-numbers, plotted versus H with $\tilde{\Gamma} = 0$ and varying ζ. (a) $\zeta \in \{0, 0.2, 1, 5, \infty\}$. (b) $\zeta \in \{0, 1, \infty\}$, with the long-wave analogue $\tilde{\alpha}_{c0}$ for stability in the limit $\kappa \to 0$ shown by the dashed curves.

of $\mathrm{Im}[\mathfrak{c}(\kappa)]$ with $\zeta = 1$, $\tilde{\Gamma} = \tilde{\alpha} = 0$ and $H = 1.45$. Figure 3.9(d) shows that $\tilde{\alpha}_{c0} < 0$ when $(\zeta, H) = (1, 1.45)$, and the bounded branch for $\mathrm{Im}[\mathfrak{c}]$ is therefore negative for $0 < \kappa \ll 1$. However, we see that $\mathrm{Im}[\mathfrak{c}]$ subsequently starts to increase and eventually becomes positive, so that the base state is stable to very long waves but unstable to an intermediate range of wave-numbers. Meanwhile, the corresponding divergent branch, indicated as the blue dashed curve, remains below the bounded branch, with $\mathrm{Im}[\mathfrak{c}] < 0$ for all κ.

In contrast, the solid orange curve in figure 3.15(a) shows that the bounded branch of $\mathrm{Im}[\mathfrak{c}(\kappa)]$ at the slightly larger value of $H = 1.5$ remains negative for all $\kappa > 0$. This time it is the first divergent branch of $\mathrm{Im}[\mathfrak{c}(\kappa)]$, indicated by the orange dashed curve, which increases and becomes positive. A bifurcation has occurred at some value of H between 1.45 and 1.5 which swaps the connections between the asymptotic behaviours of the two branches as $\kappa \to 0$ and as $\kappa \to \infty$. It is because of this bifurcation that we must take care to compute all the relevant solution branches: had we followed only the bounded branch, we would have erroneously concluded that the base state with $H = 1.5$ is stable to all wave-numbers.

An analogous bifurcation in the dependence of $\mathrm{Re}[\mathfrak{c}]$ on κ is shown in figure 3.15(b), with $\zeta = 1$, $\tilde{\Gamma} = 0$ and $\tilde{\alpha} = 1$. For $H = 1.35$ the real part of the bounded branch (plotted as a blue solid curve) tends to the positive root of (3.3.43) for large κ, and the divergent branch (blue dashed) to the corresponding negative root. Following the bifurcation, for $H = 1.55$, these behaviours are interchanged, and the bounded branch (yellow solid) connects to negative $\mathfrak{c}_\infty$ for large κ, while the divergent branch (yellow dashed) has positive real part for all κ.

3.3.8 Overview

Here we summarise the results of the high-frequency stability analysis, compare them with the pure hydrodynamic version of the problem analysed by [225], and highlight their central physical implications. As above, let us neglect surface tension in the first instance, so that the normalised problem is characterised by the three parameters H, ζ and $\tilde{\alpha}$. By reversing the scalings (3.3.15), (3.3.7) and (2.3.26), we can express $\tilde{\alpha}$ in terms of physical parameters in the form

$$\tilde{\alpha} = \frac{\cot\theta}{\varphi_0^2 \tilde{h}_0^3 \epsilon \,\mathrm{Re}} = \frac{\cot\theta}{\mathrm{Re}_\mathrm{L}}, \tag{3.3.56}$$

say. Thus the dependence of the stability behaviour on $\tilde{\alpha}$ may alternatively be thought of in terms of the "local" Reynolds number Re_L.

The base flow is stable in the limit $\kappa \to 0$ if $\tilde{\alpha}$ exceeds the critical value $\tilde{\alpha}_{c0}(H, \zeta)$. As shown in figure 3.9(d), there is a region of (H, ζ) parameter space where $\tilde{\alpha}_{c0}$ is negative, and the flow is therefore stable in the long-wave limit for all values of $\tilde{\alpha}$, i.e. for all Reynolds numbers. In contrast, as shown by [225], the pure hydrodynamic flow is always unstable in the limit $\kappa \to 0$ if the Reynolds number is sufficiently large, so the stable region implied by figure 3.9(d) must be attributed to the stabilising effects of magnetic coupling with the flow. We note in addition that the simplified theory of [56], which artificially neglects coupling between the perturbations in the flow and in the magnetic field, likewise predicts that the flow is always unstable in the limit $\kappa \to 0$ at sufficiently high Reynolds numbers.

Bearing in mind the possible bifurcation behaviour shown in figure 3.15, we can now use the numerical approach described in § 3.3.7 to trace all relevant branches of $\mathfrak{c}(\kappa)$ and thus determine the stability of the base state to disturbances of arbitrary wave-number. Again we find that, for each set of values of (H, ζ), there is a critical value $\tilde{\alpha}_c(H, \zeta)$ such that the flow is stable for $\tilde{\alpha} > \tilde{\alpha}_c$. The resulting stability diagram, generalising figure 3.9(d) to consider all wave-numbers, is shown in figure 3.16(a), where we plot $\tilde{\alpha}_c$ versus H for various fixed values of ζ. For comparison, in figure 3.16(b) we plot $\tilde{\alpha}_c$ alongside the corresponding small-κ limiting value $\tilde{\alpha}_{c0}$ (for a smaller set of ζ values, to avoid over-cluttering). We already know from figure 3.9(d) that $\tilde{\alpha}_{c0}$ is negative for some values of H and ζ, but figure 3.16 shows

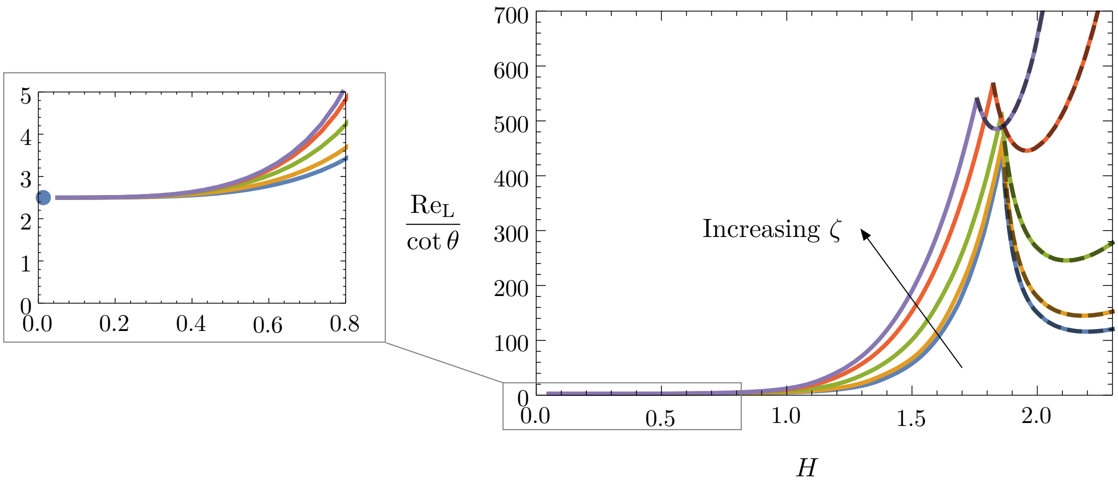

Figure 3.17: Numerically computed critical local Reynolds number $\mathrm{Re}_L\,/\cot\theta$ *as a function of* H*, for* $\zeta \in \{0, 0.2, 1, 5, \infty\}$*. The dashed curves show the critical Reynolds number in the* $\kappa \to 0$ *limit, given by* $\mathrm{Re}_L\,/\cot\theta = -\mathfrak{c}_{1,\alpha}/\mathfrak{c}_{1,0}$*, as derived in §3.3.5.1. The image left zooms into the lower-left of image right, highlighting the hydrodynamic limit derived in [225] with a blue disk.*

that $\tilde{\alpha}_c$ always remains positive. Thus, although there is a region of (H, ζ) parameter space where long waves are stable for all values of $\tilde{\alpha}$, when all wave-numbers are considered, the base state is always unstable if the Reynolds number is sufficiently large, specifically if

$$\frac{\mathrm{Re_L}}{\cot\theta} > \frac{1}{\tilde{\alpha}_c(H,\zeta)}. \tag{3.3.57}$$

For small values of H, the most dangerous modes are those with $\kappa \to 0$, and the curves for $\tilde{\alpha}_c$ and $\tilde{\alpha}_{c0}$ therefore converge. In particular, the maximum value of $\tilde{\alpha}_c$ is still $2/5$, so the flow is stable for all (H, ζ) if the local Reynolds number satisfies the criterion of [225]:

$$\frac{\mathrm{Re_L}}{\cot\theta} < \frac{5}{2}. \tag{3.3.58}$$

This observation is important, because the values of H and ζ are not fixed in advance but decrease slowly with r along the length of the divertor. In the physically relevant regime where $\beta \ll 1$, we have $\varphi_0 \sim 1$ so that $\mathrm{Re_L} \sim \tilde{h}_0(r)^3\epsilon\,\mathrm{Re}$ is a uniformly decreasing function of r and therefore, if the inequality (3.3.58) is satisfied at the inlet $r = 1$, then it is satisfied everywhere.

The critical Reynolds number defined by (3.3.57) is plotted versus H in figure 3.17. For each value of ζ, as H increases from zero, the critical Reynolds number rapidly increases from the purely hydrodynamic value of $5/2$, before suffering a slope discontinuity, at $H = H_0(\zeta)$, say. This discontinuity stems from a switch in the location of the critical wavenumber κ where the flow first loses stability. For $0 < H < H_0$, stability is lost at an intermediate non-zero value of κ, whereas, for $H > H_0$, the instability first manifests for arbitrary long wave-lengths with $\kappa \ll 1$. This explains why, for $H > H_0$, the numerical results (solid curves in figure 3.17) coincide perfectly with the dashed curves showing the critical Reynolds number $1/\tilde{\alpha}_{c0} = -\mathfrak{c}_{1,\alpha}/\mathfrak{c}_{1,0}$, as derived in § 3.3.5.1. Indeed, we can observe in figure 3.16(b) that the numerical results for $\tilde{\alpha}_c$ lie on top of the small-κ predictions $\tilde{\alpha}_{c0}$ at sufficiently large values of H.

As pointed out in § 3.3.5.1, it can be shown analytically that, in the $\zeta = \infty$ limiting case, $\tilde{\alpha}_{c0}(H) = 0$ for H at its critical value below which physical steady solutions exist (see (3.3.31) and the paragraph below). Thus the $\zeta = \infty$ purple curve in figure 3.17 diverges to infinity as H approaches its critical upper bound. Consequently, the film is stabilised for all Reynolds numbers if and only if the substrate is perfectly conducting and the film thickness is at its theoretical maximum value. Even for smaller values of ζ and H, the critical Reynolds number may become orders of magnitude larger than its hydrodynamic value of 5/2, reflecting the very strong stabilising influence of the magnetic field.

Finally, we note that surface tension stabilises the problem, particularly damping high wave-numbers, but is not effective at low wave-numbers. Therefore in regions of (H, ζ) parameter space where the problem is unstable as $\kappa \to 0$, the flow cannot be stabilised by surface tension alone. As in (3.3.56), the relevant parameter $\tilde{\Gamma}$ may be expressed in terms of $\mathrm{Re_L}$ and a local Bond number $\mathrm{Bo_L} = \tilde{h}_0^2 \,\mathrm{Bo}/\varphi_0^2$, that is,

$$\tilde{\Gamma} = \frac{1}{\mathrm{Bo_L}\,\mathrm{Re_L^3}}. \tag{3.3.59}$$

The approximate values in (2.3.26) and table 2.4 suggest that $\tilde{\Gamma}$ is likely to be large in parameter regimes relevant to a lithium divertor. If so, then we can assume that all except the smallest values of κ are stabilised by surface tension, and the asymptotic analysis as $\kappa \to 0$ from § 3.3.5 suffices to determine the stability of the flow.

3.4 Summary

In this chapter we analyse unsteady solutions of the thin-film models derived in chapter 2 in both the poloidal and toroidal cases.

In the poloidal case, the magnetohydrodynamical braking causes the fluid to be advected at a velocity that is near-independent of the film thickness. We find that the thin-film equation is linear up to exponentially small terms in the limit where $\mathrm{Ha} \gg 1$, thus nonlinear phenomena typically associated with wave propagation such as shock and rarefaction formation are strongly suppressed in regions of high-field. It follows that disturbances to the steady profile are advected with little dispersion or wave-steepening. Time-dependent disturbances introduced at the inlet may grow to the extent that the field strength increases downstream from the inlet, as higher field results in slower velocity and thicker film, but obey a global uniform bound. When the vertical component of the applied field goes through zero, the nonlinearities manifest in the vicinity of the sign change and the shock suppression is weakened.

In the toroidal case, an explicit upper bound is obtained for time-dependent disturbances introduced at the inlet, guaranteeing that these decay as they are advected along the divertor. As opposed to the poloidal case, as they propagate the disturbances steepen into shocks, as is typical for a nonlinear hyperbolic wave equation. These can be smoothed by including regularising higher-order terms corresponding to transverse gravity and/or surface tension, characterised by the small parameters α and Γ, respectively.

We show that a multiple-scales approach allows one to analyse the stability of inertial perturbations even though the reduced Reynolds number is small enough to be neglected at leading order. Our stability analysis demonstrates that coupling with the induced magnetic field always acts to stabilise the flow, in contrast with previous studies (for example [189, 221]) which conclude that a constant toroidal magnetic field has no effect on stability. We show that the problem can be stable for much larger Reynolds numbers than in the pure hydrodynamic problem, if the magnetic and geometric parameters are chosen appropriately. Similarly, there is a critical Reynolds number below which the problem is guaranteed to be stable, regardless of any other parameter values.

However, the detailed stability analysis extends beyond these simple universal results to reveal in full the complicated dependence of the stability on the local Reynolds and Bond numbers, as well as the material parameters in the problem. When surface tension is negligible, the condition for linear instability is given by

(3.3.57), in terms of the local Reynolds number, the divertor inclination angle θ, and the two parameters H and ζ. The resulting critical Reynolds number is shown as a function of H and ζ in figure 3.17. For the practitioner, the dimensionless groups H and ζ combine several physical parameters that may be selected, such as the substrate thickness and electrical conductivity, the location, inclination, and extent of the divertor, the field strength, the aspect ratio and so on (see (2.3.30)). These results allow one to tune these physical parameters to provide the largest possible critical Reynolds number, and thus the most stable flow regime.

Chapter 4

Three-Dimensional and Thermal Effects

Until now we have treated the poloidal and toroidal applied field orientations separately, which begs the question: what happens when these components are both present simultaneously? In this chapter we extend the model by taking an axisymmetric applied magnetic field comprising both poloidal and toroidal components. We find that, as a consequence of the nonlinearity of the $\boldsymbol{j} \times \boldsymbol{B}$ term, the solution is not merely the superposition of the two previous solutions. Instead, the interaction between toroidal and poloidal field components induces a toroidal flow component that does not appear in either case in isolation.

A second aim of this chapter is to take the first step towards including in the model the interaction with the core plasma impinging upon the liquid metal layer. As explained in chapter 1, the divertor is the component upon which the core plasma is exhausted, and is crucial for the successful operation of the tokamak. The hot ions impacting the divertor impart mass, momentum, and thermal energy to the free surface of the liquid film. The contribution of the mass is negligible [219] and will be ignored in this thesis. The momentum transfer is important, but its inclusion in the model will be delayed until chapter 5. In this chapter, we model the transfer of energy from the plasma, and the resulting temperature evolution within the divertor. In particular, withstanding the thermal load is what motivates a liquid metal coating, and hence this interaction is a key ingredient of a complete model.

The chapter is organised as follows: in § 4.1 we derive the governing equations for axisymmetric thin-film MHD flow when all field components are simultaneously present. We then explore features of the solution in various asymptotic limits. In § 4.2 we further extend the axisymmetric three-dimensional model by introducing temperature. We survey a variety of thermal effects to be incorporated into the model, and via a dimensional analysis retain only those that are dominant. In § 4.3 we proceed to derive the leading-order thermal model, describing the solutions in §§ 4.4 and 4.5. In § 4.6 we discuss the main solution features when the driving forces are combined in a relevant physical limit. We make concluding remarks in § 4.7.

4.1 Three-dimensional magnetic field

4.1.1 Magnetic field decomposition

In this section we consider the same axisymmetric geometry as outlined in §2.3 but now derive the governing equations when the applied field comprises both poloidal and toroidal components. We still assume that the magnetic field and flow are axisymmetric, i.e. independent of the azimuthal coordinate ϕ. The magnetic field may then be written in the form

$$\boldsymbol{B}^* = \boldsymbol{\nabla}^* \times \left(\frac{A^*}{R^*} \boldsymbol{e}_\phi \right) + \frac{B^*}{R^*} \boldsymbol{e}_\phi, \tag{4.1.1}$$

where A^* and B^* are the poloidal magnetic potential and toroidal magnetic component, respectively. As we will show, the field configuration (4.1.1) induces a flow in the toroidal direction, and so we must consider all the components of the velocity field, denoted

$$\boldsymbol{u}^* = u^* \boldsymbol{e}_r + v^* \boldsymbol{e}_y + w^* \boldsymbol{e}_\phi. \tag{4.1.2}$$

The field and velocity variables A^*, B^*, u^*, v^*, w^* are all functions of r^*, y^*, and t^*.

4.1.2 Governing equations in each region

Vacuum

In the vacuum above and below the divertor, there is no current and thus

$$\boldsymbol{\nabla}^* \times \boldsymbol{B}^* = \boldsymbol{0}. \tag{4.1.3}$$

As previously, we decompose the magnetic field components into a known spatially-varying applied component and an induced component, so $A^* = A^{\mathrm{a}*} + A^{\mathrm{i}\pm *}$ and $B^* = B^{\mathrm{a}*} + B^{\mathrm{i}\pm *}$, where the $\pm$ superscript refers to the regions above and below the divertor, respectively. Since $B^{\mathrm{i}\pm *}$ must vanish at infinity it follows from (4.1.3) that $B^{\mathrm{i}\pm *} = 0$, just as in §2.3.3. Moreover, as further explained in §2.3.3, since the toroidal field component is proportional to $1/R^*$, $B^{\mathrm{a}*}$ is a known constant.

The poloidal field in a tokamak is generated by several isolated currents running in the toroidal direction which can be modelled as the sum of axisymetric delta functions. If we choose the gauge such that $A^{\mathrm{a}*}/R^*$ is divergence-free, that is, $A^{\mathrm{a}*}$ varies only with r^* and y^*, then $A^{\mathrm{a}*}$ can be modelled as the sum of axisymmetric Green's functions of the Laplacian (multiplied by R^*).

The induced poloidal potential in the vacuum satisfies a version of Laplace's equation, namely

$$\frac{\partial}{\partial y^*}\left(\frac{1}{R^*}\frac{\partial A^{\mathrm{i}\pm *}}{\partial y^*}\right) + \frac{\partial}{\partial r^*}\left(\frac{1}{R^*}\frac{\partial A^{\mathrm{i}\pm *}}{\partial r^*}\right) = 0. \tag{4.1.4}$$

Liquid

In the fluid layer, $0 < y^* < h^*(r^*, t^*)$, we decompose the magnetic field (with an additional susceptibility factor in the toroidal component due to permeability) as

$$A^* = A^{\mathrm{a}*} + A^{\mathrm{i}*}, \tag{4.1.5}$$

$$B^* = (1+\chi)B^{\mathrm{a}*} + B^{\mathrm{i}*}. \tag{4.1.6}$$

The induction equations take the forms

$$\begin{aligned}\frac{\partial A^{\mathrm{i}*}}{\partial t^*} &= -u^*\frac{\partial}{\partial r^*}\left(A^{\mathrm{a}*} + A^{\mathrm{i}*}\right) - v^*\frac{\partial}{\partial y^*}\left(A^{\mathrm{a}*} + A^{\mathrm{i}*}\right)\\ &\qquad + \eta^* R^*\left[\frac{\partial}{\partial y^*}\left(\frac{1}{R^*}\frac{\partial A^{\mathrm{i}*}}{\partial y^*}\right) + \frac{\partial}{\partial r^*}\left(\frac{1}{R^*}\frac{\partial A^{\mathrm{i}*}}{\partial r^*}\right)\right], \qquad (4.1.7\mathrm{a})\\ \frac{\partial B^{\mathrm{i}*}}{\partial t^*} &= -u^* {R^*}^2\frac{\partial}{\partial r^*}\left(\frac{(1+\chi)B^{\mathrm{a}*} + B^{\mathrm{i}*}}{{R^*}^2}\right) - v^* {R^*}^2\frac{\partial}{\partial y^*}\left(\frac{(1+\chi)B^{\mathrm{a}*} + B^{\mathrm{i}*}}{{R^*}^2}\right)\\ &\qquad + R^*\left(\frac{\partial}{\partial y^*}\left[\frac{w^*}{R^*}\frac{\partial}{\partial r^*}\left(A^{\mathrm{a}*} + A^{\mathrm{i}*}\right)\right] - \frac{\partial}{\partial r^*}\left[\frac{w^*}{R^*}\frac{\partial}{\partial y^*}\left(A^{\mathrm{a}*} + A^{\mathrm{i}*}\right)\right]\right)\\ &\qquad + \eta^* R^*\left[\frac{\partial}{\partial y^*}\left(\frac{1}{R^*}\frac{\partial B^{\mathrm{i}*}}{\partial y^*}\right) + \frac{\partial}{\partial r^*}\left(\frac{1}{R^*}\frac{\partial B^{\mathrm{i}*}}{\partial r^*}\right)\right]. \qquad (4.1.7\mathrm{b})\end{aligned}$$

Neglecting inertial terms in anticipation of our lubrication approximation as before, and assuming axisymmetry, we find that the continuity and momentum equations are given by

$$0 = \frac{\partial}{\partial r^*}(u^* R^*) + \frac{\partial}{\partial y^*}(v^* R^*) \tag{4.1.8a}$$

$$\frac{\partial p^*}{\partial r^*} = \frac{\rho^* \nu^*}{R^*}\frac{\partial}{\partial y^*}\left[R^*\left(\frac{\partial u^*}{\partial y^*} - \frac{\partial v^*}{\partial r^*}\right)\right] + \rho^* \left|\boldsymbol{g}^*\right| \sin\theta - \frac{1}{\mu^* R^*}\left\{\frac{\partial B^{\mathrm{i}*}}{\partial r^*}\frac{(1+\chi)B^{\mathrm{a}*} + B^{\mathrm{i}*}}{R^*}\right.$$
$$\left. + \left[\frac{\partial}{\partial y^*}\left(\frac{1}{R^*}\frac{\partial A^{\mathrm{i}*}}{\partial y^*}\right) + \frac{\partial}{\partial r^*}\left(\frac{1}{R^*}\frac{\partial A^{\mathrm{i}*}}{\partial r^*}\right)\right]\frac{\partial}{\partial r^*}\left(A^{\mathrm{a}*} + A^{\mathrm{i}*}\right)\right\}, \tag{4.1.8b}$$

$$\frac{\partial p^*}{\partial y^*} = \frac{\rho^* \nu^*}{R^*}\frac{\partial}{\partial r^*}\left[R^*\left(\frac{\partial v^*}{\partial r^*} - \frac{\partial u^*}{\partial y^*}\right)\right] - \rho^* \left|\boldsymbol{g}^*\right| \cos\theta - \frac{1}{\mu^* R^*}\left\{\frac{\partial B^{\mathrm{i}*}}{\partial y^*}\frac{(1+\chi)B^{\mathrm{a}*} + B^{\mathrm{i}*}}{R^*}\right.$$
$$\left. + \left[\frac{\partial}{\partial y^*}\left(\frac{1}{R^*}\frac{\partial A^{\mathrm{i}*}}{\partial y^*}\right) + \frac{\partial}{\partial r^*}\left(\frac{1}{R^*}\frac{\partial A^{\mathrm{i}*}}{\partial r^*}\right)\right]\frac{\partial}{\partial y^*}\left(A^{\mathrm{a}*} + A^{\mathrm{i}*}\right)\right\}, \tag{4.1.8c}$$

$$0 = \rho^* \nu^* \left(\frac{\partial}{\partial y^*}\left[\frac{1}{R^*}\frac{\partial}{\partial y^*}\left(w^* R^*\right)\right] + \frac{\partial}{\partial r^*}\left[\frac{1}{R^*}\frac{\partial}{\partial r^*}\left(w^* R^*\right)\right]\right)$$
$$+ \frac{1}{\mu^* R^{*2}}\left[\frac{\partial B^{\mathrm{i}*}}{\partial y^*}\frac{\partial}{\partial r^*}\left(A^{\mathrm{a}*} + A^{\mathrm{i}*}\right) - \frac{\partial B^{\mathrm{i}*}}{\partial r^*}\frac{\partial}{\partial y^*}\left(A^{\mathrm{a}*} + A^{\mathrm{i}*}\right)\right]. \tag{4.1.8d}$$

Substrate

In the substrate, $-h^{\mathrm{s}*} < y^* < 0$, we decompose similarly with the substrate susceptibility

$$A^* = A^{\mathrm{a}*} + A^{\mathrm{is}*}, \tag{4.1.9a}$$
$$B^* = (1+\chi^{\mathrm{s}})B^{\mathrm{a}*} + B^{\mathrm{is}*}. \tag{4.1.9b}$$

The induction equations then take the forms

$$\frac{\partial A^{\mathrm{is}*}}{\partial t^*} = \eta^{\mathrm{s}*} R^* \left[\frac{\partial}{\partial y^*}\left(\frac{1}{R^*}\frac{\partial A^{\mathrm{is}*}}{\partial y^*}\right) + \frac{\partial}{\partial r^*}\left(\frac{1}{R^*}\frac{\partial A^{\mathrm{is}*}}{\partial r^*}\right)\right], \tag{4.1.10a}$$
$$\frac{\partial B^{\mathrm{is}*}}{\partial t^*} = \eta^{\mathrm{s}*} R^* \left[\frac{\partial}{\partial y^*}\left(\frac{1}{R^*}\frac{\partial B^{\mathrm{is}*}}{\partial y^*}\right) + \frac{\partial}{\partial r^*}\left(\frac{1}{R^*}\frac{\partial B^{\mathrm{is}*}}{\partial r^*}\right)\right]. \tag{4.1.10b}$$

4.1.3 Boundary conditions

Vacuum–fluid

The boundary conditions at the vacuum–liquid interface, $y^* = h^*$, are

$$A^{\mathrm{i}*} = A^{\mathrm{i}+*}, \tag{4.1.11a}$$

$$\frac{\partial A^{\mathrm{i}*}}{\partial y^*} - \frac{\partial A^{\mathrm{i}*}}{\partial r^*}\frac{\partial h^*}{\partial r^*} = (1+\chi)\left(\frac{\partial A^{\mathrm{i}+*}}{\partial y^*} - \frac{\partial A^{\mathrm{i}+*}}{\partial r^*}\frac{\partial h^*}{\partial r^*}\right) + \chi\left(\frac{\partial A^{\mathrm{a}*}}{\partial y^*} - \frac{\partial A^{\mathrm{a}*}}{\partial r^*}\frac{\partial h^*}{\partial r^*}\right), \tag{4.1.11b}$$

$$B^{\mathrm{i}*} = 0, \tag{4.1.11c}$$

$$\frac{\partial h^*}{\partial t^*} + u^*\frac{\partial h^*}{\partial r^*} = v^*. \tag{4.1.11d}$$

$$\begin{aligned} p^* = {} & 2\rho^*\nu^*\left(\frac{\partial u^*}{\partial r^*}\left(\frac{\partial h^*}{\partial r^*}\right)^2 + \frac{\partial v^*}{\partial y^*} - \left(\frac{\partial u^*}{\partial y^*} + \frac{\partial v^*}{\partial r^*}\right)\frac{\partial h^*}{\partial r^*}\right)\left(1+\left(\frac{\partial h^*}{\partial r^*}\right)^2\right)^{-1} \\ & - \gamma^*\left\{\frac{\partial^2 h^*}{\partial r^{*2}}\left(1+\left(\frac{\partial h^*}{\partial r^*}\right)^2\right)^{-3/2} + \frac{1}{R^*}\left(\cos\theta\frac{\partial h^*}{\partial r^*} - \sin\theta\right)\left(1+\left(\frac{\partial h^*}{\partial r^*}\right)^2\right)^{-1/2}\right\} \\ & - \left[\frac{1}{\mu^* {R^*}^2}\left(1+\left(\frac{\partial h^*}{\partial r^*}\right)^2\right)^{-1}\left(\frac{\partial A^*}{\partial y^*}\frac{\partial h^*}{\partial r^*} + \frac{\partial A^*}{\partial r^*}\right)^2\right]_-^+ \\ & + \left[\frac{1}{2\mu^* {R^*}^2}\left(\left(\frac{\partial A^*}{\partial y^*}\right)^2 + \left(\frac{\partial A^*}{\partial r^*}\right)^2 + {B^*}^2\right)\right]_-^+, \end{aligned} \tag{4.1.11e}$$

$$0 = \rho^*\nu^*\left\{\left(\left(\frac{\partial h^*}{\partial r^*}\right)^2 - 1\right)\left(\frac{\partial u^*}{\partial y^*} + \frac{\partial v^*}{\partial r^*}\right) - 2\left(\frac{\partial v^*}{\partial y^*} - \frac{\partial u^*}{\partial r^*}\right)\frac{\partial h^*}{\partial r^*}\right\}, \tag{4.1.11f}$$

$$0 = \rho^*\nu^*\left\{\frac{\partial w^*}{\partial y^*} - \frac{\partial w^*}{\partial r^*}\frac{\partial h^*}{\partial r^*} + \frac{w^*}{R^*}\left(\cos\theta\frac{\partial h^*}{\partial r^*} - \sin\theta\right)\right\}. \tag{4.1.11g}$$

Fluid–substrate

The boundary conditions at the fluid–substrate interface, $y^* = 0$, are

$$u^* = v^* = w^* = 0, \tag{4.1.12a}$$

$$A^{\mathrm{i}*} = A^{\mathrm{is}*}, \tag{4.1.12b}$$

$$\frac{\partial A^{\mathrm{i}*}}{\partial y^*} = \frac{1+\chi}{1+\chi^{\mathrm{s}}}\frac{\partial A^{\mathrm{is}*}}{\partial y^*} + \frac{\chi-\chi^{\mathrm{s}}}{1+\chi^{\mathrm{s}}}\frac{\partial A^{\mathrm{a}*}}{\partial y^*}, \tag{4.1.12c}$$

$$B^{\mathrm{i}*} = \frac{1+\chi}{1+\chi^{\mathrm{s}}}B^{\mathrm{is}*}, \tag{4.1.12d}$$

$$\frac{\partial B^{\mathrm{i}*}}{\partial y^*} = \frac{1+\chi}{1+\chi^{\mathrm{s}}}\frac{\sigma^*}{\sigma^{\mathrm{s}*}}\frac{\partial B^{\mathrm{is}*}}{\partial y^*}. \tag{4.1.12e}$$

Substrate–vacuum

The boundary conditions at the substrate–vacuum interface, $y^* = -h^{s*}$, are

$$A^{is*} = A^{i-*}, \tag{4.1.13a}$$

$$\frac{\partial A^{is*}}{\partial y^*} = (1+\chi^s)\frac{\partial A^{i-*}}{\partial y^*} + \chi^s \frac{\partial A^{a*}}{\partial y^*}, \tag{4.1.13b}$$

$$B^{i*} = 0. \tag{4.1.13c}$$

4.1.4 Non-dimensionalisation

We observe in the toroidal component of the momentum equation, (4.1.8d), that there are cross terms involving products of derivatives of A^{a*} and B^{a*}. These terms induce a body force that can only be balanced by viscous flow in the toroidal direction, with nonzero w^*. These terms vanish when considering the poloidal or toroidal fields in isolation (as they originate from the nonlinear $\boldsymbol{j}^* \times \boldsymbol{B}^*$ term), and thus so too does the induced toroidal flow. This observation highlights the importance of considering the fully three-dimensional field: an effect not present with either component in isolation emerges only when both components are present simultaneously.

Guided by the analyses of §§ 2.2 and 2.3, we perform the scalings

$$r^* = \mathscr{L}^* r, \qquad y^* = \epsilon \mathscr{L}^* y = \mathscr{L}^* Y, \tag{4.1.14a,b}$$

$$h^* = \epsilon \mathscr{L}^* h, \qquad h^{s*} = \epsilon \mathscr{L}^* h^s, \tag{4.1.14c,d}$$

$$u^* = \mathscr{U}^* u, \qquad v^* = \epsilon \mathscr{U}^* v, \tag{4.1.14e,f}$$

$$w^* = \Xi \mathscr{U}^* w, \qquad p^* = \rho^* \left|\boldsymbol{g}^*\right| \mathscr{L}^* \sin\theta\, p, \tag{4.1.14g,h}$$

$$B^{a*} = \frac{\Xi}{\epsilon} \mathscr{B}^* \mathscr{L}^* B^a, \qquad B^{i*} = \epsilon\, \mathrm{Rm}\, \Xi\, \mathscr{B}^* \mathscr{L}^* B^i, \tag{4.1.14i,j}$$

$$A^{a*} = \mathscr{B}^* \mathscr{L}^{*2} A^a, \qquad A^{i*} = \epsilon\, \mathrm{Rm}\, \mathscr{B}^* \mathscr{L}^{*2} A^i, \tag{4.1.14k,l}$$

where Y is the y-coordinate scaled to describe the outer region. The parameter Ξ/ϵ is the ratio of the typical magnitudes of the applied toroidal and poloidal components. Balancing the gravitational forces with the electromagnetic forces in (4.1.8b) and utilising (4.1.7b) produces the same velocity scale as (2.2.9), namely

$$\mathscr{U}^* = \frac{\rho^* \left|\boldsymbol{g}^*\right| \sin\theta}{\sigma^* \mathscr{B}^{*2}}. \tag{4.1.15}$$

Having non-dimensionalised the system (4.1.7–13) via (4.1.14), we now aim to find the leading-order system in the limit as $\epsilon \to 0$. To do so, we neglect terms of order ϵ, χ, and Rm, while retaining terms involving their ratios and considering the distinguished limit in which $\mathrm{Ha} = \mathcal{O}(1)$ as $\epsilon \to 0$. In practise, the field components are likely to be comparable, which corresponds to $\Xi = \mathcal{O}(\epsilon)$. However, we find that the influence of the toroidal field on the flow is negligible to leading order in this regime, so we focus instead on the richest asymptotic balance in the model, which occurs in the distinguished limit where $\Xi = \mathcal{O}(1)$.

4.1.5 Poloidal magnetic problem

We begin by tackling the leading-order poloidal magnetic problem. We Taylor expand the applied potential within the divertor region, as in the poloidal case (see (2.2.11)), to give

$$A^{\mathrm{a}}(r,y) \sim A^{\mathrm{a}}(r) + \epsilon y \frac{\partial A^{\mathrm{a}}}{\partial Y}(r,0) + \cdots \tag{4.1.16a}$$

$$= A_0^{\mathrm{a}}(r) + \epsilon y A_1^{\mathrm{a}}(r) + \cdots . \tag{4.1.16b}$$

Then, with the induced magnetic potential expanded as $A^{\mathrm{i}} \sim A_0^{\mathrm{i}} + \epsilon A_1^{\mathrm{i}} + \cdots$, and similarly for h, u, v, w, and p, the induction equations governing the potential in the fluid and substrate regions (4.1.7a) and (4.1.10a) take the leading-order forms

$$\frac{\partial^2 A_0^{\mathrm{i}}}{\partial y^2} = 0, \qquad \text{where } \ 0 < y < h_0 \tag{4.1.17a}$$

$$\frac{\partial^2 A_0^{\mathrm{is}}}{\partial y^2} = 0, \qquad \text{where } \ -h^{\mathrm{s}} < y < 0, \tag{4.1.17b}$$

subject to the boundary conditions (4.1.9–13), which for the potential take the leading-order forms

$$A_0^{\mathrm{i}}(r,h_0) = A_0^{\mathrm{i}+}(r,0), \tag{4.1.18a}$$

$$\frac{\partial A_0^{\mathrm{i}}}{\partial y}(r,h_0) = \frac{\chi}{\mathrm{Rm}} A_1^{\mathrm{a}}(r), \tag{4.1.18b}$$

$$A^{\mathrm{i}}(r,0) = A^{\mathrm{is}}(r,0), \tag{4.1.18c}$$

$$\frac{\partial A_0^{\mathrm{is}}}{\partial y}(r,-h^{\mathrm{s}}) = \frac{\chi^{\mathrm{s}}}{\mathrm{Rm}} A_1^{\mathrm{a}}(r), \tag{4.1.18d}$$

$$A_0^{\mathrm{is}}(r,-h^{\mathrm{s}}) = A_0^{\mathrm{i}-}(r,0), \tag{4.1.18e}$$

where we have suppressed the parametric dependence on t. The solution of (4.1.17) and (4.1.18) is given by

$$A_0^{\mathrm{i}} = \frac{\chi}{\mathrm{Rm}}(y - h_0)A_1^{\mathrm{a}}(r) + A_0^{\mathrm{i}+}(r,0), \tag{4.1.19a}$$

$$A_0^{\mathrm{is}} = \frac{\chi^{\mathrm{s}}}{\mathrm{Rm}}(y + h^{\mathrm{s}})A_1^{\mathrm{a}}(r) + A_0^{\mathrm{i}-}(r,0). \tag{4.1.19b}$$

For later reference we further deduce from (4.1.18c) that

$$A_0^{\mathrm{i}+}(r,0) - A_0^{\mathrm{i}-}(r,0) = \frac{\chi h^{\mathrm{s}} + \chi h_0}{\mathrm{Rm}}A_1^{\mathrm{a}}. \tag{4.1.20}$$

As in the purely poloidal case, the solution (4.1.19) has not determined the induced potential variation with respect to r, for which we will have to proceed to $\mathcal{O}(\epsilon)$, where the problem is given by

$$\frac{\partial^2 A_1^{\mathrm{i}}}{\partial y^2} = -u_0 A_0^{\mathrm{a}}, \qquad \text{where } \ 0 < y < h_0 \tag{4.1.21a}$$

$$\frac{\partial^2 A_0^{\mathrm{is}}}{\partial y^2} = 0, \qquad \text{where } \ -h^{\mathrm{s}} < y < 0, \tag{4.1.21b}$$

subject to the boundary conditions

$$\frac{\partial A_1^{\mathrm{i}}}{\partial y}(r,h_0) = \frac{\partial A_0^{\mathrm{i}+}}{\partial Y}(r,0), \tag{4.1.21c}$$

$$\frac{\partial A_1^{\mathrm{i}}}{\partial y}(r,0) = \frac{\partial A_1^{\mathrm{is}}}{\partial y}(r,0), \tag{4.1.21d}$$

$$\frac{\partial A_1^{\mathrm{is}}}{\partial y}(r,-h^{\mathrm{s}}) = \frac{\partial A_0^{\mathrm{i}-}}{\partial Y}(r,0). \tag{4.1.21e}$$

Integrating (4.1.21b) and imposing (4.1.21e) we find that

$$\frac{\partial A_1^{\mathrm{is}}}{\partial y} = \frac{\partial A_0^{\mathrm{i}-}}{\partial Y}(r,0). \tag{4.1.22}$$

Integrating (4.1.21a) and imposing (4.1.21c) and (4.1.21d) we find that

$$\frac{\partial A_0^{\mathrm{i}+}}{\partial Y}(r,0) - \frac{\partial A_0^{\mathrm{i}-}}{\partial Y}(r,0) = -\overline{Q}A_0^{\mathrm{a}}, \tag{4.1.23}$$

where $\overline{Q}$ is the leading-order downstream flow rate given by

$$\overline{Q} = \int_0^{h_0} u_0 \, \mathrm{d}y. \tag{4.1.24}$$

Now the induced potential A_0^{i} satisfies Laplace's equation beyond the divertor, which occupies the line segment $(r, Y) \in (r_0, r_0 + 1) \times \{0\}$, where $r_0 \cos\theta$ is the dimensionless distance of the divertor inlet from the centre. We would expect the model to become approximately two-dimensional in the limit of $r_0 \gg 1$ (as described by the poloidal case in § 2.2.3). The potential experiences a jump discontinuity along the divertor, given by (4.1.20), while its Y-derivative experiences a jump discontinuity given by (4.1.23). As in the poloidal case, A_0^{i} satisfies a Plemelj problem, here in a non-Cartesian geometry, which, in principle, could be solved to give the leading-order induced potential in the outer region, from which we can compute the potential in the inner region via (4.1.19) (see appendix A.1). We do not pursue this solution since the flow problem decouples from the induced potential to leading order.

4.1.6 Flow and toroidal magnetic problem

The decoupling of the leading-order induced poloidal field component from the flow allows for it to be solved for in isolation. We now proceed to solve the leading-order system for the flow and toroidal magnetic field, which we find are coupled. As in the toroidal case in § 2.3.4, we first derive an effective boundary condition for the leading-order toroidal component of the induced field in the fluid layer. To do so, we consider the leading-order induction equation governing B_0^{i} in the substrate, namely

$$\frac{\partial^2 B_0^{\mathrm{is}}}{\partial y^2} = 0, \tag{4.1.25}$$

subject to the boundary conditions

$$B_0^{\mathrm{is}}(0) = B_0^{\mathrm{i}}(0), \tag{4.1.26a}$$

$$\frac{\partial B_0^{\mathrm{is}}}{\partial y}(0) = \frac{\sigma^{\mathrm{s}*}}{\sigma^*} \frac{\partial B_0^{\mathrm{i}}}{\partial y}(0), \tag{4.1.26b}$$

$$B_0^{\mathrm{is}}(-h^{\mathrm{s}}) = 0. \tag{4.1.26c}$$

We have suppressed the dependence on r and t to simplify the notation. Integrating (4.1.25) and applying (4.1.26) we deduce that B_0^{i} must satisfy the Robin boundary condition

$$aB_0^{\mathrm{i}}(0) = \frac{\partial B_0^{\mathrm{i}}}{\partial y}(0), \tag{4.1.27a}$$

where

$$a = \frac{\sigma^*}{h^{\mathrm{s}}\sigma^{\mathrm{s}*}}. \tag{4.1.27b}$$

The parameter a allows the model to interpolate from the limit of a perfectly conducting substrate ($a \to 0$) to a perfectly insulating substrate ($a \to \infty$), exactly as in § 2.3.4, and can be generalised to describe a multilayer substrate as in appendix A.2.2.

We now look to retain as much of the relevant physics in our leading-order system as possible. All terms involving θ appear at leading order in one of two limits, either when $\theta = \mathcal{O}(\epsilon)$ or when $\theta = \mathcal{O}(1)$. The magnetic pressure term involving χ is retained in one of the two limits if either $\chi = \mathcal{O}(\epsilon^2\,\mathrm{Rm})$ and $\Xi = \mathcal{O}(1)$ or when $\chi = \mathcal{O}(\mathrm{Rm})$ and $\Xi = \mathcal{O}(\epsilon)$. We thus retain all of these terms for the moment, and the appropriate solution in each case can be recovered from the general solution by expanding in the relevant limit and neglecting terms formally of order $\mathcal{O}(\epsilon)$.

Similarly, we consider the distinguished limit in which $\mathrm{Bo} = \mathcal{O}(\epsilon^3)$. Then to leading order the induction, continuity, and momentum equations in the fluid layer take the forms

$$0 = \frac{2}{r}u_0 + \frac{\mathrm{d}A_0^{\mathrm{a}}}{\mathrm{d}r}\frac{\partial w_0}{\partial y} + \frac{\partial^2 B_0^{\mathrm{i}}}{\partial y^2}, \tag{4.1.28a}$$

$$0 = \frac{1}{r}\frac{\partial}{\partial r}(u_0 r) + \frac{\partial v_0}{\partial y} \tag{4.1.28b}$$

$$\frac{\partial p_0}{\partial r} = \frac{1}{\mathrm{Ha}^2}\frac{\partial^2 u_0}{\partial y^2} + 1 - \frac{u_0}{r^2\cos^2\theta}\left(\frac{\mathrm{d}A_0^{\mathrm{a}}}{\mathrm{d}r}\right)^2 - \frac{\Xi^2}{r^2\cos^2\theta}\frac{\partial B_0^{\mathrm{i}}}{\partial r}, \tag{4.1.28c}$$

$$\frac{\partial p_0}{\partial y} = -\epsilon\cot\theta - \frac{\Xi^2}{r^2\cos^2\theta}\frac{\partial B_0^{\mathrm{i}}}{\partial y}, \tag{4.1.28d}$$

$$0 = \frac{1}{\mathrm{Ha}^2}\frac{\partial^2 w_0}{\partial y^2} + \frac{1}{r^2\cos^2\theta}\frac{\mathrm{d}A_0^{\mathrm{a}}}{\mathrm{d}r}\frac{\partial B_0^{\mathrm{i}}}{\partial y}. \tag{4.1.28e}$$

The boundary conditions at $y = h_0$ become

$$B_0^{\mathrm{i}} = 0, \tag{4.1.29a}$$

$$\frac{\partial h_0}{\partial t} + \frac{\partial h_0}{\partial r} u_0 = v_0, \tag{4.1.29b}$$

$$p_0 = -\frac{\epsilon^3}{\mathrm{Bo}} \lambda - \frac{\chi}{2\,\mathrm{Rm}} \left| \boldsymbol{B}^{\mathrm{a}} \right|^2, \tag{4.1.29c}$$

$$\frac{\partial u_0}{\partial y} = 0, \tag{4.1.29d}$$

$$\frac{\partial w_0}{\partial y} = 0, \tag{4.1.29e}$$

where λ is the contribution due to surface tension and $|\boldsymbol{B}^{\mathrm{a}}|^2$ is the magnitude of the applied field, given respectively by

$$\lambda = \frac{\partial^2 h_0}{\partial r^2} + \frac{1}{r} \left(\frac{\partial h_0}{\partial r} - \frac{\tan\theta}{\epsilon} \right), \tag{4.1.29f}$$

$$|\boldsymbol{B}^{\mathrm{a}}|^2 = \frac{1}{r^2 \cos^2\theta} \left(\left(\frac{\mathrm{d}A_0^{\mathrm{a}}}{\mathrm{d}r} \right)^2 + (A_1^{\mathrm{a}})^2 + \frac{\Xi^2}{\epsilon^2} \right). \tag{4.1.29g}$$

The boundary conditions at $y = 0$ become

$$aB_0^{\mathrm{i}} = \frac{\partial B_0^{\mathrm{i}}}{\partial y}, \tag{4.1.30a}$$

$$u_0 = v_0 = w_0 = 0. \tag{4.1.30b}$$

In the usual manner, integrating (4.1.28b) and applying (4.1.29b) and (4.1.30b) produces a net conservation equation governing the evolution of $h_0(r,t)$, identical to the toroidal case (see (2.3.32)), namely

$$\frac{\partial h_0}{\partial t} + \frac{1}{r}\frac{\partial}{\partial r} \left(r \int_0^{h_0} u_0 \,\mathrm{d}y \right) = 0. \tag{4.1.31}$$

This formulation eliminates the need to solve for v_0, and we note that toroidal velocity component w_0 does not enter (4.1.31) because of the assumed cylindrical symmetry.

We may also integrate equation (4.1.28e), applying boundary conditions (4.1.29e) and (4.1.30b) to obtain w_0 as a function of B_0^{i} via

$$w_0 = -\frac{\mathrm{Ha}^2}{r^2 \cos^2\theta} \frac{\mathrm{d}A_0^{\mathrm{a}}}{\mathrm{d}r} \int_0^y B_0^{\mathrm{i}}(s) \,\mathrm{d}s. \tag{4.1.32}$$

While the integral (4.1.32) eliminates the need to solve for w_0, the toroidal fluid flux, $\int_0^{h_0} w_0 \, \mathrm{d}y$, is an interesting quantity we later consider by means of (4.1.32). It just remains to solve for the leading-order radial velocity u_0 and induced field B_0^{i}; then (4.1.31) provides an evolution equation for h_0, and w_0 may be determined from (4.1.32).

Integrating (4.1.28d) and applying (4.1.29c) we find that the pressure in the fluid layer satisfies

$$p_0 = P - \epsilon y \cot\theta - \frac{\Xi^2}{r^2\cos^2\theta} B_0^{\mathrm{i}}, \tag{4.1.33}$$

where

$$P = -\frac{\epsilon^3}{\mathrm{Bo}}\lambda - \frac{\chi}{2\,\mathrm{Rm}} \left|\boldsymbol{B}^{\mathrm{a}}\right|^2 + \epsilon h_0 \cot\theta. \tag{4.1.34}$$

Substituting (4.1.33) into (4.1.28c) we obtain the equation

$$\frac{1}{\mathrm{Ha}^2}\frac{\partial^2 u_0}{\partial y^2} + \left(1 - \frac{\partial P}{\partial r}\right) - \frac{u_0}{r^2\cos^2\theta}\left(\frac{\mathrm{d}A_0^{\mathrm{a}}}{\mathrm{d}r}\right)^2 - \frac{2\,\Xi^2}{r^3\cos^2\theta} B_0^{\mathrm{i}} = 0. \tag{4.1.35}$$

Seeking a normalisation that reduces the number of parameters in the system, we define

$$y = \frac{Y}{\Lambda\,\mathrm{Ha}}, \qquad \Upsilon = \frac{2\,\Xi}{\Lambda^2 r^2\,\mathrm{Ha}\cos\theta}, \tag{4.1.36a,b}$$

$$\alpha = \frac{a}{\Lambda\,\mathrm{Ha}}, \qquad H = \Lambda\,\mathrm{Ha}\, h_0, \tag{4.1.36c,d}$$

where we have recycled the vertical coordinate notation Y from earlier, and where Λ is the leading-order y-component of the applied poloidal field, namely

$$\Lambda = \frac{1}{r\cos\theta}\frac{\mathrm{d}A_0^{\mathrm{a}}}{\mathrm{d}r}. \tag{4.1.37}$$

We then scale the leading-order solution via

$$u_0 = \frac{1}{\Lambda^2}\left(1 - \frac{\partial P}{\partial r}\right) u_{\mathcal{G}}, \qquad B_0^{\mathrm{i}} = \frac{r^3\cos^2\theta}{2\,\Xi^2}\left(1 - \frac{\partial P}{\partial r}\right) B_{\mathcal{G}}^{\mathrm{i}}, \tag{4.1.38a,b}$$

and the system reduces to the normalised form

$$\frac{\partial^2 B_{\mathcal{G}}^{\mathrm{i}}}{\partial Y^2} + \Upsilon^2 u_{\mathcal{G}} - B_{\mathcal{G}}^{\mathrm{i}} = 0, \qquad \frac{\partial^2 u_{\mathcal{G}}}{\partial Y^2} - u_{\mathcal{G}} - B_{\mathcal{G}}^{\mathrm{i}} = -1. \tag{4.1.39a,b}$$

subject to the boundary conditions

$$B^{\mathrm{i}}_{\mathcal{G}} = \frac{\partial u_{\mathcal{G}}}{\partial Y} = 0 \quad \text{at} \quad Y = H, \tag{4.1.39c}$$

$$\alpha B^{\mathrm{i}}_{\mathcal{G}} - \frac{\partial B^{\mathrm{i}}_{\mathcal{G}}}{\partial Y} = u_{\mathcal{G}} = 0 \quad \text{at} \quad Y = 0. \tag{4.1.39d}$$

The subscript $\mathcal{G}$ employed here refers to the gravity driving the system. Later on, in §4.3.3, we employ different subscripts to denote components of the solution driven by additional thermal effects.

Naturally, system (4.1.39) generalises both the toroidal system (2.3.31) and the poloidal system (2.2.41). Boundary conditions (4.1.39c,d) retain the toroidal form (2.3.31b), while the momentum equation (4.1.39b) combines the toroidal form (2.3.31a) with the poloidal form (2.2.41a). The induction equation (4.1.39a) takes the toroidal form (2.3.31a) with the addition of the final term on the left-hand side $B^{\mathrm{i}}_{\mathcal{G}}$, which comes from the coupling to the toroidal flow, and therefore is not present in either of the canonical cases.

Isolating $u_{\mathcal{G}}$ in (4.1.39a) and substituting into (4.1.39b) provides a fourth-order ODE for $B^{\mathrm{i}}_{\mathcal{G}}$. Alternatively, $B^{\mathrm{i}}_{\mathcal{G}}$ could be isolated to yield a fourth-order equation governing $u_{\mathcal{G}}$. Explicit but unwieldy expressions for the solution are reproduced in appendix A.5. This completes the leading-order solution.

Before exploring how the system varies with respect to the normalised parameters, we remark on analytical properties of leading order solutions. The system (4.1.28–30) is even with respect to Ξ, therefore so are the solutions. However, the scalings (4.1.14) reflect that the toroidal flow and induced field are proportional to Ξ. This means that a reversal in the direction of the toroidal field will leave the downstream flow unaffected but the toroidal flow and magnetic fields will flip sign. Similarly, the system is invariant under the transform $(w_0, A^{\mathrm{a}}_0) \mapsto (-w_0, -A^{\mathrm{a}}_0)$ which explains why only the toroidal flow swaps direction if the applied component normal to the substrate changes sign.

4.1.7 Flow and magnetic field profiles

The normalised system (4.1.39) contains three free parameters: Υ, α, and H. In this section we investigate how the downstream and toroidal flow as well as the induced toroidal field vary with these parameters.

First, we consider the effects of varying Υ, which represents the toroidal field strength. As shown in figure 4.1, for small values of Υ, the induced field is weak

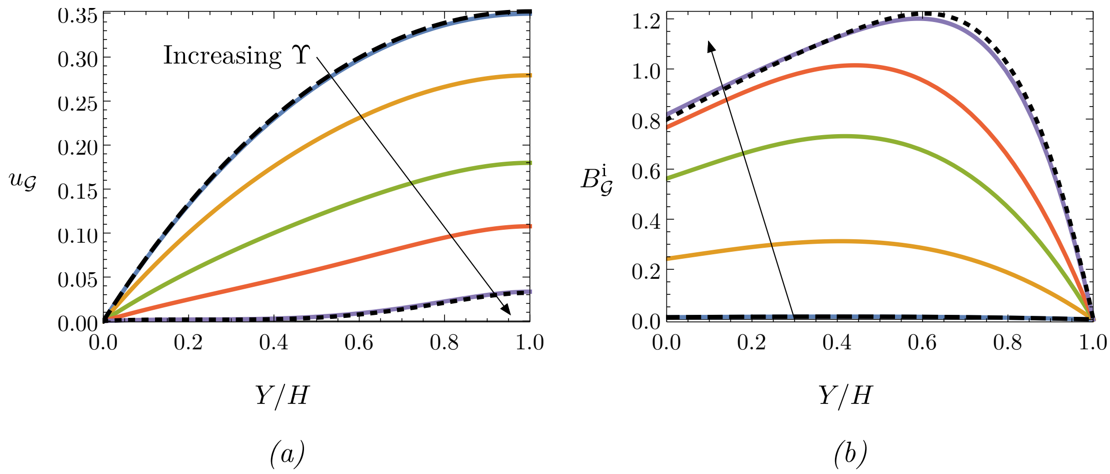

Figure 4.1: Normalised flow and field profiles where $\alpha = H = 1$, *and* $\Upsilon \in \{0.5, 3, 6, 10, 30\}$. *The black dashed curve is the asymptotic approximation for* $\Upsilon \ll 1$ *given by* (4.1.41). *The black dotted curve is the composite asymptotic expansion for the case* $\Upsilon \gg 1$ *given by* (4.1.53).

and the velocity resembles a classical parabolic hydrodynamic flow profile. As Υ increases the downstream flow is confined to a neighbourhood of the free surface, while the induced field is strengthened. To gain further analytical insight into the behaviour observed in figure 4.1, we solve the system in various asymptotic limits by means of matched asymptotic expansions.

In the limit $\Upsilon \to 0$, we take an asymptotic expansion (recycling earlier notation) of the form

$$u_{\mathcal{G}} \sim u_0 + \cdots, \qquad B^{\mathrm{i}}_{\mathcal{G}} \sim \Upsilon^2 B^{\mathrm{i}}_0 + \cdots, \tag{4.1.40a,b}$$

where the leading-order balance in (4.1.39) requires the toroidal field be of order $\mathcal{O}(\Upsilon^2)$. The downstream flow governed by (4.1.39b) then reduces to the purely poloidal case, namely

$$u_0 = 1 - \cosh Y + \sinh Y \tanh H. \tag{4.1.41a}$$

It then follows from (4.1.39) that

$$B^{\mathrm{i}}_0 = 1 + \frac{1}{2+2\alpha \tanh H}\Big[(\sinh Y - \cosh Y \tanh H)\,(Y + 2\alpha + \tanh H + \alpha Y \tanh H) - 2\,\mathrm{sech}\, H\,(\cosh Y + \alpha \sinh Y)\Big]. \tag{4.1.41b}$$

The approximation (4.1.41) agrees well with the numerical solution in figure 4.1. Physically, the toroidal magnetic field and toroidal flow are driven by the coupling of the $u_{\mathcal{G}}$ term in (4.1.39a), which is of order $\mathcal{O}(\Upsilon^2)$, and thus becomes vanishingly small as Υ decreases.

In the opposite limit, as $\Upsilon \to \infty$, we pose the expansion

$$u_{\mathcal{G}} \sim \frac{1}{\Upsilon^2} u_\infty + \cdots, \qquad\qquad B^{\mathrm{i}}_{\mathcal{G}} \sim B^{\mathrm{i}}_\infty + \cdots. \tag{4.1.42a,b}$$

Leading-order solutions then take the form

$$u_\infty = B^{\mathrm{i}}_\infty = 1. \tag{4.1.43}$$

The solutions (4.1.43) do not satisfy all of the boundary conditions; this is a singular limit, and there are boundary layers of width $\mathcal{O}(1/\sqrt{\Upsilon})$ at both the free surface and the substrate.

We examine the boundary layer at the substrate by scaling the vertical coordinate via

$$Y = \frac{\mathcal{Y}}{\sqrt{\Upsilon}}, \tag{4.1.44}$$

and write the inner solution in an asymptotic expansion of the form

$$u_{\mathcal{G}} \sim \frac{1}{\Upsilon} U_\infty(\mathcal{Y}) + \cdots, \qquad\qquad B^{\mathrm{i}}_{\mathcal{G}} \sim b_\infty(\mathcal{Y}) + \cdots, \tag{4.1.45a,b}$$

having made the scaling choices in order to provide a sensible dominant balance in (4.1.39). The inner solution then satisfies

$$\frac{\partial^2 b_\infty}{\partial \mathcal{Y}^2} + U_\infty = 0, \tag{4.1.46a}$$

$$\frac{\partial^2 U_\infty}{\partial \mathcal{Y}^2} - b_\infty = -1, \tag{4.1.46b}$$

subject to the boundary and matching conditions

$$\hat{\alpha}\, b_\infty - \frac{\partial b_\infty}{\partial \mathcal{Y}} = U_\infty = 0 \quad \text{at} \;\; \mathcal{Y} = 0, \tag{4.1.47}$$

$$b_\infty \to 1,\; U_\infty \to 0 \quad \text{as} \;\; \mathcal{Y} \to \infty, \tag{4.1.48}$$

where we are considering the distinguished limit where $\hat{\alpha} = \alpha/\sqrt{\Upsilon} = \mathcal{O}(1)$. We find that the inner solution is given by

$$U_\infty = \frac{2\hat{\alpha}}{\sqrt{2}+2\hat{\alpha}}\,\mathrm{e}^{-\mathcal{Y}/\sqrt{2}}\sin(\mathcal{Y}/\sqrt{2}), \qquad b_\infty = 1-\frac{2\hat{\alpha}}{\sqrt{2}+2\hat{\alpha}}\,\mathrm{e}^{-\mathcal{Y}/\sqrt{2}}\cos(\mathcal{Y}/\sqrt{2}). \tag{4.1.49a,b}$$

At the free surface the boundary layer has the same width, and is exposed by scaling the vertical coordinate via

$$Y = H - \frac{\mathcal{Y}}{\sqrt{\Upsilon}}, \tag{4.1.50}$$

and employing the same inner expansion (4.1.45) as at the substrate. The inner solution then satisfies the same equation, (4.1.46), subject to the same matching condition (4.1.48), and boundary conditions

$$\frac{\partial U_\infty}{\partial \mathcal{Y}}(0) = b_\infty(0) = 0, \tag{4.1.51}$$

which is solved by

$$U_\infty = \mathrm{e}^{-\mathcal{Y}/\sqrt{2}}\left[\sin(\mathcal{Y}/\sqrt{2})+\cos(\mathcal{Y}/\sqrt{2})\right], \tag{4.1.52a}$$

$$b_\infty = 1+\mathrm{e}^{-\mathcal{Y}/\sqrt{2}}\left[\sin(\mathcal{Y}/\sqrt{2})-\cos(\mathcal{Y}/\sqrt{2})\right]. \tag{4.1.52b}$$

By combining (4.1.43), (4.1.49) and (4.1.52), a composite expansion uniformly valid in Y may be constructed:

$$\begin{aligned} u_{\mathcal{G}} \sim{}& \frac{1}{\Upsilon^2}+\frac{1}{\Upsilon}\frac{2\alpha}{\sqrt{2\Upsilon}+2\alpha}\,\mathrm{e}^{-Y/\sqrt{2}}\sin\left(Y\sqrt{\frac{\Upsilon}{2}}\right)\\ &+\frac{1}{\Upsilon}\left[\sin\left((H-Y)\sqrt{\frac{\Upsilon}{2}}\right)+\cos\left((H-Y)\sqrt{\frac{\Upsilon}{2}}\right)\right]\mathrm{e}^{-(H-Y)\sqrt{\Upsilon/2}}, \end{aligned} \tag{4.1.53a}$$

$$\begin{aligned} B^{\mathrm{i}}_{\mathcal{G}} \sim{}& 1-\frac{2\alpha}{\sqrt{2\Upsilon}+2\alpha}\,\mathrm{e}^{-Y/\sqrt{2}}\cos\left(Y\sqrt{\frac{\Upsilon}{2}}\right)\\ &+\left[\sin\left((H-Y)\sqrt{\frac{\Upsilon}{2}}\right)-\cos\left((H-Y)\sqrt{\frac{\Upsilon}{2}}\right)\right]\mathrm{e}^{-(H-Y)\sqrt{\Upsilon/2}}. \end{aligned} \tag{4.1.53b}$$

The composite expansion captures the profile behaviour well, as illustrated in figure 4.1. The boundary-layer scaling reveals that, in the case of large Υ, the downstream velocity is of magnitude $\mathcal{O}(1/\Upsilon^2)$ in the bulk, but is of order $\mathcal{O}(1/\Upsilon)$ near

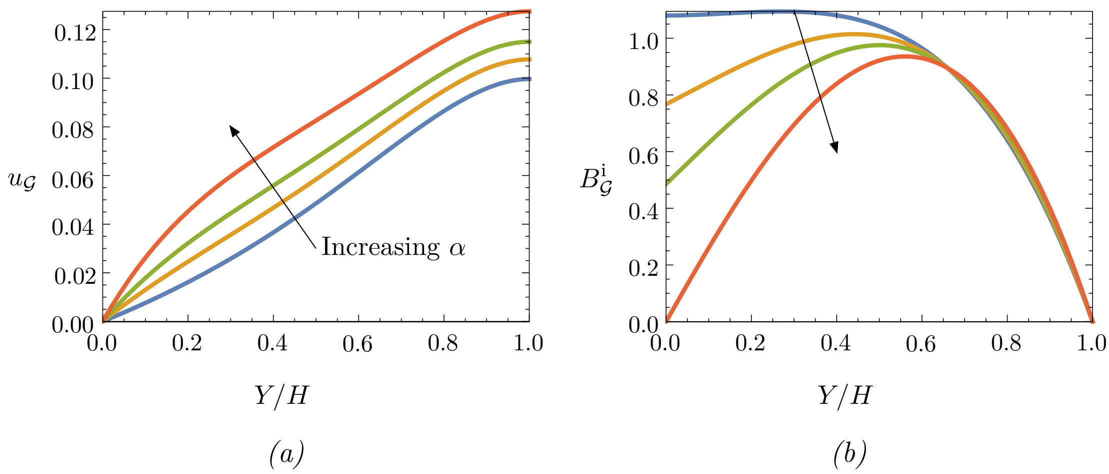

Figure 4.2: Normalised flow and field profiles where $\Upsilon = 10$, $H = 1$, and $\alpha \in \{0, 1, 3, \infty\}$.

$Y = H$. Thus the flow occurs predominantly in a neighbourhood of the free surface, as observed in figure 4.1(a). The boundary layer at $Y = 0$ is somewhat weaker, with the velocity of order $\mathcal{O}(1/\Upsilon^{3/2})$, unless the normalised substrate resistance α is also large. Since the boundary layer width is $\mathcal{O}(1/\sqrt{\Upsilon})$, most of the fluid passes through the boundary layers, not the bulk. This deviates from classical gravity-driven Hartmann flow where the viscous boundary layer adjacent to the substrate merely decelerates the bulk flow. Moreover, the boundary layer analysis reveals interesting oscillating boundary-layer profiles in both the flow velocity and the induced field, similar to the toroidal case (see figure 2.10).

Next we consider the effect of varying the parameter α. From (4.1.27) and (4.1.36) we see that α represents the transition from an insulating substrate ($\alpha = 0$) to a perfectly conducting substrate ($\alpha = \infty$). As illustrated in figure 4.2, the change manifests in the boundary condition for B^{i}_0, while the flow fields are not significantly altered for this selection of parameters.

We now consider the results of varying the normalised film thickness H, as illustrated in figure 4.3. For small H, we observe diminishing flow and field profiles. For large H, non-monotonicities manifest, with the downstream flow and toroidal magnetic field converging to uniform profiles in the bulk and variations restricted to boundary layers.

To obtain more analytical insight into the behaviour at extreme values of H, we scale

$$Y = \mathcal{Y} H, \tag{4.1.54}$$

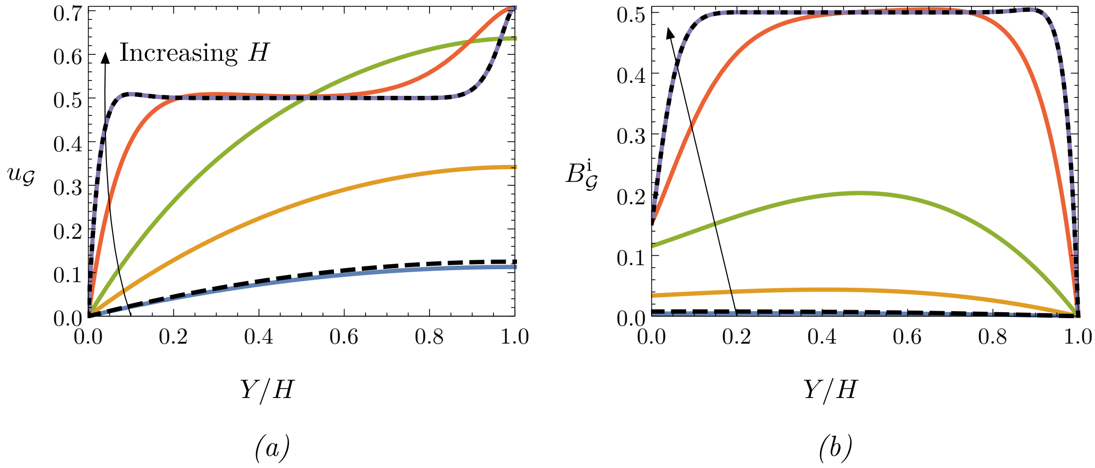

Figure 4.3: Normalised flow and field profiles where $\Upsilon = \alpha = 1$, and $H \in \{0.5, 1, 2, 10, 30\}$. The black dashed curve is the asymptotic approximation for $H \ll 1$ given by (4.1.57). The black dotted curve is the composite asymptotic expansion for the case $H \gg 1$ composing the inner and outer solutions in (4.1.58), (4.1.61) and (4.1.65).

whereby the reduced system (4.1.39) takes the form

$$\frac{1}{H^2}\frac{\partial^2 B^{\mathrm{i}}_{\mathcal{G}}}{\partial \mathcal{Y}^2} + \Upsilon^2 u_{\mathcal{G}} - B^{\mathrm{i}}_{\mathcal{G}} = 0, \tag{4.1.55a}$$

$$\frac{1}{H^2}\frac{\partial^2 u_{\mathcal{G}}}{\partial \mathcal{Y}^2} - u_{\mathcal{G}} - B^{\mathrm{i}}_{\mathcal{G}} = -1. \tag{4.1.55b}$$

subject to the boundary conditions

$$B^{\mathrm{i}}_{\mathcal{G}} = \frac{\partial u_{\mathcal{G}}}{\partial \mathcal{Y}} = 0 \quad \text{at} \quad \mathcal{Y} = 1, \tag{4.1.55c}$$

$$\alpha B^{\mathrm{i}}_{\mathcal{G}} - \frac{1}{H}\frac{\partial B^{\mathrm{i}}_{\mathcal{G}}}{\partial \mathcal{Y}} = u_{\mathcal{G}} = 0 \quad \text{at} \quad \mathcal{Y} = 0. \tag{4.1.55d}$$

Considering first the limit as $H \to 0$, while other parameters remain $O(1)$, we pose an asymptotic expansion of the form

$$u_{\mathcal{G}} \sim H^2 u_0 + \cdots, \qquad\qquad B^{\mathrm{i}}_{\mathcal{G}} \sim H^4 B^{\mathrm{i}}_0 + \cdots. \tag{4.1.56a,b}$$

The leading-order solution is then found to be

$$u_0 = \frac{\mathcal{Y}(2-\mathcal{Y})}{2}, \qquad\qquad B^{\mathrm{i}}_0 = \frac{\Upsilon^2}{24}\left(3 - 4\mathcal{Y}^3 + \mathcal{Y}^4\right). \tag{4.1.57a,b}$$

This limit corresponds to a vanishing applied field strength, whereby we see that the leading-order flow is hydrodynamic, being dominated by viscous forces, while the toroidal magnetic field and thus the associated toroidal flow is $\mathcal{O}(H^2)$ smaller than the downstream flow.

In the singular limit as $H \to \infty$ we find that, to leading order,

$$u_{\mathcal{G}} \sim \frac{1}{1+\Upsilon^2}, \qquad B^{\mathrm{i}}_{\mathcal{G}} \sim \frac{\Upsilon^2}{1+\Upsilon^2}. \tag{4.1.58a,b}$$

Boundary layers of width $\mathcal{O}(1/H)$ exist at both ends of the boundary. At the substrate we rescale the vertical coordinate

$$\mathcal{Y} = \frac{Y}{H}, \tag{4.1.59}$$

whereupon the inner solution satisfies the full equations

$$\frac{\partial^2 B^{\mathrm{i}}_{\mathcal{G}}}{\partial Y^2} + \Upsilon^2 u_{\mathcal{G}} - B^{\mathrm{i}}_{\mathcal{G}} = 0, \tag{4.1.60a}$$

$$\frac{\partial^2 u_{\mathcal{G}}}{\partial Y^2} - u_{\mathcal{G}} - B^{\mathrm{i}}_{\mathcal{G}} = -1. \tag{4.1.60b}$$

subject to boundary and matching conditions

$$\alpha\, B^{\mathrm{i}}_{\mathcal{G}} - \frac{\partial B^{\mathrm{i}}_{\mathcal{G}}}{\partial Y} = u_{\mathcal{G}} = 0 \quad \text{at } Y = 0, \tag{4.1.60c}$$

$$B^{\mathrm{i}}_{\mathcal{G}} \to \frac{\Upsilon^2}{1+\Upsilon^2},\; u_{\mathcal{G}} \to \frac{1}{1+\Upsilon^2} \quad \text{as } Y \to \infty. \tag{4.1.60d}$$

The problem (4.1.60) is solved by

$$u_{\mathcal{G}} = \frac{1}{1+\Upsilon^2}\left(1 + \frac{\mathrm{e}^{-M_+ Y}}{\alpha + M_+}\left[(\alpha\Upsilon + M_-)\sin(M_- Y) - (\alpha + M_+)\cos(M_- Y)\right]\right), \tag{4.1.61a}$$

$$B^{\mathrm{i}}_{\mathcal{G}} = \frac{\Upsilon}{1+\Upsilon^2}\left(\Upsilon - \frac{\mathrm{e}^{-M_+ Y}}{\alpha + M_+}\left[(\alpha + M_+)\sin(M_- Y) + (\alpha\Upsilon + M_-)\cos(M_- Y)\right]\right). \tag{4.1.61b}$$

where

$$M_\pm = \sqrt{\frac{\sqrt{1+\Upsilon^2} \pm 1}{2}}. \tag{4.1.62}$$

At the free surface we scale the vertical coordinate via

$$Y = 1 - \frac{\mathcal{Y}}{H}, \tag{4.1.63}$$

whereupon the inner solution satisfies the same equations, (4.1.60a) and (4.1.60b), subject to the matching condition (4.1.60d), along with the free surface boundary conditions

$$B^{\mathrm{i}}_{\mathcal{G}} = \frac{\partial u_{\mathcal{G}}}{\partial Y} = 0 \quad \text{at} \quad Y = 0, \tag{4.1.64}$$

admitting the solution

$$u_{\mathcal{G}} = \frac{1}{1+\Upsilon^2}\left(1 + \mathrm{e}^{-M_+ Y}\left[\Upsilon \sin(M_- Y) + 2M_-^2 \cos(M_- Y)\right]\right), \tag{4.1.65a}$$

$$B^{\mathrm{i}}_{\mathcal{G}} = \frac{\Upsilon}{1+\Upsilon^2}\left(\Upsilon + \mathrm{e}^{-M_+ Y}\left[2M_-^2 \sin(M_- Y) - \Upsilon \cos(M_- Y)\right]\right). \tag{4.1.65b}$$

By combining (4.1.58), (4.1.61) and (4.1.65), a composite expansion may be formed, which agrees well with the explicit solution, as illustrated in figure 4.3. This limit corresponds to a strong applied field, with the flow dominated by magnetohydrodynamic forces which lead to the observed non-monotonicities. Although the velocity and induced field are approximately uniform outside boundary layers at the substrate and the free surface, the boundary layer analysis reveals that the structure and qualitative behaviour are quite different from classical Hartmann flow, but reminiscent of the toroidal case (see figure 2.10). The solution (4.1.65) allows us to ascertain the leading-order free-surface velocity in the case of large H: $u_{\mathcal{G}} \sim (1 + 2M_-^2)/(1+\Upsilon^2)$. For the values used in figure 4.3, $\Upsilon = 1$ and $H = 30$, we find the leading-order free-surface downstream velocity to be $u_{\mathcal{G}} \sim 1/\sqrt{2} \approx 0.7071$.

Having explored how the system varies when the normalised parameters Υ, α, and H are varied independently, it is worth highlighting how the fluid flux varies as we transition from classical hydrodynamic flow in low field ($\mathrm{Ha} \ll 1$) to MHD flow in high field ($\mathrm{Ha} \gg 1$). Assuming other physical parameters are of order unity, then from (4.1.36) the normalised parameters scale like $\Upsilon \sim 1/\mathrm{Ha}$, $\alpha \sim 1/\mathrm{Ha}$, $H \sim \mathrm{Ha}$.

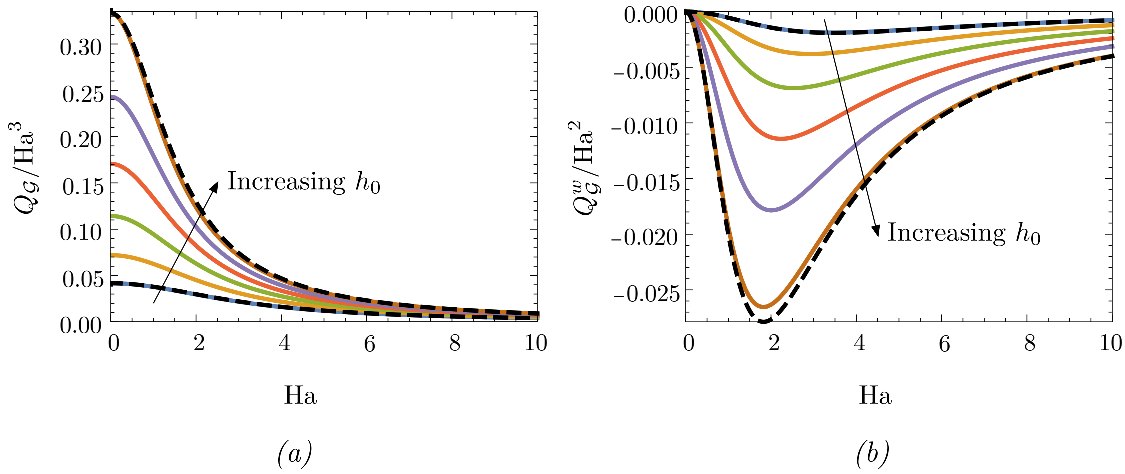

Figure 4.4: Scaled fluxes (4.1.66) *plotted as functions of the field strength via* Ha*, where* $\Upsilon = 1/\mathrm{Ha}$*,* $\alpha = 1/\mathrm{Ha}$*,* $H = \mathrm{Ha}\,h_0$*, and* $h_0 \in \{0.5, 0.6, 0.7, 0.8, 0.9, 1\}$*. The black dashed curves show the asymptotic approximations given in* (4.1.67).

The normalised downstream and toroidal fluid fluxes are defined by

$$Q_{\mathcal{G}} = \int_0^H u_{\mathcal{G}}\,\mathrm{d}Y, \qquad Q^w_{\mathcal{G}} = -\int_0^H \int_0^Y B^{\mathrm{i}}_{\mathcal{G}}(s)\,\mathrm{d}s\,\mathrm{d}Y = -\int_0^H (H-Y)B^{\mathrm{i}}_{\mathcal{G}}(Y)\,\mathrm{d}Y, \qquad (4.1.66\mathrm{a,b})$$

where we have relied on the integral of (4.1.32) for the toroidal flux. We introduce factors of $1/\mathrm{Ha}^3$ and $1/\mathrm{Ha}^2$, respectively, to undo the scalings in (4.1.15), (4.1.32) and (4.1.36) with respect to the field strength. This ensures that the scaled fluxes, $Q_{\mathcal{G}}/\mathrm{Ha}^3$ and $Q^w_{\mathcal{G}}/\mathrm{Ha}^2$, are proportional to their dimensional counterparts when all parameters are held constant except for the field strength $\mathscr{B}^*$.

In figure 4.4 we plot the scaled fluxes as functions of field strength by varying Ha while fixing $a = \Lambda = 2\,\Xi/(r^2\cos\theta) = 1$. The black dashed curves in figure 4.4 show the composite expansions derived by integrating (4.1.41), namely

$$Q_{\mathcal{G}} \sim H - \tanh H, \qquad (4.1.67\mathrm{a})$$

$$Q^w_{\mathcal{G}} \sim \frac{\Upsilon^2(H - \tanh H)}{2 + 2\alpha\tanh H}\left[2\alpha(1 - \operatorname{sech} H) - H + (1 - H\alpha)\tanh H\right], \qquad (4.1.67\mathrm{b})$$

where H, Υ, and α scale with Ha, $1/\mathrm{Ha}$, and $1/\mathrm{Ha}$, respectively as Ha is varied. The approximation (4.1.67) retains magnetic and viscous contributions to the flux. It reduces to classical hydrodynamic downstream flow and zero toroidal flow as

$H \to 0$, and recovers the flux expected from a Hartmann flow when $H \to \infty$. Figure 4.4 demonstrates that the resulting uniformly valid approximation agrees well with the full solution for all values of Ha.

We observe in figure 4.4 how the downstream flux monotonically decreases as the applied field strength increases. This is due to gravity acting downstream to induce a flow, with MHD drag decelerating the flow as the applied field strength increases. On the other hand, the toroidal flux exhibits a non-monotonicity with respect to the field strength, increasing in magnitude monotonically for low field, and then diminishing monotonically in high field. This is because the toroidal flow is induced entirely by the applied field; as the field vanishes, the flow vanishes along with it, while in the high-field regime, MHD drag decelerates the toroidal flow just as for the downstream flow. This non-monotonicity in the flux is typical of MHD-induced flows [179].

Next, we extend the model to incorporate temperature and thereby capture the thermal load that the core plasma imparts to the liquid metal layer.

4.2 Introducing thermal effects

In this section we extend the isothermal model considered until now by including temperature. We begin by surveying a class of thermoelectric and other thermal effects to determine which are physically dominant. To this end, we derive an energy equation governing the evolution of energy density within the system, and apply asymptotic analysis to reduce this in the relevant physical limit. The result is a leading-order equation governing temperature, which is coupled to the flow and the induced field through new terms introduced into the leading-order axisymmetric three-dimensional model.

We begin by introducing a class of effects that convert thermal differences into electrical potential and vice versa, known collectively as the thermoelectric effect. Current is induced along temperature gradients via the Seebeck effect, and currents driven along temperature gradients (with material property gradients) produce or consume thermal energy via the Thomson and Peltier effects [179].

4.2.1 The Seebeck effect

The Seebeck effect refers to the phenomenon by which an electromotive force is produced in the presence of temperature gradients within conductors (even in the absence of electric and magnetic fields). This is incorporated into our model by amending Ohm's law (2.1.8) to become [26, 179]

$$\boldsymbol{j}^* = \sigma^*(\boldsymbol{E}^* + \boldsymbol{u}^* \times \boldsymbol{B}^* - S^*\boldsymbol{\nabla}^*T^*), \tag{4.2.1}$$

where T^* is the temperature, and S^* is known as the Seebeck coefficient. In most metals the Seebeck coefficient is negative, expressing the fact that electrons flow down the temperature gradient, diffusing from hot to cold [179], while lithium (in both solid and liquid forms) has a positive and relatively large Seebeck coefficient, whereby electrons are induced to flow in the opposite direction. The underlying physical mechanism appears to be a quantum phenomenon, although this is not well understood (see [222] and references therein).

With the modified Ohm's law, (4.2.1), the boundary condition between two materials (2.1.19f) takes the new form

$$\begin{aligned}\left[\frac{1}{\sigma^*}\boldsymbol{j}^* \times \boldsymbol{n}\right]_-^+ &= [(\boldsymbol{u}^* \times \boldsymbol{B}^* - S^*\boldsymbol{\nabla}^*T^*) \times \boldsymbol{n}]_-^+ \\ &= [(\boldsymbol{u}^* \times \boldsymbol{B}^*) \times \boldsymbol{n}]_-^+ - [S^*]_-^+ \boldsymbol{\nabla}^*T^* \times \boldsymbol{n}, \end{aligned} \tag{4.2.2}$$

where the second equality holds provided temperatures are equal at the interface. The induction equation (2.1.10) takes the modified form

$$\frac{\partial \boldsymbol{B}^{\mathrm{i}*}}{\partial t^*} = \boldsymbol{\nabla}^* \times (\boldsymbol{u}^* \times \boldsymbol{B}^* - S^*\boldsymbol{\nabla}^*T) + \eta^*\boldsymbol{\nabla}^{*2}\boldsymbol{B}^{\mathrm{i}*}. \tag{4.2.3}$$

However, the new term in (4.2.3) vanishes in each region, since, in a homogeneous material, S depends only on T, in which case

$$\boldsymbol{\nabla}^* \times (S^*\boldsymbol{\nabla}^*T) = \boldsymbol{\nabla}^*S^* \times \boldsymbol{\nabla}^*T^* = (\boldsymbol{\nabla}^*T^* \times \boldsymbol{\nabla}^*T)\,\frac{\mathrm{d}S^*}{\mathrm{d}T^*} = 0. \tag{4.2.4}$$

Therefore the Seebeck effect manifests entirely through the modified boundary condition (4.2.2).

4.2.2 The Peltier and Thomson effects

The remaining two thermoelectric effects are the Peltier and Thomson effects. These describe the energy produced or consumed as a result of current flowing in the presence of temperature and material property gradients, as we will describe. Following [179] to incorporate these effects, the heat flux per unit volume, $\boldsymbol{Q}^*$, is modified to obey the augmented Fourier law:

$$\boldsymbol{Q}^* = -k^* \boldsymbol{\nabla}^* T^* + S^* T^* \boldsymbol{j}^*, \tag{4.2.5}$$

where k^* is the thermal conductivity. The thermal condition at a material boundary $[\boldsymbol{Q}^* \cdot \boldsymbol{n}]_-^+ = 0$, takes the form

$$k^{+*} \boldsymbol{\nabla}^* T^{+*} \cdot \boldsymbol{n} = k^{-*} \boldsymbol{\nabla}^* T^{-*} \cdot \boldsymbol{n} + \left(S^{+*} - S^{-*}\right) T^* \boldsymbol{j}^* \cdot \boldsymbol{n}. \tag{4.2.6}$$

The second term on the right-hand side of (4.2.6) describes the Peltier effect, namely an additional contribution to the energy flux at a boundary between materials with differing Seebeck coefficients.

We now apply (4.2.5) to derive an equation governing the conservation of energy. Following [169] we begin by considering magnetic energy density. Using (2.1.1c) we obtain

$$\frac{\partial}{\partial t^*} \left(\frac{|\boldsymbol{B}^*|^2}{2\mu^*} \right) = \frac{\boldsymbol{B}^*}{\mu^*} \cdot \frac{\partial \boldsymbol{B}^*}{\partial t^*} = -\frac{\boldsymbol{B}^*}{\mu^*} \cdot \left(\boldsymbol{\nabla}^* \times \boldsymbol{E}^* \right), \tag{4.2.7}$$

which, using standard vector identities, may be expressed as

$$\frac{\partial}{\partial t^*} \left(\frac{|\boldsymbol{B}^*|^2}{2\mu^*} \right) + \boldsymbol{\nabla}^* \cdot \left(\frac{\boldsymbol{E}^* \times \boldsymbol{B}^*}{\mu^*} \right) = -\frac{|\boldsymbol{j}^*|^2}{\sigma^*} - \boldsymbol{u}^* \cdot (\boldsymbol{j}^* \times \boldsymbol{B}^*) - S^* \boldsymbol{\nabla}^* T^* \cdot \boldsymbol{j}^*. \tag{4.2.8}$$

The second term on the left-hand side of (4.2.8) represents the magnetic energy flux given by the so-called Poynting vector.

The rate of change of kinetic energy density is given by

$$\frac{\partial}{\partial t^*} \left(\frac{\rho^*}{2} |\boldsymbol{u}^*|^2 \right) = \frac{1}{2} |\boldsymbol{u}^*|^2 \frac{\partial \rho^*}{\partial t^*} + \rho^* \boldsymbol{u}^* \cdot \frac{\partial \boldsymbol{u}^*}{\partial t^*}. \tag{4.2.9}$$

Again using standard identities, it follows from (2.1.16) that

$$\begin{aligned} \frac{\partial}{\partial t^*} \left(\frac{\rho^*}{2} |\boldsymbol{u}^*|^2 \right) + \boldsymbol{\nabla}^* \cdot \left(\frac{\rho^*}{2} |\boldsymbol{u}^*|^2 \boldsymbol{u}^* \right) = \boldsymbol{\nabla}^* \cdot (\overline{\boldsymbol{\tau}}^* \cdot \boldsymbol{u}^*) - \rho^* \nu^* \left(\boldsymbol{\nabla}^* \boldsymbol{u}^* : \boldsymbol{\nabla}^* \boldsymbol{u}^* \right) \\ + \boldsymbol{u}^* \cdot (\boldsymbol{j}^* \times \boldsymbol{B}^*) + \rho^* \boldsymbol{u}^* \cdot \boldsymbol{g}^*, \end{aligned} \tag{4.2.10}$$

where $\overline{\boldsymbol{\tau}}^*$ is the viscous stress tensor defined in (2.1.17).

We next consider the conservation of internal energy density. Denoting internal energy per unit mass by e^*, and applying standard thermodynamic relations [169], along with our augmented Fourier law (4.2.5), we obtain

$$\frac{\partial\left(\rho^* e^*\right)}{\partial t^*} + \boldsymbol{\nabla}^* \cdot \left(\rho^* e^* \boldsymbol{u}^*\right) = \boldsymbol{\nabla}^* \cdot \left(k^* \boldsymbol{\nabla}^* T^*\right) - \boldsymbol{\nabla}^* \left(T^* S^*\right) \cdot \boldsymbol{j}^* + H^*, \tag{4.2.11}$$

where H^* is any source of heating.

Before we combine the rates of change of energy density, we must determine the heat source H^* that closes the conservation system by accounting for all energy balances. The source term $\boldsymbol{u}^* \cdot (\boldsymbol{j}^* \times \boldsymbol{B}^*)$ expresses magnetic energy converted into kinetic energy, hence it appears in (4.2.8) with a negative sign, and in (4.2.10) with a positive sign. The term $\rho^* \boldsymbol{u}^* \cdot \boldsymbol{g}^*$ in (4.2.10) expresses a gain in kinetic energy from the work done by the gravitational field. The energy source terms $\left|\boldsymbol{j}^*\right|^2 / \sigma^*$ in (4.2.8), and $\rho^* \nu^* \left(\boldsymbol{\nabla}^* \boldsymbol{u}^* : \boldsymbol{\nabla}^* \boldsymbol{u}^*\right)$ in (4.2.10) appear with negative signs. These are the ohmic and viscous losses, respectively, and these losses in magnetic and kinetic energies are balanced by gains in the internal energy which must appear in the heat source H^*. Similarly, the term $S^* \boldsymbol{\nabla}^* T^* \cdot \boldsymbol{j}^*$ in (4.2.8) represents magnetic energy converted to thermal energy (or vice versa, depending on its sign) and contributes to H^*. Assuming that there are no other significant contributions to internal energy, we therefore find that the heat source is given by

$$H^* = \frac{\left|\boldsymbol{j}^*\right|^2}{\sigma^*} + \rho^* \nu^* \left(\boldsymbol{\nabla}^* \boldsymbol{u}^* : \boldsymbol{\nabla}^* \boldsymbol{u}^*\right) + S^* \boldsymbol{\nabla}^* T^* \cdot \boldsymbol{j}^*. \tag{4.2.12}$$

Now we combine the rates of change of magnetic, kinetic, and internal energies from (4.2.8), (4.2.10) and (4.2.11) to obtain a bulk energy equation. We find that the total bulk energy density satisfies

$$\begin{aligned}\frac{\partial}{\partial t^*}\left(\frac{\left|\boldsymbol{B}^*\right|^2}{2\mu^*} + \frac{\rho^*}{2}\left|\boldsymbol{u}^*\right|^2 + \rho^* e^*\right) + \boldsymbol{\nabla}^* \cdot \left(\frac{\boldsymbol{E}^* \times \boldsymbol{B}^*}{\mu^*} + \left(\frac{\rho^*}{2}\left|\boldsymbol{u}^*\right|^2 + \rho^* e^*\right)\boldsymbol{u}^*\right) \\ = \rho^* \boldsymbol{u}^* \cdot \boldsymbol{g}^* + \boldsymbol{\nabla}^* \cdot \left(k^* \boldsymbol{\nabla}^* T^* + \overline{\boldsymbol{\tau}}^* \cdot \boldsymbol{u}^*\right) - T^* \frac{\mathrm{d}S^*}{\mathrm{d}T^*} \boldsymbol{\nabla}^* T^* \cdot \boldsymbol{j}^*,\end{aligned} \tag{4.2.13}$$

The final term on the right-hand side of (4.2.13) describes the Thomson effect.

We now follow [179] in a dimensional analysis showing that in the presence of a strong magnetic field it is reasonable to neglect the Peltier and Thomson effects. We begin by showing that the magnitude of the thermoelectric current density is at most $\mathcal{O}\left(\sigma^* S^* \left|\boldsymbol{\nabla}^* T^*\right|\right)$. This estimate follows from (2.1.4) and the final term in (4.2.1), provided the velocity is not too large. Let us therefore consider the velocity scale $\mathscr{U}^*$ based on gravity as well as thermoelectrics. Recall from the isothermal case that a balance between gravitational and electromagnetic forces produces the scale (4.1.15), whereby $\mathscr{U}^* \approx 10^{-3}\,\mathrm{m/s}$. Then since $\left|\boldsymbol{\nabla}^* T^*\right| \geq 100\,\mathrm{K/m}$ we find that the ratio of the final two terms in the thermoelectric current density (4.2.1) satisfies

$$\frac{\mathscr{U}^* \mathscr{B}^*}{S^* \left|\boldsymbol{\nabla}^* T^*\right|} \leq 1. \tag{4.2.14}$$

In the thermoelectric-driven case, when inertial and gravitational forces are neglected we expect there to be two distinguished limits: high- and low-field. In the high-field limit, the thermoelectrical forces driving the flow are balanced by MHD drag, resulting in no net current [179]. This results in a balance of the final two terms of (4.2.1), and hence

$$\frac{\mathscr{U}^* \mathscr{B}^*}{S^* \left|\boldsymbol{\nabla}^* T^*\right|} \sim 1. \tag{4.2.15}$$

In the low-field limit, $\mathrm{Ha} \lesssim 1$, the MHD damping is not significant and instead the thermoelectric force is balanced by viscous damping in (2.1.18), from which it follows that

$$\frac{\mathscr{U}^* \mathscr{B}^*}{S^* \left|\boldsymbol{\nabla}^* T^*\right|} \sim \mathrm{Ha}^2 \lesssim 1. \tag{4.2.16}$$

Therefore we conclude that the magnitude of the thermoelectric current density is $\mathcal{O}\left(\sigma^* S^* \left|\boldsymbol{\nabla}^* T^*\right|\right)$, which is what we set out to demonstrate.

Assuming the liquid metal is maintained at an operating temperature less than $T^* \leq 1000\,\mathrm{K}$, it then follows that the ratio of the Peltier term to the conduction term in (4.2.6) can be no larger than

$$\frac{\sigma^* S^{*2} T^*}{k^*} = \mathcal{O}(10^{-2}), \tag{4.2.17}$$

using parameter values from table 2.2.

Writing internal energy as $e^* = c^* T^*$, where c^* is the specific heat, we find from (4.2.11) that the equation governing the evolution of the temperature is

$$\rho^* c^* \frac{\partial T^*}{\partial t^*} = \boldsymbol{\nabla}^* \cdot \left(k^* \boldsymbol{\nabla}^* T^* - \rho^* c^* T^* \boldsymbol{u}^*\right) + \frac{|\boldsymbol{j}^*|^2}{\sigma^*} + \rho^* \nu^* \left(\boldsymbol{\nabla}^* \boldsymbol{u}^* : \boldsymbol{\nabla}^* \boldsymbol{u}^*\right) \\ - T^* \frac{\mathrm{d}S^*}{\mathrm{d}T^*} \boldsymbol{\nabla}^* T^* \cdot \boldsymbol{j}^*. \qquad (4.2.18)$$

The ratio of the Thomson contribution to the conduction term in (4.2.18) is thus of order

$$T^* \frac{\mathrm{d}S^*}{\mathrm{d}T^*} \sigma^* S^* \left|\boldsymbol{\nabla}^* T^*\right| \frac{\mathscr{H}^*}{k^*} \approx \mathcal{O}(10^{-5}), \qquad (4.2.19)$$

again using parameter values from tables 2.1 and 2.2.

We conclude that the Peltier and Thomson effects may both be neglected in parameter regimes of interest.

4.2.3 Joule heating and viscous dissipation

In this section we show that, as for the Peltier and Thomson effects, both Joule heating and viscous dissipation — the second and third terms on the right-hand side of (4.2.18), respectively — can be neglected.

When using parameter values from tables 2.1 and 2.2 we find that the ratio of viscous dissipation to conduction, known as the Brinkman number, is of the order

$$\frac{\rho^* \nu^* \mathscr{U}^{*2}}{\mathscr{H}^* k^* \left|\boldsymbol{\nabla}^* T^*\right|} \approx 10^{-4}, \qquad (4.2.20)$$

even when we use a fast velocity scale $\mathscr{U}^* = 0.25\,\mathrm{m/s}$ [179] and a relatively small temperature gradient $|\boldsymbol{\nabla}^* T^*| = 100\,\mathrm{K/m}$. Similarly, the ratio of Joule heating to conduction is of order

$$\sigma^* S^{*2} \left|\boldsymbol{\nabla}^* T^*\right| \frac{\mathscr{H}^*}{k^*} \approx 10^{-4}, \qquad (4.2.21)$$

even when using a large temperature gradient of $|\boldsymbol{\nabla}^* T^*| = 10^4\,\mathrm{K/m}$. Hence these sources of heat may also be neglected.

4.2.4 Thermal boundary conditions

In our model, as in an operational tokamak, we incorporate cooling channels below the divertor plates, which maintain the bottom of the plates at a given temperature profile $T^{-*}(r^*)$.

At the free surface, the liquid metal is insulated by the vacuum. However, there is a substantial energy input from the core plasma, of order $\mathscr{C}^* \approx 10^7\,\mathrm{W/m^2}$ [61]. Additionally, energy is emitted from the divertor via electromagnetic radiation. This thermal radiation is governed by the Stefan–Boltzmann law [120] whereby the radiative energy flux emitted from the surface of the divertor Ω^* is given by

$$\Omega^* = \epsilon\,\sigma_0^*\,T^{*4}, \tag{4.2.22}$$

where ϵ is the thermal emissivity, $\sigma_0^* \approx 5.7\times10^{-8}\,\mathrm{W/m^2\,K^4}$ is the Stefan–Boltzmann constant. Theoretical modelling using the Drude model [172] predicts that $\epsilon < 0.1$ as long as $T^* < 2000\,\mathrm{K}$, well within the temperature range of interest, and experiments [173] suggest that $\epsilon \approx 0.046$ when $T^* < 650\,\mathrm{K}$.

The thermal flux at the free surface is thus $\mathscr{C}^* - \Omega^*$. The ratio of these two terms is

$$\frac{\Omega^*}{\mathscr{C}^*} \approx 10^{-3}, \tag{4.2.23}$$

for $T^* = 1400\,\mathrm{K}$, which is at the extreme upper limit of the intended operating regime. Therefore thermal radiation may be neglected in the model, at least in the region where the plasma is impinging.

Another boundary effect to be incorporated is thermocapillarity [159]. A temperature gradient along the boundary leads to a surface-tension gradient and thus a shear stress that can drive flow. This effect is modelled by an additional term in the boundary condition (2.1.22b), which takes the form

$$(\overline{\boldsymbol{\tau}}^* \cdot \boldsymbol{n}) \times \boldsymbol{n} = \frac{\mathrm{d}\gamma^*}{\mathrm{d}T^*}\boldsymbol{\nabla}^* T^* \times \boldsymbol{n} + [(\overline{\boldsymbol{m}}^* \cdot \boldsymbol{n}) \times \boldsymbol{n}]_-^+ . \tag{4.2.24}$$

The relative importance of this additional term is quantified by its ratio to the surface shear, which is of order

$$\frac{|\boldsymbol{\nabla}^* T|\,\mathscr{H}^*}{\rho^*\nu^*\mathscr{U}^*}\left|\frac{\mathrm{d}\gamma^*}{\mathrm{d}T^*}\right| \approx 10, \tag{4.2.25}$$

using parameter values from tables 2.1 and 2.2 and $|\boldsymbol{\nabla}^* T^*|/\mathscr{U}^* = 10^5\,\mathrm{K\,s/m^2}$. We deduce that thermocapillarity is an important contribution to retain.

To summarise §§ 4.2.1 to 4.2.3, we introduce the Seebeck effect which modifies Ohm's law as per (4.2.1). We neglect the other two thermoelectric effects that would generate heat, the Peltier and Thomson effects, as they are negligible in comparison with thermal conduction. Similarly we neglect Joule heating and viscous dissipation, but include thermocapillarity.

4.3 TEMHD model

In §4.2 we discuss the dominant thermal effects that are to be incorporated in the thermoelectric–MHD (TEMHD) model, namely the Seebeck effect and thermocapillarity. Thus the model's governing equations are to be supplemented by the heat equation governing the evolution of temperature, namely

$$\frac{\partial T^*}{\partial t^*} + \boldsymbol{u}^* \cdot \boldsymbol{\nabla}^* T^* = \kappa^* \boldsymbol{\nabla}^{*2} T^*, \tag{4.3.1}$$

where $\kappa^* = k^*/\rho^* c^*$ is the thermal diffusivity (assumed constant in each region). We impose continuity of temperature and thermal flux at material boundaries, that is,

$$[T^*]_-^+ = [k^* \boldsymbol{\nabla}^* T^* \cdot \boldsymbol{n}]_-^+ = 0. \tag{4.3.2}$$

We consider the bottom of the substrate to be cooled to some given temperature profile that may vary spatially,

$$T^* = T^{-*}(r^*) \quad \text{at} \quad y^* = -h^{\mathrm{s}*}. \tag{4.3.3}$$

At the liquid–vacuum free surface the continuity condition for thermal flux is

$$k^* \boldsymbol{\nabla}^* T^* \cdot \boldsymbol{n} = \mathscr{C}^*(r^*, t^*) \quad \text{at} \quad y^* = h^*, \tag{4.3.4}$$

where $\mathscr{C}^*$ is the thermal load the plasma imparts to the fluid, which varies along the free-surface. Some initial condition must also be imposed for T^* at $t^* = 0$.

4.3.1 Non-dimensionalisation

We non-dimensionalise with the scalings in (4.1.14), and scale the temperature via

$$T^* = T^{-*}(r_0^*) + (\Delta T^*)\, T, \tag{4.3.5}$$

where ΔT^* is a characteristic temperature jump in the range $\lfloor 1,\ 5 \rceil \times 10^2\,\mathrm{K}$. In practice, the operating temperature is constrained significantly below the boiling point as the sputtering yield increases with temperature [6, 7] (see also [213] exploring the dependence on angle of incidence). The dimensionless cooling profile is denoted

$$T^-(r) = C\frac{T^{-*}(r^*) - T^{-*}(r_0^*)}{\Delta T^*}, \tag{4.3.6}$$

where C is a dimensionless constant we will define shortly.

In the fluid region of our assumed axisymmetric conical geometry, $0 < y < h$, the heat equation (4.3.1) takes the dimensionless form

$$\epsilon^2 \mathrm{Pe}\frac{\partial T}{\partial t} + \epsilon^2 \mathrm{Pe}\left(u\frac{\partial T}{\partial r} + v\frac{\partial T}{\partial y}\right) = \frac{\epsilon^2}{R}\frac{\partial}{\partial r}\left(R\frac{\partial T}{\partial r}\right) + \frac{1}{R}\frac{\partial}{\partial y}\left(R\frac{\partial T}{\partial y}\right), \tag{4.3.7a}$$

while in the substrate, $-h^{\mathrm{s}} < y < 0$ the dimensionless form is

$$\epsilon^2 \mathrm{Pe}\frac{\kappa^*}{\kappa^{\mathrm{s}*}}\frac{\partial T^{\mathrm{s}}}{\partial t} = \frac{\epsilon^2}{R}\frac{\partial}{\partial r}\left(R\frac{\partial T^{\mathrm{s}}}{\partial r}\right) + \frac{1}{R}\frac{\partial}{\partial y}\left(R\frac{\partial T^{\mathrm{s}}}{\partial y}\right), \tag{4.3.7b}$$

where Pe denotes the Peclét number, defined in table 2.4. The dimensionless boundary conditions are

$$\frac{\partial T}{\partial y} - \epsilon^2\frac{\partial h}{\partial r}\frac{\partial T}{\partial r} = C\mathfrak{p}(r,t)\sqrt{1+\epsilon^2\left(\frac{\partial h}{\partial r}\right)^2} \qquad \text{at} \quad y = h, \tag{4.3.8a}$$

$$T - T^{\mathrm{s}} = \frac{\partial T}{\partial y} - \frac{k^{*\mathrm{s}}}{k^*}\frac{\partial T^{\mathrm{s}}}{\partial y} = 0 \qquad \text{at} \quad y = 0, \tag{4.3.8b}$$

$$T^{\mathrm{s}} = CT^- \qquad \text{at} \quad y = -h^{\mathrm{s}}, \tag{4.3.8c}$$

where $C\mathfrak{p}$ is the dimensionless thermal load of the core plasma on the divertor, C being the magnitude, given by

$$C = \frac{\mathscr{C}^*\mathscr{H}^*}{k^*\Delta T^*} \approx 1, \tag{4.3.8d}$$

using values from tables 2.1 and 2.2, and $\mathfrak{p}(r,t)$ denoting the spatial- and temporal-dependence of the thermal flux density.

We now proceed to neglect small terms to produce a leading-order model. In the first instance, we consider the asymptotic limit in which $\epsilon^2\mathrm{Pe}$ is negligible and $\kappa^*/\kappa^{\mathrm{s}*} = \mathcal{O}(1)$ as $\epsilon \to 0$. In § 5.6 we will revisit the magnitude of $\kappa^*/\kappa^{\mathrm{s}*}$ and argue that time-dependence may be important in the substrate, justifying the distinguished limit in which $\kappa^*/\kappa^{s*} = \mathcal{O}(1/\epsilon)$.

4.3.2 Leading-order thermal model

We now consider the leading-order thermal model in the limit as $\epsilon \to 0$. We neglect terms of order ϵ and $\epsilon^2\mathrm{Pe}$, and consider the distinguished limit where k^{s*}/k^*, κ^*/κ^{s*}, and C are all $\mathcal{O}(1)$, while $\theta = \mathcal{O}(\epsilon)$ as $\epsilon \to 0$. The leading-order thermal model (4.3.7) and (4.3.8) then decouples from the flow equations, taking the form

$$\frac{\partial^2 T_0}{\partial y^2} = 0, \qquad \text{where } \ 0 < y < h_0, \tag{4.3.9a}$$
$$\frac{\partial^2 T_0^s}{\partial y^2} = 0, \qquad \text{where } \ -h^s < y < 0, \tag{4.3.9b}$$

subject to

$$\frac{\partial T_0}{\partial y} = C\mathfrak{p}(r,t) \qquad \text{at } \ y = h_0, \tag{4.3.9c}$$
$$T_0 - T_0^s = \frac{\partial T_0}{\partial y} - \frac{k^{s*}}{k^*}\frac{\partial T_0^s}{\partial y} = 0 \qquad \text{at } \ y = 0, \tag{4.3.9d}$$
$$T_0^s = CT^- \qquad \text{at } \ y = -h^s. \tag{4.3.9e}$$

The system (4.3.9) is solved by

$$T_0 = C\mathfrak{p}(r,t)\left(y + \frac{h^s k^*}{k^{s*}}\right) + CT^-(r), \tag{4.3.10a}$$
$$T_0^s = \frac{k^*}{k^{s*}}C\mathfrak{p}(r,t)\,(y + h^s) + CT^-(r). \tag{4.3.10b}$$

Armed with the leading-order temperature profiles (4.3.10), we now return to the flow and magnetic problem.

4.3.3 Flow and magnetic model

We now impose the known temperature field (4.3.10) to incorporate the thermoelectric and thermocapillary effects in a leading-order thin-film model. The problem is nearly identical to the isothermal system (4.1.7–13), with only the modification of two boundary conditions: the influence of the Seebeck effect at the fluid–substrate boundary $y^* = 0$, whereby boundary condition (4.1.12e) becomes

$$\frac{\partial B^{i*}}{\partial y^*} = \frac{1+\chi}{1+\chi^{s}} \frac{\sigma^*}{\sigma^{s*}} \frac{\partial B^{is*}}{\partial y^*} + \frac{R^*}{\eta^*} \frac{\partial T^*}{\partial r^*} \left[S^*\right]_-^+ , \tag{4.3.11}$$

and the addition of thermocapillarity terms at the free surface $y^* = h^*$ in boundary condition (4.1.11f) which now reads

$$\begin{aligned} 0 = \rho^* \nu^* &\left\{ \left(\left(\frac{\partial h^*}{\partial r^*} \right)^2 - 1 \right) \left(\frac{\partial u^*}{\partial y^*} + \frac{\partial v^*}{\partial r^*} \right) - 2 \left(\frac{\partial v^*}{\partial y^*} - \frac{\partial u^*}{\partial r^*} \right) \frac{\partial h^*}{\partial r^*} \right\} \\ &+ \frac{\mathrm{d}\gamma^*}{\mathrm{d}T^*} \left(\frac{\partial T^*}{\partial r^*} + \frac{\partial h^*}{\partial r^*} \frac{\partial T^*}{\partial y^*} \right) \sqrt{1 + \left(\frac{\partial h^*}{\partial r^*} \right)^2}. \end{aligned} \tag{4.3.12}$$

Non-dimensionalising via (4.1.14) and (4.3.5), the leading-order system is identical to its isothermal counterpart (4.1.28–30), except for the modification of these two boundary conditions.

Firstly, in deriving the effective boundary condition (4.1.27), the Seebeck contribution appears, and the effective boundary condition (4.1.30a) becomes

$$a B_0^{i} = \frac{\partial B_0^{i}}{\partial y} - r \cos\theta \, \frac{\mathcal{S}}{\Xi} \frac{\partial T_0}{\partial r} \quad \text{at} \ \ y = 0, \tag{4.3.13}$$

where $\mathcal{S}$ is a dimensionless constant expressing the relative magnitude of current density induced by the Seebeck effect versus electromagnetic induction, given by

$$\mathcal{S} = \frac{\Delta T^* (S^* - S^{s*})}{\mathscr{B}^* \mathscr{U}^* \mathscr{L}^*}. \tag{4.3.14}$$

Secondly, the free-surface shear condition (4.1.29d) now has a thermocapillarity contribution and takes the form

$$\frac{\partial u_0}{\partial y} = -\mathcal{T} \left(\frac{\partial T_0}{\partial r} + \frac{\partial h_0}{\partial r} \frac{\partial T_0}{\partial y} \right) \quad \text{at} \ \ y = h_0, \tag{4.3.15}$$

where $\mathcal{T}$ is a dimensionless quantity measuring the surface tension gradient relative to the viscous stress, given by

$$\mathcal{T} = \frac{\epsilon \Delta T^*}{\rho^* \nu^* \mathscr{U}^*} \left(- \frac{\mathrm{d}\gamma^*}{\mathrm{d}T^*} \right), \tag{4.3.16}$$

and we assume that the surface tension gradient $\mathrm{d}\gamma^*/\mathrm{d}T^*$ is a constant. There is no additional complexity in the more general case of temperature-dependent surface tension gradients, however, for liquid lithium [37] this term is well approximated by a constant $\mathrm{d}\gamma^*/\mathrm{d}T \approx -10^{-4}\,\mathrm{N/m\,K}$. The quantity $\mathcal{T}$ may be expressed $\mathcal{T} = \mathrm{Ma}/\mathrm{Pe}$, where the Marangoni number is given by

$$\mathrm{Ma} = \frac{\Delta T^* \mathscr{H}^*}{\rho^* \nu^* \kappa^*}\left(-\frac{\mathrm{d}\gamma^*}{\mathrm{d}T^*}\right), \tag{4.3.17}$$

and represents the relative magnitude of thermocapillary flow versus thermal diffusion.

Using (4.1.15) along with tables 2.1 to 2.3 we find that $\mathcal{S}$ may be as large as 10, and $\mathcal{T}$ may be as large as 100. We therefore retain both of these additional contributions at leading order, in the distinguished limit in which $\mathcal{S} = \mathcal{O}(1)$ and $\mathcal{T} = \mathcal{O}(1)$ as $\epsilon \to 0$.

The thermal leading-order system, comprising the isothermal leading-order system (4.1.28–30) with the two modified boundary conditions (4.3.13) and (4.3.15), possesses three inhomogeneous forcing terms: gravitational, thermoelectric, and thermocapillary. By linearity, the solution may be decomposed into the sum of three solutions, each forced by a single inhomogeneity. The component driven by gravity and pressure is identical to that studied in §4.1.6, while the two new components will be denoted with subscripts $\mathcal{S}$ and $\mathcal{T}$, representing the Seebeck and thermocapillary driving forces, respectively.

With the same arguments as in §4.1.6, the leading-order system for both thermal inhomogeneities may be reduced to a system of equations governing the downstream flow and induced toroidal magnetic field. In the thermoelectrically-driven case, we normalise by employing the scalings

$$u_0 = \frac{2\,\Xi\,\mathcal{S}C}{\Lambda^3\,\mathrm{Ha}\,r^2\cos\theta}\frac{\partial}{\partial r}\left[p\frac{h^{\mathrm{s}}k^*}{k^{\mathrm{s}*}} + T^-\right]u_{\mathcal{S}}, \tag{4.3.18a}$$

$$B_0^{\mathrm{i}} = \frac{\mathcal{S}Cr\cos\theta}{\Lambda\,\mathrm{Ha}\,\Xi}\frac{\partial}{\partial r}\left[p\frac{h^{\mathrm{s}}k^*}{k^{\mathrm{s}*}} + T^-\right]B_{\mathcal{S}}^{\mathrm{i}}, \tag{4.3.18b}$$

whereupon the system (4.1.28–30) with the modified boundary condition (4.3.13) takes the form

$$\Upsilon^2 u_{\mathcal{S}} - B_{\mathcal{S}}^{\mathrm{i}} + \frac{\partial^2 B_{\mathcal{S}}^{\mathrm{i}}}{\partial Y^2} = \frac{\partial^2 u_{\mathcal{S}}}{\partial Y^2} - u_{\mathcal{S}} - B_{\mathcal{S}}^{\mathrm{i}} = 0, \tag{4.3.19a}$$

$$B_{\mathcal{S}}^{\mathrm{i}}(H) = \frac{\partial u_{\mathcal{S}}}{\partial Y}(H) = 0, \tag{4.3.19b}$$

$$\alpha B_{\mathcal{S}}^{\mathrm{i}}(0) - \frac{\partial B_{\mathcal{S}}^{\mathrm{i}}}{\partial Y}(0) + 1 = u_{\mathcal{S}}(0) = 0. \tag{4.3.19c}$$

In the thermocapillarity-driven case, we use the scalings

$$u_0 = -\frac{\mathcal{T}C}{\Lambda\,\mathrm{Ha}}\frac{\partial}{\partial r}\left[p\left(h_0 + \frac{h^{\mathrm{s}}k^*}{k^{\mathrm{s}*}}\right) + T^-\right] u_{\mathcal{T}}, \tag{4.3.20a}$$

$$B_0^{\mathrm{i}} = -\frac{\mathcal{T}C\Lambda r^3\cos^2\theta}{2\,\Xi^2\,\mathrm{Ha}}\frac{\partial}{\partial r}\left[p\left(h_0 + \frac{h^{\mathrm{s}}k^*}{k^{\mathrm{s}*}}\right) + T^-\right] B_{\mathcal{T}}^{\mathrm{i}}, \tag{4.3.20b}$$

whereupon the system (4.1.28–30) with the two modified boundary condition (4.3.15) takes the normalised form

$$\Upsilon^2 u_{\mathcal{T}} - B_{\mathcal{T}}^{\mathrm{i}} + \frac{\partial^2 B_{\mathcal{T}}^{\mathrm{i}}}{\partial Y^2} = \frac{\partial^2 u_{\mathcal{T}}}{\partial Y^2} - u_{\mathcal{T}} - B_{\mathcal{T}}^{\mathrm{i}} = 0, \tag{4.3.21a}$$

$$B_{\mathcal{T}}^{\mathrm{i}}(H) = \frac{\partial u_{\mathcal{T}}}{\partial Y}(H) - 1 = 0, \tag{4.3.21b}$$

$$\alpha B_{\mathcal{T}}^{\mathrm{i}}(0) - \frac{\partial B_{\mathcal{T}}^{\mathrm{i}}}{\partial Y}(0) = u_{\mathcal{T}}(0) = 0. \tag{4.3.21c}$$

The systems (4.3.19) and (4.3.21) are of the same form as the gravity-driven system (4.1.39). The only difference is the inhomogeneity that appears in the momentum equation in the gravity-driven case, at the substrate boundary in the thermoelectric case (4.3.19c), and at the free-surface in the thermocapillarity-driven case (4.3.21b). This inhomogeneity is what drives the solution, and we will see that, when the MHD forces flatten the velocity and field profiles, variation is relegated to boundary layers in the vicinity of the inhomogeneity.

Explicit solutions of systems (4.3.19) and (4.3.21) are shown in appendix A.5. In the next two sections we analyse how solutions vary with the free parameters.

4.4 Thermoelectrically-driven system

In this section we analyse solutions of the thermoelectrically-driven system (4.3.19), varying the only three free parameters: Υ, α, and H.

First, we consider the effects of varying Υ as illustrated in figure 4.5. As Υ increases the downstream flow and toroidal induced field diminish, their variations being squeezed into a region near the substrate. To gain further analytical insight into the underlying flow and induced field, we solve the system in various asymptotic limits by means of matched asymptotic expansions. In the limit $\Upsilon \to 0$, we take asymptotic expansions (recycling earlier notation) of the form

$$u_{\mathcal{S}} \sim u_0 + \cdots\,, \qquad B_{\mathcal{S}}^{\mathrm{i}} \sim B_0^{\mathrm{i}} + \cdots\,. \tag{4.4.1a,b}$$

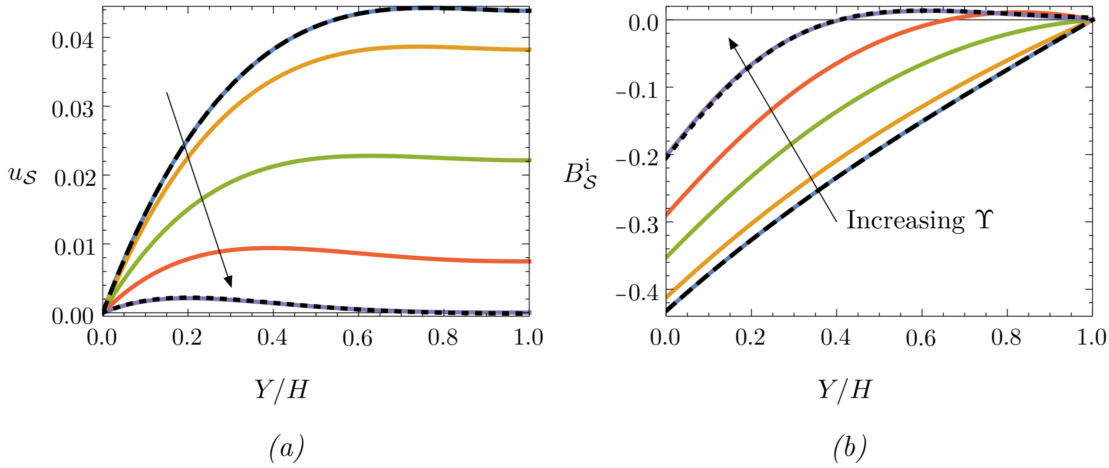

Figure 4.5: Normalised flow and field profiles where $\alpha = H = 1$, and $\Upsilon \in \{0, 2, 5, 10, 30\}$. The black dashed curve is the asymptotic approximation for $\Upsilon \ll 1$ given by (4.4.2). The black dotted curve is the composite asymptotic expansion for the case $\Upsilon \gg 1$ given by (4.4.5).

Field	**Feature**	**Formula**	**In figure 4.5**
$u_{\mathcal{S}}$	Maximum location	$Y = \pi/\left(2\sqrt{2\Upsilon}\right)$	≈ 0.2028
	Maximum	$\sqrt{2}\left[\Upsilon \mathrm{e}^{\pi/4}\left(\sqrt{2\Upsilon} + 2\alpha\right)\right]^{-1}$	≈ 0.0022
$B^{\mathrm{i}}_{\mathcal{S}}$	Minimum (at substrate)	$-2\left(\sqrt{2\Upsilon} + 2\alpha\right)^{-1}$	≈ -0.2052
	Sign change location	$Y = \pi/\sqrt{2\Upsilon}$	≈ 0.4056
	Maximum location	$Y = 3\pi/\left(2\sqrt{2\Upsilon}\right)$	≈ 0.6084
	Maximum	$\sqrt{2}\left[\mathrm{e}^{3\pi/4}\left(\sqrt{2\Upsilon} + 2\alpha\right)\right]^{-1}$	≈ 0.0138

Table 4.1: Features of the thermoelectric system (4.3.19) in the asymptotic limit $\Upsilon \gg 1$ deduced from the leading-order approximation (4.4.5). Numerical approximations are given after substituting the parameter values $\alpha = H = 1$ and $\Upsilon = 30$ as used in figure 4.5.

The induced field decouples from the flow, to leading order, and is given by

$$B^{\mathrm{i}}_0 = -\frac{\sinh(H - Y)}{\cosh H + \alpha \sinh H}. \tag{4.4.2a}$$

The leading-order downstream flow is then given by

$$u_0 = \frac{Y \cosh Y - \sinh Y \left(\operatorname{sech}^2 H + Y \tanh H\right)}{2 + 2\alpha \tanh H}. \tag{4.4.2b}$$

The approximation (4.4.2) agrees well with the full solution illustrated in figure 4.5.

The boundary layer analysis uncovers interesting flow features: the downstream flow profile is neither monotonic, as in poloidal case of Hartmann flow, nor oscillatory, as in the toroidal case.

In the limit as $\Upsilon \to \infty$, the flow and induced field are zero to all orders in the bulk. This outer solution does not satisfy the inhomogeneous boundary condition (4.3.19c), reflecting the fact that there is boundary layer near the substrate. This layer has width $\mathcal{O}(1/\sqrt{\Upsilon})$, and is revealed by scaling the vertical coordinate via

$$Y = \frac{\mathcal{Y}}{\sqrt{\Upsilon}}, \tag{4.4.3}$$

and considering an inner solution of the form

$$u_{\mathcal{S}} \sim \Upsilon^{-3/2} U_{\mathcal{S}} + \cdots, \qquad B^{\mathrm{i}}_{\mathcal{S}} \sim \Upsilon^{-1/2} b_{\mathcal{S}} + \cdots. \tag{4.4.4a,b}$$

We maintain the parameter α at leading order by considering the distinguished limit where $\alpha \sim \sqrt{\Upsilon}$. Matching with the zero outer solution, we find that the inner solution is given by

$$U_{\mathcal{S}} = \frac{2\mathrm{e}^{-\mathcal{Y}/\sqrt{2}} \sin(\mathcal{Y}/\sqrt{2})}{\sqrt{2} + 2\alpha/\sqrt{\Upsilon}}, \qquad b_{\mathcal{S}} = -\frac{2\mathrm{e}^{-\mathcal{Y}/\sqrt{2}} \cos(\mathcal{Y}/\sqrt{2})}{\sqrt{2} + 2\alpha/\sqrt{\Upsilon}}. \tag{4.4.5a,b}$$

Boundary layer solution (4.4.5) agrees closely with the full solution, as illustrated in figure 4.5. The boundary layer analysis exposes oscillatory profiles in the fluid velocity and induced field, as well as the scaling laws $u_{\mathcal{S}} \sim \Upsilon^{-1/2}$ and $B^{\mathrm{i}}_{\mathcal{S}} \sim \Upsilon^{-3/2}$. The outer solution is exponentially small, and (4.4.5) is therefore uniformly valid; the agreement with the full solution is good for all Y. Furthermore, the approximation (4.4.5) reveals much of the structure of the flow and the induced field, allowing us to find closed-form expressions of several interesting features, some of which are tabulated in table 4.1.

Next we consider the effect of varying the parameter α, which represents the transition from a perfectly conducting substrate ($\alpha = 0$) to a perfectly insulating substrate ($\alpha = \infty$). As illustrated in figure 4.6, the change manifests in the boundary condition for B^{i}_0, which drives the whole system. As the substrate becomes more insulating, the Seebeck effect becomes less effective in driving a downstream current. This means that the toroidal field and downstream flow are commensurably weaker. Quantitatively, from (4.3.19c) we expect both of the fields to be of

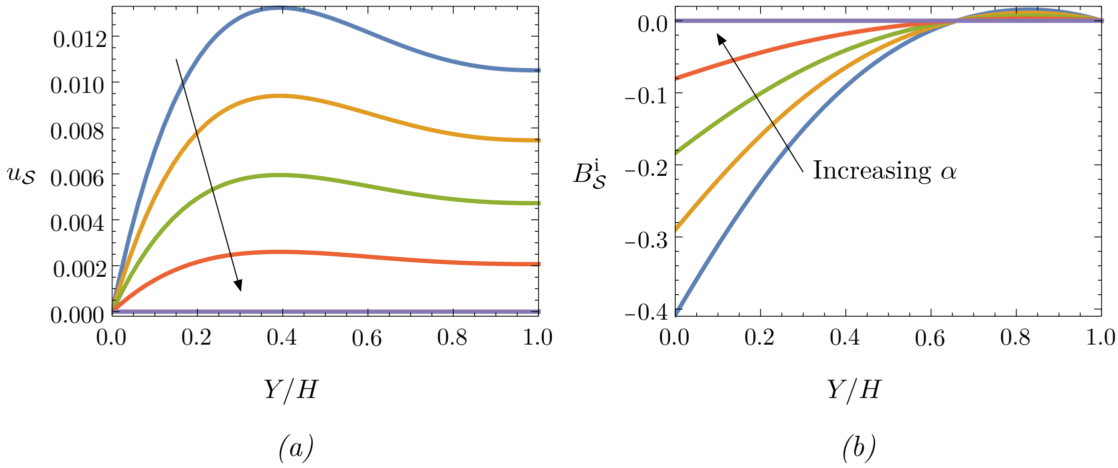

Figure 4.6: Normalised flow and field profiles where $\Upsilon = 10$, $H = 1$, and $\alpha \in \{0, 1, 3, 10, \infty\}$.

order $\mathcal{O}(1/\alpha)$ when $\alpha \gg 1$.

Finally, we explore the effect of varying H, as illustrated in figure 4.7. For small H we observe diminishing flow velocities and the induced field strengths. As H increases, both the downstream flow and induced field become stronger, until approximately $H = \mathcal{O}(1)$, at which point, for increasing H the flow and induced field in the bulk tend to zero, while boundary layers near the substrate contain all their variation. This non-monotonicity is a manifestation of the typical low-field and high-field behaviour in MHD-induced flow and fields.

To obtain more analytical insight into the behaviour at extreme values of H, we scale

$$Y = \mathcal{Y}H. \tag{4.4.6}$$

In the limit $H \to 0$ we expand the velocity and induced field asymptotically via

$$u_{\mathcal{S}} \sim H^3 u_0, \qquad B^{\mathrm{i}}_{\mathcal{S}} \sim H B^{\mathrm{i}}_0, \tag{4.4.7a,b}$$

to find that the leading-order system admits the solution

$$u_0 = \frac{\mathcal{Y}^3 - 3\mathcal{Y}^2 + 3\mathcal{Y}}{6(1+\alpha)}, \qquad B^{\mathrm{i}}_0 = \frac{\mathcal{Y} - 1}{1+\alpha}. \tag{4.4.8a,b}$$

The leading-order solution (4.4.8) reveals interesting dependence on $\mathcal{Y}$: the induced field varies linearly, while the downstream velocity is cubic with respect to $\mathcal{Y}$. This behaviour contrasts with the typical quadratic flow profile expected of a very thin

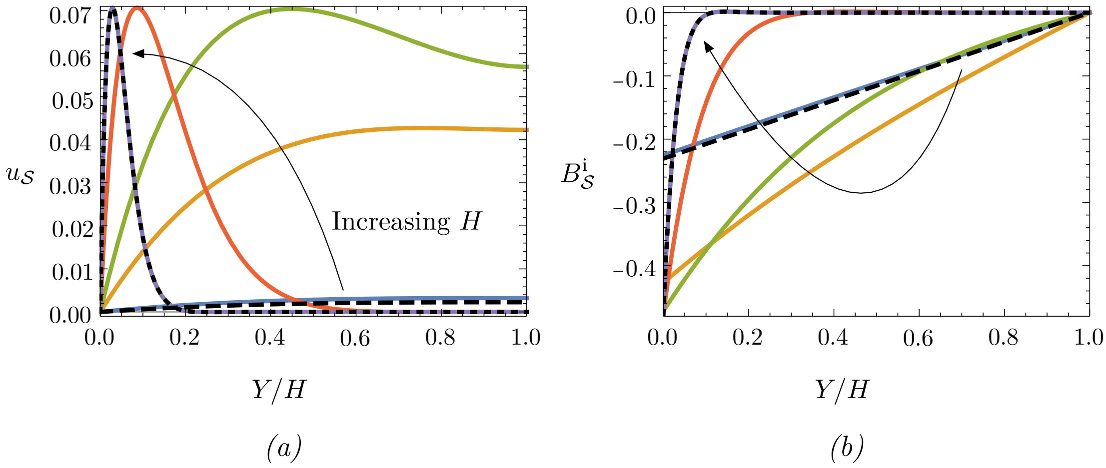

Figure 4.7: Normalised flow and field profiles where $\Upsilon = \alpha = 1$, and $H \in \{0.3, 1, 2, 10, 30\}$. The black dashed curve is the asymptotic approximation for $H \ll 1$ given by (4.4.8)*. The black dotted curve is the approximation for the case $H \gg 1$ given by* (4.4.9)*.*

viscous-dominated film.

In the singular limit $H \to \infty$, the outer solution vanishes to leading order, and there is a boundary layer at the substrate of width $\mathcal{O}(1/H)$ in $\mathcal{Y}$, in which the original equations are restored. Matching to zero in the far field, we find that the inner solution at the boundary layer is given by

$$u_{\mathcal{S}} \sim \frac{\mathrm{e}^{-M_+ Y} \sin(M_- Y)}{\Upsilon(\alpha + M_+)}, \qquad B^{\mathrm{i}}_{\mathcal{S}} \sim -\frac{\mathrm{e}^{-M_+ Y} \cos(M_- Y)}{\alpha + M_+}, \tag{4.4.9a,b}$$

where $M_\pm$ are defined in (4.1.62). Once more, the boundary layer analysis reveals interesting oscillations in the velocity and induced magnetic field profiles, reminiscent of the purely toroidal case. The closed-form approximation (4.4.9) provides leading-order estimates for the substrate induced field and maximum downstream velocity. We find that $B^{\mathrm{i}}_{\mathcal{S}}(0) \sim -1/(\alpha + M_+)$, and the velocity has a maximum at $Y = (1/M_-)\tan^{-1}(M_-/M_+)$. Setting $\Upsilon = \alpha = 1$ and $H = 30$ as in figure 4.7, we obtain $B^{\mathrm{i}}_{\mathcal{S}}(0) \approx -0.4765$ while the velocity obtains a maximum of $u_{\mathcal{S}} \approx 0.0707$ at $Y/H = (\pi/8H)\sqrt{2(\sqrt{2}+1)} \approx 0.0288$.

By analogy with the analysis at the end of § 4.1.7, we consider the variation with Ha while keeping all other parameters fixed. As before, assuming all other parameters are $\mathcal{O}(1)$, the normalised parameters scale like $\Upsilon \sim 1/\,\mathrm{Ha}$, $\alpha \sim 1/\,\mathrm{Ha}$, $H \sim \mathrm{Ha}$. We define the scaled downstream and toroidal fluid fluxes, $Q_{\mathcal{S}}/\,\mathrm{Ha}^3$ and

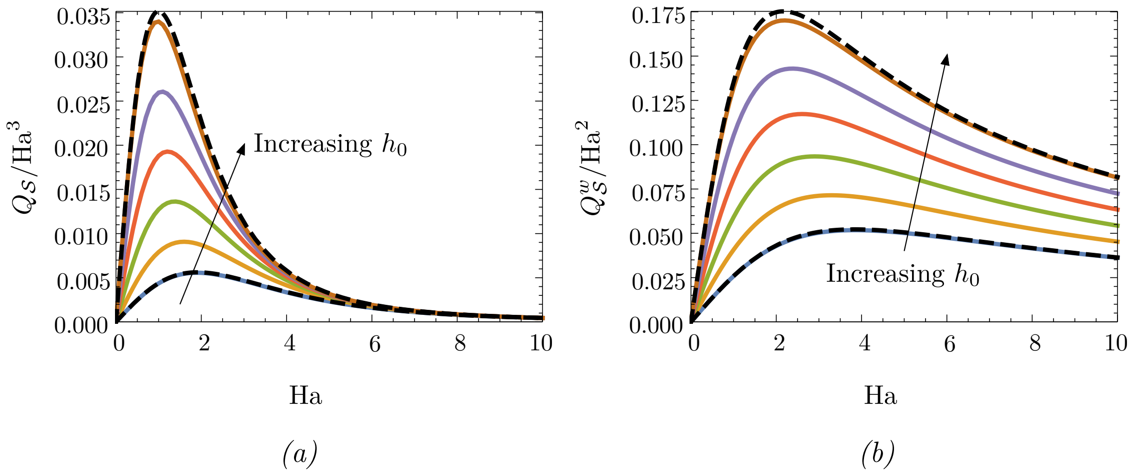

Figure 4.8: Scaled fluxes (4.4.10) *plotted as functions of the field strength via* Ha*, where* $\Upsilon = 1/\mathrm{Ha}$*,* $\alpha = 1/\mathrm{Ha}$*,* $H = \mathrm{Ha}\, h_0$*, and* $h_0 \in \{0.5, 0.6, 0.7, 0.8, 0.9, 1\}$*. The black dashed curves show the asymptotic approximations given in* (4.4.11)*.*

$Q^w_{\mathcal{S}}/\mathrm{Ha}^2$, respectively, where

$$Q_{\mathcal{S}} = \int_0^H u_{\mathcal{S}}\,\mathrm{d}Y, \qquad Q^w_{\mathcal{S}} = -\int_0^H (H-Y)B^{\mathrm{i}}_{\mathcal{S}}(Y)\,\mathrm{d}Y. \tag{4.4.10a,b}$$

As above, factors of $1/\mathrm{Ha}^3$ and $1/\mathrm{Ha}^2$ ensure that the scaled values are proportional to their dimensional counterparts when only the field strength $\mathscr{B}^*$ varies.

In figure 4.8 we plot the scaled flux as a function of field strength via Ha. The black dashed curves in figure 4.8 show the composite expansions derived by integrating (4.4.2), whereby

$$Q_{\mathcal{S}} \sim \frac{2\,\mathrm{sech}\,H\,\sinh^4(H/2)}{\cosh H + \alpha \sinh H}, \qquad Q^w_{\mathcal{S}} \sim \frac{H\coth H - 1}{\alpha + \coth H}. \tag{4.4.11a,b}$$

In figure 4.8 we observe that approximations (4.4.11) are uniformly valid over low- and high-field regimes, as they retain both viscous and magnetic contributions.

We further observe in figure 4.8 that both fluxes exhibit non-monotonic dependence on the field strength, and vanish as the applied field strength tends to zero. This is because in the thermoelectric case the current that drives the Seebeck effect and produces an induced field can only couple to produce both flow components in the presence of an applied field. As the applied field strength is increased from zero, these flows strengthen, until $\mathrm{Ha} = \mathcal{O}(1)$, at which point they begin to diminish for increasing Ha, as MHD drag decelerates them. The result is another manifestation of the flux non-monotonicity, as discussed in § 4.1.7. It is worth noting that the leading-order downstream flux $Q_{\mathcal{S}}$ in (4.4.11a) is monotonic with respect to H and bounded, with $Q_{\mathcal{S}} \sim H^4/8$ for $H \ll 1$, and $Q_{\mathcal{S}} \sim 1/(2+2\alpha)$ for $H \gg 1$. This is reminiscent of the bounded downstream flux in the purely toroidal case (see figure 2.11), albeit without the non-monotonic oscillations.

Having examined the thermoelectrically-driven component of the solution, we proceed to analyse the thermocapillarity-driven component.

4.5 Thermocapillarity-driven system

In this section we explore solutions of the thermocapillarity-driven system (4.3.21) while varying the three free parameters Υ, α, and H.

Beginning with variations in Υ, as shown in figure 4.9, we observe that for small values of Υ the downstream flow profile is predominantly flat and of order unity, while the toroidal induced field is very small. As Υ increases, the downstream flow vanishes in the bulk with a small shear-driven boundary layer near the free surface, while the induced magnetic field increases in magnitude until a point where it diminishes in the bulk, and all variation is relegated to a boundary layer near the free surface. Despite the net flux being positive, the fluid is actually flowing backwards throughout most of the fluid depth.

We proceed to find asymptotic approximations of the solutions, first in the limit as $\Upsilon \to 0$ by taking the asymptotic expansions

$$u_{\mathcal{T}} \sim u_0 + \cdots , \qquad B^{\mathrm{i}}_{\mathcal{T}} \sim \Upsilon^2 B^{\mathrm{i}}_0 + \cdots . \tag{4.5.1a,b}$$

The leading-order solution is found to be given by

$$u_0 = \frac{\sinh Y}{\cosh H}, \quad B^{\mathrm{i}}_0 = \frac{(1+\alpha H)\sinh Y + [H - Y - (1+\alpha Y)\tanh H]\cosh Y}{2\cosh H + 2\alpha \sinh H}, \tag{4.5.2a,b}$$

which captures the full solution accurately, as seen in figure 4.9. The asymptotic analysis reveal that, even in this limit, as the toroidal coupling vanishes, the MHD effects exerted by the poloidal field still add curvature to the downstream velocity flow profile, resulting in a sinh profile rather than a linear one, as encountered in classical hydrodynamic flow driven by surface shear.

Next, when $\Upsilon \to \infty$ both downstream flow and toroidal induced field vanish

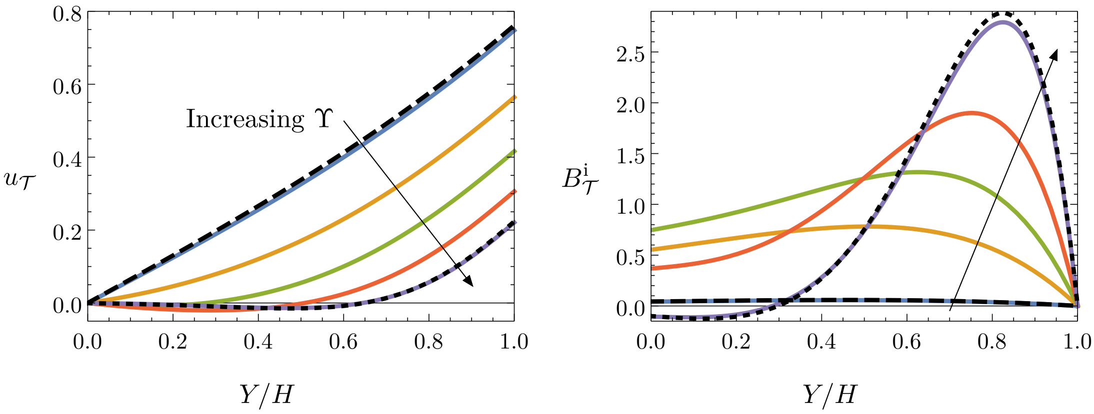

(a) *(b)*

Figure 4.9: Normalised flow and field profiles where $\alpha = H = 1$, and $\Upsilon \in \{1, 5, 10, 20, 40\}$. The black dashed curve is the asymptotic approximation for $\Upsilon \ll 1$ given by (4.5.2). The black dotted curve is the composite asymptotic expansion for the case $\Upsilon \gg 1$ given by (4.5.5).

Field	**Feature**	**Formula**	**In figure 4.9**
$u_{\mathcal{T}}$	Minimum location	$Y = H - 3\pi/\left(2\sqrt{2\Upsilon}\right)$	≈ 0.4731
	Minimum	$-\mathrm{e}^{-3\pi/4}/\sqrt{\Upsilon}$	≈ -0.0150
	Sign change location	$Y = H - \pi/\sqrt{2\Upsilon}$	≈ 0.6488
	Maximum (at free surface)	$\sqrt{2/\Upsilon}$	≈ 0.2236
$B^{\mathrm{i}}_{\mathcal{T}}$	Sign change location	$Y = H - \pi\sqrt{2}/\sqrt{\Upsilon}$	≈ 0.2975
	Maximum location	$Y = H - \pi/\left(2\sqrt{2\Upsilon}\right)$	≈ 0.8244
	Maximum	$\mathrm{e}^{-\pi/4}\sqrt{\Upsilon}$	≈ 2.8836

Table 4.2: Features of the thermocapillary system (4.3.21) in the asymptotic limit $\Upsilon \gg 1$ deduced from the leading-order approximation (4.5.5). Numerical approximations are given after substituting the parameter values $\alpha = H = 1$ and $\Upsilon = 40$ as used in figure 4.9.

in bulk to leading-order, with all variation occurring in a boundary layer of width $\mathcal{O}(1/\sqrt{\Upsilon})$ driven by the inhomogeneity at free surface. We study this layer via the scaling

$$Y = H - \frac{\mathcal{Y}}{\sqrt{\Upsilon}}, \tag{4.5.3}$$

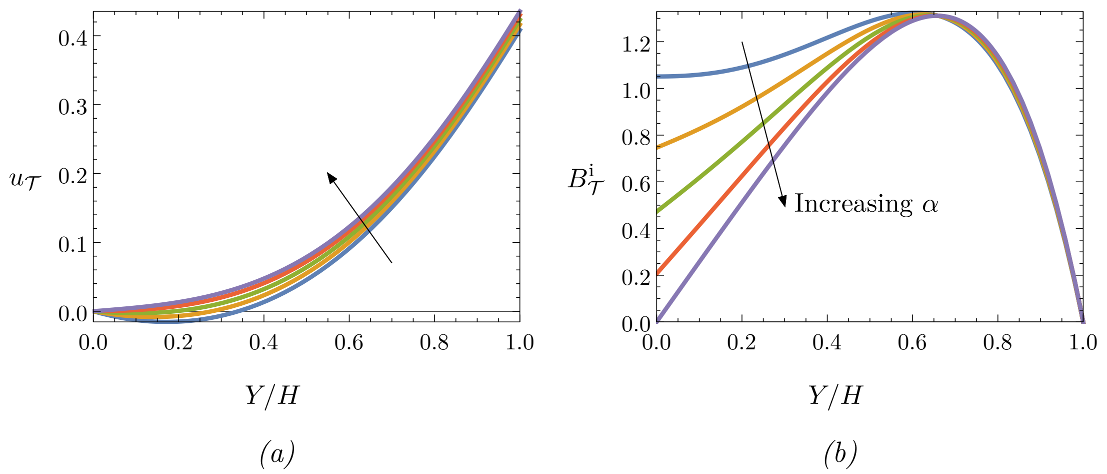

Figure 4.10: Normalised flow and field profiles where $\Upsilon = 10$, $H = 1$, and $\alpha \in \{0, 1, 3, 10, \infty\}$.

and inner expansions of the form

$$u_\mathcal{T} \sim \frac{1}{\sqrt{\Upsilon}} U_\infty + \cdots , \qquad B^{\mathrm{i}}_\mathcal{T} \sim \sqrt{\Upsilon}\, b_\infty + \cdots . \tag{4.5.4a,b}$$

Matching with zero in the bulk, we find that the leading-order inner solution is given by

$$U_\infty = \sqrt{2}\mathrm{e}^{-\mathcal{Y}/\sqrt{2}} \cos\left(\mathcal{Y}/\sqrt{2}\right), \qquad b_\infty = \sqrt{2}\mathrm{e}^{-\mathcal{Y}/\sqrt{2}} \sin\left(\mathcal{Y}/\sqrt{2}\right). \tag{4.5.5a,b}$$

The boundary layer analysis uncovers the familiar oscillations, and, being uniformly valid in Y, is accurate in capturing the behaviour of the full solution, as shown in figure 4.9. The approximation (4.5.5) further predicts several key features of the flow and induced field profiles, and how they scale with system parameters, some of which we tabulate in table 4.2.

Next, we observe how variations in α affect the solution in figure 4.10. As in the gravity-driven and thermoelectrically-driven cases of §§ 4.1.7 and 4.4, respectively, we find that the variation changes the substrate boundary condition of the induced toroidal field, however, the influence on the downstream flow is rather weak. Despite the change being rather small its predominant effect is to change the downstream shear at the substrate which may be close to zero. Since the no-slip condition requires zero velocity at the substrate boundary, the changes in the induced field can change the sign of the shear, and thus may induce negative velocities in the vicinity of the substrate for sufficiently small α.

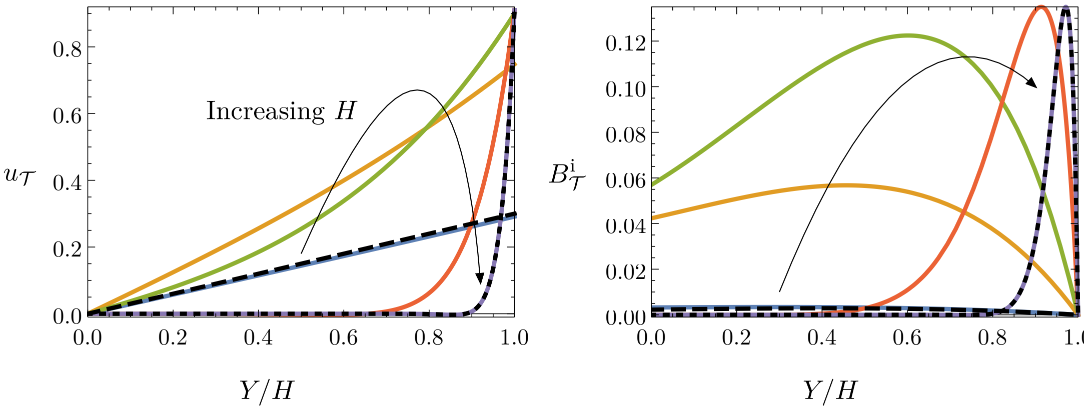

(a) *(b)*

Figure 4.11: Normalised flow and field profiles where $\Upsilon = \alpha = 1$, and $H \in \{0.5, 1, 2, 10, 30\}$. The black dashed curve is the asymptotic approximation for $H \ll 1$ given by (4.5.8). The black dotted curve is the composite asymptotic expansion for the case $H \gg 1$ composing the inner and outer solutions in (4.5.9).

Next, we illustrate how the solution varies with changes in the value of H in figure 4.11. There is a striking similarity between the profiles in this case, figure 4.11(a) and figure 4.11(b), and the profiles in the thermoelectrically-driven case, figure 4.7(b) and figure 4.7(a), respectively. The roles of the velocity and induced field are reversed, and similarly the location of the inhomogeneity driving the system switches from the substrate to the free surface. This similarity is a reflection of the duality in the underlying equations (4.3.19) and (4.3.21) when $\Upsilon = 1$. Small discrepancies stem from the fact that $\alpha \neq 0$ in these calculations, and thus the boundary conditions for the velocity and induced field are not exactly interchangeable.

Just as in §4.4, we explore the limits of small and large H by scaling the vertical coordinate via

$$Y = \mathcal{Y}H. \tag{4.5.6}$$

In the limit as $H \to 0$, we take the asymptotic expansions of the form

$$u_{\mathcal{T}} \sim H u_0 + \cdots, \qquad B^{\mathrm{i}}_{\mathcal{T}} \sim H^3 B^{\mathrm{i}}_0 + \cdots. \tag{4.5.7a,b}$$

It then follows that the leading order solution is given by

$$u_0 = Y, \qquad B_0^{\mathrm{i}} = \frac{\Upsilon^2\left[1+\alpha Y - Y^3(1+\alpha)\right]}{6(1+\alpha)}. \tag{4.5.8a,b}$$

This limit recovers a linear downstream velocity profile, typical of classical hydrodynamic flow driven by surface shear. Alongside this, the induced field exhibits interesting cubic variation. The duality noted above is manifest in the linear dependence of u_0 on Y, and cubic dependence of B_0^{i} on Y (compared to the reverse dependence in the same limit of the thermoelectric case in (4.4.8)).

In the singular limit $H \to \infty$, the outer solution is zero in the bulk, and a boundary layer of width $\mathcal{O}(1/H)$ in $\mathcal{Y}$ is present near the free surface in which original equations are restored. Matching to the zero outer solution, the leading-order solution is given by

$$u_{\mathcal{T}} \sim \frac{\mathrm{e}^{-M_+(H-Y)}\cos(M_-(H-Y))}{M_+}, \qquad B_{\mathcal{T}}^{\mathrm{i}} \sim \frac{\Upsilon\mathrm{e}^{-M_+(H-Y)}\sin(M_-(H-Y))}{M_+}, \tag{4.5.9a,b}$$

where $M_\pm$ are defined in (4.1.62). These solutions agree well with the full solutions plotted in figure 4.11. The boundary layer analysis reveals the usual oscillations, and allows us to pin down the leading-order maximum downstream velocity at the free surface: $u_{\mathcal{T}}(H) \sim 1/M_+$. Moreover, we find that the peak in the leading-order induced field occurs at $Y/H = 1 - (1/M_- H)\tan^{-1}(M_+/M_-)$. For the values used in figure 4.11, $\Upsilon = 1$ and $H = 30$, the maximum downstream velocity is approximately $1/M_+ = \sqrt{2(\sqrt{2}-1)} \approx 0.9102$, the induced field has a maximum value of $B_{\mathcal{T}}^{\mathrm{i}} \sim 0.1350$ occurring at $Y/H = 1-(\pi/8H)\sqrt{2(\sqrt{2}+1)} \approx 0.9712$.

Finally, following the now familiar recipe, we consider the variation when varying Ha with all other parameters fixed, scaling $\Upsilon \sim 1/\mathrm{Ha}$, $\alpha \sim 1/\mathrm{Ha}$, $H \sim \mathrm{Ha}$. We define the scaled downstream and toroidal fluid fluxes, $Q_{\mathcal{T}}/\mathrm{Ha}^2$ and $Q_{\mathcal{T}}^w/\mathrm{Ha}$, respectively, where

$$Q_{\mathcal{T}} = \int_0^H u_{\mathcal{T}}\,\mathrm{d}Y, \qquad Q_{\mathcal{T}}^w = -\int_0^H (H-Y)B_{\mathcal{T}}^{\mathrm{i}}(Y)\,\mathrm{d}Y. \tag{4.5.10a,b}$$

The scaled fluxes are plotted in figure 4.12, where the black dashed curves in fig-

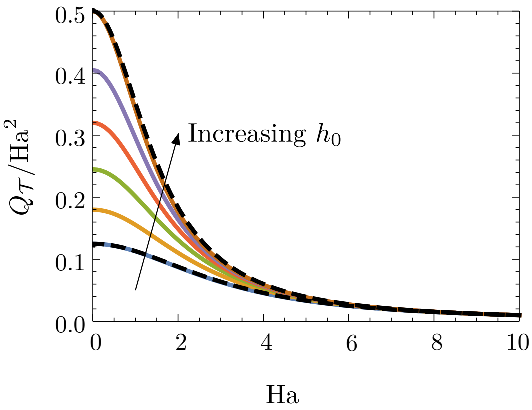

(a)

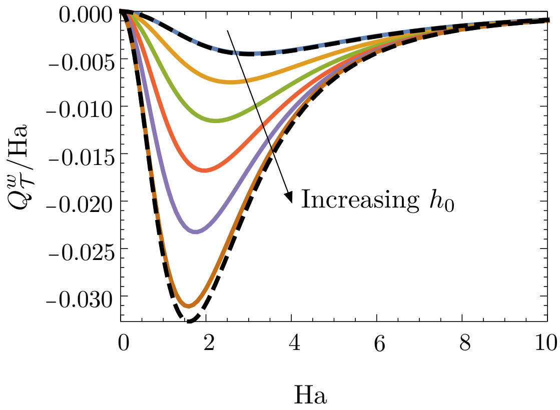

(b)

Figure 4.12: Scaled fluxes (4.5.10) *plotted as functions of the field strength via* Ha*, where* $\Upsilon = 1/\mathrm{Ha}$*,* $\alpha = 1/\mathrm{Ha}$*,* $H = \mathrm{Ha}\, h_0$*, and* $h_0 \in \{0.5, 0.6, 0.7, 0.8, 0.9, 1\}$*. The black dashed curves show the asymptotic approximations given in* (4.5.11)*.*

ure 4.12 show the composite expansions derived by integrating (4.4.2), namely

$$Q_\mathcal{T} \sim 1 - \operatorname{sech} H, \quad Q_\mathcal{T}^w \sim \Upsilon^2 \operatorname{sech} H \left(\frac{H(3 + H\alpha) - (1 - H\alpha)\tanh H}{2 + 2\alpha \tanh H} - \sinh H \right). \tag{4.5.11a,b}$$

Good agreement between the scaled fluxes and their approximations (4.5.11) reflects the uniform validity of the approximations. Similarly to the gravity-driven case, we observe in figure 4.12 monotonicity of the downstream flux, driven by thermocapillarity and decelerated by MHD, alongside the familiar non-monotonicity of the toroidal flux, being driven entirely by MHD forces. Just as in the thermoelectric case, in the limit as $\Upsilon \to 0$, the downstream flux $Q_\mathcal{T}$ in (4.5.11a) is monotonic with respect to H as well as bounded: $Q_\mathcal{T} \sim H^2/2$ when $H \ll 1$ while $Q_\mathcal{T} \sim 1$ when $H \gg 1$.

This concludes the analysis for the thermoelectrically-driven component of the system.

4.6 Combining the three components

In this penultimate section, we comment on the combination of the three components driven by gravity, the Seebeck effect, and thermocapillarity for realistic parameter values. Combining the scaled components (4.1.38), (4.3.18) and (4.3.20), we see that the downstream velocity and toroidal induced field are given by

$$u_0 = \frac{1}{\Lambda^2}\left(1 - \frac{\partial P}{\partial r}\right) u_{\mathcal{G}} + \frac{2\,\Xi\,\mathcal{S}C}{\Lambda^3\,\mathrm{Ha}\,r^2\cos\theta}\frac{\partial}{\partial r}\left[p\frac{h^{\mathrm{s}}k^*}{k^{\mathrm{s}*}} + T^-\right] u_{\mathcal{S}}$$
$$- \frac{\mathcal{T}C}{\Lambda\,\mathrm{Ha}}\frac{\partial}{\partial r}\left[p\left(h_0 + \frac{h^{\mathrm{s}}k^*}{k^{\mathrm{s}*}}\right) + T^-\right] u_{\mathcal{T}}, \tag{4.6.1}$$

$$B_0^{\mathrm{i}} = \frac{r^3\cos^2\theta}{2\,\Xi^2}\left(1 - \frac{\partial P}{\partial r}\right) B_{\mathcal{G}}^{\mathrm{i}} + \frac{\mathcal{S}Cr\cos\theta}{\Lambda\,\mathrm{Ha}\,\Xi}\frac{\partial}{\partial r}\left[p\frac{h^{\mathrm{s}}k^*}{k^{\mathrm{s}*}} + T^-\right] B_{\mathcal{S}}^{\mathrm{i}}$$
$$- \frac{\mathcal{T}C\Lambda r^3\cos^2\theta}{2\,\Xi^2\,\mathrm{Ha}}\frac{\partial}{\partial r}\left[p\left(h_0 + \frac{h^{\mathrm{s}}k^*}{k^{\mathrm{s}*}}\right) + T^-\right] B_{\mathcal{T}}^{\mathrm{i}}. \tag{4.6.2}$$

As will be done in chapters 5 and 6, we focus on the limit in which the toroidal applied field is of comparable magnitude to the poloidal field: $\Xi \ll 1$. When other parameters are $\mathcal{O}(1)$, it follows that $\Upsilon = \mathcal{O}(\Xi)$, and therefore we may leverage the previously studied asymptotic limit $\Upsilon \ll 1$. From the leading-order scalings (4.1.40) and (4.5.1) we see that $B_{\mathcal{G}}^{\mathrm{i}}$ and $B_{\mathcal{T}}^{\mathrm{i}}$ both scale with a factor of Υ^2 and therefore make $\mathcal{O}(1)$ contributions to the induced field B_0^{i}. On the other hand, from (4.4.1) we see that $B_{\mathcal{S}}^{\mathrm{i}} = \mathcal{O}(1)$, and therefore makes a dominant contribution of $\mathcal{O}(1/\,\Xi)$ (this is not in fact singular, as the non-dimensionalisation (4.1.14) incorporates a factor of Ξ). The induced field is therefore dominated by the thermoelectric contribution. Physically, this reflects the fact that, in the gravity- and thermocapillarity-driven cases the toroidal coupling drives the induced toroidal field, which is therefore weak in the limit where $\Xi \ll 1$, while it is the applied poloidal field that drives the induced toroidal field with the thermoelectric forcing.

The opposite is true of the downstream velocity, where the thermoelectric contribution is of order $\mathcal{O}(\Xi)$, and thus negligible compared with the dominant contributions of order $\mathcal{O}(1)$ from the gravity- and thermocapillarity-driven flows. The combined downstream flux will thus retain its monotonic dependence on Ha, as each component is monotonic. The ratio of the thermocapillary contribution to the gravity contribution is given by

$$\mathcal{R} = \frac{\dfrac{\mathcal{T}C\Lambda}{\mathrm{Ha}}\dfrac{\partial}{\partial r}\left[p\left(h_0 + \dfrac{h^{\mathrm{s}}k^*}{k^{\mathrm{s}*}}\right) + T^-\right]}{\left(1 - \dfrac{\partial P}{\partial r}\right)}. \tag{4.6.3}$$

From (4.3.16) we find that when varying the field strength (holding all other parameters fixed) $\mathcal{T} \sim \mathrm{Ha}^2$. We thus deduce from ratio (4.6.3) that, for increasing field

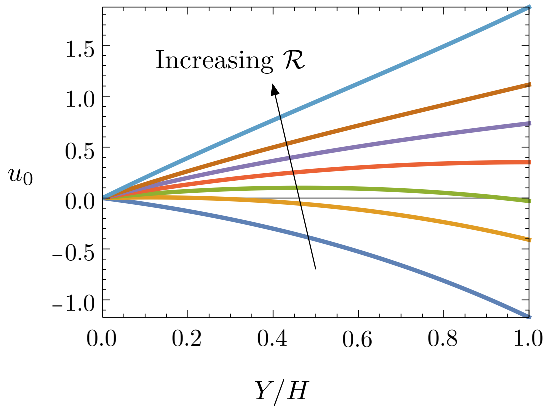

(a) $H = 1$.

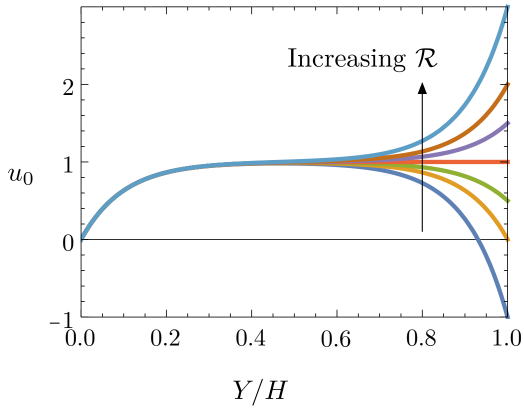

(b) $H = 10$.

Figure 4.13: Combined velocity profiles u_0 given by (4.6.4) for two values of the scaled film thickness H where $(1 - \partial P/\partial r)/\Lambda^2 = 1$ and $\mathcal{R} \in \{-2, -1, -0.5, 0, 0.5, 1, 2\}$.

strength, the thermocapillary contribution becomes more important. Physically, this is because the MHD drag causes the gravity-driven flow to scale with $1/\,\mathrm{Ha}^2$ while the thermocapillary flow scales with $1/\,\mathrm{Ha}$.

From the above discussion, we infer that the downstream velocity is dominated by the gravitational and thermocapillary contributions, and that the limit where $\Upsilon \ll 1$ is relevant for physically realistic parameters values. We therefore combine the leading-order approximations for $u_{\mathcal{G}}$ and $u_{\mathcal{T}}$, derived in the limit where $\Upsilon \ll 1$ and given by (4.1.41) and (4.5.2), respectively, to write the leading-order velocity as

$$u_0 \sim \frac{1}{\Lambda^2}\left(1 - \frac{\partial P}{\partial r}\right)\left[(1 - \cosh Y + \sinh Y \tanh H) - \mathcal{R}\frac{\sinh Y}{\cosh H}\right]. \tag{4.6.4}$$

Velocity profiles u_0 for various values of $\mathcal{R}$ and $H = \mathrm{Ha}\,\Lambda h_0$ are plotted in figure 4.13. Since $\mathcal{R}$ may take either sign, the thermocapillary flow may either reinforce or oppose the gravitational flow. We see for $H = 1$ that, as the relative magnitude of the thermocapillary contribution $\mathcal{R}$ increases, the flow profile becomes dominated by the nearly-linear sinh profile, respecting the sign of $\mathcal{R}$ (which may change within the divertor due to temperature gradient changing sign). For larger H, and thus stronger MHD effects, the Hartmann flow profile (uniform in the bulk with a viscous boundary layer at the substrate) is more strongly manifest, and variations in $\mathcal{R}$ are expressed at a free-surface boundary layer.

Beyond the dependence on field strength, the ratio (4.6.3), and thus the thin-film equation (4.1.31), depend strongly on the location and movement of the external plasma, as well as its heat and momentum flux densities and the shape the free surface has locally adopted. The focus of the next two chapters is understanding how this multitude of factors influence the downstream velocity and ultimately shape the free surface.

4.7 Summary

In §§ 2.2 and 2.3 we consider the applied field to comprise either the poloidal components or the toroidal component in isolation. A poloidal flow field is sufficient to satisfy the leading-order equations in both cases. In this chapter we include all components of the applied field simultaneously, and find that terms involving the products of the poloidal and toroidal components appear in the toroidal component of the momentum equation. These new terms can only be balanced by a nonzero toroidal component of the flow. This new flow component may be understood as the result of the nonlinearity of the $\boldsymbol{j}^* \times \boldsymbol{B}^*$ term: the product terms vanish when considering either field component in isolation, but the study of the full applied field is crucial to understanding the flow, as it is not merely a superposition of each separate solution.

The magnitudes of the toroidal flow and induced field are both $\mathcal{O}(\Xi \mathscr{U}^*)$ where $\mathscr{U}^*$ is the magnitude of the downsteam flow and Ξ/ϵ is the ratio of the applied toroidal field to the poloidal field (see (4.1.14)). When the toroidal applied field is at least an order of magnitude larger than its poloidal counterpart, thus $\Xi \gtrsim 1$, the toroidal induction couples with the streamwise flow to leading order. We have quantified the effect of this coupling and, through a careful boundary layer analysis in the case of $\Upsilon \gg 1$ (where Υ is proportional to Ξ as per (4.1.36)) shown that the bulk flow is decelerated to a uniform profile of order $\mathcal{O}(1/\Upsilon^2)$ except in boundary layers of width $\mathcal{O}(1/\sqrt{\Upsilon})$ where the flow is only decelerated to speeds of order $\mathcal{O}(1/\Upsilon)$. Thus it is in these boundary layers where most of the fluid passes. On the other hand, when the toroidal and poloidal applied fields are of comparable magnitude, thus $\Xi \lesssim \epsilon$, the toroidal induced field and flow are negligible and the problem reduces to the purely poloidal case.

We deduce that, for the gravity-driven toroidal flow to be non-negligible, the toroidal applied field must be significantly stronger than the poloidal applied field. This regime may be relevant if the poloidal field changes sign along the divertor, in which case local to the vanishing field the toroidal field may be significantly stronger. However, in general, we do not expect to observe a strong gravity-driven toroidal flow.

The toroidal component of the fluid flow exhibits a non-monotonic dependence on field strength. This non-monotonic variation is typical of MHD-induced flows where there are two canonical regimes: a low-field regime in which induced fields increase with increasing field strength, and a high-field regime in which induced fields are decelerated by increasing field strength [179]. The downstream flow is driven by gravity, and thus decreases monotonically with applied field strength: the higher the field, the more MHD drag.

In § 4.2 we extend the model to include temperature, surveying several thermal effects to conclude, via a dimensional analysis, that the Seebeck effect and thermocapillarity are the dominant ones to be retained, while other effects may be neglected. In the asymptotic limit in which the fluid film is thin and its downstream velocity relatively slow, the temperature distribution is dominated by thermal conduction and thus decouples from the flow to leading order. This allows for the decomposition of the leading-order system into three components driven by different mechanisms: gravity (identical to the isothermal case), the Seebeck effect, and thermocapillarity, where the latter two thermal effects are dependent on the decoupled temperature field.

The Seebeck effect manifests in an inhomogeneity at the fluid–substrate boundary. Undoing (4.1.14), (4.1.32) and (4.3.18) we deduce that the magnitude of the thermoelectrically-driven toroidal flow is proportional to $\mathcal{O}(\mathcal{S}\mathscr{U}^*) = \mathcal{O}(\Delta T^* \Delta S^*)$. In contrast to the gravity-driven flow, there is no dependence on Ξ since it is the poloidal applied field that is driving this flow component. Thus, even when the toroidal applied field is comparable to the poloidal applied field, we expect a non-negligible toroidal flow.

That the Seebeck effect does not drive a downstream flow (other than through coupling) is due to the assumption of axisymmetry: symmetry-breaking substrate undulation in the azimuthal direction ϕ, including the singular undulations of a trench geometry, is required to directly drive a downstream flow component. From the scaling (4.3.18a) we find that the magnitude of the downstream velocity driven by coupling is proportional to Ξ, and so when the applied field components are of similar magnitude, we expect this flow component to be negligible.

A non-monotonic dependence on field strength is exhibited by both the downstream and toroidal flow components, as both of these flows are MHD-induced: the Seebeck current drives a flow through the Lorentz force, only in the presence of an applied magnetic field.

From (4.1.14), (4.1.32) and (4.3.20) we find that the third forcing inhomogeneity, thermocapillarity, drives a downstream flow with magnitude proportional to $\mathcal{O}(\epsilon \Delta T^* \mathrm{d}\gamma^*/\mathrm{d}T^*)$. No toroidal component is directly induced by thermal gradients in an axisymmetric configuration. However, just as in the isothermal gravity-driven case, a toroidal flow and magnetic field are induced by the toroidal coupling. The case of small Ξ is revealed in the limit of $\Upsilon \ll 1$, in which case the magnitudes of these toroidal fields are both proportional to $\mathcal{O}(\Xi \mathscr{U}^*)$ and are again negligible.

The standard non-monotonic dependence of the toroidal flow on Ha reflects the usual MHD-induced low- and high-field regimes. The downstream flow depends monotonically on the field strength, being decelerated for increasing field strength.

Equipped with the the leading-order velocity and induced magnetic field profiles when temperature is taken into account, we proceed in chapter 5 to include the final model component: transfer of momentum. With these dominant interactions encapsulated in the model, we will be well positioned to investigate the dynamics of the free surface in physically relevant operating regimes. In particular, we seek to address the question of how the free surface evolves when the impinging plasma is not stationary.

Chapter 5

The Plasma Wind

5.1 Introduction

In chapter 4, we establish an axisymmetric thermal model for the flow of a conducting fluid on a solid substrate in the presence of a strong magnetic field, incorporating the plasma as a heating source at the free surface. Including the external thermal load captures one crucial component of the interaction of the liquid metal with the core plasma. However, the hot ions impacting the divertor also impart momentum to the fluid. The aim of this chapter is to include this momentum transfer into the model, and assess its influence on the fluid film.

With their relatively low energies on the order of 10 keV [61], the ions penetrate only the top surface of the thin film [77], and thus the transfer of momentum can be adequately modelled as a pressure and shear applied to the free surface. Moreover, the strike point — the location at which the plasma exhaust is directed to impact the divertor — is controllable within the tokamak. Of particular interest is the case when the strike point is oscillated, so as to spread the heat load. To protect the solid substrate along the extent of the divertor, we must ensure that the liquid does not thin or dry out due to the impacting plasma. This requirement leads us to the focus of this chapter: what is the effect of a moving localised momentum source applied to the free surface of a thin film of flowing fluid?

Previous work on the dynamics at the liquid metal–plasma interface has focused on Kelvin–Helmholtz [135], Rayleigh–Taylor [88], Rayleigh–Plateau [132], and electrohydrodynamic instabilities [82], as well as boiling-induced droplet ejection [183]. This chapter focuses on a different aspect of the interface by exploring the pressure- and thermocapillarity-driven deflections of the free surface.

In much of the previous work on thin films, the gas above the viscous liquid film is modelled as a passive atmosphere at constant pressure and temperature. However our model must include a pressure and heat source that varies in both space and time. Such a term has been modelled previously in situations in which an external flow has a significant effect on the behaviour of the fluid film, such as jet-stripping and blade coating processes (see [101, 164, 202] and references therein). Applications in microfluidics have used Marangoni forcing to achieve strikingly similar results [75]. These previous studies focus primarily on pressure profiles that either are fixed or move at constant speed, and on corresponding steady or travelling-wave solutions for the thin film response, when they exist. In this chapter we instead consider fully time-dependent flow caused by an oscillating pressure/heat profile. This approach allows us to extend previous studies to find solutions in regions of parameter space where steady or travelling-wave solutions do not exist.

We find that this problem contains two central characteristic time-scales: the time-scale corresponding to the motion of the source, and the response time-scale of the free surface. Thus the problem is naturally separated into three regimes. When the time-scale associated with the motion of the pressure is much longer than the free surface deformation time-scale, the system is quasi-steady: the free surface adopts its steady state profile and varies only parametrically with the location of the applied pressure. At the other extreme, when the pressure oscillates much faster than the time for the free surface to deform, a multiple scales analysis shows that the free surface evolves under the influence of an effective pressure, given by the average pressure over one period of its oscillation. This means that the momentum load is spread across the sweeping range (along with the heat load), and the resulting deflections in the free surface are correspondingly smaller.

Finally, when the two time-scales in the problem are of similar magnitude, a direct numerical simulation reveals that the deflections can become much larger than in the two extreme cases described above. We explore the causes of this resonance and find that there are two mechanisms leading to the increased deflection magnitude. The dominant mechanism comes into play when the applied pressure sweeps at a speed close to the downstream wave propagation speed. In this case, the pressure propagates at a similar speed to the trough that it has created, thus magnifying its thinning influence. An unexpected secondary effect that also leads to a local maximum in the free-surface deflection is a non-local wave interaction, whereby a trough generated upstream coincides on its propagation downstream with a trough being generated later in the oscillation cycle.

An additional thermal time-scale enters the problem under relevant physical conditions that we discuss.

We emphasise that, while we present numerical results only for MHD flow when the applied poloidal field and toroidal fields are of similar magnitude for the sake of clarity, the phenomena described are essentially hydrodynamic. Therefore, the results presented below would be qualitatively preserved in other flow regimes, including the toroidal case and classical hydrodynamic flows.

The chapter is organised as follows. In § 5.2 we outline the isothermal thin-film equation with the added pressure term to be studied. In § 5.3, § 5.4 and §5.5, we explore the three regimes of low, high, and moderate frequency sweeping, respectively. In § 5.6 we consider the inclusion of thermal effects. In § 5.7 we summarise our findings.

5.2 The moving pressure source

Modelling the dynamics of the core plasma in the sheath region adjacent to the fluid film requires knowledge of several physical features of the plasma that are not well known [155, 166]. Just as we did with the thermal load of the plasma, we choose to model only the influence of the momentum transfer on the fluid film. As mentioned in §5.1, it is adequate to model this as an externally applied pressure and shear at the fluid boundary. Strong experimental evidence provides a good approximation of the magnitude and form of this momentum flux [43, 146].

The external pressure and shear are incorporated into the stress balances by additional source terms in the free-surface boundary conditions (2.1.22). Denoting the typical size of the pressure term $\mathscr{P}^*$, and non-dimensionalising with the usual scalings (4.1.14) and (4.1.15), we write the dimensionless pressure exerted on the fluid at the boundary as $A\boldsymbol{p}(r,t)$, where A is the pressure amplitude defined by

$$A = \frac{\mathscr{P}^*}{\rho^* \, |\boldsymbol{g}| \, \mathscr{L}^* \sin\theta}, \tag{5.2.1}$$

and $\boldsymbol{p}$ is the spatial- and time-dependence of the momentum flux density. We take $\boldsymbol{p}$ coinciding with the thermal flux density (see the paragraph containing (4.3.8d)), the sources differing only in their amplitudes, as these both originate from the core plasma impinging upon the fluid coating the divertor. From tables 2.1 and 2.4 we see that $A = \mathcal{O}(1)$ which is the distinguished limit we are interested in.

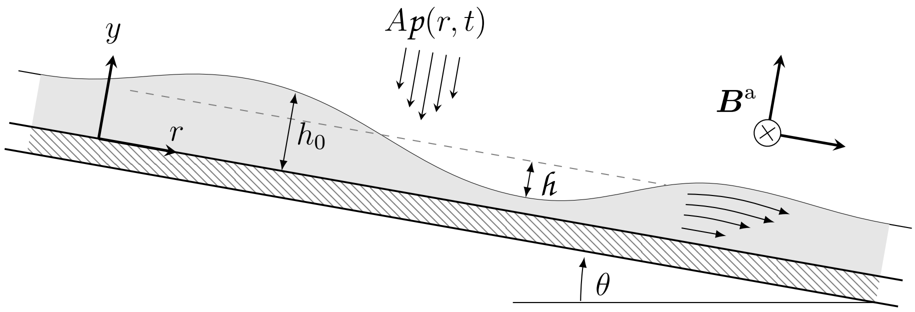

Figure 5.1: Schematic of two-dimensional thin film flow on an inclined plane subject to an externally applied magnetic field $\boldsymbol{B}^{\mathrm{a}}$ and pressure Ap.

We assume, in the first instance, that the shear stress exerted by the impinging plasma is negligible to leading order (as in [117]), and the only change to the leading-order system (4.1.28–30) is in the pressure boundary condition (4.1.29c), where the term $Ap(r,t)$ must be added to the right-hand side. Relaxing this assumption poses no additional complexity, and merely requires adding an extra inhomogeneous boundary condition. A summarising schematic of the situation is sketched in figure 5.1. In solving the leading-order system, the pressure retains the same form as in (4.1.33) and the term $Ap(r,t)$ is added to P in (4.1.34).

In this chapter we focus on the deflections caused to the free surface, in the case where the toroidal and poloidal fields are of comparable magnitude, thus $\Xi = \mathcal{O}(\epsilon)$ and so $\Upsilon \ll 1$. As described in §4.6, the contribution to the downstream flow driven by the Seebeck effect is negligible, and only gravity, pressure, and thermocapillary effects drive the leading-order downstream flow. In this case, the thin film equation governing the evolution of the free surface (4.1.31), takes the form

$$\frac{\partial h_0}{\partial t} + \frac{1}{r}\frac{\partial}{\partial r}\left\{ r Q_{\mathcal{G}}(h_0, r)\left(1 - A\frac{\partial p}{\partial r} - \alpha\frac{\partial h_0}{\partial r} + \frac{\epsilon^3}{\mathrm{Bo}}\frac{\partial \lambda}{\partial r} + b\right)\right.$$
$$\left. - r\mathcal{T}C\, Q_{\mathcal{T}}(h_0, r)\frac{\partial}{\partial r}\left[p\left(h_0 + \frac{h^{\mathrm{s}} k^*}{k^{\mathrm{s}*}}\right) + T^-\right]\right\} = 0, \qquad (5.2.2)$$

where $\alpha = \epsilon \cot\theta$, $b = (\chi/2\,\mathrm{Rm})\mathrm{d}\left|\boldsymbol{B}^{\mathrm{a}}\right|^2/\mathrm{d}r$ with $\left|\boldsymbol{B}^{\mathrm{a}}\right|^2$ defined in (4.1.29g), λ is the capillary contribution defined in (4.1.29f), and the flux functions $Q_{\mathcal{G}}$ and $Q_{\mathcal{T}}$ denote the purely local dependence of the fluid flux on the film height driven by gravity and thermocapillarity, respectively. When $\Upsilon \ll 1$, we find from (4.1.67a) and (4.5.11a) that the flux functions (now incorporating scaling factors) are given

$$Q_{\mathcal{G}} = \frac{h_0}{\Lambda^2}\left(1 - \frac{\tanh(\mathrm{Ha}\,\Lambda h_0)}{\mathrm{Ha}\,\Lambda h_0}\right), \qquad Q_{\mathcal{T}} = \frac{1 - \mathrm{sech}(\mathrm{Ha}\,\Lambda h_0)}{\mathrm{Ha}^2\,\Lambda^2}. \qquad (5.2.3\mathrm{a,b})$$

The typical length-scale of the horizontal extent of the strike point, that is, over which $p(r,t)$ varies in space, is on the order of 1 cm. This turns out to be of the same order as the capillary length-scale

$$\mathscr{L}_{\mathrm{c}}^* = \left(\frac{\gamma^* \mathscr{H}^*}{\rho^* \, |\boldsymbol{g}| \sin\theta}\right)^{1/3} \approx 1\,\mathrm{cm}, \tag{5.2.4}$$

according to parameters from tables 2.1 and 2.2. We thus adopt this capillary length-scale, centring the coordinate system at the strike point (or the centre of the strike point oscillations), by defining new variables and parameters

$$r = r_{\mathrm{strike}} + \frac{\mathscr{L}_{\mathrm{c}}^*}{\mathscr{L}^*}\hat{r}, \quad t = \frac{\mathscr{L}_{\mathrm{c}}^*}{\mathscr{L}^*}\hat{t}, \quad \alpha = \frac{\mathscr{L}_{\mathrm{c}}^*}{\mathscr{L}^*}\hat{\alpha}, \quad A = \frac{\mathscr{L}_{\mathrm{c}}^*}{\mathscr{L}^*}\hat{A}, \quad \mathcal{T} = \frac{\mathscr{L}_{\mathrm{c}}^*}{\mathscr{L}^*}\hat{\mathcal{T}}. \tag{5.2.5a–e}$$

We subsequently drop the hats for convenience. With this refined choice of length-scale, the aspect ratio is given by

$$\epsilon = \frac{\mathscr{H}^*}{\mathscr{L}_{\mathrm{c}}^*} = \mathrm{Bo}^{1/3}, \tag{5.2.6}$$

which remains small (as per table 2.4).

Since the external magnetic field $\boldsymbol{B}^{\mathrm{a}}$ varies on the length-scale of the entire divertor, which is of order $1\,\mathrm{m} \gg \mathscr{L}_{\mathrm{c}}^*$, we expect $\boldsymbol{B}^{\mathrm{a}}$ (and thus b) to be approximately constant (and of magnitude 1 by our choice of non-dimensionalisation). Then both $Q_{\mathcal{G}}$ and $Q_{\mathcal{T}}$ no longer exhibit spatial dependence, and take the forms

$$Q_{\mathcal{G}}(h_0) = h_0\left(1 - \frac{\tanh(\mathrm{Ha}\, h_0)}{\mathrm{Ha}\, h_0}\right), \qquad Q_{\mathcal{T}}(h_0) = \frac{1 - \mathrm{sech}(\mathrm{Ha}\, h_0)}{\mathrm{Ha}^2}. \tag{5.2.7a,b}$$

Having rescaled to the capillary length-scale, we retain only the term of highest-order derivative in λ, namely $\partial^2 h_0/\partial x^2$ (see (4.1.29f)). In the case where the substrate temperature is constant, the thin film equation (5.2.2) then reduces to

$$\begin{aligned}\frac{\partial h_0}{\partial t} + \frac{\partial}{\partial r}\Bigg\{Q_{\mathcal{G}}(h_0)\left(1 - A\frac{\partial p}{\partial r} - \alpha\frac{\partial h_0}{\partial r} + \frac{\partial^3 h_0}{\partial r^3} + b\right)& \\ -\mathcal{T} C\, Q_{\mathcal{T}}(h_0)\frac{\partial}{\partial r}\left[p\left(h_0 + \frac{h^{\mathrm{s}} k^*}{k^{\mathrm{s}*}}\right)\right]\Bigg\} &= 0.\end{aligned} \tag{5.2.8}$$

In the absence of the external plasma, i.e. when $A = C = 0$, equation (5.2.8) admits an exact solution $h_0 = \mathrm{const} = 1$ without loss of generality. We therefore write

$$h_0(r,t) = 1 + \mathscr{h}(r,t), \tag{5.2.9}$$

where $\mathscr{h}$ is the deflection of the free surface due to the applied pressure (see figure 5.1), and the central quantity in this chapter. The deflection satisfies the equation

$$\frac{\partial \mathscr{h}}{\partial t} + \frac{\partial}{\partial r}\left[\mathcal{Q}(\mathscr{h})\left(1 - A\frac{\partial \mathscr{p}}{\partial r} - \alpha\frac{\partial \mathscr{h}}{\partial r} + \frac{\partial^3 \mathscr{h}}{\partial r^3}\right) - \mathcal{C}\,\mathcal{T}(\mathscr{h})\frac{\partial}{\partial r}\left[\mathscr{p}\left(\mathscr{h} + 1 + \iota\right)\right]\right] = 0, \tag{5.2.10a}$$

where $\mathcal{Q}(\mathscr{h}) = Q_{\mathcal{G}}(h_0) = Q_{\mathcal{G}}(1+\mathscr{h})$, and similarly $\mathcal{T}(\mathscr{h}) = Q_{\mathcal{T}}(1+\mathscr{h})$, while we simplify the notation by defining $\mathcal{C} = \mathcal{T}C$ and $\iota = h^{\mathrm{s}}k^*/k^{\mathrm{s}*}$. Although we focus on the specific forms (5.2.7), the features of solutions to equation (5.2.10a) are robust to a wide range of flux functions $\mathcal{Q}$ and $\mathcal{T}$, so the results presented in this chapter are qualitatively similar for different field orientations and flow regimes.

We will consider applied pressure profiles $\mathscr{p}(r,t)$ that are strongly localised in r and assume that the influence on the free surface is likewise localised, so that

$$\mathscr{h} \to 0 \quad \text{as} \quad r \to \pm\infty. \tag{5.2.10b}$$

Finally, we focus on the case of a pressure source that oscillates to and fro in the r-direction. In a tokamak, the plasma exhausted from the core region towards the divertor may be controlled to sweep the strike point, where the plasma jet impacts the divertor, up and down and thus spread the heat load over a larger area. The general form for such an oscillating pressure will be

$$\mathscr{p}(r,t) = \mathcal{P}\big(r - \ell\mathcal{R}(ft)\big), \tag{5.2.11}$$

where $\mathcal{P}$ is the stationary pressure profile, ℓ is the sweeping amplitude, $\mathcal{R}$ is the 2π-periodic time profile, and f is the frequency. For the sake of simplicity, and unless otherwise stated, we will use for $\mathcal{P}$ a Gaussian centred at zero,

$$\mathcal{P}(r) = \mathrm{e}^{-r^2}, \tag{5.2.12}$$

and a sinusoidal sweeping profile

$$\mathcal{R}(t) = \sin t. \tag{5.2.13}$$

Later on we will demonstrate that the results are robust to changes in the pressure and time-sweeping profiles.

To summarise, in this chapter we investigate how the deflection $\hbar$ of the free surface of a thin film flowing along a solid substrate, governed by (5.2.10) depends on the movement of the plasma source. In the first instance, we explore the deflections caused by only the pressure exerted by the plasma by fixing $\mathcal{C} = 0$. We note that the problem contains two time-scales: the intrinsic relaxation time-scale of the free surface, and the time-scale associated with the imposed plasma oscillations. The dimensionless parameter f is the ratio of these two time-scales, and it is therefore natural to split the analysis into three cases: $f \ll 1$, $f \sim 1$, and $f \gg 1$. We will consider these cases separately. The cases of low and high frequency, $f \ll 1$ and $f \gg 1$, respectively, admit a separation of time-scales which allows analytical progress to be made in § 5.3 and § 5.4, respectively. The intermediate case $f \sim 1$ admits no such simplifications, and a full numerical simulation will be carried out and the results described in §5.5. In §5.6 we extend the results for the non-isothermal case $\mathcal{C} \neq 0$.

5.3 Slow sweeping

5.3.1 Quasi-steady approximation

In this section we consider the case of low frequency oscillations, that is, where $f \ll 1$. In this regime, the time it takes for the applied pressure to move a nominal distance is much longer than the time it takes for the free surface to respond to the pressure. Thus the problem becomes quasi-steady: to leading order in f, the free-surface deflection $\hbar$ attains a steady state which simply translates with the location of the pressure source.

To justify this result formally, we transform to local variables that travel with the moving source by defining

$$\xi = r - \ell\,\mathcal{R}(ft), \qquad \tau = ft, \tag{5.3.1}$$

so that (5.2.10a) becomes

$$f\left(\frac{\partial \hbar}{\partial \tau} - \ell \dot{\mathcal{R}}(\tau)\frac{\partial \hbar}{\partial \xi}\right) + \frac{\partial}{\partial \xi}\left[\mathcal{Q}(\hbar)\left(1 - A\mathcal{P}'(\xi) - \alpha\frac{\partial \hbar}{\partial \xi} + \frac{\partial^3 \hbar}{\partial \xi^3}\right)\right] = 0. \tag{5.3.2}$$

Here and henceforth, the prime in $\mathcal{P}'(\xi)$ and dot in $\dot{\mathcal{R}}(\tau)$ are used to denote ordinary differentiation. To leading order in f, the first term in (5.3.2) is negligible and we are left with the ordinary differential equation

$$\frac{\mathrm{d}}{\mathrm{d}\xi}\left[\mathcal{Q}(\hbar)\left(1 - A\frac{\mathrm{d}\mathcal{P}}{\mathrm{d}\xi} - \alpha\frac{\mathrm{d}\hbar}{\mathrm{d}\xi} + \frac{\mathrm{d}^3 \hbar}{\mathrm{d}\xi^3}\right)\right] = 0 \tag{5.3.3}$$

for $\hbar(\xi)$. To compute solutions of (5.3.3), we implement a full time-dependent solver designed for lubrication-type equations [230] and run the simulation until the solution reaches steady state. An ODE solver that directly solves (5.3.3) was also implemented for the sake of validation, particularly for cases where A is large.

From the numerical simulations shown in figure 5.2, we observe that all solutions are characterised by a peak in the free surface upstream of the strike point $\xi = 0$ and a trough at, or slightly downstream of, the strike point. The magnitude of the free-surface displacement increases approximately proportionally to the amplitude A of the imposed pressure source, but decreases with increasing transverse gravitational component α. In figure 5.2(c) we show how these effects compete when both A and α are increased simultaneously. We see that the deflections become larger, suggesting that, in this setting, the applied pressure is more dominant than transverse gravity. However we note that, unlike when A is increased in isolation, the upstream peak is significantly damped and more spread out, so that transverse gravity increases the far-field influence of the localised pressure peak. Since both A and α scale with $(\sin\theta)^{-2/3}$ as $\theta \to 0$, figure 5.2(c) could model the effects of decreasing the inclination angle θ while keeping everything else constant.

We note that the solutions in figure 5.2 with relatively small values of α exhibit upstream oscillations leading into the strike region, while those with larger values of α do not. To investigate the far-field behaviour of the solution, we seek decaying exponential solutions of the form $\hbar(\xi) \sim \mathrm{e}^{c\xi}$ as $\xi \to \pm\infty$. Provided the pressure is a Gaussian (or similar) which vanishes faster than any exponential, it follows from (5.3.3) that c satisfies

$$c^3 - \alpha c = -\frac{\mathcal{Q}'(0)}{\mathcal{Q}(0)} = -L, \tag{5.3.4}$$

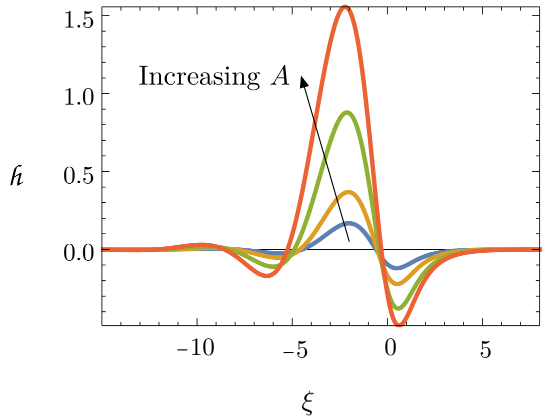

(a) $A \in \{0.5, 1, 2, 3\}$ and $\alpha = 0$.

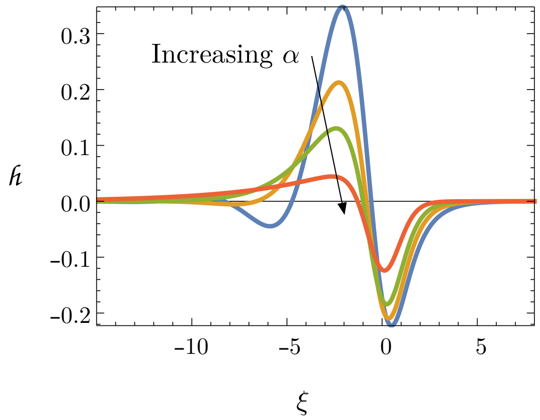

(b) $A = 1$ and $\alpha \in \{0.1, 1, 2, 5\}$.

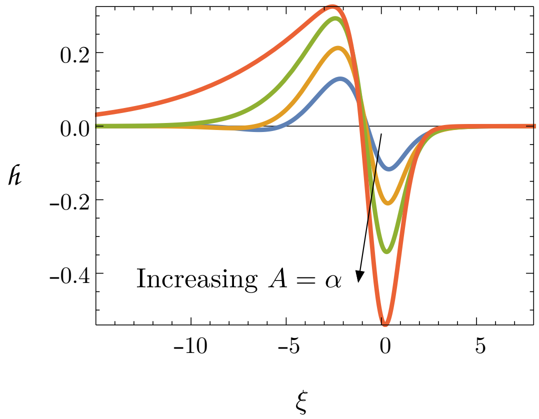

(c) $A = \alpha \in \{0.5, 1, 2, 5\}$.

Figure 5.2: Steady free-surface deflections $\hbar(\xi)$ found by numerical solution of (5.3.3).

say. We assume that the flux is a monotonic increasing function of the film height, and L is therefore a positive constant (for the Hartmann flow flux function (5.2.7a) given by $L = \mathrm{Ha}\left(1 + \mathrm{sech}^2\,\mathrm{Ha}\right) / (\mathrm{Ha} + \tanh \mathrm{Ha}) \approx 10/11$ with $\mathrm{Ha} = 10$). Equation (5.3.4) always has precisely one real, negative root, and two other roots with positive real part. We conclude that the downstream behaviour (as $\xi \to +\infty$) is unconditionally monotonic, while the upstream behaviour is either monotonic or oscillatory, depending on whether the two non-negative roots of (5.3.4) are real or complex. Elementary manipulation of (5.3.4) then reveals that upstream oscillations occur if and only if

$$\frac{\alpha^3}{L^2} < \frac{27}{4}. \tag{5.3.5}$$

For the Hartmann flow model used in our computations, (5.3.5) reduces to $\alpha \lesssim 1.77$, and indeed we see in figure 5.2(b) that the upstream oscillations are suppressed in the solutions where $\alpha \geq 2$. As pointed out in § 5.2, α is usually small in practice. Henceforth we will therefore take $\alpha = 0$ in our calculations, in which case (5.3.5) is satisfied identically, and we will always expect to observe upstream free-surface oscillations.

5.3.2 Varying the applied pressure

Next we demonstrate that the free surface profile is robust to the form of the applied pressure, $\mathcal{P}$. To see this, we consider two families of nascent delta functions, a Gaussian family given by

$$\mathcal{P}_\Delta(r) = \frac{1}{\Delta}\,\mathrm{e}^{-(r/\Delta)^2}, \tag{5.3.6}$$

and a sinc family given by

$$\mathcal{P}_\Delta(r) = \frac{1}{\Delta\sqrt{\pi}}\,\mathrm{sinc}\left(\frac{r}{\Delta}\right) = \frac{1}{r\sqrt{\pi}}\,\sin\left(\frac{r}{\Delta}\right). \tag{5.3.7}$$

For all positive values of Δ, both (5.3.6) and (5.3.7) satisfy

$$\int_{-\infty}^{\infty} \mathcal{P}_\Delta(r)\,\mathrm{d}r = \sqrt{\pi}, \tag{5.3.8}$$

and, in the limit $\Delta \to 0$, they each approach a Dirac delta function.

The profiles (5.3.6) and (5.3.7) are qualitatively different, in that (5.3.6) is positive for all r, while (5.3.7) and its derivatives change sign infinitely many times, as shown in figure 5.3(a). Despite this, the different pressure profiles produce very similar free surface deflections, as shown in figure 5.3(b). These results highlight the fact that, provided the pressure source is localised, the free surface profile is shaped largely by capillarity, and not by the particular form of $\mathcal{P}$ away from the origin. For the sake of the numerical simplicity we will henceforth continue to use a Gaussian in simulations.

Furthermore, we note the similarity between free surface profiles for a wide range of the characteristic width parameter Δ, as illustrated in figure 5.4. For larger Δ, the pressure profile is more spread out and the resulting deflection profile exhibits somewhat damped peaks and troughs. As Δ decreases, we see a sharper transition local to the origin as equation (5.3.3) becomes singular there. In the limit $\Delta \to 0$, we see that $\mathcal{P}$ approaches a delta function which forces a jump discontinuity in the first derivative of $\hbar$. The continuity of $\hbar(\xi)$, as well as the jump discontinuity in

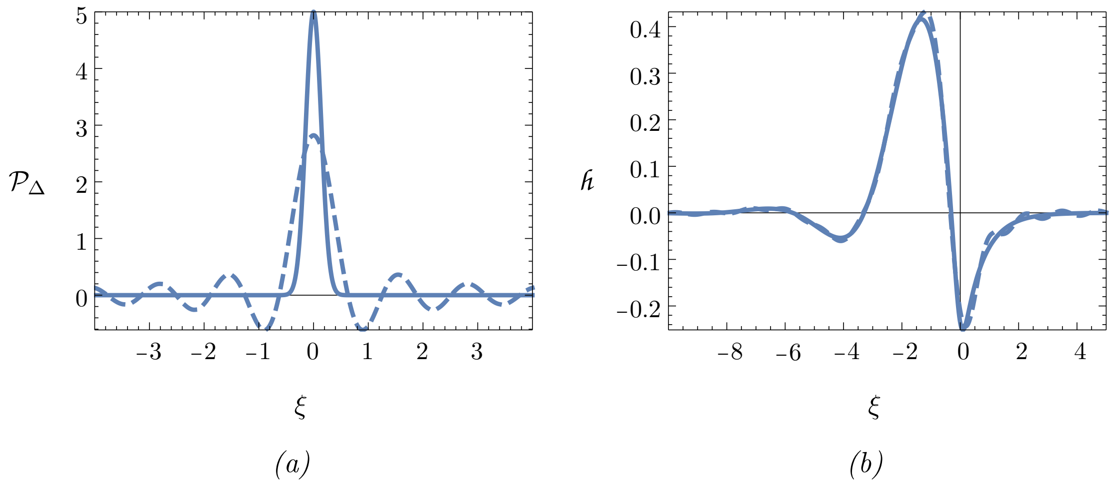

Figure 5.3: (a) Nascent delta function $\mathcal{P}_\Delta$ given by (5.3.6) (solid curve), and (5.3.7) (dashed curve) where $\Delta = 0.2$. (b) Steady-state free-surface deflection profiles, namely solutions to (5.3.3), where $A = 1$, $\alpha = 0$, and the applied pressures match those from (a).

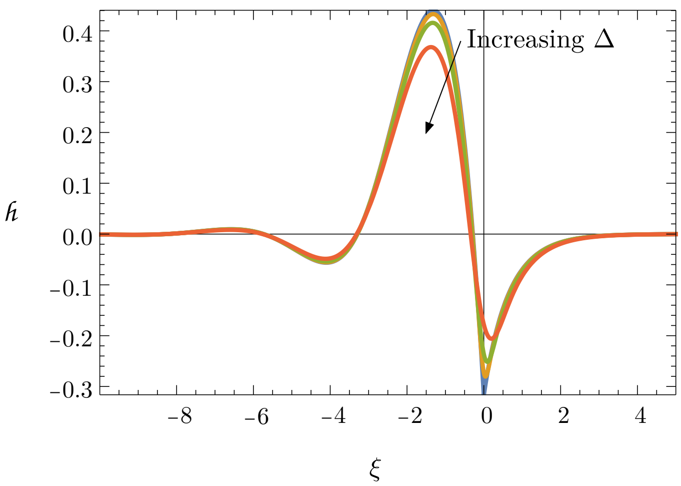

Figure 5.4: Steady-state free-surface deflection profiles, namely solutions to (5.3.3), where $A = 1$, $\alpha = 0$, and the applied pressure is given by (5.3.6) with $\Delta \in \{0.001, 0.1, 0.2, 0.4\}$.

$\hbar'(\xi)$ of magnitude $A\sqrt{\pi} \approx 1.77$ when $A = 1$ can be observed in figure 5.4.

5.3.3 Large-amplitude applied pressure

The solutions plotted in figure 5.2 demonstrate that, unsurprisingly, the magnitude of the free-surface deflection $\hbar$ increases as the amplitude A of the imposed pressure increases and as the gravitational parameter α decreases. However, we will now argue that, however large the applied pressure, it is impossible for the deflection ever to become so large that the film thickness h_0 reaches zero, which would correspond to dry-out of the liquid film. To see this, we integrate (5.3.3), applying vanishing boundary conditions to both the pressure and the deflection to give

$$1 - \alpha \frac{\mathrm{d}\hbar}{\mathrm{d}\xi} + \frac{\mathrm{d}^3 \hbar}{\mathrm{d}\xi^3} = \frac{\mathcal{Q}(0)}{\mathcal{Q}(\hbar)} + A\frac{\mathrm{d}\mathcal{P}}{\mathrm{d}\xi}. \tag{5.3.9}$$

If the pressure gradient is large enough for the film thickness $h_0 = \hbar + 1$ to approach zero, then the flux function $\mathcal{Q}(\hbar) = Q_{\mathcal{G}}(h_0)$ likewise approaches zero. For the Hartmann flux function (5.2.7a) used in our simulations, we have $Q_{\mathcal{G}}(h_0) = \mathcal{O}\left(h_0^3\right)$ when $h_0 \ll 1/\,\mathrm{Ha}$. A dominant balance in (5.3.9) then suggests the scaling law

$$\min h_0 \propto \left(-A\frac{\mathrm{d}\mathcal{P}}{\mathrm{d}\xi}\right)^{-1/3} \quad \text{when} \quad -A\frac{\mathrm{d}\mathcal{P}}{\mathrm{d}\xi} \gg 1 \text{ and } h_0 \ll 1/\,\mathrm{Ha}\,. \tag{5.3.10}$$

There is also an intermediate regime where $1/\,\mathrm{Ha} \ll h_0 \ll 1$. In this case the flux function, to leading order in $(\mathrm{Ha}\, h_0)^{-1}$, satisfies $Q_{\mathcal{G}}(h_0) = \mathcal{O}(h_0)$, and then a dominant balance in (5.3.9) suggests that

$$\min h_0 \propto \left(-A\frac{\mathrm{d}\mathcal{P}}{\mathrm{d}\xi}\right)^{-1} \quad \text{when} \quad -A\frac{\mathrm{d}\mathcal{P}}{\mathrm{d}\xi} \gg 1 \text{ and } 1/\,\mathrm{Ha} \ll h_0 \ll 1. \tag{5.3.11}$$

Both of the scalings (5.3.10) and (5.3.11) can be observed in our numerical simulations. As illustrated in figure 5.5, the minimum film thickness scales with $A^{-1/3}$ as the amplitude A of the applied pressure tends to infinity, while for large enough Ha there is an intermediate region where the minimum film thickness scales with A^{-1}.

In general, even if other physics is included, viscous hydrodynamic effects will usually dominate when the film thickness is small. We can therefore expect the limiting behaviour $Q_{\mathcal{G}}(h_0) = \mathcal{O}\left(h_0^3\right)$, and consequently the dependence (5.3.10) of the minimum thickness on the applied pressure gradient, to be quite general, at least for flow with no slip on a rigid substrate. We conclude that, although the minimum film thickness tends to zero as $A \to \infty$, it can never reach zero as long as the applied pressure remains finite.

5.4 Fast sweeping

If $f \gg 1$, then the characteristic time-scale on which the applied pressure sweeps is significantly faster than the time it takes for the fluid to deform under the applied

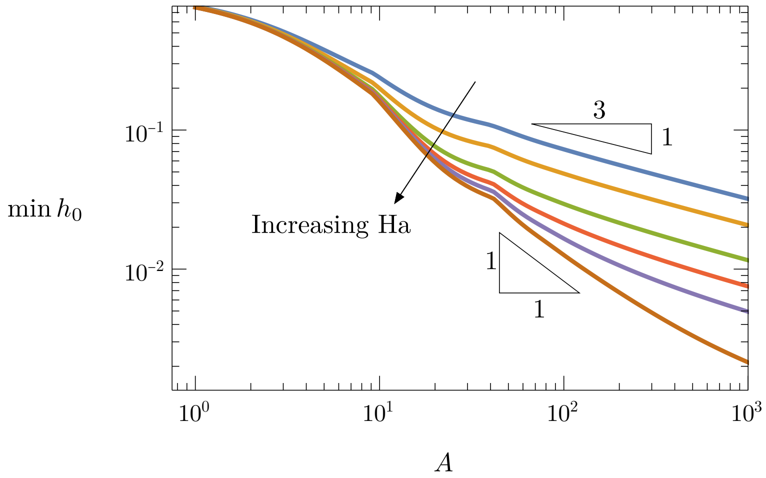

Figure 5.5: Minimal film thickness as a function of the applied pressure amplitude, A, where $\mathrm{Ha} \in \{10, 20, 50, 100, 200, 1000\}$ *and* $\alpha = 0$.

pressure. In this case we can expect the sweeping to have the effect of spreading the momentum load just as it does the heat load. To analyse this limit, we pose a multiple scales ansatz, where the "slow" time variable t and the "fast" variable $\tau = ft$, are considered independent. Moreover we assume that $\hbar(r, t, \tau)$ is 2π-periodic with respect to τ, and that the applied pressure has no slow-time dependence, that is,

$$p(r, \tau) = \mathcal{P}\big(r - \ell\mathcal{R}(\tau)\big). \tag{5.4.1}$$

We then pose the asymptotic expansion

$$\hbar \sim \hbar_0 + \frac{1}{f}\,\hbar_1 + \cdots\,, \tag{5.4.2}$$

and find that the leading-order term is a function only of the slow time-scale, that is, $\hbar_0 = \hbar_0(r, t)$.

At $O(1/f)$, the solvability condition for $\hbar_1$ provides an evolution equation for the leading-order film thickness, namely

$$\frac{\partial \hbar_0}{\partial t} + \frac{\partial}{\partial r}\left[\mathcal{Q}(\hbar_0)\left(1 - A\frac{\mathrm{d}\overline{p}}{\mathrm{d}r} - \alpha\frac{\partial \hbar_0}{\partial r} + \frac{\partial^3 \hbar_0}{\partial r^3}\right)\right] = 0, \tag{5.4.3a}$$

where

$$\overline{p}(r) = \frac{1}{2\pi}\int_0^{2\pi} p(r, \tau)\,\mathrm{d}\tau. \tag{5.4.3b}$$

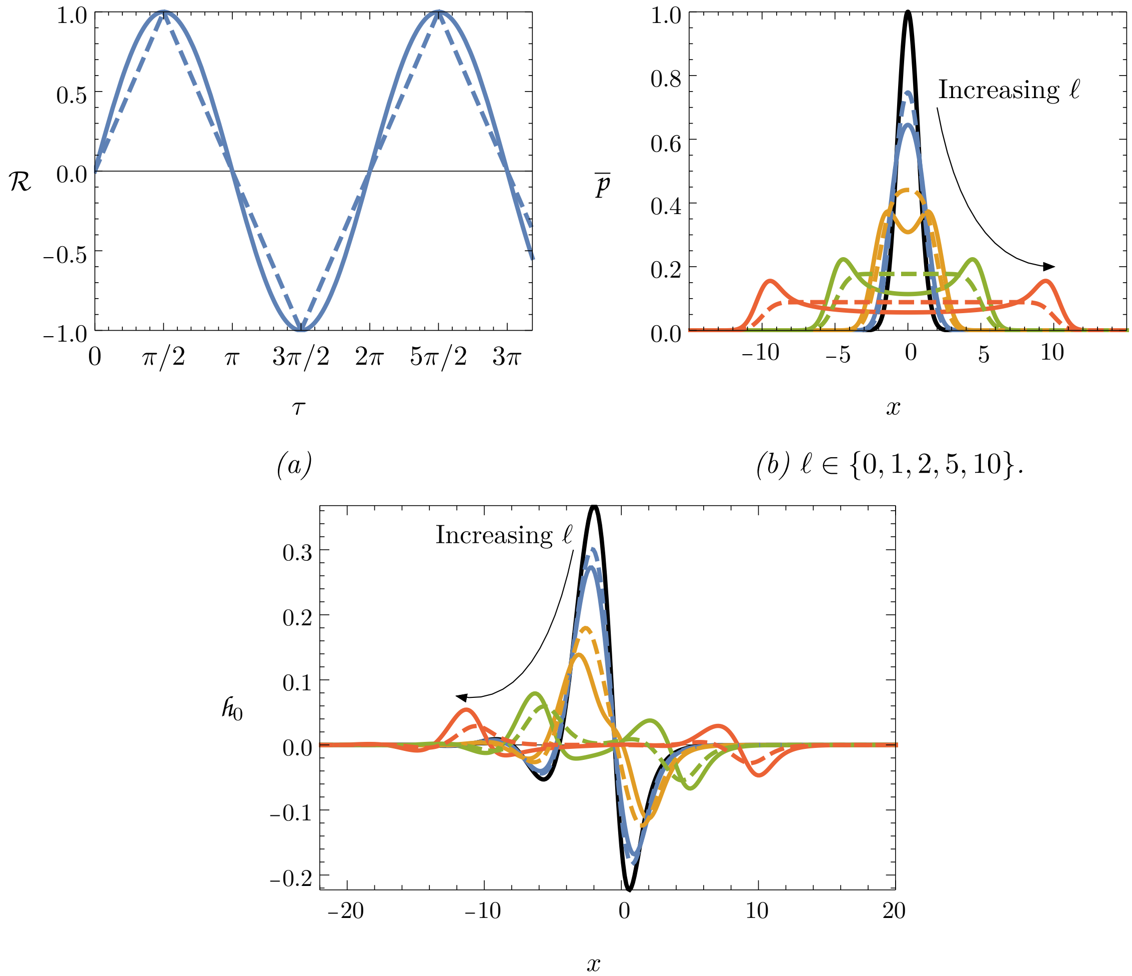

(a) *(b)* $\ell \in \{0, 1, 2, 5, 10\}$.

(c) $\ell \in \{0, 1, 2, 5, 10\}$.

Figure 5.6: (a) Sweeping profiles $\mathcal{R}(\tau)$*:* $\mathcal{R}(\tau) = \sin\tau$ *is the solid curve, and the dashed curve shows a triangle wave that linearly interpolates the peaks and troughs of the sine curve. (b) Time-averaged applied pressure profiles calculated from* (5.4.3b) *with both fast-time functions from graph (a). (c) Steady multiples-scales solutions of* (5.4.3) *for the averaged profiles in graph (b) where* $A = 1$ *and* $\alpha = 0$.

Equation (5.4.3a) is identical to (5.2.10a) except that the applied pressure is replaced by a time-independent *effective applied pressure* which has been averaged over the fast time-scale. This analysis therefore confirms the earlier stated intuition that the effect of sufficiently fast sweeping is to spread the momentum load.

The solid curves in figure 5.6(b) show the effective pressure profile $\overline{p}(r)$ for a Gaussian underlying pressure source (5.2.12), a sinusoidal sweeping profile (5.2.13), and various values of the sweeping amplitude ℓ. We observe that, the larger the amplitude ℓ of the oscillations, the smaller the magnitudes of the maximal and minimal pressure, and the wider the region over which the profile is spread, as expected. For sufficiently large ℓ, the effective pressure profile produced with a sinusoidal sweeping profile $\mathcal{R}(\tau)$ exhibits a peak at either end, where $\mathcal{R}(\tau)$ is stationary, so the pressure maximum lingers there. For comparison, we show using dashed curves the corresponding effective pressures when the sweeping profile $\mathcal{R}(\tau)$ is a triangle wave, and these end peaks do not appear. Nevertheless, for small values of ℓ it is the sinusoidal $\mathcal{R}(\tau)$ that produces the smaller magnitude effective pressure and pressure gradient.

Since the effective pressure $\overline{p}(r)$ is time-independent, the solution $\hbar_0$ of (5.4.3a) ultimately converges to a steady state, as will be demonstrated below in §5.5.1 by direct numerical simulation. We compute the steady-state solution $\hbar_0(r)$ of (5.4.3) using the same procedure as that used for the regime where $f \ll 1$ in §5.3, and results are illustrated in figure 5.6(c). We find that the steady profiles, like the effective pressures, exhibit smaller deflections for larger values of the sweeping amplitude ℓ. Similarly to the pressure profiles, for small values of ℓ sinusoidal oscillations cause smaller free-surface deflections than the triangle-wave sweeping profile $\mathcal{R}(\tau)$, while for larger values of ℓ the situation is reversed.

In summary, the analysis of this section confirms that lateral oscillations of the pressure source at sufficiently high frequency can indeed be used to spread the momentum load and significantly reduce the deflection of the thin film.

5.5 Intermediate sweeping

5.5.1 Numerical investigation

In §§5.3 and 5.4, we have shown that the equilibrium free-surface deflection problem becomes effectively steady in the limits of both low-frequency and high-frequency sweeping. In the former case, the governing equation (5.3.3) is quasi-steady, and the free-surface deflection depends only parametrically on the location of the pressure source; in the latter case, the governing equation (5.4.3a) is driven by a steady time-averaged effective pressure $\overline{p}(r)$, and the deflection ultimately reaches a steady state, possibly after some transient.

The accuracy of these asymptotic limits is illustrated in figure 5.7. In figure 5.7(a), we show time-dependent numerical solutions computed with small but nonzero values of f. As the value of f decreases, the difference between the solutions evaluated at two different values of t tends to zero, indicating that the solution is

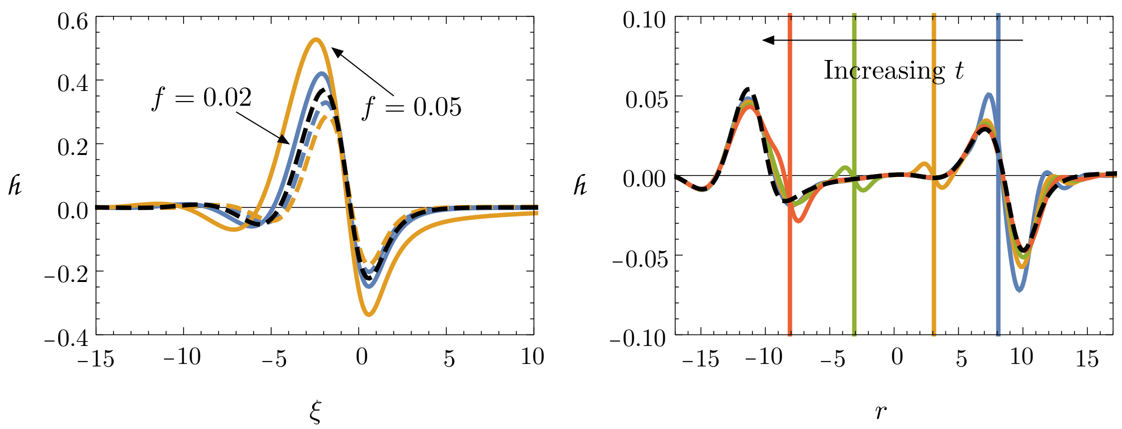

(a)

(b) $t = 14\pi + (1/2 + i/5)\pi/f$, *for* $i = 1, \ldots, 4$.

Figure 5.7: Time-dependent numerical solutions of the problem (5.2.10) *with* $\mathcal{C} = 0$ *and* $\ell = 10$ *for various values of* f *evaluated at various times* t*: (a) evaluated at* $t = \pi$ *(dashed) and* $t = 2\pi$ *(solid), with* $f = 0.02$ *(blue) and* $f = 0.05$ *(orange); the black dashed curve shows the quasi-steady solution to* (5.3.3) *valid in the limit* $f \to 0$*. (b)* $f = 10 \gg 1$*; the vertical lines show the centre of the applied pressure profile at each value of* t*. The black dashed curve shows the steady solution of* (5.4.3)*, valid in the limit* $f \to \infty$*.*

becoming quasi-steady, and both converge to the solution of (5.3.3), which is valid in the limit $f \to 0$. In figure 5.7(b), we show time-dependent numerical solutions computed with a large but finite value of f. The simulation is first run up to $t = 14\pi$, allowing initial transients to decay, and then we plot time intervals corresponding to half-oscillations. We observe a small localised ripple that follows the locus of the moving pressure source (indicated by the vertical lines), but otherwise the solution remains close to the steady solution of the multiple-scales model (5.4.3), valid in the limit $f \to \infty$

In this section we study the intermediate regime of moderate frequency by direct numerical simulation of (5.2.10) (in the isothermal case where $\mathcal{C} = 0$) to compute the deflection $\hbar(r, t)$. When $f = \mathcal{O}(1)$, the applied pressure contains an order unity time dependence and there exists no steady state solution for $\hbar(r, t)$. To compare results from this regime to those from §§5.3 and 5.4, we must therefore consider some relevant functionals of the solution $\hbar$. In the context of a divertor, the main focus is to maintain small deflections, and thus it is natural to consider the supremal and infimal deflections, $\sup_{r,t} \hbar(r, t)$ and $\inf_{r,t} \hbar(r, t)$. To remove the dependence of these functionals on the arbitrary initial conditions, we will consider the limit

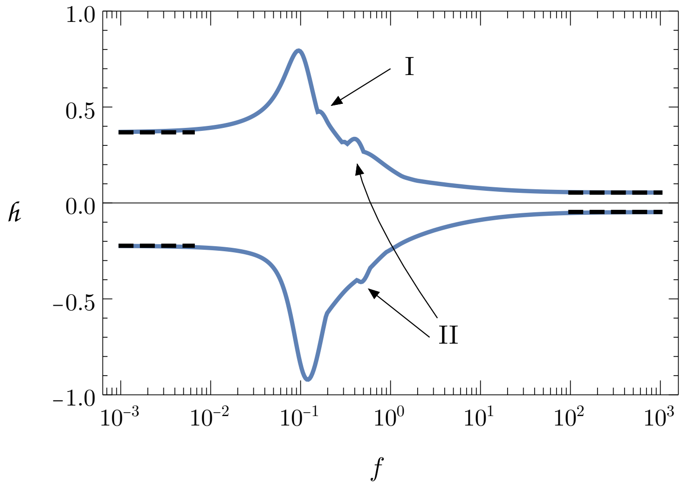

Figure 5.8: Extremal free-surface deflections $\liminf \mathscr{h}$ *and* $\limsup \mathscr{h}$ *as functions of the sweeping frequency* f*, where* $\ell = 10$*,* $A = 1$ *and* $\alpha = 0$*. The extrema of the leading-order solutions as* $f \to 0$ *and as* $f \to \infty$ *are indicated by black dashed lines. Labels I and II mark anomalous local behaviours discussed in § 5.5.4.*

extrema, $\lim_{T\to\infty} \sup_{|r|<X,\, t>T} \mathscr{h}(r,t)$ and $\lim_{T\to\infty} \inf_{|r|<X,\, t>T} \mathscr{h}(r,t)$ for some large X and T. We compute these by running the simulations for large times, taking $X \gg \ell$, and excluding an initial period of time T such that deflections caused by initial conditions have propagated beyond the $|r| < X$ window.

In figure 5.8, we plot the extreme values of the displacement, computed as described above, versus the dimensionless frequency f with the other parameter values $\ell = 10$, $A = 1$ and $\alpha = 0$. As f becomes very small, both $\liminf \mathscr{h}$ and $\limsup \mathscr{h}$ become independent of f and approach constant values in agreement with results of the $f \to 0$ analysis from § 5.3, which are indicated by black dashed lines in figure 5.8. For very large values of f, the extremal values of $\mathscr{h}$ likewise approach constant values, which are somewhat smaller due to the spreading effect of the pressure sweeping, and also consistent with results of the multiple-scales analysis from §5.4. However, as f increases from small to large values, the extremal deflections do not vary monotonically, but increase to a significant peak at a critical intermediate value of the frequency f before decreasing again. This apparent resonance occurs when the applied pressure sweeps at a similar speed to the propagation speed of free-surface deformations, so the pressure peak spends a long time at the trough in the free surface. We will explore this effect in § 5.5.2 by analysing travelling-wave solutions of (5.2.10) for the simpler case where the pressure source moves at constant speed.

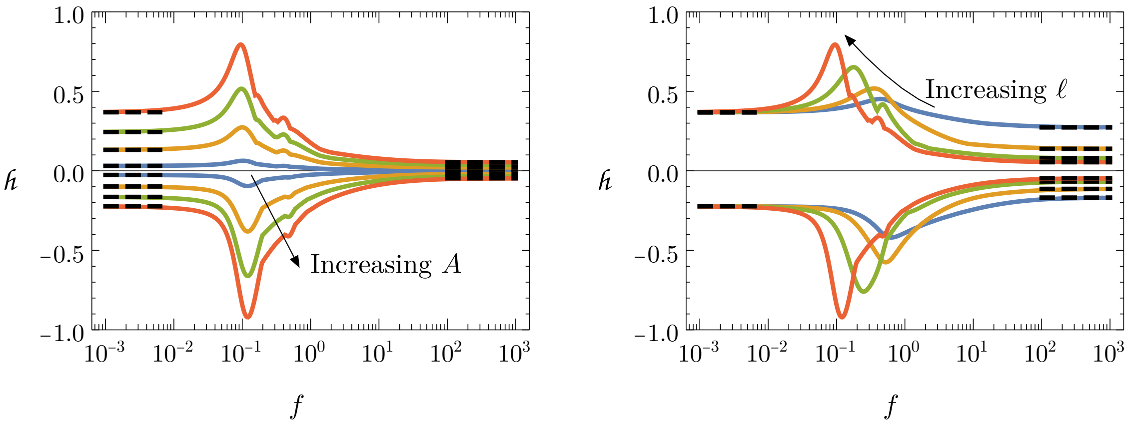

(a) $\ell = 10$ *and* $A \in \{0.1, 0.4, 0.7, 1\}$. *(b)* $A = 1$ *and* $\ell \in \{1, 2, 5, 10\}$.

Figure 5.9: Extremal free-surface deflections, $\liminf \hbar$ *and* $\limsup \hbar$ *as functions of the sweeping frequency,* f*, where* $\alpha = 0$.

In figure 5.9, we show the effects on the response diagram of varying the pressure source amplitude A and the sweeping amplitude ℓ. Unsurprisingly, the free-surface response increases roughly proportionally with the forcing amplitude A. As ℓ increases, the principal peaks in the response occur at smaller values of f such that $\ell f \sim 1$, corresponding to keeping the maximum sweeping velocity constant. The magnitude of the response also increases with increasing ℓ, since the pressure source then spends longer moving close to the intrinsic propagation speed of free-surface disturbances. This effect will be explored further in § 5.5.3 by studying the local behaviour when the sweeping speed is not constant but stationary at the intrinsic propagation speed. Finally, in § 5.5.4 we explore the appearance of smaller local peaks in the free-surface response, for example those labelled I and II in figure 5.8.

5.5.2 Travelling waves

To investigate the origin of the peak in the response diagram in figure 5.8, we first consider travelling-wave solutions with constant wave-speed V. For applied pressure and free-surface deflection of the forms $p(r,t) = \mathcal{P}(\xi)$ and $\hbar(r,t) = \hbar(\xi)$, with $\xi = r - Vt$, the governing equation (5.2.10) (when $\mathcal{C} = 0$) reduces to the ordinary differential equation

$$\frac{\mathrm{d}^3 \hbar}{\mathrm{d}\xi^3} = A\frac{\mathrm{d}\mathcal{P}}{\mathrm{d}\xi} - 1 + \frac{\mathcal{Q}(0) + V\hbar}{\mathcal{Q}(\hbar)}, \tag{5.5.1}$$

when the transverse gravitational parameter α is assumed to be neglible. In principle, equation (5.5.1) can be solved numerically, subject to $\hbar \to 0$ as $\xi \to \pm\infty$. Versions of equation (5.5.1) have been studied previously with various forms of the flux function $\mathcal{Q}$ and the forcing term $\mathcal{P}$, for example by [75, 101, 164], all of which report that the solution of the steady nonlinear problem may exhibit non-existence and non-uniqueness. We are especially interested in how the amplitude of the response depends on the travelling wave speed V, and we will see that useful insight may be gained by considering the linearised problem for small $\hbar$.

Let us therefore consider the case where the amplitude A of the applied pressure is small. The free-surface deflection $\hbar$ is then likewise expected to be of order A, and to leading order in A equation (5.5.1) reduces to the linearised equation

$$\frac{\mathrm{d}^3\hbar}{\mathrm{d}\xi^3} + L\hbar = A\frac{\mathrm{d}\mathcal{P}}{\mathrm{d}\xi}, \tag{5.5.2}$$

where

$$L = \frac{\mathcal{Q}'(0) - V}{\mathcal{Q}(0)}. \tag{5.5.3}$$

For a stationary frame, with $V = 0$, the definition (5.5.3) of L is equivalent to the previous definition in (5.3.4) from § 5.3.1. When V is nonzero L need not be positive but, provided the pressure profile $\mathcal{P}(\xi)$ is even, we can nevertheless restrict our attention to non-negative values of L by exploiting the invariance of equation (5.5.2) under the transformation $(\xi, L) \mapsto (-\xi, -L)$. Thus a solution of (5.5.2) with $L < 0$ can be obtained by just flipping the sign of ξ in the corresponding solution where the sign of L is flipped.

The solution of (5.5.2) with $L > 0$, subject to vanishing far-field conditions, may be written in the form

$$\hbar(\xi) = -\frac{A}{3L^{2/3}}\int_0^\infty \left\{ \mathrm{e}^{-s}\mathcal{P}\left(\xi - \frac{s}{L^{1/3}}\right) + 2\mathrm{e}^{-s/2}\cos\left(\frac{\sqrt{3}\,s}{2} + \frac{\pi}{3}\right)\mathcal{P}\left(\xi + \frac{s}{L^{1/3}}\right)\right\}\mathrm{d}s. \tag{5.5.4}$$

In figure 5.10 we plot typical solutions for $\hbar(\xi)$, where we have used a Gaussian pressure profile. We observe that the free-surface displacement scales with $A/L^{1/3}$ and approaches a function of $L^{1/3}\xi$ as $L \to 0$, and the variables in figure 5.10 are scaled accordingly. The limiting behaviour as $L \to 0$ resembles that seen previously in figure 5.4: decreasing the value of L increases the natural relaxation length-scale of the system, which effectively makes the applied pressure source more localised. By approximating $\mathcal{P}$ by a delta function, the leading-order solution in this limit is

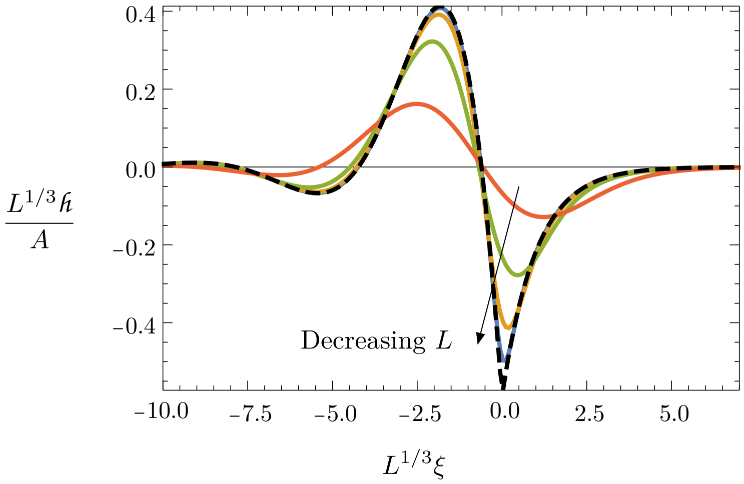

Figure 5.10: Solutions of the linear travelling-wave problem (5.5.2) *with Gaussian applied pressure* $\mathcal{P}(\xi) = \mathrm{e}^{-\xi^2}$ *given in* (5.5.4)*, where* $L \in \{0.01, 0.1, 1, 10\}$*. The dashed curve shows the limit as* $L \to 0$ *given by* (5.5.5).

thus found to be given by

$$\hbar \sim -\frac{A\sqrt{\pi}}{3L^{1/3}} \begin{cases} 2\mathrm{e}^{L^{1/3}\xi/2} \cos\left(\dfrac{\sqrt{3}\,L^{1/3}\xi}{2} - \dfrac{\pi}{3}\right) & \xi < 0, \\ \mathrm{e}^{-L^{1/3}\xi} & \xi > 0, \end{cases} \tag{5.5.5}$$

which is plotted as a black dashed curve in figure 5.10.

We deduce that, as $L \to 0$, the solution $\hbar(\xi)$ of the linear equation (5.5.2) becomes unbounded, with magnitude of order $L^{-1/3}$, while the minimum in the film thickness approaches the strike point $\xi = 0$. This is true in particular when the applied pressure profile is Gaussian, but also whenever the pressure is localised such that $\mathcal{P}\left(s/L^{1/3}\right)$ approaches a delta function as $L \to 0$.

The linearisation that gave rise to equation (5.5.2) is only valid if the amplitude of the solution is sufficiently small, i.e. if $A/L^{1/3}$ is sufficiently small. Travelling-wave solutions with $\mathcal{O}(1)$ amplitude satisfy the nonlinear equation (5.5.1). However, in figure 5.11(a), we show that numerical solutions of (5.5.1) are well approximated by the linearised solution (5.5.4), even for moderate values of A. Figure 5.11(b) shows numerical solutions of the nonlinear travelling-wave equation (5.5.1) for different values of the wave-speed V. The qualitative behaviour is similar to the linearised solutions shown in figure 5.10. There is an apparent symmetry as the signs of ξ and $L \approx 1 - V$ are switched, and the amplitude of the response increases

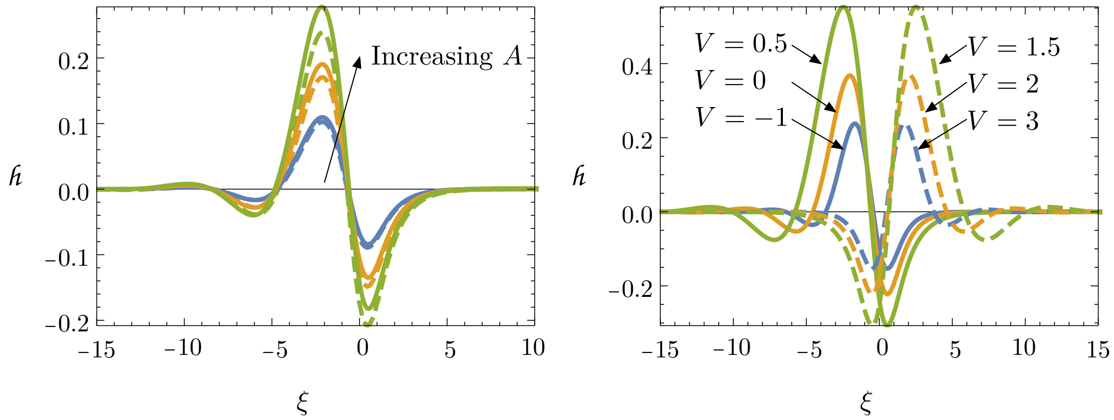

(a) $A \in \{0.3, 0.5, 0.7\}$. *(b)*

Figure 5.11: (a) Solutions of the nonlinear travelling-wave equation (5.5.1) *(solid curves), compared with solutions of the linearised equation* (5.5.2) *(dashed curves) where* $V = 0.2$ *and the applied pressure profile is the Gaussian* (5.2.12) *with amplitude* A*. (b) Solutions of the nonlinear travelling-wave equation* (5.5.1) *with* $A = 1$*, Gaussian pressure profile* (5.2.12) *and values of* V *as indicated.*

dramatically as V approaches 1, corresponding to $L \approx 0$.

The analysis of this section shows that, for a pressure source moving at constant speed, the maximum negative free surface deflection is expected to occur when the parameter L is small, i.e. when the propagation speed V is close to the characteristic speed $\mathcal{Q}'(0)$ of the underlying hyperbolic version of the PDE (5.2.10). For the case of sinusoidal sweeping of the pressure source, the propagation speed is obviously not constant, but it is instantaneously stationary at its maximum and minimum values, namely $\pm V_{\max}$ where $V_{\max} = \ell f$. We therefore hypothesise that the minimum film thickness in this case should occur when $\ell f = \mathcal{Q}'(0) \approx 1$ for the Hartmann flux function (5.2.7a) with $\mathrm{Ha} \gg 1$. This hypothesis is confirmed in figure 5.12(a), where we plot the value of f that minimises h versus ℓ. Since the magnitude of the response increases with increasing ℓ, we use gradually decreasing values of the pressure amplitude A, such that the film thickness does not become too small. It is evident that, as ℓ increases, the behaviour converges to the predicted trend $\ell f \sim 1$, which is marked as a black dashed curve.

In figure 5.12(b), we show how the minimum film thickness varies with the sweeping amplitude ℓ; as in figure 5.12(a), steadily decreasing values of A are used to prevent h from becoming too small. We note that the results computed with different values of A appear to collapse when $\hbar$ is normalised with A. Moreover,

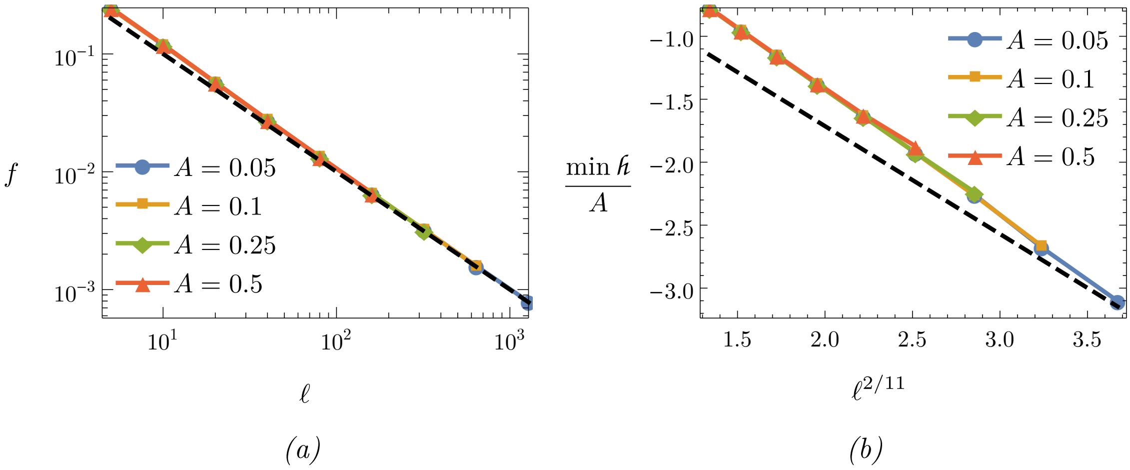

Figure 5.12: (a) Sweeping frequency f that minimises the film thickness h in the full nonlinear simulation plotted versus sweeping amplitude ℓ, for a range of values of the pressure amplitude A. The black dashed curve shows the behaviour $\ell f \sim 1$ predicted for $\ell \gg 1$. (b) Minimal deflection $\hbar$ normalised by A, computed from the full nonlinear simulation, as a function of $\ell^{2/11}$, for various values of the pressure amplitude A. The black dashed curve shows the asymptotic prediction (5.5.14)*, which corresponds here to* $\min \hbar/A \sim -0.856681\,\ell^{2/11}$.

as ℓ increases, the minimum film thickness decreases, in agreement with figure 5.9. Figure 5.12(b) indicates that $\min \hbar/A$ scales with $\ell^{2/11}$ when ℓ is large, for reasons that will be explained in the next section, by exploring in more detail the behaviour when the propagation speed is stationary but not constant.

5.5.3 Perturbed travelling wave problem

We recall that the free-surface displacement $\hbar$ in a frame that propagates with the moving pressure source is governed by the PDE (5.3.2), which may be written in the form

$$f\frac{\partial \hbar}{\partial \tau} + \frac{\partial}{\partial \xi}\left[-\ell f \dot{\mathcal{R}}(\tau)\hbar + \mathcal{Q}(\hbar)\left(1 - A\mathcal{P}'(\xi) + \frac{\partial^3 \hbar}{\partial \xi^3}\right)\right] = 0, \tag{5.5.6}$$

when the parameter α is neglected. To investigate the behaviour seen in figure 5.9, we wish to consider solutions where the sweeping amplitude ℓ is large but the frequency f is small, such that their product is order one. At first glance, it appears that the first term in (5.5.6) is then negligible, and the problem becomes quasi-steady, reducing to the travelling-wave equation (5.5.1) with the propation speed V depending parametrically on τ. However, we have argued above in § 5.5.2 that

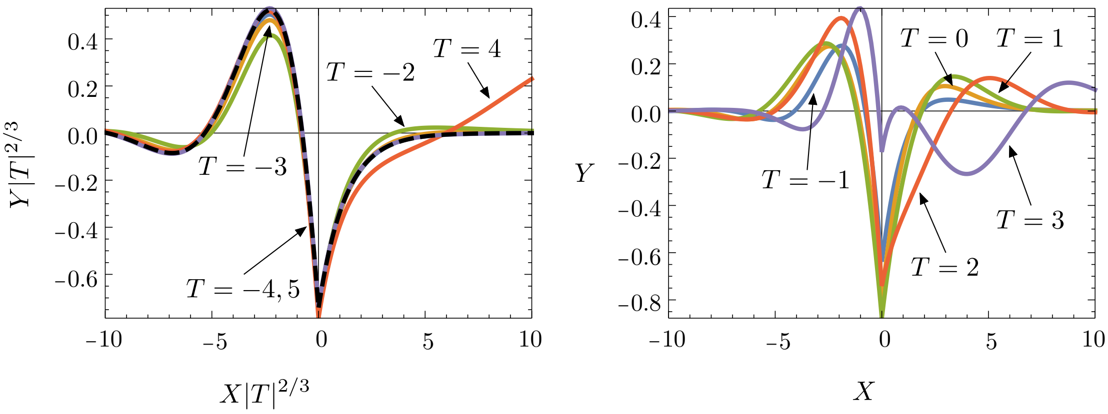

(a) Larger values of $|T|$. *(b) Smaller values of $|T|$.*

Figure 5.13: The solution $Y(X,T)$ given by equation (5.5.10) plotted versus X for various values of T. In (a), the variables X and Y are scaled with $|T|^{2/3}$ to reflect the self-similarity, and the limiting solution as $|T| \to \infty$, given by (5.5.12), is plotted as a dotted black curve; the solutions for $T = -4$ and $T = 5$ are virtually indistinguishable from the limiting solution.

large-amplitude response is expected when V is close to the characteristic speed $\mathcal{Q}'(0)$ and, indeed, the linearised equation (5.5.2) has no bounded solutions when $V = \mathcal{Q}'(0)$. We therefore seek in this section a distinguished limit where $V(\tau)$ is stationary at the critical value $\mathcal{Q}'(0)$, and the local behaviour is fully unsteady.

We simplify matters by again linearising for small $|\hbar|$ and A, and restrict our attention to sinusoidal sweeping with $\mathcal{R}(\tau) = \sin\tau$. Then the sweeping velocity $V(\tau) = \ell f \dot{\mathcal{R}}(\tau) \approx \ell f\,(1 - \tau^2/2)$ is stationary at $\tau = 0$, and we take $\ell f = \mathcal{Q}'(0)$ so that the stationary velocity is equal to the characteristic value $\mathcal{Q}'(0)$. Thus, close to $\tau = 0$, equation (5.5.6) may be approximated by

$$\frac{f}{\mathcal{Q}(0)}\frac{\partial \hbar}{\partial \tau} + \frac{\ell f}{2\mathcal{Q}(0)}\,\tau^2\frac{\partial \hbar}{\partial \xi} + \frac{\partial^4 h}{\partial \xi^4} = A\mathcal{P}''(\xi). \tag{5.5.7}$$

We normalise (5.5.7) with the scalings

$$\tau = \left(\frac{\mathcal{Q}(0)}{\mathcal{Q}'(0)}\right)^{1/11} \ell^{-3/11}T, \quad \xi = \left(\frac{\mathcal{Q}(0)}{\mathcal{Q}'(0)}\right)^{3/11} \ell^{2/11}X, \quad \hbar = A\left(\frac{\mathcal{Q}(0)}{\mathcal{Q}'(0)}\right)^{3/11} \ell^{2/11}Y. \tag{5.5.8}$$

When $\ell \gg 1$, the scalings (5.5.8) correspond to asymptotically small values of τ, which justifies *a posteriori* our Maclaurin expansion of the propagation speed $V(\tau)$. Moreover, the scale for ξ is asymptotically large, which implies that the pressure forcing term $\mathcal{P}(\xi)$ may be approximated by a delta function over $\mathcal{O}(1)$ values of X, as in the small-L limit from §5.5.2. Thus, to lowest order as $\ell \to \infty$, equation (5.5.7) reduces to the canonical PDE

$$\frac{\partial Y}{\partial T} + \frac{T^2}{2}\frac{\partial Y}{\partial X} + \frac{\partial^4 Y}{\partial X^4} = \sqrt{\pi}\,\delta''(X). \tag{5.5.9}$$

The solution of (5.5.9) subject to $Y(X,T) \to 0$ as $X \to \pm\infty$ and as $T \to -\infty$ may be written in the form

$$Y(X,T) = -\frac{2}{\sqrt{\pi}}\int_0^\infty G\left(\frac{X}{s} - \frac{T^2 s^3}{2} + \frac{T s^7}{2} - \frac{s^{11}}{6}\right) \mathrm{d}s, \tag{5.5.10}$$

where

$$G(z) := \int_{-\infty}^{\infty} k^2 \mathrm{e}^{-k^4 + \mathrm{i}kz}\,\mathrm{d}k = \frac{\Gamma(3/4)}{2}\,{}_0\mathrm{F}_2\left(\frac{1}{4};\frac{1}{2};\frac{z^4}{256}\right) - \frac{\Gamma(1/4)}{16} z^2\,{}_0\mathrm{F}_2\left(\frac{3}{4};\frac{3}{2};\frac{z^4}{256}\right) \tag{5.5.11}$$

with ${}_0\mathrm{F}_2$ denoting a generalised hypergeometric function. The solution (5.5.10) is plotted versus X for various values of T in figure 5.13. As $|T| \to \infty$, the solution becomes self-similar, with

$$Y(X,T) \sim -\frac{2^{1/3}\sqrt{\pi}}{3|T|^{2/3}} \begin{cases} 2\mathrm{e}^{X|T|^{2/3}/2^{4/3}} \cos\left(\dfrac{\sqrt{3}\,X|T|^{2/3}}{2^{4/3}} - \dfrac{\pi}{3}\right) & X < 0, \\ \mathrm{e}^{-X|T|^{2/3}/2^{1/3}} & X > 0, \end{cases} \tag{5.5.12}$$

which matches with the travelling-wave solution (5.5.5). In figure 5.13(a), we scale X and Y with $|T|^{2/3}$ to demonstrate convergence to the similarity solution (5.5.12), which is plotted as a dashed black curve.

It follows from (5.5.12) that the behaviours as $T \to -\infty$ and as $T \to +\infty$ are equivalent but, as shown in figure 5.13(b), the behaviour when $T = \mathcal{O}(1)$ does not respect this symmetry. In particular, we observe that the minimum value of Y occurs at $X = 0$ when $T \approx 1$. This observation is supported by figure 5.14, where we plot the normalised displacement at the origin, $Y(0,T)$, versus T. The red dashed curves demonstrate convergence to the similarity solution (5.5.12), with

$$Y(0,T) \sim -\frac{2^{1/3}\sqrt{\pi}}{3|T|^{2/3}} \quad \text{as} \quad |T| \to \infty. \tag{5.5.13}$$

The minimum value of $Y(0,T)$ is approximately -0.881655 when $T \approx 1.19518$. By

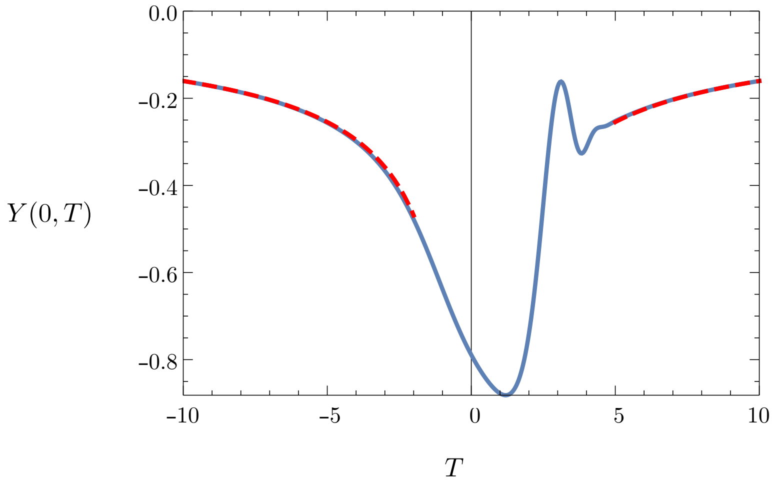

Figure 5.14: Normalised free-surface displacement at the origin, $Y(0,T)$, versus normalised time T; the large-$|T|$ behaviour (5.5.13) *is shown by the red dashed curves.*

undoing the scalings (5.5.8), we infer that the minimal free-surface displacement $\hbar$ should behave like

$$\min \hbar \sim -0.881655 \left(\frac{\mathcal{Q}(0)}{\mathcal{Q}'(0)} \right)^{3/11} \ell^{2/11}, \tag{5.5.14}$$

when $\ell \gg 1$ and $\ell f \sim \mathcal{Q}'(0)$. Figure 5.12(b) shows fairly good convergence of our computed numerical solutions to the predicted behaviour (5.5.14), which is plotted as a black dashed curve. Because of the very small exponent 2/11, extremely large values of ℓ are needed for the predicted behaviour (5.5.14) to convincingly emerge.

Since we have only analysed the linearised version of the problem, these results are only strictly valid while the free-surface displacement remains relatively small; this is why we reduce the value of A while increasing the value of ℓ in the results shown in figure 5.12. Nevertheless, our analysis explains and quantifies the behaviour observed in figure 5.9: the extremal response occurs when $\ell f \sim 1$, and increases with both the amplitude A of the applied pressure and the sweeping amplitude ℓ.

5.5.4 Higher-order resonances

In this section we explain the occurrence of the smaller local kinks and peaks in the response diagram of extremal displacement $\hbar$ versus frequency f, labelled I and II in figure 5.8.

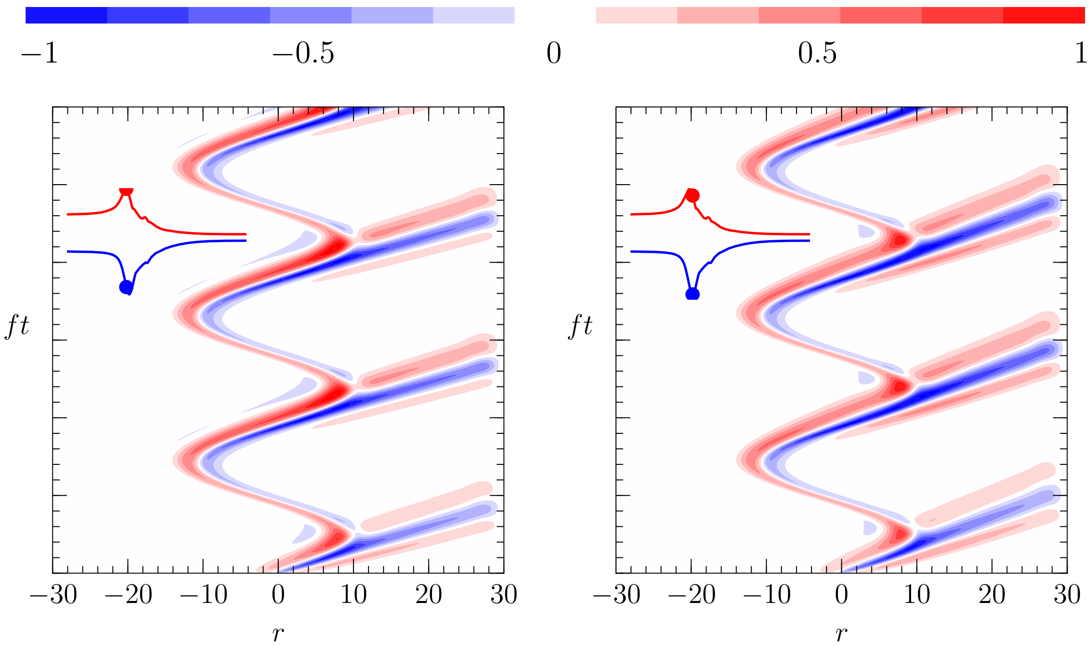

(a) $f = 0.095$*, the global maximum.* *(b)* $f = 0.12$*, the global minimum.*

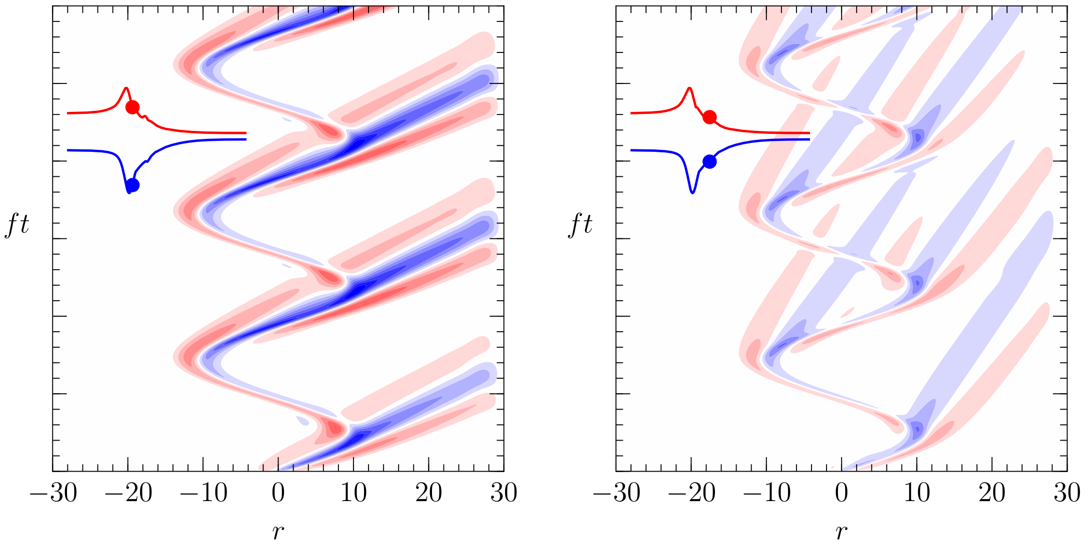

(c) $f = 0.15$*, the first gradient discontinuity.* *(d)* $f = 0.45$*, the local peak due to wave interaction.*

Figure 5.15: Time-dependent solutions of (5.2.10) *for the free-surface displacement* $\hbar(r,t)$ *with zero initial conditions and various values of the sweeping frequency parameter* f*, where* $A = 1$*,* $\mathcal{C} = 0$*, and* $\alpha = 0$*. The pressure, given by* (5.2.11)*, is a sinusoidally moving Gaussian with* $\ell = 10$*. Each plot contains an inset duplicate of figure 5.8 with small discs marking the extrema for the corresponding value of* f*. Each solution was evolved until time* $t = 20/f$*, and the time axis scaled to show the same number of oscillations in each case. The values of* f *were chosen to exhibit special features of the response diagram in figure 5.8.*

The behaviour of the solution $\hbar(r,t)$ in the (r,t)-plane as the frequency is varied is shown in figure 5.15. Figures 5.15(a) and 5.15(b) show solutions at values of f that maximise the maximal film thickness and minimise the minimal film thickness respectively. These both occur close to $f = \mathcal{Q}'(0)/\ell \approx 0.1$ here, in agreement with the travelling-wave analysis from §5.5.2. In particular, we observe in figure 5.15(b) a blue wave, corresponding to a local minimum in the film thickness, which appears to detach and propagate downstream from each inflection point in the pressure source locus. Again, this supports our hypothesis from § 5.5.2 that the minimum film thickness should occur when the translation velocity of the pressure source is stationary at the linear wave-speed $\mathcal{Q}'(0) \approx 1$.

Figure 5.15(c) shows the solution at the particular frequency marked I in figure 5.8. The maxima in $\hbar$ are indicated by the red contours in figure 5.15(c), and we observe that, at this critical frequency $f_0 \approx 0.15$, the locally maximal values of $\hbar$ upstream and downstream of the pressure source exactly coincide. Thus the slope discontinuity in the response diagram seen in figure 5.8 occurs when the location of the global supremal displacement switches, from the upstream maximum for $f < f_0$ to the downstream maximum for $f > f_0$. This switch is illustrated more explicitly in figure 5.16, where we show several local extrema competing to be the global extremum as f is varied. The local extrema are selected from partitions of the (r,t) and (ξ,t) spaces (and their intersections) based on the signs of r and ξ: upstream $(r < 0)$ and downstream $(r > 0)$ of the origin, and upstream $(\xi < 0)$ and downstream $(\xi > 0)$ of the strike point.

The local peak in the response marked II in figure 5.8 is caused by a global wave interaction. The corresponding solution in the (r,t)-plane is shown in figure 5.15(d). Consider the blue wave, corresponding to a local minimum, shed from the pressure source close to its left-most position $r \approx -10$ at $ft \approx 3\pi/2$. This wave propagates downstream at the intrinsic wave-speed $\mathcal{Q}'(0) \approx 1$ and interacts with the pressure source for a second time near its right-most position $r \approx +10$ at $ft \approx 9\pi/2$. What distinguishes this particular value of the frequency is that the blue wave is tangent to the locus of the pressure source twice, and so benefits twice from the amplification effect discussed in §5.5.2, where the propagation speed and the intrinsic wave-speed coincide.

This kind of long-range interaction can occur when a characteristic with speed $\mathrm{d}r/\mathrm{d}t = \mathcal{Q}'(0)$ is tangent to the sweeping profile $r = \ell \sin(ft)$ at $ft_1 = 3\pi/2 + \phi$ and again at $ft_2 = (2n + 1/2)\pi - \phi$, where $\phi \in (0, \pi/2]$ and n is a positive integer.

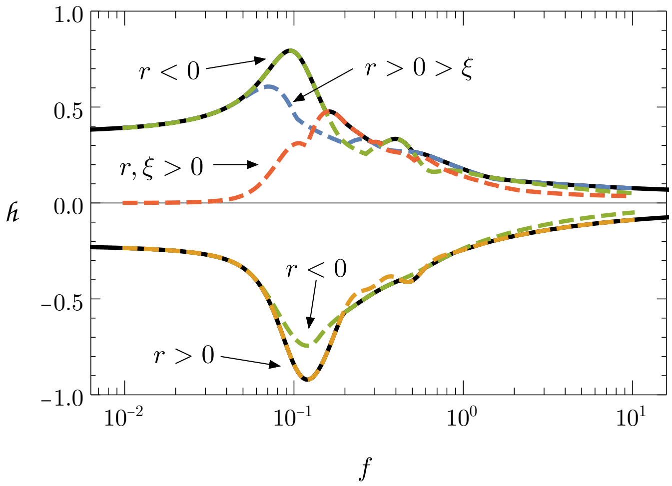

Figure 5.16: Local and global extrema of the free-surface displacement $\hbar$ plotted versus the sweeping frequency f, with $A = 1$, $\alpha = 0$ and $\ell = 10$. The dashed curves show local extrema from regions upstream ($r < 0$) and downstream ($r > 0$) of the origin, upstream ($\xi < 0$) and downstream ($\xi > 0$) of the strike point, as well as from intersections of these partitions. The underlying black curves show the global extrema.

It is straightforward to show that ϕ must satisfy the transcendental equation

$$\phi + \cot\phi = \left(n - \frac{1}{2}\right)\pi, \tag{5.5.15}$$

for an interaction where the pressure completes approximately $2n-1$ lengths of the sweeping region in time to coincide downstream with the deflection that it created upstream. The corresponding critical frequency is then given by

$$\ell f = \mathcal{Q}'(0)\,\mathrm{cosec}\,\phi. \tag{5.5.16}$$

The first interaction mode $n = 1$ gives $\phi = \pi/2$ and $\ell f = \mathcal{Q}'(0)$, which just reproduces the critical frequency for the principal response peak. The second mode $n = 2$ gives $\phi \approx 0.219$ and hence $\ell f \approx 4.6\mathcal{Q}'(0)$, which is indeed close to the critical value of f identified in figure 5.15(d) when $\ell = 10$ and $\mathcal{Q}'(0) \approx 1$. In principle, higher-order interaction modes should occur when $\ell f/\mathcal{Q}'(0) \approx 7.79$, 10.9, 14.1, …, but in practice the effect appears to be swamped by nonlinearity and damping, and we have been unable to discern any further local maxima in the response.

The analysis thus far has assumed that the plasma imparts no thermal load onto the liquid metal having fixed $\mathcal{C} = 0$. In the next section we reinstate the effects of heat transfer by considering $\mathcal{C} \neq 0$, and investigate how this influences the free surface deflections.

5.6 The hot plasma wind

In §§5.3 to 5.5, the thermocapillary flow induced by the thermal load of the plasma was neglected by setting $\mathcal{C} = 0$ in (5.2.10). In this section, we present results incorporating the thermal effects by allowing $\mathcal{C} \neq 0$. We continue to assume that the substrate is cooled uniformly, and, in the first instance, we continue to assume thermal quasi-steadiness of the substrate whereby $\kappa^*/\kappa^{s*} = \mathcal{O}(1)$ (see the left-hand side of (4.3.7b)). In § 5.6.3 we extend the model by considering the richer distinguished limit in which $\kappa^*/\kappa^{s*} = \mathcal{O}(1/\epsilon)$.

Unless stated otherwise, all simulations in this section employ the default parameter values

$$\alpha = 0, \qquad A = \iota = 1, \qquad \mathrm{Ha} = \mathcal{C} = 10. \tag{5.6.1a–c}$$

5.6.1 Steady profiles

We begin by exploring steady solutions of (5.2.10) for a stationary plasma source, i.e. $p(r,t) = \mathcal{P}(r)$, in which case the deflections satisfy

$$\mathcal{Q}(\hbar)\left(1 - A\frac{\mathrm{d}\mathcal{P}}{\mathrm{d}r} - \alpha\frac{\mathrm{d}\hbar}{\mathrm{d}r} + \frac{\mathrm{d}^3\hbar}{\mathrm{d}r^3}\right) - \mathcal{C}\,\mathcal{T}(\hbar)\frac{\mathrm{d}}{\mathrm{d}r}\left[\mathcal{P}\left(\hbar + 1 + \iota\right)\right] = \mathcal{Q}(0). \tag{5.6.2}$$

There are four free parameters that we are interested in varying: $A \geq 0$, $\alpha \geq 0$, $\iota \geq 0$, and $\mathcal{C}$. We recall that A represents the magnitude of the external pressure, the geometric parameter α represents the contribution of transverse gravity, while ι is a measure of the thermal conductivity of the substrate. The limit $\iota \to \infty$ corresponds to a thermally insulating substrate, while $\iota \to 0$ models a perfectly thermally conducting substrate. The signed parameter $\mathcal{C}$ represents the thermocapillarity-induced deflections. While typically $\mathcal{C} > 0$ because the surface tension gradient with respect to temperature, $\mathrm{d}\gamma^*/\mathrm{d}T$, is negative, for the sake of completeness we will also consider cases where $\mathcal{C} < 0$ relevant for a small class of interesting fluids for which $\mathrm{d}\gamma^*/\mathrm{d}T^* > 0$ in some temperature range. These so-called self-rewetting fluids are of interest in heat transfer applications. Aqueous solutions of higher alcohols at sufficiently high concentrations are an example of a family of fluids that have been found to exhibit this property [103, 209].

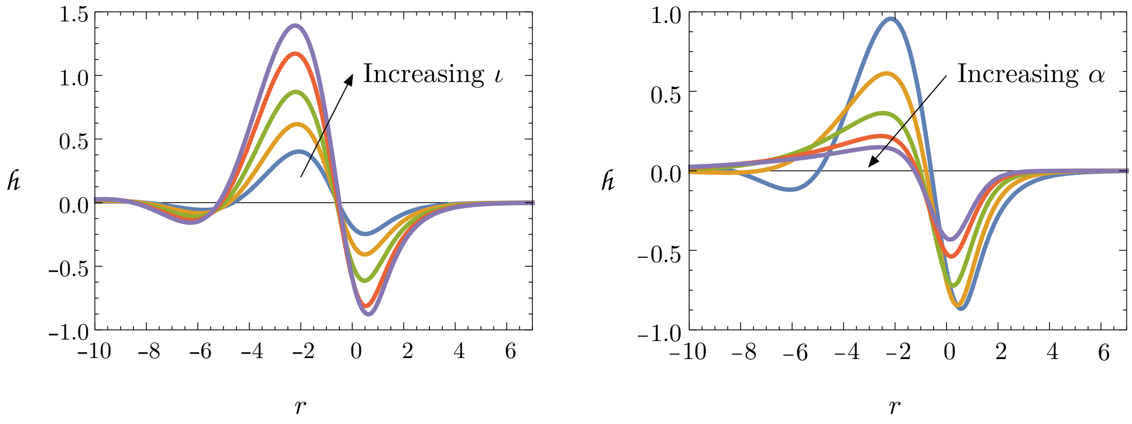

(a) $A = 1,\ \alpha = 0,\ \iota \in \{0, 5, 10, 15, 20\}$.

(b) $\iota = 20,\ A = 0,\ \alpha \in \{0, 1, 2, 3, 4\}$.

Figure 5.17: Steady deflection profiles satisfying (5.6.2), *for various values of* ι, α, *and* A, *with all other parameters given in* (5.6.1).

In figure 5.17(a) we plot solutions of (5.6.2) for varying values of ι. The deflections are amplified as ι increases, reflecting the fact that the more thermally insulating the substrate, the more dominant the thermocapillary-induced deflections, as the substrate cooling is less effective. Choosing the largest value of ι from figure 5.17(a), and neglecting the pressure exerted by the plasma by setting $A = 0$, we then vary the influence of transverse gravity, α, in figure 5.17(b). Increasing α damps the extreme peaks and spreads out the deflections over a wider region, as in the isothermal case. The choice of $A = 0$ highlights the fact that thermocapillary forces suffice to induce free-surface deflections even when the surface pressure is negligible.

In figure 5.18 we plot solutions of (5.6.2) as $\mathcal{C}$ takes both negative and positive values. As $\mathcal{C}$ increases from zero the deflections are amplified (solid curves in figure 5.18(a)). As $\mathcal{C}$ decreases below zero to -45 the deflections become smaller (dotted curves in figure 5.18(a)), and as $\mathcal{C}$ decreases further beyond $\mathcal{C} < -45$ the deflections are again amplified (figure 5.18(b)).

Notably, the sign of the deflections reverses as $\mathcal{C}$ passes through -45: for $\mathcal{C} < -45$ the deflections are positive downstream of the strike point, and negative upstream of it (preceded further upstream by the usual oscillations). We explore this sign reversal by isolating the coefficient of the forcing term $\mathrm{d}\mathcal{P}/\mathrm{d}r$ in (5.6.2), which is given by $-A\mathcal{Q}(\hbar) - \mathcal{C}\,\mathcal{T}(\hbar)(\hbar + 1 + \iota)$. To see why this is a useful quantity, note that if $\mathcal{P}$ is constant, then there are no deflections; $\hbar = 0$. It is thus the plasma gradient term $\mathrm{d}\mathcal{P}/\mathrm{d}r$ that drives the deflections. It then suffices to substitute $\hbar = 0$ into the expression for the coefficient and equate to zero to obtain the condition for

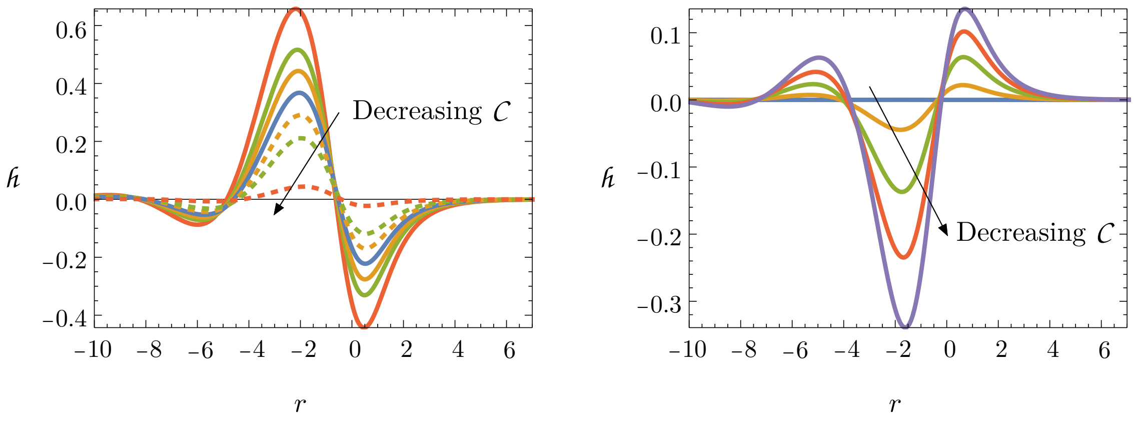

(a) $\mathcal{C} \in \{-40, -20, -10, 0, 10, 20, 40\}$. *(b)* $\mathcal{C} \in \{-45, -50, -60, -70, -80\}$.

Figure 5.18: Steady deflection profiles satisfying (5.6.2)*, for a range of* $\mathcal{C}$ *values, with all other parameters given in* (5.6.1)*.*

vanishing deflections, namely

$$\mathcal{C} = -\frac{\mathcal{Q}(0)}{\mathcal{T}(0)} \frac{A}{1+\iota}. \tag{5.6.3}$$

In the typical case of large Hartmann number, neglecting only exponentially small terms from (5.2.7) we find that

$$\mathcal{Q}(\mathscr{h}) \sim 1 + \mathscr{h} - \frac{1}{\mathrm{Ha}}, \qquad \mathcal{T}(\mathscr{h}) \sim \frac{1}{\mathrm{Ha}^2}. \tag{5.6.4a,b}$$

Criterion (5.6.3) then takes the form

$$\mathcal{C} \sim -\frac{\mathrm{Ha}(\mathrm{Ha}-1)A}{1+\iota} = -45, \tag{5.6.5}$$

for the values (5.6.1) used to produce figure 5.18.

Physically, when $\mathcal{C} > 0$, the thermocapillary forces act to reinforce the effect of the applied pressure; driving the fluid away from the strike point, thinning the film locally. However, when $\mathcal{C} < 0$, the thermocapillary forces change direction and act against the applied pressure. The reversal of the deflection direction as $\mathcal{C}$ passes through a critical value is thus explained as a force balance: for $\mathcal{C}$ above the critical $\mathcal{C}$ threshold the applied pressure dominates to determine the deflections, and beyond it the thermocapillary forces dominate.

To recap, we illustrate how the steady deflections are affected when A, α, ι, and $\mathcal{C}$ are varied. In the next section, we explore the way these parameters influence

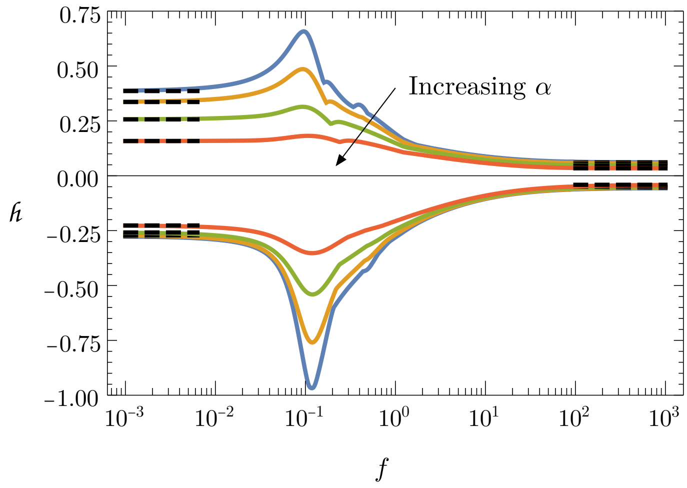

Figure 5.19: Response diagram showing the most extreme deflections $\hbar$ as a function of the sweeping frequency f, for $\alpha \in \{0.25, 0.5, 1, 2\}$ and $\ell = 10$, while other parameters are given in (5.6.1).

the time-dependent deflections.

5.6.2 Dynamic phenomena

Having used the static profiles to understand the influence of the free parameters, we proceed to examine their effect on the thin film dynamics. We follow the same approach as in § 5.5: numerically solving the time-dependent equations governing the deflections, (5.2.10), and plotting response diagrams illustrating the maximal and minimal deflections (when neglecting the impact of the initial conditions) as a function of the sweeping frequency f. We compare these to the slow and fast sweeping asymptotic limits that will be plotted at the extremes of each response diagram as black dashed lines. The leading-order slow and fast sweeping limits are obtained just as before: steady solutions are sought after all appearances of $p(r, t)$ are replaced by $\mathcal{P}(\xi)$ (along with replacing r by ξ) in the slow limit $f \ll 1$, and $\overline{p}(r)$ in the fast limit $f \gg 1$.

We have seen in the stationary case that thermocapillarity can act to amplify undesirable deflections. On the other hand, we have previously seen that increasing either the sweeping radius ℓ or the gravitational parameter α acts to reduce the deflections (see figures 5.9(b) and 5.18(b)). This remains true in the time-dependent problem, as illustrated for α in figure 5.19.

For positive $\mathcal{C}$ we find also in the dynamic case that increasing ι results in amplified deflections, as apparent from figure 5.20. While the film thickness modelled

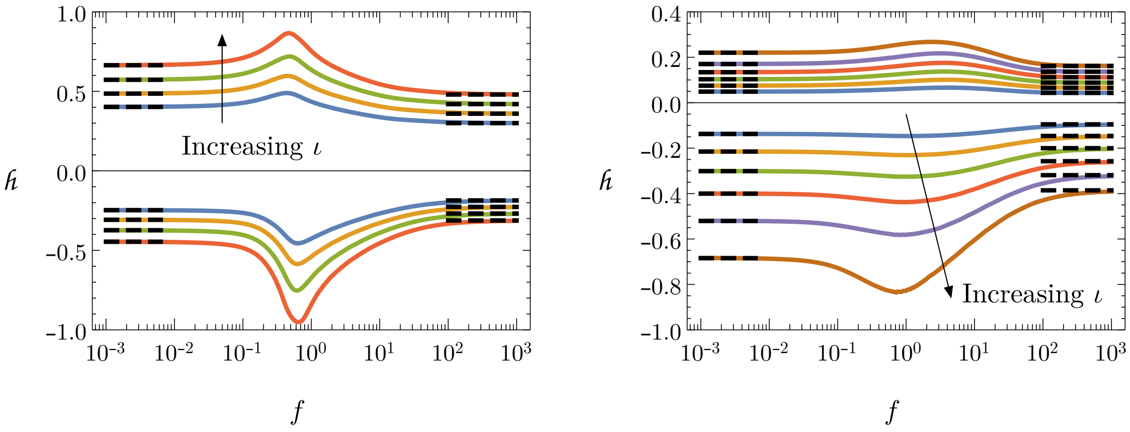

(a) $\alpha = 0$, $\iota \in \{0, 2, 4, 6\}$.

(b) $\alpha = 5$, $\iota \in \{0, 5, 10, 15, 20, 25\}$.

Figure 5.20: Response diagrams showing the extremal deflections $\hbar$ *as a function of the sweeping frequency* f*, for* $\ell = 1$ *and different values of* α *and* ι*, while other parameters are given in* (5.6.1).

by (5.2.10) cannot become zero in finite time, it remains important to avoid large deflections. In figure 5.20(a) we see that, with $\alpha = 0$, only values up to $\iota \approx 6$ are sustainable before the film becomes dangerously thin as $\hbar$ approaches -1. When damping is increased to $\alpha = 5$, values of up to $\iota \approx 25$ are sustainable before the film thins significantly, as evident in figure 5.20(b).

The threshold (5.6.5) of $\mathcal{C} \sim -\mathrm{Ha}(\mathrm{Ha}-1)A/(1+\iota) = -45$ (for the default parameters (5.6.1)) is also manifest in the dynamic simulations, as in figure 5.21. As $\mathcal{C}$ decreases, the deflections diminish until they become vanishingly small when $\mathcal{C} \sim -45$. When $\mathcal{C}$ is further decreased beyond its critical value, the deflections increase in amplitude, as seen in figure 5.21(b). The extrema have a qualitatively different envelope beyond the threshold, as the deflections are of a different form (as observed in the static case; see figure 5.18).

The film thickness, despite remaining strictly positive for all time, becomes dangerously thin for the choice of parameters in figure 5.21, with deflections attaining a minimum near $\hbar \approx -1$. With the deflections being reinforced for positive $\mathcal{C}$, this would not be a safe region of parameter space within which to be operating. Again decreasing ℓ and increasing α allows us to operate safely with negative values of $\mathcal{C}$, as illustrated in figure 5.22. In figure 5.22(a) we see that if the sweeping radius is reduced to $\ell = 1$, the deflections are reduced and values of up to $\mathcal{C} = 50$ are sustainable. In figure 5.22(b) we see that increased transverse gravity of $\alpha = 1$ allows us to sustain deflections up to $\mathcal{C} = 35$.

In this section, we explore how the magnitude of the extremal deflections varies

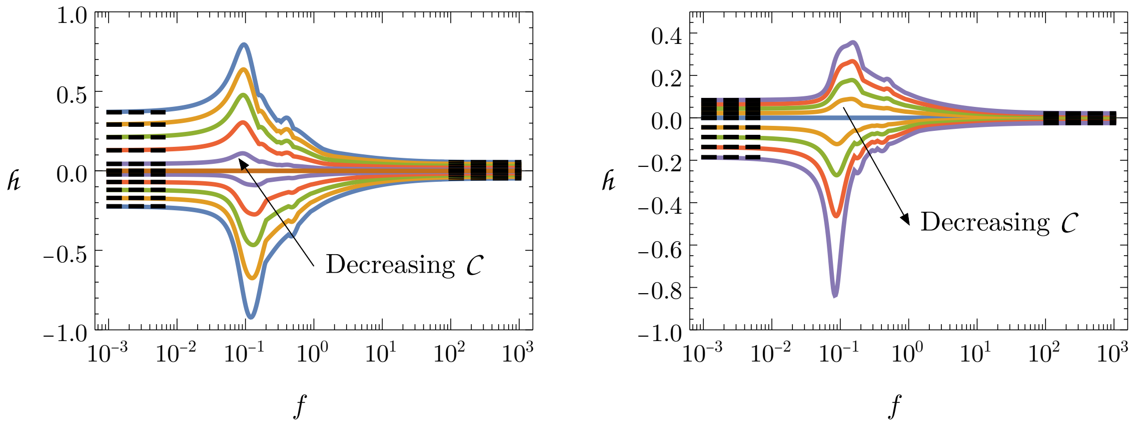

(a) $\mathcal{C} \in \{0, -10, -20, -30, -40, -45\}$. *(b)* $\mathcal{C} \in \{-45, -50, -55, -60, -65\}$.

Figure 5.21: Response diagrams showing the extremal deflections $\hbar$ *as a function of the sweeping frequency* f*, for different values of* $\mathcal{C}$*, where* $\ell = 10$ *and other parameters are given in* (5.6.1).

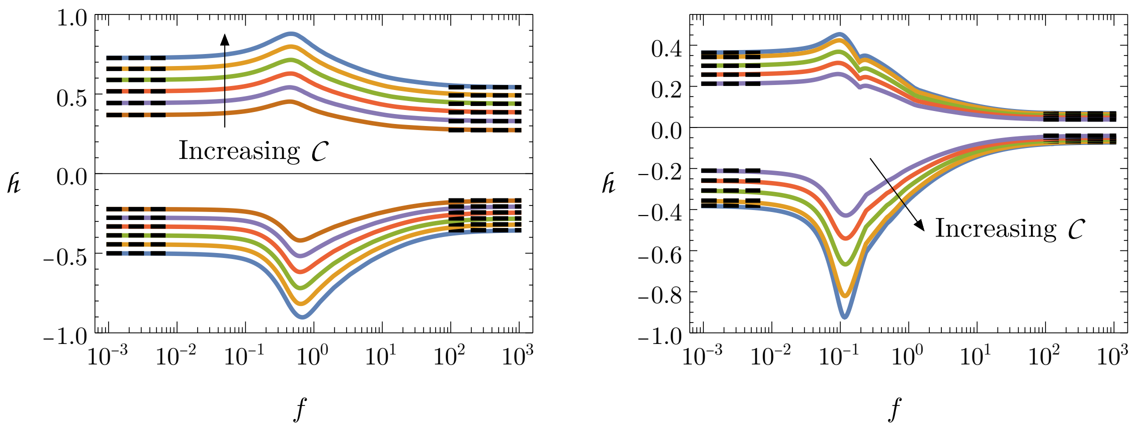

(a) $\ell = 1$, $\alpha = 0$, $\mathcal{C} \in \{0, 10, 20, 30, 40, 50\}$. *(b)* $\ell = 10$, $\alpha = 1$, $\mathcal{C} \in \{0, 10, 20, 30, 35\}$.

Figure 5.22: Response diagrams showing the extremal deflections $\hbar$ *as a function of the sweeping frequency* f*, for different values of* $\mathcal{C}$*,* ℓ*, and* α*, while other parameters are given in* (5.6.1).

with α, ι, and $\mathcal{C}$. The deflections are damped for increasing α, and amplified for increasing ι. For given A, Ha, and ι, a critical $\mathcal{C}$ exists, above or below which the pressure-induced deflections are reinforced or counteracted by thermocapillarity, respectively. The most resonant frequency appears to be invariant to changes in all of the parameters α, ι, and $\mathcal{C}$. The analysis in § 5.5.2 outlines the expectation that the most resonant frequency is $f \sim \mathcal{Q}'(0)/\ell$, and these results suggest that this expectation persists in the thermal case. In the next section, we relax the thermal quasi-steady assumption in the substrate.

5.6.3 Reintroducing a thermal time-scale

In this section, we extend the leading-order thermal model (4.3.9) derived in §4.3. Focusing on the time-dependence in the substrate, we see from (4.3.7b) that the coefficient of the term $\partial T^{\mathrm{s}}/\partial t$ is

$$\Omega = \epsilon^2 \mathrm{Pe} \frac{\kappa^*}{\kappa^{\mathrm{s}*}}. \tag{5.6.6}$$

Until now, we have considered both $\epsilon^2\mathrm{Pe}$ and Ω to be negligible as $\epsilon \to 0$. The coefficient Ω is derived assuming that, within the substrate, the variations in the vertical direction scale with $\mathscr{H}^*$. However, the vertical extent of the substrate is typically somewhat larger than the film thickness $h^{\mathrm{s}} = \mathscr{H}^{\mathrm{s}*}/\mathscr{H}^* \gg 1$. If we were to scale the vertical coordinate with $\mathscr{H}^{\mathrm{s}*}$, we would derive a larger dimensionless quantity describing the relative importance of time-dependence in the substrate, namely

$$\Omega^{\mathrm{s}} = \epsilon^2 \mathrm{Pe} \frac{\kappa^*}{\kappa^{\mathrm{s}*}} (h^{\mathrm{s}})^2. \tag{5.6.7}$$

Furthermore, the time-scale of the system governing the deflections (5.2.10) has been scaled by a factor of $\mathcal{O}(100)$ in (5.2.5), making the thermal time-scales more relevant. That is, $\Omega \mapsto \Omega(\mathscr{L}^*/\mathscr{L}^*_{\mathrm{c}}) =: \hat{\Omega}$ and $\Omega^{\mathrm{s}} \mapsto \Omega^{\mathrm{s}}(\mathscr{L}^*/\mathscr{L}^*_{\mathrm{c}}) =: \hat{\Omega}^{\mathrm{s}}$, where we henceforth drop the hats.

Guided by these two observations, we include temporal variations in the substrate by considering the distinguished limit where $\kappa^*/\kappa^{\mathrm{s}*} = \mathcal{O}(1/\epsilon^2)$, in which case the time-dependence is reinstated at leading order without having to rescale the vertical coordinate in the substrate. In this revised limit, the thermal model takes an almost identical form to system (4.3.9); the only change being that the right-hand side of (4.3.9b) is replaced by the time-derivative term $\Omega\, \partial T^{\mathrm{s}}_0/\partial t$, and an initial condition on the temperature in the substrate is imposed. The extended thermal model, dropping the zero subscript, takes the form

$$0 = \frac{\partial^2 T}{\partial y^2}, \quad \text{where } \ 0 < y < h, \tag{5.6.8a}$$

$$\Omega \frac{\partial T^{\mathrm{s}}}{\partial t} = \frac{\partial^2 T^{\mathrm{s}}}{\partial y^2}, \quad \text{where } \ -h^{\mathrm{s}} < y < 0, \tag{5.6.8b}$$

subject to

$$
\begin{aligned}
\frac{\partial T}{\partial y} &= C\mathfrak{p}(r,t) && \text{at } \ y = h, && (5.6.9\text{a})\\
T - T^{\text{s}} = \frac{\partial T}{\partial y} - \frac{k^{\text{s}*}}{k^{*}}\frac{\partial T^{\text{s}}}{\partial y} &= 0 && \text{at } \ y = 0, && (5.6.9\text{b})\\
T^{\text{s}} &= CT^{-} && \text{at } \ y = -h^{\text{s}}, && (5.6.9\text{c})\\
T^{\text{s}} &= f(r,y) && \text{at } \ t = 0. && (5.6.9\text{d})
\end{aligned}
$$

We solve the extended thermal model (5.6.8) and (5.6.9) by separation of variables, as detailed in appendix A.6, where we find that the temperature in the fluid layer is given by

$$
T(r,y,t) = (y+\iota)\,C\mathfrak{p}(r,t) + CT^{-}(r) - \iota C\nu(r,t) - \zeta(r,t), \tag{5.6.10}
$$

where ν reflects the finite thermal storage capacity of the substrate, and ζ contains the initial conditions. These quantities are defined respectively by

$$
\nu(r,t) = \sum_{n\geq 1}\frac{2}{\Lambda_n}\int_0^t \frac{\partial \mathfrak{p}}{\partial t}(r,s)\,\mathrm{e}^{-\Lambda_n(t-s)/\Omega^{\text{s}}}\,\mathrm{d}s, \quad \zeta(r,t) = \sum_{n\geq 1}(-1)^n F_n(r)\,\mathrm{e}^{-\Lambda_n t/\Omega^{\text{s}}}, \tag{5.6.11a,b}
$$

where

$$
\Lambda_n = \pi^2\left(n-\frac{1}{2}\right)^2, \qquad F_n(r) = 2\int_{-1}^{0} F(r,Y)\sin\left[\pi\left(n-\frac{1}{2}\right)(Y+1)\right]\mathrm{d}Y, \tag{5.6.11c,d}
$$

for the function F defined (with the initial substrate condition $f(r,y)$) by

$$
F(r,Y) = f(r,h^{\text{s}}Y) - (Y+1)\,\iota C\mathfrak{p}(r,0) - CT^{-}(r). \tag{5.6.11e}
$$

Including the thermal time-scale introduces the additional ν and ζ terms in the temperature profile (5.6.10). The time variation in these new terms depends exclusively on the term Ω^{s} and no other system parameter. This validates our earlier assertion that it is indeed Ω^{s} that measures the relative importance of temporal variations in the substrate temperature. The influence of the initial substrate temperature is captured by $\zeta(r,t)$, which decays and becomes negligible after an initial transient. However, sufficiently rapid variations in the plasma temperature can cause persistent dynamic effects through $\nu(r,t)$.

The temperature (5.6.10) may be used in (4.3.15) to extend the equation governing the free-surface deflections (5.2.10), which takes the extended form

$$\frac{\partial \hbar}{\partial t} + \frac{\partial}{\partial r}\left[\mathcal{Q}(\hbar)\left(1 - A\frac{\partial p}{\partial r} - \alpha\frac{\partial \hbar}{\partial r} + \frac{\partial^3 \hbar}{\partial r^3}\right)\right.$$
$$\left. -\mathcal{C}\,\mathcal{T}(\hbar)\frac{\partial}{\partial r}\left(p\,(\hbar + 1 + \iota) - \iota\nu - \frac{\zeta}{C}\right)\right] = 0. \tag{5.6.12}$$

We now aim to solve this extended deflection equation (5.6.12) numerically, to produce free-surface response diagrams for order one values of $\Omega^{\mathrm{s}} > 0$. This requires that we first address several implementation obstacles, as described below.

Numerical implementation issues

Direct numerical integration of the integral (5.6.11a) for ν is prohibitively time-consuming when solving the PDE (5.6.12). It is useful to observe that the integral may be re-expressed as follows: defining the function $\mathcal{V}_r^n$ via

$$\mathcal{V}_r^n(t_0, t_1) = \int_{t_0}^{t_1} \frac{\partial p}{\partial t}(r,s)\,\mathrm{e}^{-\Lambda_n(t_1 - s)/\Omega^{\mathrm{s}}}\,\mathrm{d}s, \tag{5.6.13}$$

we have the identities $\mathcal{V}_r^n(0,0) = 0$, and

$$\nu(r,t) = \sum_{n\geq 1} \frac{2}{\Lambda_n}\mathcal{V}_r^n(0,t). \tag{5.6.14}$$

We may develop an additive formula for increments in time by noting that

$$\begin{aligned}
\mathcal{V}_r^n(0, t+\delta) &= \int_0^{t+\delta} \frac{\partial p}{\partial t}(r,s)\,\mathrm{e}^{-\Lambda_n(t+\delta-s)/\Omega^{\mathrm{s}}}\,\mathrm{d}s \\
&= \mathrm{e}^{-\Lambda_n\delta/\Omega^{\mathrm{s}}}\int_0^{t} \frac{\partial p}{\partial t}(r,s)\,\mathrm{e}^{-\Lambda_n(t-s)/\Omega^{\mathrm{s}}}\,\mathrm{d}s + \int_t^{t+\delta} \frac{\partial p}{\partial t}(r,s)\,\mathrm{e}^{-\Lambda_n(t+\delta-s)/\Omega^{\mathrm{s}}}\,\mathrm{d}s \\
&= \mathrm{e}^{-\Lambda_n\delta/\Omega^{\mathrm{s}}}\mathcal{V}_r^n(0,t) + \mathcal{V}_r^n(t, t+\delta).
\end{aligned} \tag{5.6.15}$$

Therefore, having calculated $\nu(r,t)$ via $\mathcal{V}_r^n(0,t)$ (for some finite set of n values), we may calculate $\nu(r, t+\delta)$ by reusing $\mathcal{V}_r^n(0,t)$ and calculating $\mathcal{V}_r^n(t, t+\delta)$. For $\delta \ll 1$ this calculation is simply integration over a small domain, for which standard quadrature schemes (for example Simpson's rule [36]) are accurate and fast. Moreover, since our numerical framework implements the method of lines to solve the PDE (5.6.12), the time-stepping procedure naturally takes small steps forward in time, ensuring that $\delta \ll 1$. Furthermore, the spatial discretisation uses a static set of nodes, allowing us to store a fixed set of $\{\mathcal{V}_r^n\}_{(r,n)\in\mathcal{R}\times\mathcal{N}}$ in memory, where $\mathcal{R}$ is the set of nodes known in advance, and $\mathcal{N} = \{1, 2, \dots, N\}$ is the set of terms to be taken from the series expansion, truncated at some finite point N.

In practice, we must truncate the series expansions of ν and ζ at a finite $n = N$. Truncation error in the ζ-expansion is straightforward — coefficients F_n decay according to the smoothness of f with respect to y, accelerated by an exponential term — and manifests merely as a slightly different initial condition, which does not influence the response diagrams plotting long-time behaviour. Therefore we focus on the truncation error of the ν-expansion.

Since $\partial p/\partial t$ and its derivatives are uniformly bounded in space and time (the bound being a function only of ℓ and f), it follows that $\mathcal{V}_r^n(0,t)$ and its derivatives are uniformly bounded in space and time. Therefore, the series of term-by-term derivatives converges uniformly to $\partial\nu/\partial r$, with coefficients decaying like $\mathcal{O}(1/\Lambda_n) = \mathcal{O}(1/n^2)$.

In order to choose N to meet precision requirements, we establish a tight bound on the decay of expansion coefficients. It turns out that, since $\Lambda_n \to \infty$ as $n \to \infty$, the terms $\mathcal{V}_r^n$ decay like $\mathcal{O}(1/n)$ as $n \to \infty$, which enables us to establish the desired bound. To see this, define the partial sums ν_N by

$$\nu_N = \sum_{n=1}^{N} \frac{2}{\Lambda_n} \int_0^t \frac{\partial p}{\partial t}(r,s)\, \mathrm{e}^{-\Lambda_n(t-s)/\Omega^{\mathrm{s}}}\, \mathrm{d}s. \tag{5.6.16}$$

We are interested in quantifying the rate of decay of $|\nu - \nu_N|$. Writing the uniform bound $\left|\partial p/\partial t\right| \le P$, we find that

$$|\nu - \nu_N| \le \sum_{n>N} \frac{2}{\Lambda_n} \int_0^t \left|\frac{\partial p}{\partial t}(r,s)\right| \mathrm{e}^{-\Lambda_n(t-s)/\Omega^{\mathrm{s}}}\, \mathrm{d}s \le \frac{2P\Omega^{\mathrm{s}}}{\pi^4} \sum_{n\ge N} \frac{1}{n^4} \le \frac{2P\Omega^{\mathrm{s}}}{3\pi^4(N-1)^3}. \tag{5.6.17}$$

Thus we expect $|\nu - \nu_N| = \mathcal{O}(1/N^3)$ as $N \to \infty$. This prediction is confirmed numerically in figure 5.23, where we also see the dependence $|\nu - \nu_N| \propto \Omega^{\mathrm{s}}$. To obtain a truncation error of less than ϵ, it then suffices to choose $N > (2P\Omega^{\mathrm{s}}/3\pi^4\epsilon)^{1/3}$.

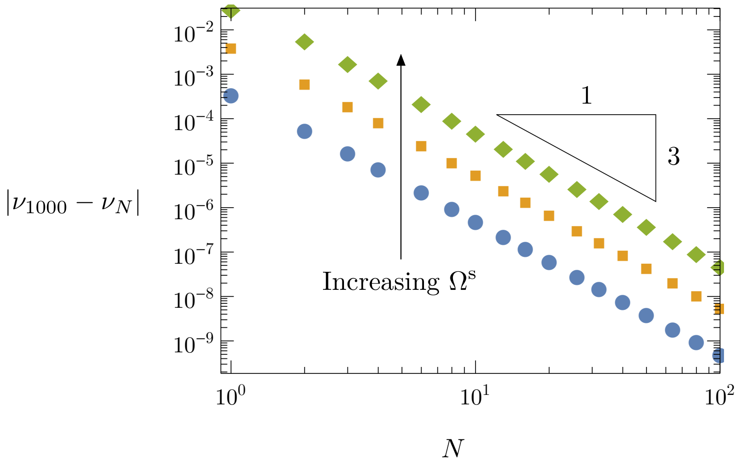

Figure 5.23: Convergence of the series expansion of ν illustrated by plotting the remainder as a function of N where $\Omega^s \in \{0.01, 0.1, 1\}$, $\ell = 10$, $f = 1$, $r = 1$, $t = \pi$. The decay rate $\mathcal{O}(\Omega^s/N^3)$ is apparent for all N.

Evaluating the integral asymptotically when $t\Lambda_n/\Omega^{\mathrm{s}} \gg 1$, we find that

$$|\nu - \nu_N| \leq \sum_{n>N} \frac{2}{\Lambda_n} \left| \int_0^t \frac{\partial p}{\partial t}(r, s) \mathrm{e}^{-\Lambda_n (t-s)/\Omega^{\mathrm{s}}} \, \mathrm{d}s \right| \sim \frac{2\Omega^{\mathrm{s}}}{3\pi^4 N^3} \left| \frac{\partial p}{\partial t}(r, t) \right|. \tag{5.6.18}$$

Therefore we expect the truncation error $|\nu - \nu_N|$ to be close to its bound (5.6.17) when $\partial p/\partial t$ is near its maximum, and significantly reduced when $\left|\partial p/\partial t\right| \ll 1$.

An alternative estimate, when $\Omega^{\mathrm{s}} \ll 1$, may be obtained via repeated integration by parts, to show that ν admits the asymptotic expansion

$$\nu \sim - \sum_{n,m \geq 1} \frac{\partial^m p}{\partial t^m}(r, t) \frac{2(\Omega^{\mathrm{s}})^m}{(-\Lambda_n)^{m+1}}. \tag{5.6.19}$$

In practice, the optimal place to truncate the series in m depends on the quantity $\ell f \, \Omega^{\mathrm{s}}/\Lambda_n$. This formula has the advantage that there are no integrals to evaluate, and thus finds good use in testing numerical implementations.

Finally, we address the choice of initial condition $f(r, y)$. When Ω^{s} is large, a long transient is required for the temperature to transition from its initial condition to its long-time behaviour. This is particularly cumbersome in the thermal case, where the additional terms ν and ζ are particularly computationally demanding, even with the improvements described above. In particular, when plotting the dynamic response diagrams, we are only interested in the long-time behaviour, independent of initial conditions (see the discussion in §5.5.1). A helpful approach is to bootstrap the numerical solution by carefully selecting the initial condition to approximate the thermal limit cycle, as described below.

Consider the extended thermal problem (5.6.8) and (5.6.9) with a long thermal time-scale $\Omega \gg 1$. A separation of scales exists with respect to the plasma oscillations that occur on a fixed time-scale of order $\mathcal{O}(1)$. Employing the multiple-scales limit where $t \mapsto (t, \tau)$ and $\tau = t/\Omega$ (with these two time-scales assumed independent, and the solution 2π-periodic in the fast time-scale t), we expand $T \sim T_0 + (1/\Omega)T_1 + \cdots$ and similarly for T^{s}. At the leading order $\mathcal{O}(\Omega)$, we find that T_0^{s} does not depend on t. At the next order $\mathcal{O}(1)$, using the t-periodicity we find a solvability condition that the temperature satisfies, namely

$$0 = \frac{\partial^2 T_0}{\partial y^2}, \quad \text{where } \ 0 < y < h, \tag{5.6.20a}$$

$$\frac{\partial T_0^{\mathrm{s}}}{\partial \tau} = \frac{\partial^2 T_0^{\mathrm{s}}}{\partial y^2}, \quad \text{where } \ -h^{\mathrm{s}} < y < 0, \tag{5.6.20b}$$

subject to the boundary conditions

$$\frac{\partial T_0}{\partial y} = C\mathfrak{p}(r,t) \qquad \text{at } \ y = h, \tag{5.6.21a}$$

$$\overline{T_0} - T_0^{\mathrm{s}} = \frac{\partial \overline{T_0}}{\partial y} - \frac{k^{\mathrm{s}*}}{k^*}\frac{\partial T_0^{\mathrm{s}}}{\partial y} = 0 \qquad \text{at } \ y = 0, \tag{5.6.21b}$$

$$T_0^{\mathrm{s}} = CT^- \qquad \text{at } \ y = -h^{\mathrm{s}}, \tag{5.6.21c}$$

where $\overline{T_0}$ denotes the fast-time-averaged temperature in the fluid. The steady state solution with respect to τ is given by

$$T_0 = CT^-(r) + y\, C\mathfrak{p}(r,t) + \iota C\, \overline{\mathfrak{p}}(r), \tag{5.6.22a}$$

$$T_0^{\mathrm{s}} = CT^-(r) + \frac{k^*}{k^{\mathrm{s}*}}(y + h^{\mathrm{s}})C\, \overline{\mathfrak{p}}(r). \tag{5.6.22b}$$

The quasi-steady fluid temperature profile (5.6.22a) exhibits t-dependence, while the steady substrate temperature (5.6.22b) does not. This time independence makes the substrate temperature (5.6.22b) a suitable choice of initial condition: for $\Omega \gg 1$, this will accurately describe long-time behaviour, while for $\Omega \lesssim 1$ the system will need only an $\mathcal{O}(1)$ transient to leave this state. Substituting the temperature (5.6.22b) for the initial condition f, we find that ζ takes the form

$$\frac{\zeta(r,t)}{C} = \iota \sum_{n \geq 1} \frac{2}{\Lambda_n} \left(\mathfrak{p}(r,0) - \overline{\mathfrak{p}}(r)\right) \mathrm{e}^{-\Lambda_n t/\Omega^{\mathrm{s}}}. \tag{5.6.23}$$

Having addressed the implementation issues encountered when extending the thermal model, we now proceed to discuss the effect of varying Ω^{s} on the deflection response diagram.

Response diagram for finite thermal time-scale

With three independent time-scales, there are many distinguished asymptotic limits to be explored. The point of reintroducing the thermal time-scale is to explore the effects of thermal inertia, and so the limit of most interest is $\Omega^{\mathrm{s}} \gtrsim \mathcal{O}(1)$.

In figure 5.24 we plot the response diagram for solutions to the thermal deflection equation (5.6.12) for increasing values of Ω^{s}. The extremal deflections are significantly damped as Ω^{s} increases, reflecting how thermal inertia becomes increasingly important for larger Ω^{s}. For small thermal inertia, the heat load on the fluid is quickly distributed through the substrate allowing surface temperatures to rise, leading to greater streamwise thermal gradients. As thermal inertia increases, the characteristic temperature time-scale in the substrate increases resulting in less rise in the substrate temperatures, leading to smaller streamwise thermal gradients and ultimately smaller deflections.

We now highlight the two limiting cases of $\Omega^{\mathrm{s}} \to \infty$ and $\Omega^{\mathrm{s}} \to 0$, for which the governing dynamic is simplified allowing us to gain useful insight. First, as Ω^{s} becomes increasingly large, a separation of time-scales emerges — the same as that used to derive (5.6.22) — whereby the leading-order substrate temperature responds to an averaged thermal flux. Taking the leading-order solution (5.6.22), along with constant T^{-}, the thermal deflection equation (5.6.12) takes the form

$$\frac{\partial \hbar}{\partial t} + \frac{\partial}{\partial r}\left[\mathcal{Q}(\hbar)\left(1 - A\frac{\partial p}{\partial r} - \alpha\frac{\partial \hbar}{\partial r} + \frac{\partial^3 \hbar}{\partial r^3}\right) - \mathcal{C}\,\mathcal{T}(\hbar)\frac{\partial}{\partial r}\left[p\left(\hbar + 1\right) + \iota\overline{p}\right]\right] = 0. \tag{5.6.24}$$

Equation (5.6.24) is almost identical to (5.2.10a); with only the heat flux density multiplying ι replaced by its fast-time average. The response diagram corresponding to solutions of (5.6.24) appears as the inner black dotted curve in figure 5.24.

In the opposite limit, $\Omega^{\mathrm{s}} \to 0$, the governing dynamic corresponds to the original quasi-steady deflection equation (5.2.10a) and is represented by the outer black dotted curve in figure 5.24. The corresponding asymptotic limits for $f \ll 1$ and $f \gg 1$ appear in figure 5.24 as black dashed lines.

We observe in figure 5.24 that, as $\Omega^{\mathrm{s}} \to 0$, the response curves tend uniformly to

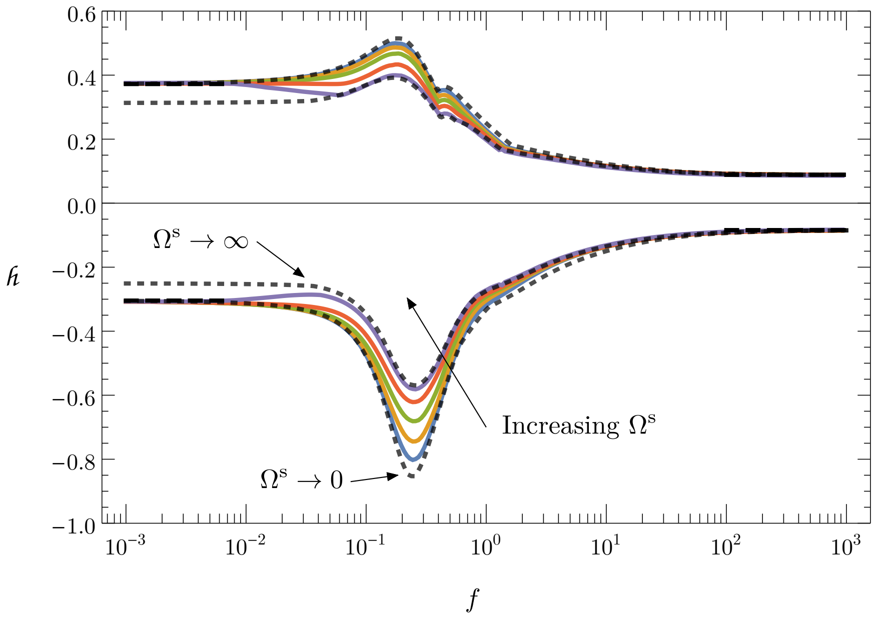

Figure 5.24: Response diagram showing the extremal deflections $\hbar$ as a function of the sweeping frequency f for solutions to the extended deflection equation (5.6.12) *with the thermal time-scale reinstated such that $\Omega^s \in \{1, 2, 4, 10, 100\}$. The outer dotted curve shows the limiting case* (5.2.10a) *of $\Omega^s \to 0$, while the inner dotted curve shows the multiple-scales limit* (5.6.24) *of $\Omega^s \to \infty$. Black dashed lines show the large-f and small-f asymptotic limits for the case of $\Omega^s \to 0$. Other parameters used were $\ell = \iota = 5$, $\alpha = 0.5$, $\mathcal{C} = 5$, with the rest given in* (5.6.1)*.*

the limiting case of $\Omega^s \to 0$ (the outer black dotted curve). However, for increasing Ω^s, while there is good agreement with the limiting case of $\Omega^s \to \infty$ (the inner black dotted curve) for $f \gtrsim 0.1$, they tend back to the $\Omega^s \to 0$ limit for small f. This is because the limiting case (5.6.24) of $\Omega^s \to \infty$ assumes a separation of scales whereby $\Omega^s \gg 1/f$. Thus, when $f \lesssim 1/\Omega^s$ this assumption breaks down as the oscillations time-scale becomes comparable to the thermal scale, and the deflections are described to leading-order by the steady solutions studied in §5.6.1. The steady solutions are time-independent and therefore independent of Ω^s, which explains why all curves converge as $f \to 0$.

The transition, from approximating the $\Omega^s \to \infty$ limiting case to reverting to the $\Omega^s \to 0$ limit, is made possible by the third time-scale, and explains the new non-monotonicity observable in figure 5.24: while all response curves plotted until now trace monotonically from $f \ll 1$ to the global extremum, the curve corresponding to $\Omega^s = 100$ first diminishes in magnitude as f increases from $f \ll 1$ to $f \approx 0.06$, then turns at a local extremum and increases in magnitude towards the global extremum near $f \approx 0.2$. This non-monotonicity establishes a new local optimum that may be exploited to suppress free surface deflections.

We further observe that the deflections all converge to the same limit for large f, independent of Ω^{s}. This is explained by the fact that, to leading-order in $1/f$ for sufficiently large f, both the pressure and thermal processes respond to a quasi-steady (time-averaged) flux density. Therefore there is no leading-order change when varying the time-dependence parameter Ω^{s}.

We have found that increasing substrate thermal conductivity ι enhances the free-surface deflections, while increasing Ω^{s} decreases them. How may we tailor the divertor design to utilise these mechanisms and achieve damping? Changing the specific heat of the liquid metal or substrate, while keeping all other material properties fixed, would increase Ω^{s} in isolation, but might prove to be a challenging materials problem. Changing the thermal conductivity of the liquid metal or the substrate would similarly increase Ω^{s}, however, this would also increase ι by the same proportion. Changing the divertor geometry by choosing the substrate thickness $h^{\mathrm{s}} \gg 1$ allows a change in Ω^{s}, also at the expense of an increase in ι, however, not in proportion: $\iota \propto h^{\mathrm{s}}$, while $\Omega^{\mathrm{s}} \propto (h^{\mathrm{s}})^2$. It might therefore be tempting to think that increasing h^{s} would overall favour a diminishing of the free-surface displacements; unfortunately, this does not turn out to be the case.

We have seen in figure 5.24 that, for extreme values of $f \ll 1$ or $f \gg 1$ the free-surface response tends to the $\Omega^{\mathrm{s}} = 0$ limit, for which we know ι enhances deflections. For intermediate f and $\Omega^{\mathrm{s}} \gg 1$, deflections are approximated by solutions to the limiting case (5.6.24), whereby deflections are also monotonic with respect to ι, as illustrated in figure 5.25(a). In figure 5.25(a) we plot with black dashed lines the approximations of each displacement curve in the limit as $f \to 0$ and $f \to \infty$, which are given by steady state computations as follows. The extremal deflections in the limit as $f \to \infty$ are computed as before; by replacing appearances of $\boldsymbol{p}$ in (5.6.24) by their fast-time-averaged $\overline{\boldsymbol{p}}$, and extracting extrema from the steady-state profile. In the $f \to 0$ limit, since (5.6.24) contains two separate flux densities, $\boldsymbol{p}(r,t)$ and $\overline{\boldsymbol{p}}(r)$, we find that the minimal deflection is well approximated when $\boldsymbol{p}$ is centred at its left-most displacement, $r = -\ell$, while the maximal deflection is given at the right-most displacement $r = \ell$. This is because the thermal influence from the substrate $\overline{\boldsymbol{p}}(r)$ has extrema at these locations, and thus when the pressure and direct thermal influence from the plasma, $\boldsymbol{p}$, are located above these peaks they reinforce the displacements.

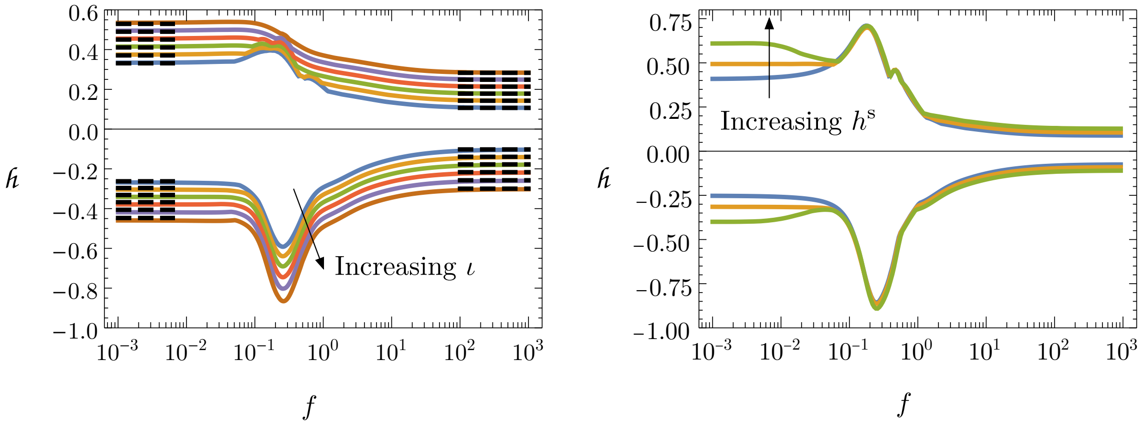

(a) $\iota \in \{10, 20, 30, 40, 50, 60\}$. (b) $h^s \in \{1, 5, 10\}$.

Figure 5.25: Response diagram showing the extremal deflections $\hbar$ as a function of the sweeping frequency f with $\alpha = 0.5$, $\ell = 5$, $\mathcal{C} = -5$, and other parameters given in (5.6.1). (a) Response for infinite thermal inertia, governed by (5.6.24) for various ι. The black dashed lines approximate the limiting behaviour for $f \to 0$ and $f \to \infty$. These are found from the steady states of (5.6.24) where $p(r,t) = \mathcal{P}(r \pm \ell)$ and $p(r,t) = \overline{p}(r)$, respectively. (b) Response for finite thermal inertia, governed by (5.6.12) with varying h^s, where thermal inertia and substrate thermal conductivity given, respectively, by $\Omega^s = (h^s)^2$ and $\iota = h^s$.

We deduce that the only regime where changing h^{s} might serve to diminish deflections is for intermediate f in the transition from $\Omega^{\mathrm{s}} \sim 1$ to $\Omega^{\mathrm{s}} \gg 1$. However, it turns out that the increase in thermal inertia for increasing Ω^{s} is balanced by the increase in thermal conductivity ι in the parameter range of interest, as illustrated in figure 5.25(b). We therefore deduce that, in the parameter range of interest, no substantial damping can come from changing h^{s}.

5.7 Summary

In this chapter, we incorporate in the model the momentum transferred to the fluid coating from the impinging plasma, and investigate the free-surface deformations driven by an oscillating plasma jet. The isothermal problem exhibits two natural time-scales: that characteristic of the motion of the applied pressure, and that characteristic of the free surface deforming under the pressure. This allows us to consider three separate regimes: where the pressure moves on a time-scale significantly slower or faster than the relaxation time, and where these time-scales are similar.

When the pressure moves slowly, the problem is quasi-steady, and the free surface deflections are given by a steady-state profile that varies parametrically with time. When the pressure moves quickly, a formal multiple scales analysis shows that the momentum is spread along the length of the pressure oscillation. This results in the free surface deforming under an effective pressure given by the time-averaged pressure profile, which results in smaller pressure gradients and therefore causes smaller deflections than in the quasi-steady case. When the pressure moves in the intermediate regime, the deflections can be significantly amplified. This large response is primarily caused by the pressure moving at a speed similar to the speed at which deflections of the free surface propagate downstream, so the pressure remains close to the trough it has created for a long time.

We use linearised models to quantify how the amplification of the free-surface response depends on the amplitude and frequency of the pressure oscillations. We demonstrate that the linear theory gives surprisingly good agreement with numerical solutions of the full nonlinear model for a wide range of parameter values. Nonetheless, it must be acknowledged that there are fundamental differences between the linear and nonlinear theories. The linear travelling-wave equation (5.5.2) admits bounded solutions that vanish in the far field for all values of L apart from the critical value $L = 0$, corresponding to $V = \mathcal{Q}'(0)$, i.e. to the propagation speed being equal to the underlying characteristic wave speed. In contrast, as shown in [101] for example, the nonlinear version (5.5.1) in general exhibits non-existence of solutions for a range of values of V close to $\mathcal{Q}'(0)$. Our unsteady simulations, however, in principle allow us to find solutions for any parameter values, including those regions of parameter space where steady or travelling-wave solutions do not exist.

While the numerical simulations presented in this chapter are for a particular magnetohydrodynamic flow, the phenomena described are generic, and apply to magnetohydrodynamic flows with different field orientations, as well as the classical hydrodynamic case. It is for this reason that the Marangoni forcing in [75], although it is derived from a different mechanism entirely, results in a term analogous to the pressure gradient in our model, and has a similar effect on the free surface.

There may be applications in which it is desirable to induce large resonant deflections. However, in the tokamak divertor, the goal is to maintain a uniform coating of the substrate. In this case, the smallest possible deflections are desirable, and are obtained by sweeping the pressure with high frequency and sufficiently large amplitude. If the system is unable to attain such high frequencies, then low frequencies should be used instead, to avoid the resonant range in which dangerous thinning of the film may occur.

In § 5.6 we extend these results to the thermal case. The two central thermal parameters introduced in the thin-film equation governing the free-surface deflections are ι and $\mathcal{C}$, representing the thermal conductivity of the substrate and the thermocapillarity-driven deflections, respectively. The deflections are amplified as these values increase. A dimensionless thermal time-scale in the substrate may also be relevant if the substrate is thick, $h^{\mathrm{s}} \gg 1$, in which case thermal inertia becomes significant. This additional time-scale presents several numerical challenges that need to be addressed in order to incorporate it tractably in a numerical solution. We find that increasing thermal inertia acts to delay (within the substrate) the thermal response to the heat load, whereby the temperatures in the fluid remain lower, thermal gradients are reduced, and thus thermocapillary-induced deflections are diminished. To exploit this in the divertor, material properties should be chosen to maximise Ω^{s} in isolation; changing the substrate thickness serves, overall, to enhance free-surface deflections. Finally, we note that the deflection amplification due to thermal effects preserves the features of the free-surface response: the most resonant frequency and the frequency of the local kinks and peaks remain unchanged as the thermal parameters vary.

In this chapter, we focus on the deflections caused by the external plasma through both momentum and energy transfer. However, we have neglected effect of the substrate cooling by considering T^{-} constant. In the next chapter we explore how spatial variations in $T^{-}(r)$ may also be leveraged to minimise the free-surface deflections.

Chapter 6

Optimal Substrate Cooling

The thermal models discussed in chapters 4 and 5 incorporate a Dirichlet temperature boundary condition on the lower side of the substrate, denoted by $T^{-}(r)$, representing the substrate temperature that is imposed by the cooling channels. We have thus far neglected its effect on the free-surface deflections, having assumed T^{-} to be constant. In this chapter, we relax this assumption and focus solely upon the effect of customising this cooling profile.

The imposed cooling temperature profile is conducted through the substrate to the liquid metal free surface, thereby inducing thermal gradients, affecting the thermocapillary flow, and ultimately the free-surface deflections. In the fusion context, large deflections make the liquid metal free surface more susceptible to atomisation and ejection which lead to depletion of the liquid metal and impurities that can contaminate the core plasma. It is thus of interest to consider the question: how can we optimally cool the divertor substrate in order to minimise the free-surface deflections? We are naturally led to address this question within the framework of optimal control theory.

While neglecting surface tension allows us to solve the optimal cooling problem and obtain simple solutions, including these higher-order effects leads to an oft-forgotten optimal control singularity. We explore the structure of the singular optimal control, and discuss approaches to regularise the singularity for the sake of practical application.

The chapter is organised as follows. In §6.1 we formalise the problem statement. In §6.2, we provide a brief and self-contained overview of to relevant results from optimal control theory. In §6.3 we discuss numerical approaches in optimal control theory and proceed to solve the optimal cooling problem in the absence of capillarity. In §6.5 we reinstate capillarity and show that the associated optimal cooling profile

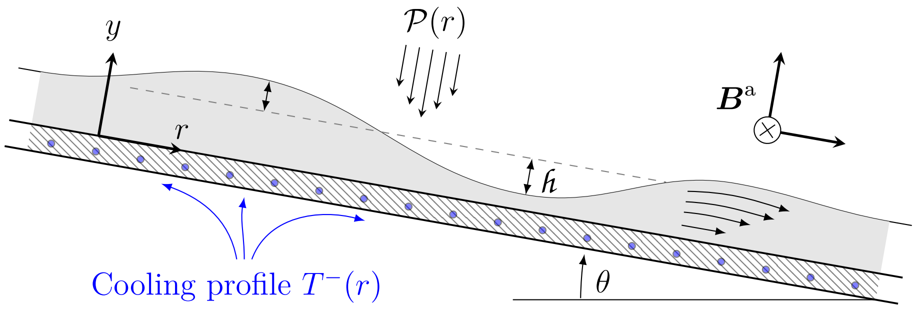

Figure 6.1: Schematic of the configuration for the optimal cooling problem. Blue circles along the lower side of the substrate indicate cooling channels which impose an arbitrary Dirichlet temperature boundary condition of $T^{-}(r)$.

is singular, and survey the relevant parts of the literature dealing with this class of problem. In § 6.7 we consider practical ways to regularise the singularity. Finally, in § 6.8 we summarise our results.

6.1 The optimal control problem statement

For this entire chapter we consider the plasma above the liquid metal to be stationary (or oscillating sufficiently fast so as to be effectively stationary), and take the steady thermal deflection equation (5.6.2), assuming a spatially varying temperature at the base of the substrate $T^{-}(r)$, to give the deflection equation

$$\mathcal{Q}(\hbar)\left(1 - A\frac{\mathrm{d}\mathcal{P}}{\mathrm{d}r} - \alpha\frac{\mathrm{d}\hbar}{\mathrm{d}r} + \frac{\mathrm{d}^3\hbar}{\mathrm{d}r^3}\right) - \mathcal{C}\,\mathcal{T}(\hbar)\left(\frac{\mathrm{d}}{\mathrm{d}r}\left[\mathcal{P}\left(\hbar + 1 + \iota\right)\right] + \frac{\mathrm{d}T^{-}}{\mathrm{d}r}\right) = \mathcal{Q}(0). \tag{6.1.1}$$

The quantity under our control is the temperature profile $T^{-}(r)$. From the deflection equation (6.1.1), we see that T^{-} alters the deflections only through its gradient (as only temperature gradients induce thermocapillary flow). In this chapter, we will only encounter the effects of temperature gradients, and thus refer to the cooling profile and its gradient interchangeably.

As illustrated in the schematic figure 6.1, the cooling channels in the substrate will be spaced at some finite distance apart. Moreover, in addition to material constraints and a limited available cooling power, we mention in §4.3 that considerations such as sputtering will constrain the desired absolute operating temperatures. Thus we assume that the cooling gradient is to be uniformly bounded, say, $|\mathrm{d}T^{-}/\mathrm{d}r| \leq U$.

We now look to formulate a functional that quantifies the deflections $\hbar(r)$. For the sake of simplicity, we begin the analysis by considering the 2-norm of the deflections

$$\|\hbar\|_2^2 = \int_{-R}^{R} \hbar(r)^2 \,\mathrm{d}r, \tag{6.1.2}$$

over some finite (but sufficiently large) domain $[-R, R]$. We will subsequently see why there is no loss in generality from considering the infinite domain. Later on we will also discuss more general norms, including terms involving the control $T^-(r)$ and the derivative of $\hbar$.

With this initial formulation, we may pose the following constrained optimal control problem: amongst all admissible cooling profiles, we seek that which minimises the deflections, that is,

$$\min_{|\mathrm{d}T^-/\mathrm{d}r| \le U} \frac{1}{2} \left\| \hbar\left(r; \frac{\mathrm{d}T^-}{\mathrm{d}r}\right) \right\|_2^2, \tag{6.1.3}$$

where $\hbar$ is subject to the deflection equation (6.1.1).

It may seem at first glance that the physical problem is ill-posed due to the lack of boundary conditions for $\hbar$. Were this not an optimisation problem this would certainly be the case; however, the optimisation problem is well posed [113], as we shall shortly explain in the literature overview of §6.2. In this particular problem, this nuance is of little consequence: we will see that sufficiently far from the strike point all optimal deflections are completely suppressed. Thus the support of the deflections $\hbar$ will be confined to a region around the origin. It is for this reason that choosing a finite domain $[-R, R]$ sacrifices no generality, and we may choose to set $\hbar$ (and its derivatives) to zero at the boundaries with no change to the result.

At the outset, we may determine the unconstrained optimiser. To do so, we need a control that ensures the 2-norm of $\hbar$ is minimal. One candidate for $\hbar$ is the best-case scenario: zero deflections. Substituting $\hbar = 0$ into (6.1.1), we can solve for the unconstrained optimal control $u_\infty = \mathrm{d}T_\infty^-/\mathrm{d}r$ via

$$u_\infty = \frac{\mathrm{d}T_\infty^-}{\mathrm{d}r} = -\left(\frac{AQ(0)}{\mathcal{C}\,\mathcal{T}(0)} + 1 + \iota\right)\frac{\mathrm{d}\mathcal{P}}{\mathrm{d}r}. \tag{6.1.4}$$

The solution (6.1.4) is nothing other than $\mathrm{d}\mathcal{P}/\mathrm{d}r$ scaled by a constant. Physically, $\mathrm{d}T_\infty^-/\mathrm{d}r$ induces a thermocapillary forcing that precisely balances the deflections driven by the thermocapillarity and pressure induced by the external plasma. We will see that this unconstrained control provides a key ingredient in the constrained optimal control.

6.2 Review of optimal control theory

For the sake of completeness, in this section we briefly recall relevant parts of optimal control literature. We begin with the system state $x : [0, \tau] \to \mathbb{R}^n$, an n-dimensional vector function of time, where τ is the terminal time, subject to some autonomous dynamic f,

$$\frac{\mathrm{d}x}{\mathrm{d}t} = f(x(t), u(t)), \tag{6.2.1}$$

influenced by an admissible scalar control $u \in \mathcal{U}$, where $\mathcal{U}$ is the set of admissible controls. The state is subject to $k \geq 0$ initial and terminal conditions

$$g(x(0), x(\tau)) = 0, \tag{6.2.2}$$

where $g : \mathbb{R}^n \times \mathbb{R}^n \to \mathbb{R}^k$. We are interested in the fixed-time problem of minimising the functional

$$\min_{u \in \mathcal{U}} \int_0^\tau L(x, u) \, \mathrm{d}t, \tag{6.2.3}$$

subject to (6.2.1) and (6.2.2), where τ is fixed *a-priori*. An important class of problems we will not cover here is the free-time problem where τ is unknown, to be determined by the optimisation.

Following Pontryagin [162], we introduce another vector function called the costate or adjoint (in analogy with Lagrange multipliers that adjoin the differential constraints to the functional) which we denote $\lambda(t) = (\lambda_1(t), \ldots, \lambda_n(t)) \in \mathbb{R}^n$. Defining the Hamiltonian

$$H = \lambda^T f(x, u) + \lambda_0 L(x, u), \tag{6.2.4}$$

we require that the costate satisfy

$$\frac{\mathrm{d}\lambda}{\mathrm{d}t} = -\nabla_x H(x, \lambda), \tag{6.2.5}$$

and the transversality conditions

$$\lambda(0) = \nabla_{x(0)}\, \mu^T g(x(0), x(\tau)), \qquad \lambda(\tau) = -\nabla_{x(\tau)}\, \mu^T g(x(0), x(\tau)), \tag{6.2.6a}$$

where $\mu \in \mathbb{R}^k$ is some constant vector. We briefly explain the transversality conditions by way of example, referring the reader to [113] for further discussion and examples.

Consider the case where $k = n$ initial conditions are specified in (6.2.2), say

$$g(x(0), x(\tau)) = x(0) - x_0, \tag{6.2.7}$$

for some initial conditions vector $x_0 \in \mathbb{R}^n$. The transversality conditions (6.2.6) then take the form

$$\lambda(0) = \mu, \qquad\qquad \lambda(\tau) = 0. \tag{6.2.8a,b}$$

That is, the costate is free initially at $t = 0$, and zero at the terminal time $t = \tau$. Similarly, had we specified the terminal state $x(\tau)$, the costate would be free at the terminal time, and zero initially. In general, for every initial condition we specify of $x_i(0)$ the corresponding costate $\lambda_i(0)$ is free, and so too for the terminal time. Thus we find that any subset of initial and terminal conditions may be specified of the state, and the transversality conditions complement these to yield $2n$ conditions for $2n$ ODEs. In particular, in our problem we leave the state free at both boundaries (space r will play the role of time t as the independent variable), which results in vanishing boundary conditions for the costate and the expected overall number of boundary conditions.

Having introduced the adjoint equations and the Hamiltonian, we state Pontryagin's celebrated Maximum/Minimum Principle (for more explicit technical requirements and a proof of the theorem, we refer the reader to [71, 113, 162] and references therein) which we subsequently refer to as PMP: For any optimal state and associated admissible control (x^*, u^*) satisfying (6.2.1) and (6.2.2), there exists a constant λ_0^* and an absolutely continuous costate $\lambda^*(t)$ satisfying (6.2.5) and (6.2.6) such that

$$H(x^*, u^*, \lambda^*) = \min_{u \in \mathcal{U}} H(x^*, u, \lambda^*), \tag{6.2.9}$$

and at all time, not all λ_0^* and $\lambda^*(t) = (\lambda_1^*(t), \ldots, \lambda_n^*(t))^T$ are zero. We have used asterisks to denote optimal state, control, and costate variables as is conventional in the literature. To simplify the notation (and so as not to confuse these quantities with dimensional quantities) we drop the asterisks from now on.

Of particular interest are models in which the control appears affinely in the dynamics $f(x, u)$, and functional integrand $L(x, u)$, and the admissible set is bounded at each time t, say $|u(t)| \leq U$. In this case, it follows from (6.2.4) that the Hamiltonian is also affine with respect to the control, and we write

$$H = \psi(x, \lambda) + u\, \phi(x, \lambda). \tag{6.2.10}$$

It follows from PMP (6.2.9) that if $\phi \neq 0$ the control is given by $u = -U \operatorname{sign}(\phi)$. For this reason ϕ is called the switching function, and the control, which may switch discontinuously between its upper and lower bound, is called a bang-bang control. A time interval (known as an arc) for which $\phi \neq 0$ is called a non-singular arc (see [17] for an in-depth discussion of the nature of the singularity).

On a singular arc, where $\phi = 0$, the Hamiltonian is independent of the control. We can, in general, still derive the optimal control by differentiating the identity $\phi = 0$ and substituting all state and costate derivatives by the right-hand sides of (6.2.1) and (6.2.5) until we first obtain an expression in which, when evaluated along the singular arc, the control u appears. The control can only appear affinely, allowing us to isolate u, giving the form of the optimal control. It transpires that the number of derivatives required must be even [115], and so we define the local order of a singular arc on the interval (t_0, t_1) to be the lowest integer m such that

$$\frac{\partial}{\partial u}\left(\frac{\partial^{2m}\phi}{\partial t^{2m}}\right) \neq 0, \tag{6.2.11}$$

for all $t \in (t_0, t_1)$ according to the procedure described above (see [115] for the nuanced but important distinction between local order and intrinsic order). We now use this definition to describe a further necessary condition of optimality.

PMP is a first-order condition that is necessary for optimality, analogous to the Euler–Lagrange equations of the Calculus of Variations. The optimality of singular arcs — where the Hamiltonian is independent of the control — was a subject of much uncertainty early on in the literature [168]. The generalised Legendre-Clebsch (GLC) condition settled much of this uncertainty, constituting a necessary condition that must be satisfied on singular arcs. The GLC condition is analogous to a higher-order local convexity condition, and requires that for a singular arc of local order

m on $t \in (t_0, t_1)$, the inequality

$$(-1)^m \frac{\partial}{\partial u}\left(\frac{\partial^{2m}\phi}{\partial t^{2m}}\right) \geq 0, \tag{6.2.12}$$

is satisfied for all $t \in (t_0, t_1)$. The strengthened GLC holds when the inequality (6.2.12) is strong.

In most applications it is assumed that $\lambda_0 \neq 0$. Since the costate is defined up to a multiplicative constant, this assumption allows for the normalisation $\lambda_0 = 1$, without loss of generality. Cases in which $\lambda_0 = 0$ are called abnormal.

We now apply the above theory to our optimal control problem (6.1.3) minimising the free-surface deflections via thermal control of the substrate cooling.

6.3 Optimal cooling without capillarity

It is instructive to begin by considering a simplified form of the problem (6.1.3) where the third-order capillarity term is negligible. Recall from the derivation of the deflection equation in §5.2 that we rescaled the horizontal coordinate with the capillary length. In cases where the capillary length is significantly shorter than the length-scale of the plasma flux density (on the order of $\mathcal{O}(1)$ cm), capillarity is negligible on the plasma flux density length-scale, i.e. $\mathrm{Bo} \gg (100\epsilon)^3$, and may be neglected. The optimal cooling problem then reads

$$\min_{|u|\leq U} \frac{1}{2}\|\hbar\|_2^2, \tag{6.3.1a}$$

subject to the first-order deflection equation

$$\begin{aligned}\frac{\mathrm{d}\hbar}{\mathrm{d}r} = \frac{1}{\alpha\mathcal{Q}(\hbar) + \mathcal{C}\,\mathcal{T}(\hbar)\mathcal{P}}\Bigg[&\mathcal{Q}(\hbar)\left(1 - A\frac{\mathrm{d}\mathcal{P}}{\mathrm{d}r}\right) - \mathcal{Q}(0)\\ &-\mathcal{C}\,\mathcal{T}(\hbar)\left((\hbar + 1 + \iota)\frac{\mathrm{d}\mathcal{P}}{\mathrm{d}r} + u\right)\Bigg],\end{aligned} \tag{6.3.1b}$$

where we denote $u = \mathrm{d}T^-/\mathrm{d}r$.

To employ PMP as outlined in §6.2, we require an autonomous system. A standard lifting procedure may be used to turn equation (6.3.1b) into a two-dimensional autonomous system. Introducing the auxiliary variable a, we write

$$\frac{\mathrm{d}\hbar}{\mathrm{d}r} = f(\hbar, a, u), \qquad \frac{\mathrm{d}a}{\mathrm{d}r} = 1. \tag{6.3.2a,b}$$

where the dynamic f is defined by

$$f(\hbar, a, u) = \frac{1}{\alpha \mathcal{Q}(\hbar) + \mathcal{C}\,\mathcal{T}(\hbar)\mathcal{P}(a)} \left[\mathcal{Q}(\hbar)\left(1 - A\frac{\mathrm{d}\mathcal{P}}{\mathrm{d}r}(a)\right) - \mathcal{Q}(0) \right.$$
$$\left. - \mathcal{C}\,\mathcal{T}(\hbar)\left((\hbar + 1 + \iota)\frac{\mathrm{d}\mathcal{P}}{\mathrm{d}r}(a) + u\right)\right], \qquad (6.3.2c)$$

and subject to the boundary condition

$$a(-R) = -R. \qquad (6.3.3)$$

System (6.3.2) is now autonomous of dimension $n = 2$, thus the costate is also two-dimensional $\lambda = (\lambda_1, \lambda_2)^T$. The Hamiltonian takes the form

$$H = \lambda_1 f(\hbar, a, u) + \lambda_2 + \frac{\lambda_0}{2}\hbar^2, \qquad (6.3.4)$$

where λ_0 is a constant. The costate satisfies the adjoint equations

$$\frac{\mathrm{d}\lambda_1}{\mathrm{d}r} = -\lambda_1 \frac{\partial f}{\partial \hbar} + \lambda_0 \hbar, \qquad \frac{\mathrm{d}\lambda_2}{\mathrm{d}r} = -\lambda_1 \frac{\partial f}{\partial a}. \qquad (6.3.5a,b)$$

subject to the three boundary conditions

$$\lambda_1(-R) = \lambda_1(R) = \lambda_2(R) = 0. \qquad (6.3.6)$$

It follows from (6.3.6) and the nontriviality of (λ_0, λ) guaranteed by PMP that $\lambda_0 \neq 0$. Therefore, without loss of generality, we take $\lambda_0 = 1$.

The dynamic f is affine with respect to u, while the functional integrand does not depend on the control, therefore, the switching function $\phi = \partial H/\partial u$, determines the optimal control. We find that the switching function is given by

$$\phi = \lambda_1 \frac{\partial f}{\partial u} = -\lambda_1 \frac{\mathcal{C}\,\mathcal{T}(\hbar)}{\alpha \mathcal{Q}(\hbar) + \mathcal{C}\,\mathcal{T}(\hbar)\mathcal{P}(a)}. \qquad (6.3.7)$$

The flux function $\mathcal{T}$ is positive (see the definitions following (5.2.10a)), therefore $\operatorname{sign}(\phi) = -\operatorname{sign}(\mathcal{C}\lambda_1)$, and then it follows from (6.3.7) that the optimal control takes the form $u = U \operatorname{sign}(\mathcal{C}\lambda_1)$ on non-singular arcs (where $\lambda_1 \neq 0$). As described earlier, singular arcs are time intervals over which the switching function vanishes. When $\phi = 0$ it follows that $\lambda_1 = 0$ and therefore $\mathrm{d}\lambda_1/\mathrm{d}r = 0$ on this interval. Then from (6.3.5) we infer that $\hbar = 0$, in which case the optimal control is given by the unconstrained optimum (6.1.4). We have thus completely determined the optimal control (as a function of the yet unknown state and costate):

$$u = \begin{cases} U\,\mathrm{sign}(\lambda_1), & \lambda_1 \neq 0, \\ u_\infty, & \lambda_1 = 0. \end{cases} \tag{6.3.8}$$

We check that singular arcs, if they exist, satisfy the strengthened GLC condition. First, we must calculate the local order of singular arcs. When $\mathrm{d}\phi/\mathrm{d}r$ is expanded as described in §6.2, we find, as anticipated, no dependence on u. Differentiating once more, we find that on all singular arcs

$$(-1)\,\frac{\partial}{\partial u}\left(\frac{\mathrm{d}^2\phi}{\mathrm{d}r^2}\right) = \left(\frac{\mathcal{C}\,\mathcal{T}(0)}{\alpha\mathcal{Q}(0) + \mathcal{C}\,\mathcal{T}(0)\mathcal{P}(a)}\right)^2 > 0. \tag{6.3.9}$$

Therefore the local order of all singular arcs is $m = 1$ and the strengthened GLC condition is satisfied.

With the optimal control determined via PMP, it remains only to solve the so-called two-point boundary value problem comprising the four ODEs given in (6.3.2) and (6.3.5) and four boundary conditions (6.3.3) and (6.3.6). These systems are typically challenging to solve, even numerically. In § 6.4 we introduce a numerical method to accomplish this, and compare it to an alternative numerical approach for solving the optimal control problem more directly.

6.4 Numerical approaches in optimal control

There are two primary approaches described in the literature for finding numerical solutions to optimal control problems. The first is known as the direct approach, whereby the optimal control problem is discretised and solved as a nonlinear program (NLP) using standard techniques. The second approach, the indirect approach, is to solve the boundary value problem arising from PMP. This dichotomy may be thought of as a case of discretise-then-optimise versus optimise-then-discretise, respectively.

Each approach has advantages and disadvantages, and which is more suitable depends on features of the problem at hand (see [116, 198, 232] and references therein). In this section, we implement one direct and one indirect method.

6.4.1 Direct approach

The direct method is implemented by discretising the spatial domain into N intervals. We describe a control that is constant on each interval (higher order control discretisations are constructed similarly), denoting its value on interval j by u_j, for $j = 1, \ldots, N$. Beginning on the left-hand side of the domain and denoting the (in our case unspecified) initial condition by $\hbar_0 = \hbar(-R)$, we integrate the differential equation (6.3.1b) over interval $j = 1$ (using any chosen numerical integration scheme) to give the state on the right-hand side of the interval, say $\hbar_1(\hbar_0, u_1)$, where we emphasise the dependence on $\hbar_0$ and u_1. Integrating on interval $j = 2$ using $\hbar_1$ as the initial condition, we obtain $\hbar_2(\hbar_1, u_2)$, and so forth. Ultimately, we arrive at an approximation for the state at all interval endpoints $\{\hbar_j\}$. Denoting the discretisation (using any chosen numerical quadrature scheme) of the objective (6.3.1a) by $\mathcal{L}(\{\hbar_j\})$, we may write the discrete optimal control problem in the form

$$\min_{\hbar_0, \{u_j\}} \mathcal{L}(\{\hbar_j\}), \tag{6.4.1a}$$

subject to

$$|u_j| \leq U. \tag{6.4.1b}$$

This approach is called a single-shooting approach, because the NLP includes only $\hbar_0$ as a decision variable in the optimisation. It turns out that this formulation suffers from severe convergence issues, which are most easily alleviated by a multiple-shooting approach [16], whereby the values $\{\hbar_k\}_{k \in K}$, for some index set $K \subseteq \{1, \ldots, N\}$, are augmented with decision variables $\left\{\tilde{\hbar}_k\right\}_{k \in K}$. Each new variable $\tilde{\hbar}_k$ is used as the initial condition in the integration on interval $j = k$, and additional constraints are added to enforce continuity between the variables and their augmented counterparts. This is equivalent to partitioning the spatial domain into $|K| + 1$ partitions, applying a single-shooting approach on each partition, and ensuring that the partitions are continuously stitched. For the purpose of demonstration, we highlight how this would be done when $K = \{2\}$. Augmenting $\hbar_2$ with the variable $\tilde{\hbar}_2$, we use this new variable as the initial condition for integrating on interval $j = 2$ instead of $\hbar_2$, so that $\hbar_3 = \hbar_3\left(\tilde{\hbar}_2, u_2\right)$. We also add the constraint

$\tilde{\hbar}_2 = \hbar_2$, to give the revised NLP, namely

$$\min_{\hbar_0, \tilde{\hbar}_2, \{u_j\}} \mathcal{L}(\{\hbar_j\}), \tag{6.4.2a}$$

subject to

$$\tilde{\hbar}_2 = \hbar_2, \qquad |u_j| \leq U. \tag{6.4.2b}$$

The trade-off for improving the convergence is a higher-dimensional NLP. To obtain maximal control resolution, we implement a multiple shooting method where K is exhaustive, that is, $K = \{1, \dots, N\}$.

The discrete formulation is encoded using CasADi, a framework that performs automatic differentiation to extract useful derivative information to be passed to the NLP solver [9]. We use the IPOPT solver, which employs an interior-point method [211].

6.4.2 Indirect approach

The indirect method we employ here is the forward-backward sweep method [129]. An initial guess is made for the costate $\lambda(r)$ and initial condition $\hbar(-R)$. Then the *forward* dynamic (6.3.1b) is integrated numerically using these guesses, to give the first iterate of the state $\hbar(r)$. This iterate is then employed in solving the adjoint problem (6.3.5) and (6.3.6) *backwards* to produce an updated iterate of the costate. This procedure is repeated until convergence is obtained whereby the updates are negligible and the first boundary condition in (6.3.6) is satisfied; $\lambda_1(-R) = 0$ which is never explicitly enforced. This method is closely related to the method of successive approximations [31, 116]. It requires a sufficiently good initial guess for the costate but still does not exhibit robust convergence for this deflection problem. Nonetheless it is useful to compare with the results of the direct approach, as we do in figure 6.2, where we find good agreement between the two methods.

The rest of the numerical results presented in this chapter use the direct approach, as it was found to be faster and to exhibit more robust convergence on the problems considered (in fact, the chattering solutions that we will encounter below make the indirect method ill-posed [27]). While this approach does not leverage PMP directly, we will see that PMP is indispensable in understanding the structure

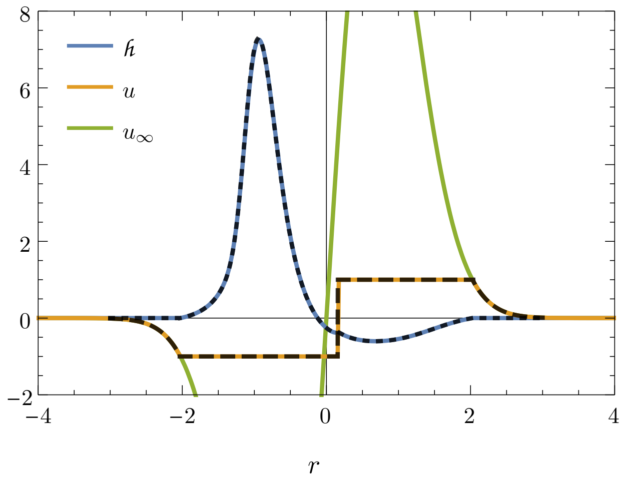

Figure 6.2: Solutions of the first-order problem (6.3.1) *using the direct (solid coloured curves) and indirect (broken black curves) numerical approaches where* $U = 1$ *and other parameters are defined in* (6.4.3)*.*

of the solution. Unless stated otherwise all figures use the parameter choices

$$\mathcal{C} = \mathrm{Ha} = 10, \qquad \iota = 5, \qquad U = A = 1, \qquad \alpha = 0, \qquad \mathcal{P}(r) = \mathrm{e}^{-r^2}. \qquad \text{(6.4.3a–e)}$$

In figure 6.3 we plot the solutions for various control bounds U. We first note that the control is of the form predicted by PMP (6.3.8): for small enough U, the optimal control u is bang-bang in a region around the strike point where $u_\infty > U$. Beyond this region the control coincides with the unconstrained optimum on singular arcs and the deflections vanish. For larger U, an additional inner region emerges in close proximity to the strike point where the control is singular, coinciding with the unconstrained optimal control u_∞. Outside this local inner region it takes on a constant value, and finally singular arcs extend beyond the bang-bang region extending to the far-field just as in the first case. This confirms the earlier comment that the choice of domain $[-R, R]$ does not matter for sufficiently large R (that depends on U), since the deflections are suppressed outside a neighbourhood of the origin.

We further observe that, as the control bound U is increased, greater control increasingly suppresses deflections. The force of gravity causes the upstream deflection to be significantly more pronounced than its downstream counterpart, and is also the reason why the control switch (from $u = -U$ to $u = U$ for the bang-bang controls with small U, or the centre of the inner singular region for larger U) occurs downstream of the strike point $r = 0$.

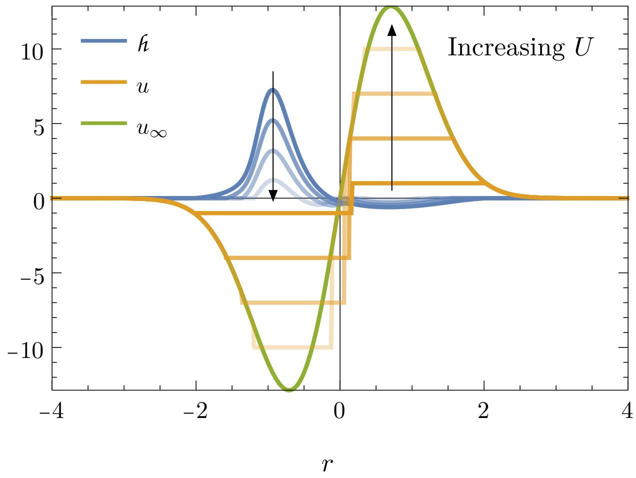

Figure 6.3: Solutions of the first-order problem (6.3.1) *for various control bounds* $U \in \{1, 4, 7, 10\}$ *with other parameters defined in* (6.4.3).

This completes the solution for the first-order optimal control problem (6.3.1). We now reinstate capillarity, and proceed with an analogous approach. The results transpire to be remarkably different from those for the first-order problem, uncovering an interesting phenomenon regarding the transition from non-singular to singular arcs.

6.5 Reinstating capillarity

In this section, we reinstate capillarity, and the optimal control problem is the full problem given by (6.1.3).

To apply PMP, we lift equation (6.1.1) to a four-dimensional autonomous system by introducing three auxiliary variables via

$$\frac{\mathrm{d}\hbar}{\mathrm{d}r} = a_1, \qquad \frac{\mathrm{d}a_1}{\mathrm{d}r} = a_2, \qquad \frac{\mathrm{d}a_2}{\mathrm{d}r} = f(\hbar, a_1, a_3, u), \qquad \frac{\mathrm{d}a_3}{\mathrm{d}r} = 1, \tag{6.5.1a–d}$$

where the dynamic f is given by

$$f = \frac{\mathcal{Q}(0)}{\mathcal{Q}(\hbar)} - \left(1 - A\frac{\mathrm{d}\mathcal{P}}{\mathrm{d}r}(a_3) - \alpha\, a_1\right) + \mathcal{C}\frac{\mathcal{T}(\hbar)}{\mathcal{Q}(\hbar)}\left((\hbar + 1 + \iota)\frac{\mathrm{d}\mathcal{P}}{\mathrm{d}r}(a_3) + a_1\mathcal{P}(a_3) + u\right), \tag{6.5.1e}$$

subject to the boundary condition

$$a_3(-R) = -R. \tag{6.5.2}$$

The normal Hamiltonian takes the form

$$H = \lambda_1 a_1 + \lambda_2 a_2 + \lambda_3 f(\hbar, a_1, a_3, u) + \lambda_4 + \frac{1}{2}\hbar^2, \tag{6.5.3}$$

where the four-dimensional costate λ satisfies

$$\frac{\mathrm{d}\lambda_1}{\mathrm{d}r} = -\lambda_3 \frac{\partial f}{\partial \hbar} - \hbar, \qquad \frac{\mathrm{d}\lambda_3}{\mathrm{d}r} = -\lambda_2, \tag{6.5.4a,c}$$

$$\frac{\mathrm{d}\lambda_2}{\mathrm{d}r} = -\lambda_1 - \lambda_3 \frac{\partial f}{\partial a_1}, \qquad \frac{\mathrm{d}\lambda_4}{\mathrm{d}r} = -\lambda_3 \frac{\partial f}{\partial a_3}. \tag{6.5.4b,d}$$

subject to the boundary conditions

$$\lambda_1(-R) = \lambda_2(-R) = \lambda_3(-R) = 0, \tag{6.5.5a}$$

$$\lambda_1(R) = \lambda_2(R) = \lambda_3(R) = \lambda_4(R) = 0. \tag{6.5.5b}$$

The full problem (6.1.3) is affine in the control, and the switching function is given by

$$\phi = \frac{\partial H}{\partial u} = \lambda_3 \frac{\partial f}{\partial u} = \lambda_3 \mathcal{C} \frac{\mathcal{T}(\hbar)}{\mathcal{Q}(\hbar)}. \tag{6.5.6}$$

Similarly to the first-order case, we find that $\operatorname{sign}(\phi) = \operatorname{sign}(\mathcal{C}\lambda_3)$ since $\mathcal{T} > 0$. Therefore singular arcs are characterised by $\lambda_1 = \lambda_2 = \lambda_3 = \hbar = a_1 = a_2 = 0$, from which we find that the optimal control will take its unconstrained value u_∞. The optimal control is thus determined by the state and costate according to

$$u = \begin{cases} -U \operatorname{sign}(\mathcal{C}\lambda_3), & \lambda_3 \neq 0, \\ u_\infty, & \lambda_3 = 0. \end{cases} \tag{6.5.7}$$

We now calculate the local order of singular arcs, and check the GLC condition. We find that for $i = 1, \ldots, 5$, the expressions $\mathrm{d}^i\phi/\mathrm{d}r^i$ do not depend explicitly on u along singular arcs in the sense described in §6.2, while

$$(-1)^3 \frac{\partial}{\partial u}\left(\frac{\mathrm{d}^6\phi}{\mathrm{d}r^6}\right) = \left(\mathcal{C}\frac{\mathcal{T}(0)}{\mathcal{Q}(0)}\right)^2 > 0. \tag{6.5.8}$$

We conclude that the local order of all singular arcs is $m = 3$, and that trajectories along singular arcs satisfy the strengthened GLC condition.

Using the direct numerical method detailed above, we solve the full optimal

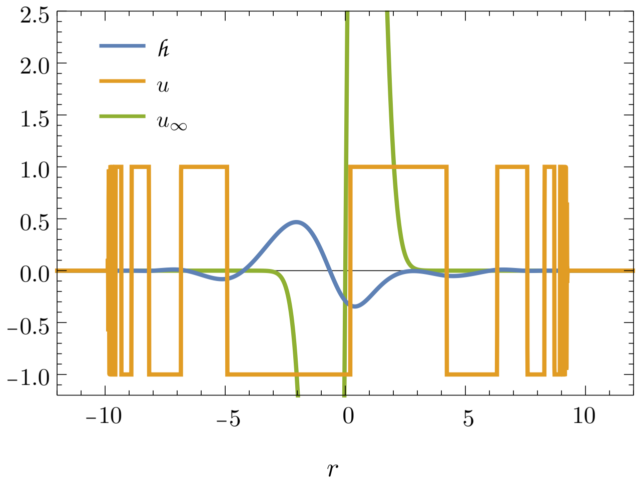

Figure 6.4: Solution of the full problem (6.1.3) *with the parameters defined in* (6.4.3).

control problem (6.1.3) with capillarity reinstated. We plot the numerical solution in figure 6.4 with bound $U = 1$, where we see the optimal control appears to be of the form described in (6.5.7), bang-bang (with many switches) in a non-singular region around the strike point, and coinciding with the unconstrained optimum u_∞ beyond this region. Despite the optimal control form (6.5.7) being analogous to its first-order counterpart (6.3.8), the computed control in figure 6.4 looks completely different from that in figure 6.3, switching many more times within the more extensive bang-bang region. To understand what is happening we must take a detour to visit an oft-forgotten optimal control phenomenon: chattering.

6.6 Chattering

6.6.1 Fuller's phenomenon: chattering controls

In the 1960's A. T. Fuller first considered [54] the seemingly simple optimal control problem of minimising the square displacement of a particle while controlling its acceleration:

$$\min_{|u|\le 1} \frac{1}{2}\int_0^\tau x_1(t)^2\,\mathrm{d}t, \tag{6.6.1a}$$

subject to

$$\frac{\mathrm{d}x_1}{\mathrm{d}t} = x_2, \qquad \frac{\mathrm{d}x_2}{\mathrm{d}t} = u, \qquad (x_1(0), x_2(0)) = x_0. \tag{6.6.1b–d}$$

The domain size τ is assumed to be sufficiently large, in the case of $x_0 = (0.18, 0.6)$ it suffices to take $\tau \approx 2.3$, as we will see. Considering the normal problem, the Hamiltonian takes the form

$$H = \lambda_1 x_2 + \lambda_2 u + \frac{1}{2}x_1^2, \tag{6.6.2}$$

where the costate satisfies

$$\frac{\mathrm{d}\lambda_1}{\mathrm{d}r} = -x_1, \qquad \frac{\mathrm{d}\lambda_2}{\mathrm{d}r} = -\lambda_1, \tag{6.6.3a,b}$$

subject to

$$\lambda_1(R) = \lambda_2(R) = 0. \tag{6.6.4}$$

This is an affine control problem, and we find that the switching function is given by

$$\phi = \frac{\partial H}{\partial u} = \lambda_2. \tag{6.6.5}$$

It follows that singular arcs are characterised by the state, costate, and control all vanishing, while non-singular arcs are bang-bang. The control is thus given by

$$u = -\operatorname{sign}(\lambda_2). \tag{6.6.6}$$

In figure 6.5 we plot the numerical solution of (6.6.1) for $x_0 = (0.18, 0.6)$. We see that the solution has steered the particle to zero by $t \approx 2.3$ and so any τ larger than this will give the same solution. Most strikingly, we observe the same dense switching as in the deflection problem. Fuller's problem (6.6.1) is sufficiently simple so as to admit a closed-form solution [54, 55, 126, 220]. We outline the key features of this solution, which subsequently motivate a similar study in our original deflection problem.

The optimal solution comprises a non-singular bang-bang arc, along which the particle is steered to arrive at the origin with zero velocity. This is followed by a singular arc, on which the particle remains at the origin. Crucially, there is no such non-singular arc that contains a finite number of switches, as was possible in the first-order problem in § 6.4. Instead, the bang-bang control switches infinitely many times in a finite interval. This phenomenon is called Fuller's phe-

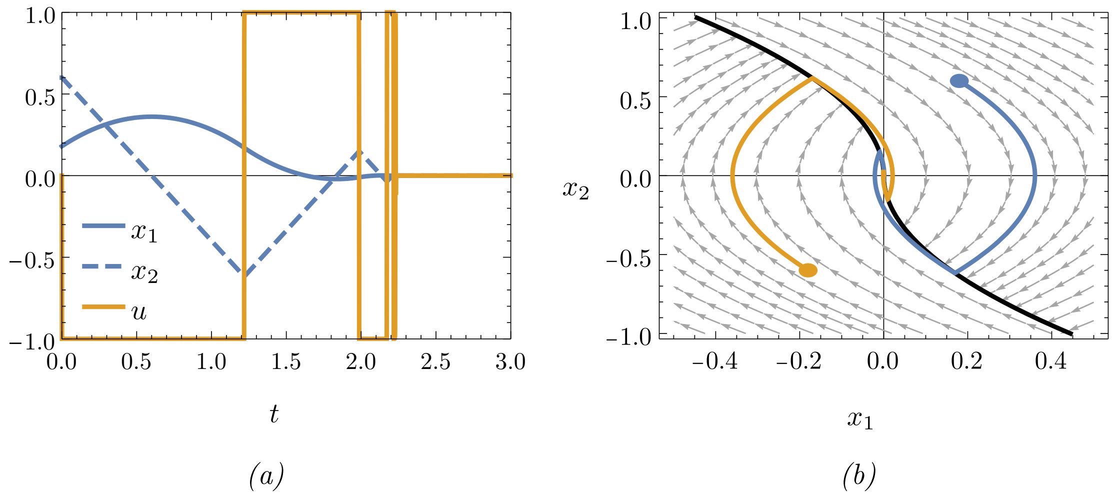

Figure 6.5: Numerical solution of (6.6.1)*: (a) with* $x_0 = (0.18, 0.6)$ *and* $\tau \geq 3$*; (b) phase portrait showing flow field (grey arrows), the switching surface (black curve) defined by* (6.6.7)*, and two chattering trajectories with initial conditions* $x_0 = \pm(0.18, 0.6)$ *marked by disks (blue corresponding to* $+$ *and yellow to* $-$*).*

nomenon or chattering (or sometimes Zeno behaviour in reference to Zeno and his paradox [118], see also [13, 53, 126, 205] for discussions about related but distinct notions of chattering). Chattering was for a long time considered anomalous and largely neglected [175]. Its neglect led to misleading results and conflicts in the literature (for example, see [130] who point out that a theorem from the well-known and highly-cited [93] needs an additional assumption having neglected Fuller's phenomenon; [130] is then corrected for a different reason by [115], following which [163] counters). The seminal work by Kupka [102] proved that for sufficiently high-order systems chattering is ubiquitous (see [229] for a further discussion and an extension of Kupka's results), and it has subsequently been studied extensively [174], with much work focusing on conditions that bound the number of switches to guarantee no chattering will occur [3, 192].

The phase portrait in figure 6.5(b) shows how trajectories spiral towards the origin. Trajectories follow the flow field given by $u = \pm 1$ on either side of the switching surface (where the switching function ϕ changes sign). The switching surface is given by [231]

$$x_1 = -\xi\, x_2 |x_2|, \quad \text{where} \quad \xi = \sqrt{\frac{\sqrt{33} - 1}{24}}. \tag{6.6.7}$$

From the phase portrait we see how trajectories cross the switching surface transversely, with none leading directly to the origin. We deduce that solutions must switch infinitely many times.

We follow an approach from [115, 193] to prove that chattering must take place at a junction between a non-singular and singular arc, by considering the switching function ϕ. Differentiating and using (6.6.1), (6.6.3) and (6.6.6) we find that, on the non-singular arc, ϕ satisfies the fourth-order nonlinear ODE

$$\frac{\mathrm{d}^4\phi}{\mathrm{d}t^4} = -\operatorname{sign}(\phi). \tag{6.6.8}$$

Consider a junction at $t = 0$ (without loss of generality, as (6.6.8) is autonomous), with the non-singular arc extending locally into the region $t < 0$. If no chattering occurs, then the solution of (6.6.8) will be locally analytic. In this case, assume, without loss of generality, that $\phi > 0$ in some vicinity of the origin, so the right-hand side of (6.6.8) is -1. Integrating (6.6.8), we find that locally

$$\phi = -\frac{t^4}{24} < 0, \tag{6.6.9}$$

a contradiction. The assumption of local analiticity is wrong, and instead, at any such junction there is infinite switching. We now look to extract information regarding the nature of this switching by studying the spirals in figure 6.5(b).

The equation (6.6.8) is invariant under the transform $\phi(t) \mapsto J^4\phi(t/J)$. We leverage this symmetry to uncover the structure of the switching [126], by looking for a self-similar solution of (6.6.8). Let us assume that the solution has adjacent zeroes at t_0 and t_1 where $t_0 < t_1 < 0$, and $\phi > 0$ on the segment $t \in [t_0, t_1]$. Integrating (6.6.8) we find that on $[t_0, t_1]$

$$\phi(t) = \frac{t^4}{24} + at^3 + bt^2 + ct + d. \tag{6.6.10}$$

We now look to utilise self-similarity to determine the unknown constants a, b, c, d, and J. To do so, we construct an extension onto an adjacent segment $[t_1, t_2] = [t_0/J, t_1/J]$ by the self-similar mapping. We require continuity up to the third derivative at the point of overlap $t = t_1$, namely

$$\phi(t_1) = J^4\phi(t_1/J), \qquad \frac{\mathrm{d}^2\phi}{\mathrm{d}t^2}(t_1) = J^2\frac{\mathrm{d}^2\phi}{\mathrm{d}t^2}(t_1/J), \tag{6.6.11a,c}$$

$$\frac{\mathrm{d}\phi}{\mathrm{d}t}(t_1) = J^3\phi(t_1/J), \qquad \frac{\mathrm{d}^3\phi}{\mathrm{d}t^3}(t_1) = J\frac{\mathrm{d}^3\phi}{\mathrm{d}t^3}(t_1/J). \tag{6.6.11b,d}$$

Substituting (6.6.10) into (6.6.11) we find that

$$a = -\frac{t_1}{3(1+J)}, \quad b = \frac{t_1^2}{2(1+J^2)}, \quad c = -\frac{t_1^3}{3(1+J^3)}, \quad d = \frac{t_1^4}{12(1+J^4)}. \quad \text{(6.6.12a–d)}$$

Finally, imposing that $\phi(t_1) = 0$, we find that J satisfies

$$J^4 - 3J^3 - 4J^2 - 3J + 1 = 0. \tag{6.6.13}$$

The roots of this quartic are obtainable in closed form. There are only two real roots, one is given by

$$J = \frac{1}{4}\left(3 + \sqrt{33} + \sqrt{26 + 6\sqrt{33}}\right) \approx 4.13016, \tag{6.6.14}$$

and the other is simply $1/J$. Successive zeros are separated by distances that form a geometric progression, so J and $1/J$ describe the same sequence in different directions.

To recap, a local analysis proves that the non-singular arc is not analytic at a junction point, from which we deduce that infinite switching occurs [193]. The dynamics admits self-similar switching: a self-similar solution may be constructed on a given segment, and then extended along successive segments whose lengths form a geometric progression of ratio $J \approx 4.13016$ accumulating at the junction. These switches coincide with transverse crossings of the switching curve in the phase portrait shown in figure 6.5(b).

Having recovered information about the switching structure in Fuller's problem, we return to the deflection problem and attempt to apply a similar approach.

6.6.2 Chattering in deflection control

We attempt to apply the two strategies we found useful in Fuller's problem to the deflections problem: a local analysis to prove that chattering must occur at a junction, and self-similarity to uncover the switching structure.

The junctions joining non-singular to singular arcs in figure 6.4 are located relatively far from the strike point, where $|r| \approx 10$ and since $\mathcal{P}(r) = \mathrm{e}^{-r^2}$, quantities driven by the external plasma are exceedingly small. Similarly, since $\hbar$ is continuous, and identically zero on the singular arc, we may assume that $\hbar$ and its derivatives are negligible. When these terms are neglected, f defined in (6.5.1e) admits the approximation

$$f \approx \mathcal{C}\,\frac{\mathcal{T}(0)}{\mathcal{Q}(0)}\,u. \tag{6.6.15}$$

From (6.5.1), (6.5.4), (6.5.6) and (6.6.15), assuming that derivatives $\mathrm{d}^i\phi/\mathrm{d}x^i$ are negligible for $i = 0, \ldots, 5$, we then deduce that, local to the junction in the non-singular region, the switching function satisfies

$$\frac{\mathrm{d}^6\phi}{\mathrm{d}r^6} \approx \Psi \operatorname{sign}\phi, \quad \text{where } \Psi = U\left(\mathcal{C}\frac{\mathcal{T}(0)}{\mathcal{Q}(0)}\right)^2. \tag{6.6.16}$$

Since $\Psi > 0$, as opposed to the negative sign in Fuller's problem, the local analysis fails to provide a contradiction: assuming $\phi > 0$ and locally analytic results in $\phi = \Psi t^6/6! > 0$. While there is still a rich geometric structure of trajectories near the junction [229], this analysis is unable to uncover it.

Nevertheless, the switching equation (6.6.16) still respects a symmetry similar to that in Fuller's problem, and is invariant under the transform $\phi(t) \mapsto J^6\phi(t/J)$. Note that the form of the symmetry validates the earlier assumption of vanishingly small derivatives up to fifth order near the junction. Just as before, we seek a self-similar solution which has adjacent zeros at $t_0 < t_1$, and from (6.6.15) should be of the form

$$\phi(t) = \frac{t^6}{6!} + \sum_{i=0}^{5} c_i t^i. \tag{6.6.17}$$

Constructing a self-similar copy on the adjacent segment $[t_1, t_2] = [t_0/J, t_1/J]$ and requiring continuity of derivatives up to order 5 at the overlapping point $t = t_1$, gives six constraints for six unknowns c_i as functions of J. Finally, enforcing that $\phi(t_1) = 0$, we find that J is a root of the polynomial P defined by

$$P(J) = J^8 - 7J^7 - 2J^6 + 8J^5 + 17J^4 + 8J^3 - 2J^2 - 7J + 1. \tag{6.6.18}$$

We infer from the symmetry of the coefficients of P that $P(J) = 0$ if and only if $P(1/J) = 0$, as we expect. Therefore it suffices to look for real roots in the interval $(-1, 1)$, and we see by plotting $P(J)$ in figure 6.7(a) that there are two. The inverses of these two roots are $J \approx 1.73691$ and $J \approx 7.07175$.

Using the smaller of the two values $J \approx 1.73691$ we draw a phase portrait in figure 6.6 showing how the switching function spirals self-similarly toward the

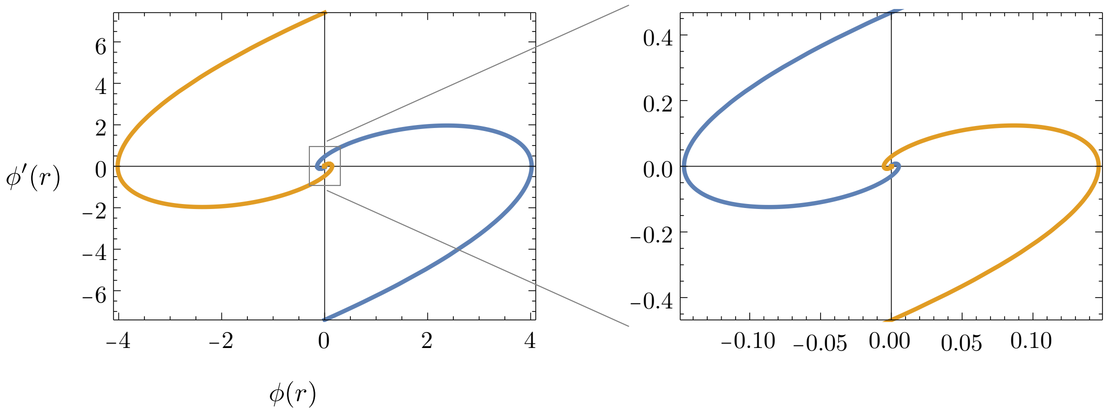

Figure 6.6: Trajectories of the switching function ϕ constructed from (6.6.17) shown in the phase plane, spiralling to the origin self-similarly with similarity ratio $J \approx 1.73691$. The image right is zoomed in from the centre of the image left.

origin.

In figure 6.7(b) we zoom in on a section of figure 6.4, and take two adjacent switching points $(t_0, t_1) \approx (11.83, 12.82)$ as the benchmark interval. Using $J \approx 1.73691$, we predict adjacent switching points as well as their accumulation point (the junction point). For switching points beyond the benchmark interval $t > t_1$, including the junction point, we find excellent agreement (we mark only four such switches because the separation is no longer clearly visible). Switching points preceding the benchmark interval $t < t_0$ show slightly diminishing agreement as the approximation (6.6.15) breaks down as we approach the origin. We conclude that the self-similar dynamic deduced above explains the chattering behaviour.

Having pinned down the chattering structure, we proceed to consider various approaches to tame the chattering.

6.7 Regularising the control singularity

We have seen that when the full dynamic (6.1.1) (including capillarity) governs the deflections, the optimal control exhibits chattering, characterised by an infinite number of switches between the non-singular arc and the singular one. In practice, such a cooling profile cannot be realised, and so we must seek to regularise this chattering.

The direct numerical method discretises the control, and thus cannot switch infinitely many times, offering a natural, albeit implicit, regularisation. However,

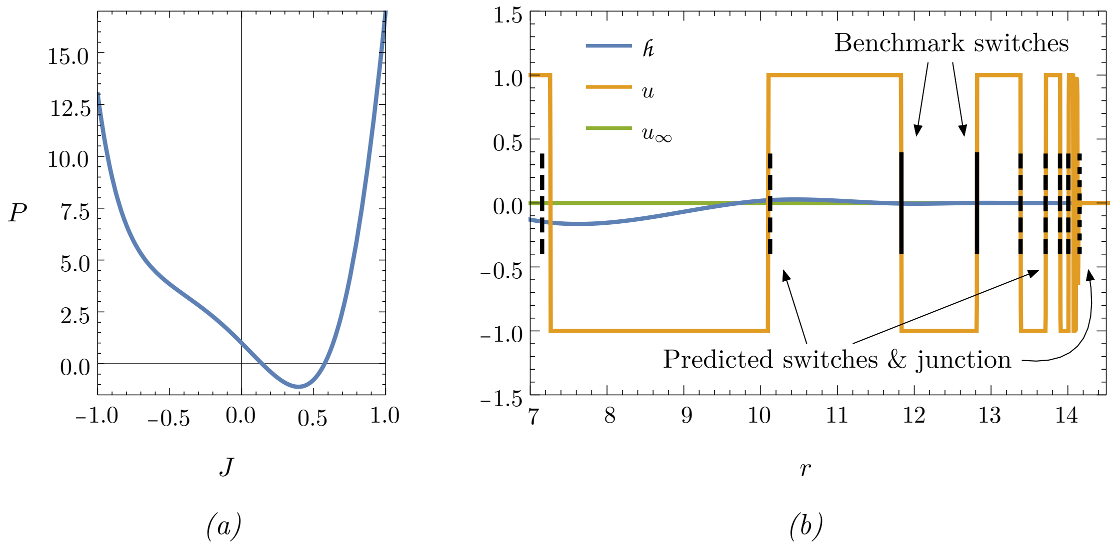

Figure 6.7: (a) Polynomial $P(J)$ defined in (6.6.18). *(b) A section of the plot in figure 6.4, where* $(t_0, t_1) \approx (11.83, 12.82)$ *are the benchmark switching points (marked by solid black lines), and the geometric ratio* $J \approx 1.73691$ *is used to predict adjacent switching points (dashed lines), as well as the junction point (dotted line).*

the switching still occurs at intolerably high frequency. While courser discretisation would suppress this, we seek a more robust formulation.

The most rigorous approach taken in the literature [27] is to add an additional penalty term to the object function, so that it becomes

$$\frac{1}{2}\|\hbar\|_2^2 + \epsilon\,\mathrm{TV}(u), \tag{6.7.1}$$

where TV denote the total variation and ϵ is a small parameter. Optimal solutions will be those of bounded variation, and thus can switch only a finite number of times. As $\epsilon \to 0$, the total variation of the optimal control tends to ∞ as the number of switches diverges. Thus, the parameter $\epsilon > 0$ does not generate a space of solutions that are feasibly engineered.

Instead, we propose a more practical approach of keeping the generic bang-bang or unconstrained form (6.5.7), while predetermining a finite number of switches n. This reduces the problem to an n-dimensional optimisation problem of determining the optimal switching locations.

In the case of $n = 3$, we denote the switching locations by $r_{\mathrm{L}} < r_{\mathrm{C}} < r_{\mathrm{R}}$, where

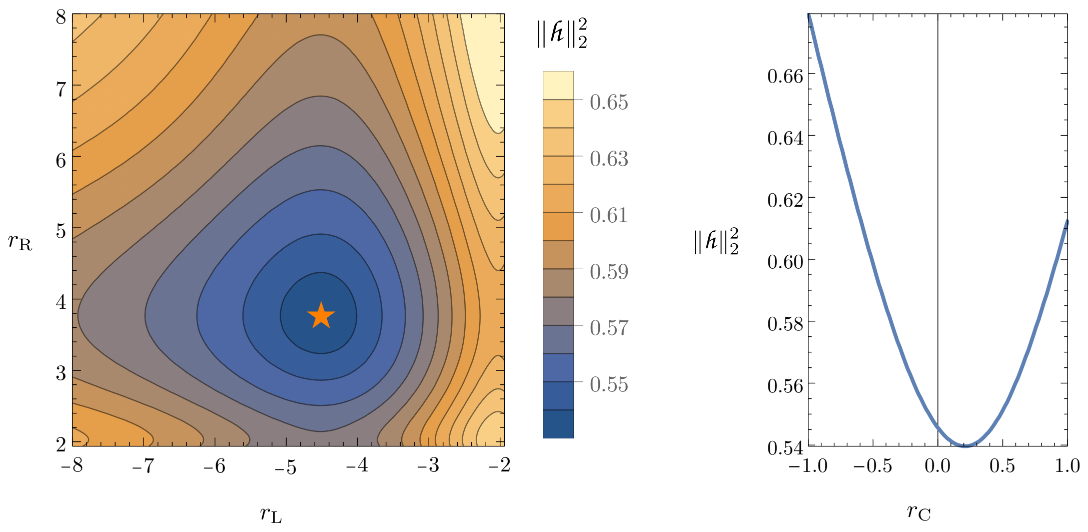

(a) *(b)*

Figure 6.8: Value of the objective function $\|\hbar\|_2^2$ *on subspaces of the* (r_L, r_C, r_R) *parameter space in the vicinity of the local minimum* $(r_L, r_C, r_R) \approx (-4.53, 0.21, 3.77)$ *marked on the contour plot in (a) by an orange star. (a) Vary* r_L *and* r_R *keeping* $r_C = 0.21$*; (b) Vary* r_C *keeping* $(r_L, r_R) = (-4.53, 3.77)$*. Other parameters are defined in* (6.4.3).

the control is given by

$$u(r) = \begin{cases} u_\infty(r), & r < r_{\mathrm{L}}, \\ -U, & r_{\mathrm{L}} \leq r < r_{\mathrm{C}}, \\ U, & r_{\mathrm{C}} \leq r < r_{\mathrm{R}}, \\ u_\infty(r), & r \geq r_{\mathrm{R}}. \end{cases} \tag{6.7.2}$$

Discretising the $(r_{\mathrm{L}}, r_{\mathrm{C}}, r_{\mathrm{R}})$ parameter space in $\mathbb{R}^3$ around the origin, we may apply standard optimisation tools to find the minimum. In figure 6.8 we show the objective function on subspaces of the parameter space. There is a local minimum at $(r_{\mathrm{L}}, r_{\mathrm{C}}, r_{\mathrm{R}}) \approx (-4.53, 0.21, 3.77)$ where the objective function takes the value of $\|\hbar\|_2 \approx 0.7346$. The high-frequency switching solution in figure 6.4 achieves $\|\hbar\|_2 \approx 0.7222$, showing that the relative increase in objective for the significantly simpler control is approximately 1.7%. The deflection profiles for both of these optima are shown in figure 6.9.

A straightforward physical explanation of the convex optimality structure of figure 6.8 is available by exploring the deflection profiles while varying r_{L} and r_{R} separately, as shown in figure 6.10. In figure 6.10(a), we see that the effect of devia-

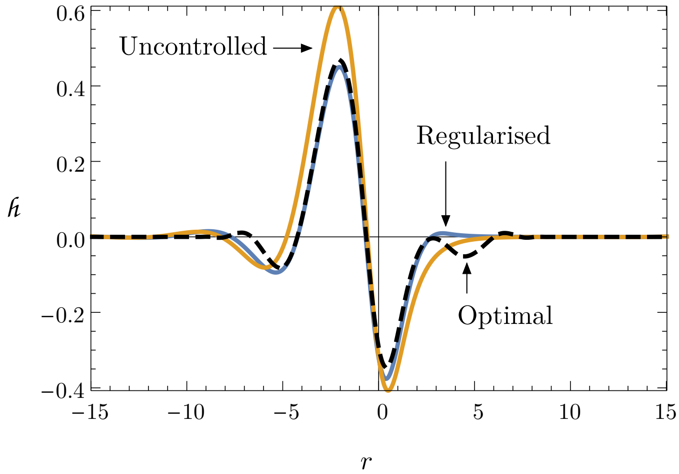

Figure 6.9: Deflection profiles $\hbar$ *for the chattering optimum (dashed black curve) and the regularisation with only three switches (blue curve). These are noticeable improvements over the uncontrolled deflection profile* ($U = 0$, *orange curve). All other parameters are given in* (6.4.3)*.*

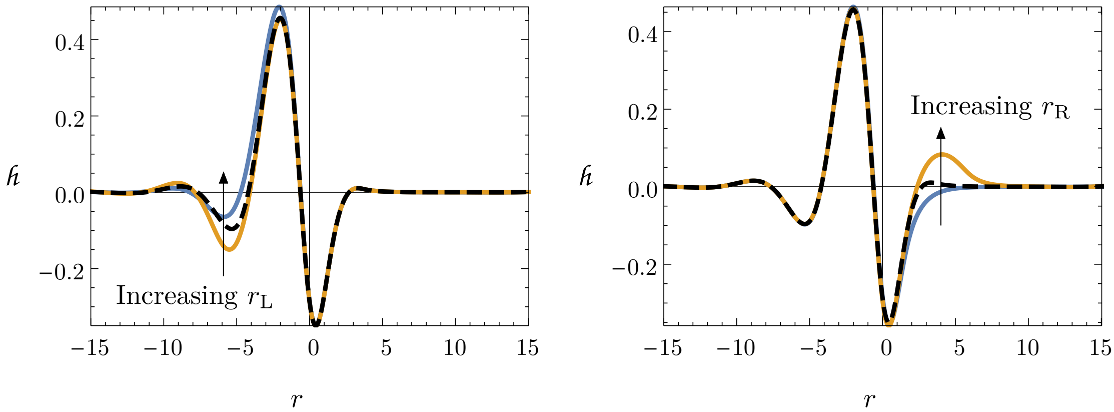

(a) $r_L \in \{-2, -4.53, -6\}$

(b) $r_R \in \{2, 3.76, 6\}$

Figure 6.10: Deflection profiles $\hbar$ *using the fixed-switches control* (6.7.2) *for various values of* r_L *and* r_R *with* $r_C = 0.21$. *The local minimum deflection profile is drawn as a black dashed curve.*

tions in the left-hand control boundary r_L from its optimal value, lead to amplified upstream features (peaks for $r_\mathrm{L} = -2$, the blue curve, and troughs for $r_\mathrm{L} = -6$, the orange curve). Similarly in figure 6.10(b) changes to the right-hand control boundary location r_R amplify downstream deflection features. These changes are driven by changing the extent of the cooling gradient, which in turn induces a different thermocapillary flow that does not optimally balance the deflecting forces.

We conclude with remarks regarding alternative objective functions. When other p-norms or the ∞-norm are used as the objective functional we obtain comparable

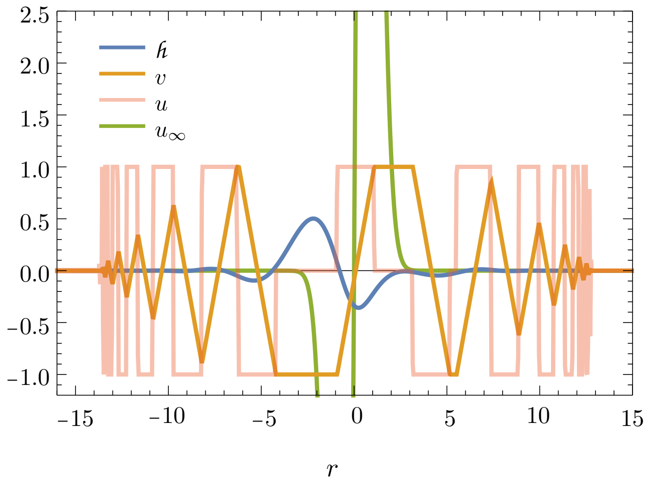

Figure 6.11: Optimal solution of the time-averaged-control system obtained from the full problem (6.1.3) *by replacing appearances of the control u by the state variable v, governed by* $\mathrm{d}v/\mathrm{d}r = u$*. The constraints $|v|, |u| \leq 1$ are imposed, with other parameters defined in* (6.4.3).

results to those presented in this section. While it might be tempting to think that derivative information of $\hbar$ is missing from the formulation, it transpires that employing a Sobolev norm, where we minimise, say, $\|\hbar\|_2^2 + \|\mathrm{d}\hbar/\mathrm{d}r\|_2^2$ does not prevent chattering, nor does a 2-norm on the control [27].

It might be tempting to think that we can suppress chattering if we could bound the control derivative in some sense (the control need not be everywhere differentiable). This can be achieved by employing an averaging technique common in feedback control [114] to replace u by its time-integral. Appearances of the control u are replaced with a state variable v, governed by $\mathrm{d}v/\mathrm{d}r = u$ where u remains the system control. The state v is subject to the original control constraint $|v| \leq U$, and we impose a new constraint $|u| \leq V$ to bound the derivative of v (where it exists). There is an inherent trade-off in choosing the value V. In the limit as $V \to \infty$ we converge to the original system, and thus to effectively suppress chattering we need a relatively small value for V. However, decreasing V more tightly constrains the control and thus results in increased penalties. We show the solution for $U = V = 1$ in figure 6.11, where we see that the chattering persists, but is modulated by a linear envelope (repeating this time-averaging produces polynomial envelopes of higher degree). The optimal solution in figure 6.11 achieves $\|\hbar\|_2 \approx 0.7701$, some 4.8% worse than the regularised optimum, and is vastly more difficult to engineer. We deduce that this poor performance is the result of the bounded derivative not providing sharp control, especially in the vicinity of the origin.

6.8 Summary

In this chapter, we explore how to design an ideal substrate cooling profile $T^{-}(r)$ so as to minimise free-surface deflections. The formulation naturally takes the form of an optimal control problem, for which Pontryagin's Maximum Principle provides the form of the optimal control: since the problem is affine in the control, the control is bang-bang on non-singular arcs, and coincides with its unconstrained optimum on singular arcs where the deflections vanish. We briefly survey numerical methods in optimal control theory, and compare both a direct method (discretise-then-optimise) and an indirect method (optimise-then-discretise). For the problem studied in this chapter, the direct method proves more robust.

When neglecting capillarity, the optimal control exhibits solutions comprising a region around the origin with a non-singular arc, and for large enough values of the control bound U a small singular subregion around the origin that is again singular, in which deflections can be suppressed. Beyond the non-singular arc(s), there are always singular arcs out to the far-field. These solutions exhibit a finite number of junctions (points where an arc switches between non-singular and singular).

When the higher-order capillarity term is reinstated, Pontryagin's Maximum Principle produces a problem of apparently the same form as without capillarity. Numerical solutions show that the optimal control is non-singular over a region around the origin (more extensive than the non-singular region when capillarity is neglected), and beyond this region singular arcs extend to the far-field, along which the deflections are suppressed. The crucial difference in this case is that the control chatters at junctions joining the non-singular and singular arcs: on the non-singular arc, the control bangs from its upper bound to its lower bound, switching an infinite number of times in a vicinity of the junction. We recall Fuller's problem and show how, locally, our optimal control problem is approximately analogous to a third-order Fuller's problem. A simple local analysis that works at lower order to reveal the chattering, does not work at order three. However, the dynamics respects a symmetry that allows us to leverage self-similarity to uncover the local structure of the switching.

Several regularisation approaches to suppress the chattering are discussed. Taking only a known, finite number of switches is one such technique that has several key advantages. Firstly, of key industrial importance, the simple control structure imposed ensures that the optimal strategy will be practical to engineer. Secondly, given a forward model, optimising the design reduces to solving a classical optimisation problem where standard tools are effective and widely available. Finally, in terms of the objective function, the price for deviating from the unregularised optimum can be negligibly small. An example with typical parameters shows that having just three switches results in a loss of less than two percent of the unregularised objective. The cooling strategy obtained with this regularisation is essentially uniform beyond a neighbourhood of the origin, in which the substrate temperature decreases around a point slightly downstream of the strike point.

In this chapter we consider a steady plasma above the liquid layer. It would be of interest to extend the results to the case of an unsteady plasma, in particular, an oscillating jet as discussed in chapter 5. Using the forward model from chapter 5 allows for a direct application of the regularised approach described above.

Chapter 7

Conclusion and Outlook

The final section of each chapter contains a detailed overview of the results presented within. This final chapter is divided into two: in §7.1 we synthesise these summaries into an outline of the overall thesis. In § 7.2 we discuss directions for future work stemming from this thesis.

7.1 Thesis summary

In chapter 1, we detail how the success of the nuclear fusion enterprise will depend, in large part, on our ability to maintain a stable liquid metal divertor that can withstand a large thermal load from the core plasma. This necessitates careful study of the MHD flow of a liquid metal in the presence of a strong applied field, under the influence of an impinging plasma.

In chapter 2, we derive the governing MHD equations and boundary conditions. We then simplify these equations in the asymptotic limit where the fluid is thin relative to the divertor length, and the induced field is weak relative to the applied field. These reductions allow us to find leading-order solutions for two-dimensional flow in two canonical orientations of the applied field: the poloidal case, where the field lies exclusively in the plane parallel to the flow, and the toroidal case, where the applied field is orthogonal to the flow. These two cases reveal an intricate catalogue of flow behaviours due to the MHD influences.

In the poloidal case, the leading-order flow decouples from the induced field and, as in classical Hartmann flow, adopts an approximately uniform, decelerated profile for high field ($\mathrm{Ha} \gg 1$) with a thin viscous boundary layer adjacent to the substrate. The leading-order induced field depends non-locally on the flow and film height.

The induced field exhibits logarithmic singularities at the flow endpoints, which may be regularised by appropriately modelling the way the fluid enters and exits the domain. It is noteworthy that in other asymptotic regimes (for example, when the induced field is not small relative to the applied field, either because magnetic diffusivity is relatively small or because material susceptibility is not small), the leading-order flow no longer decouples from the induced field, and one ends up with a non-local forcing term in the thin-film equation for the fluid thickness h, akin to the electrohydrodynamical flows studied in [66, 200, 201].

In the toroidal case, we find that the influence of the magnetic field is weaker: it significantly affects the flow if $\epsilon\,\mathrm{Ha} = \mathcal{O}(1)$, compared with the poloidal case where $\mathrm{Ha} = \mathcal{O}(1)$ suffices. When the field does influence the flow, it exerts an MHD drag to decelerate the flow. In the high-field limit, the bulk adopts a uniform profile as it decelerates to zero, and all variation is relegated to boundary layers. Unlike in Hartmann layers, the fluid flow through these layers may exhibit exotic profiles including backflow. Furthermore, we find that the leading-order fluid flow rate is a non-monotonic bounded function of the film height, and this can lead to singularities in the free surface profile. We argue that the exotic flow profiles belong to a region of parameter space where the free surface is singular, and thus do not expect to observe these in practice.

A key concern in the fusion context is maintaining the liquid film coating in the face of transient events. Having investigated the steady flow and free-surface profiles, we turn our attention to in chapter 3 to the stability of the thin film to unsteady perturbations.

In the poloidal case, excluding regions near where the magnetic field vanishes, we find that the thin-film equation is linear up to exponentially small corrections, and thus nonlinear phenomena typically associated with wave propagation such as shock and rarefaction formation are strongly suppressed. It follows that disturbances to the steady profile are advected with little dispersion or wave-steepening. Time-dependent disturbances introduced at the inlet may grow to the extent that the field strength increases downstream from the inlet, as higher field results in slower velocity and thicker film, but admit a global uniform bound. For an applied field with a sign change in the vertical component, the shock suppression is weakened local to the sign change. Matched asymptotic expansions expose the modulation a disturbance undergoes as it passes through the region of low field, and uncover how large or rapidly oscillating disturbances need to be to form shocks.

In the toroidal case, an explicit upper bound for time-dependent disturbances introduced at the inlet guarantees that these decay as they are advected along the divertor. As opposed to the poloidal case, as they propagate the disturbances steepen into shocks, as expected for a nonlinear hyperbolic wave equation. These can be smoothed by including regularising higher-order terms corresponding to transverse gravity and surface tension.

A multiple-scales approach allows one to analyse the stability of inertial perturbations. Our stability analysis demonstrates that coupling with the induced magnetic field always acts to stabilise the flow, guaranteeing stability for much larger Reynolds numbers than in the pure hydrodynamic problem.

Treating the poloidal and toroidal regimes separately for simplicity allows us to compare unique flow and stability features in both field orientations. However, it raises the question of what happens in a real-world scenario. We address this in chapter 4 by considering the system when both poloidal and toroidal applied field components are combined simultaneously. We find that the interaction between these two field components and the flow drives a flow in the toroidal direction. The magnitude of this new flow component is proportional to Ξ, where Ξ/ϵ is the ratio of the applied toroidal field to the poloidal field. When the toroidal applied field is at least an order of magnitude larger than its poloidal counterpart, thus $\Xi \gtrsim 1$, the toroidal induction couples with the streamwise flow to leading order. When the toroidal and poloidal applied fields are of comparable magnitude, thus $\Xi \lesssim \epsilon$, the toroidal induced field and flow are negligible and the problem reduces to the purely poloidal case.

The thermal load imparted by the plasma jet is a crucial component of what we set out to model. Having considered the flow in isolation from the core plasma, we further extend the model to incorporate thermal effects. A dimensional analysis suggests that the Seebeck effect and thermocapillarity are the dominant effects to be retained. In the asymptotic limit in which the fluid film is thin and its downstream velocity slow, the temperature distribution is dominated by thermal conduction and thus decouples from the flow to leading order. This allows for the decomposition of the leading-order system into three components driven by different mechanisms: gravity (identical to the isothermal case), the Seebeck effect, and thermocapillarity, where the latter two thermal effects are dependent on the decoupled temperature field.

The Seebeck effect manifests in an inhomogeneity at the fluid–substrate boundary that drives the flow and induced fields. In contrast to the gravity-driven flow, the toroidal velocity is independent of Ξ since it is the poloidal applied field that drives the toroidal flow. Thus, even when the toroidal applied field is comparable to the poloidal applied field, the Seebeck effect may drive a non-negligible toroidal flow. The Seebeck effect drives a downstream flow only through coupling, and therefore vanishes in the limit of comparable poloidal and toroidal applied fields $\Xi \ll 1$. That the Seebeck effect does not drive a downstream flow directly is due to the assumption of axisymmetry: symmetry-breaking substrate undulation in the azimuthal direction ϕ is required to directly drive a downstream flow component.

Thermocapillarity drives a downstream flow with magnitude proportional to the temperature gradient and heat load from the core plasma. No toroidal component is directly induced by thermal gradients in the axisymmetric configuration. However, just as in the isothermal gravity-driven case, a toroidal flow and magnetic field are induced by the toroidal coupling, which will be negligible when all field components are comparable.

In chapter 5 we add one final piece to the model, taking into account the momentum transferred when the plasma impinges on the liquid metal. We look first at how the momentum transfer affects the free surface in the isothermal model when the external plasma is oscillating back and forth above the liquid metal, as is done in a tokamak.

The isothermal problem exhibits two natural time-scales: that characteristic of the motion of the applied pressure, and that characteristic of the free surface deforming under the pressure. When the pressure moves slowly relative to free-surface deformations, the problem is quasi-steady, and the free surface deflections are given by a steady-state profile. When the pressure moves quickly, a multiple scales analysis shows that the free surface deforms under an effective pressure given by the time-averaged pressure profile. This results in smaller pressure gradients and therefore causes smaller deflections than in the quasi-steady case. When the pressure moves at a speed similar to the speed at which deflections of the free surface propagate downstream, the deflections can be dangerously amplified. Analysis of the resonance exhibited in this intermediate regime sheds new light on the non-existence results encountered previously in the literature.

Thermal effects act to amplify the free-surface disturbances, causing more intense film deflections at resonant sweeping frequencies. A thermal time-scale in the substrate may also be relevant if the substrate is significantly thicker than the fluid film. In this case, thermal inertia becomes significant and acts, within the substrate, to delay the thermal response to the heat load ultimately reducing thermocapillary-induced deflections. We infer that it would it would be advantageous to increase the thermal inertia in the system. While increasing the substrate thickness achieves this, it also results in an increase in effective substrate thermal conductivity. Overall, this leads to an amplification of the free-surface deflections, and so this does not provide a strategy to reduce film disturbances.

In chapter 6 we explore an alternative strategy to minimise the fluid displacement by designing an ideal substrate cooling profile. The formulation naturally takes the form of an optimal control problem. When neglecting capillarity, the optimal cooling profile is constant in the far field, and is roughly V-shaped around a point slightly downstream of the strike point. When capillarity is reinstated numerical solutions show that the optimal temperature gradients switch at high frequency. We exploit a symmetry in the dynamics to uncover the local structure of the switching, to find that these switches occur infinitely many times over a finite extent of the divertor. For the purposes of producing an optimal cooling strategy that can be feasibly engineered, we discuss various regularisation strategies. Simply taking a small, fixed number of switches suppresses the chattering and is simplest to manufacture and is shown, for typical parameter values, to cost only a couple of percent in the optimal objective.

The ultimate aim of this thesis is to develop a modelling framework to assess the feasibility of a liquid metal divertor. Taking into account the dominant forces acting upon such a liquid metal, under realistic operating conditions, our results provide the practitioner with a suite of insights to help guide system parameter choices affecting the liquid-metal divertor behaviour. We hope that the interesting mathematical problems encountered along the way contribute to the broader mathematical literature on thin-film and magnetohydrodynamic flows.

7.2 Outlook

In this section we outline potential future research directions the work in this thesis naturally leads on to.

We limit our attention in this work to the simplest axisymmetric geometry that allows for nonzero gradient in the applied toroidal field. In practice, there will be small deviations from axisymmetry due to manufacturing inaccuracies and engineering constraints. Moreover, transient plasma events can induce asymmetrical forcing on the flow. It is therefore of great scientific interest to investigate the stability of known axisymmetric equilibrium solutions to symmetry-breaking perturbations of the flow and magnetic field. Such an analysis in the hydrodynamic case (see, for example, [81, 199]) predicts the possibility of instability to span-wise perturbations, resulting in the formation of fingers. Previous works have appealed to Squire's theorem to argue that the two-dimensional analysis suffices, however this is not applicable to MHD flow (cf. [86]).

In this thesis we consider the plasma to be a known source of momentum and energy, however, in certain regimes there might be a coupling between the plasma and the free surface [206]. A more complete approach would be to incorporate and couple the sheath dynamics [155, 166] with the MHD free-surface flow (see [95]).

In chapter 6 we pose the optimal cooling problem in the case where the plasma is steady (or quasi-steady if oscillations are sufficiently fast). It would be interesting to consider the optimal cooling profile in the dynamic case of an oscillating plasma. What effect, if any, this would have on the chattering is unclear.

Finally, an interesting and important subject unaddressed in this thesis regards the creation of a local dry spot, and the conditions required to induce its wetting by the flow. Dry spots may form for a number of reasons, for example, violent transient events in the plasma impinging on the divertor, inadequate pumping of fluid onto the divertor, and so on.

Various approaches have been adopted in the literature regarding the hydrodynamic problem. One early approach is to compare the total mechanical energies, that is, surface and kinetic energies, of a fully-wetted flow to a partially-wetted, rivulet flow [134]. The geometry of a rivulet is assumed to be a cylindrical cap, parametrised by a known contact angle and unknown radius of curvature. Two further unknowns that characterise the problem are the ratio of wet-to-dry area in the rivulet, and the critical film height — above which the dry spot will vanish and below which it will remain stable. Equating flow rates and energies of both wetted and rivulet flows, and requiring that the energy in the rivulet flow be a feasible minimum provides three constraints to determine the three unknowns. In the case of flow with a poloidal field, in the limit as $\mathrm{Ha} \to \infty$, we find that the rivulet energy is affine with respect to the ratio of wet-to-dry area, where the gradient of the relationship is positive. This means that there does not exist a local minimum in the energy, and the global minimum occurs when the ratio is zero, which suggests that the critical film height is also zero and all dry spots are unstable. Note that this is true when the energies include magnetic energy, since by equating flow rates of the uniform flow the cross-sectional areas of both the wetted and rivulet flows must be the same, and so the magnetic energies will be as well.

A separate approach to modelling dry patches has sought similarity solutions to the equation governing the free surface assuming a self-similar boundary [42, 187, 218]. While producing interesting free-surface profiles that qualitatively match key features of experimental results, this approach fails to find the existence of a critical film height for the stability of a dry patch. In fact, in some cases it finds a minimum flow rate for a solution to even exist, or that the free surface diverges near the contact point, or cannot satisfy an arbitrary contact-angle condition. These drawbacks are understood to be the result of the breakdown of the lubrication approximation in an inner region near the contact line.

A further approach to finding the critical flow height is to consider a force balance local to the region of the stagnation point in a dry patch [72]. Upstream from the stagnation point and dry spot, the flow is described by the standard model of flow down an inclined plane, where we know the pressure and velocity within the fluid layer. At the stagnation point the velocity is zero, allowing us to deduce the hydrodynamic pressure from Bernoulli's principle for an ideal fluid. The force exerted by the pressure is balanced by surface tension forces, from which one can derive the criterion for a stable dry spot: the dry patch is considered unstable if the downstream force at the contact point exceeds the surface tension forces that keep the fluid stationary and sustain the dry patch.

This final approach seems amenable to an MHD extension, where the magnetic pressures contribute to the pressure terms. However, it remains to be seen how the redirection of current in a dry spot might affect the flow and thus the stability of the dry spot. To this end, a fully three-dimensional configuration should be examined.

We firmly believe that the knowledge gap separating us from a sustainable energy future is bridgeable. This future — in which we have the energy resources to help us pursue a full life, while guaranteeing generations after us have the very same opportunity — is within our grasp, if we are willing to reach for it. It is our sincere hope that this work brings us one step closer toward realising this vision.

Appendix A

A.1 Plemelj problem

In this appendix we employ the Plemelj formulae to the poloidal problem from §2.2.3 to determine the x-variation of the induced magnetic field. In the outer vacuum region we describe the divertor by the line segment $(x, Y) \in [0, 1] \times \{0\}$. The external induced potential A_0^{i} solves Laplace's equation in the vacuum, and satisfies the jump conditions (2.2.24) and (2.2.32) across the divertor. This describes a leading-order global problem, which may be solved with the Plemelj formulae [2].

To this end, we define

$$w(z) = \frac{\partial A_0^{\mathrm{i}}}{\partial Y} + \mathrm{i}\frac{\partial A_0^{\mathrm{i}}}{\partial x}, \tag{A.1.1}$$

where $z = x + \mathrm{i}Y$, and we suppress the dependence on t to simplify the notation. Requiring that $w(z)$ be holomorphic ensures, by the Cauchy-Riemann equations, that A_0^{i} satisfies Laplace's equation in the region beyond the divertor. It then follows from the jump conditions (2.2.24) and (2.2.32) and the Plemelj formulae, that

$$w(z) = \frac{1}{2\pi} \int_0^1 \frac{b(\xi) + a'(\xi)}{\xi - z} \, \mathrm{d}\xi + f(z), \tag{A.1.2}$$

where $f(z)$ is any function holomorphic in $\mathbb{C} \setminus \{0, 1\}$. Requiring that $w(z)$ have at most a logarithmic singularity at the divertor endpoints implies that any singularities in $f(z)$ at the endpoints are removable, and thus f is entire [2]. Furthermore, requiring that $w(z) \to 0$ as $z \to \infty$ to satisfy condition (2.1.32) that the induced field vanishes in the far field, implies that $f(z)$ must likewise tend to zero at infinity, and thus by Liouville's theorem be equal to zero. Taking real and imaginary parts of (A.1.2) gives the x- and (negative) Y-components, respectively, of the induced field everywhere outside the divertor.

Using the Plemelj formulae again on the imaginary part of (A.1.2), we obtain the limiting values as we approach the divertor from above and below, which are given by

$$\left.\frac{\partial A_0^{\mathrm{i}\pm}}{\partial x}\right|_{Y=0} = -\frac{1}{2\pi} \fint_0^1 \frac{b(\xi)}{\xi - x}\,\mathrm{d}\xi \pm \frac{a'(x)}{2}. \tag{A.1.3}$$

A.2 Magnetic boundary condition for layered substrates

A.2.1 Poloidal field

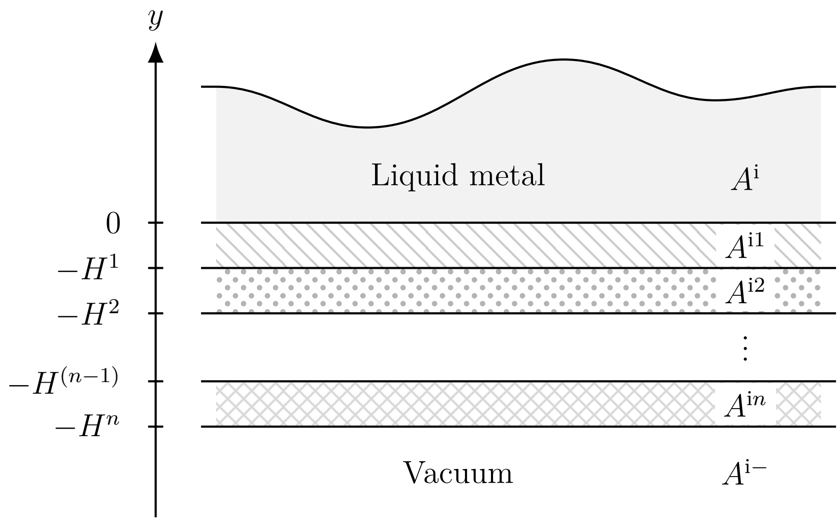

Figure A.1: Schematic of the composite substrate, and notation for the potential in each layer, and vertical coordinate separating adjacent layers.

In this appendix we extend the leading-order poloidal solution (2.2.34) to the case where the substrate is a composite material, comprising n layers. We assume that each layer has a different magnetic susceptibility and dimensionless thickness, denoted χ^k and h^k, respectively. The induced potential in the kth layer is denoted $A^{\mathrm{i}k}$, where we have replaced the superscript 's' with the layer index 'k'. Moreover, we define the partial sums of the layer thicknesses by

$$H^\ell = \sum_{k=1}^{\ell} h^k, \tag{A.2.1}$$

so that the interface between layer ℓ and $\ell + 1$ is at $y = -H^\ell$, as illustrated in figure A.1.

The leading-order induced potential is linear with respect to y in each substrate (from (2.2.12)) and the interface conditions at $y = -H^\ell$, (2.2.21a) and (2.2.21b), take the form

$$A_0^{\mathrm{i}\ell} = A_0^{\mathrm{i}(\ell+1)}, \quad \frac{\partial A_0^{\mathrm{i}\ell}}{\partial y} = \frac{\partial A_0^{\mathrm{i}(\ell+1)}}{\partial y} + \frac{\chi^\ell - \chi^{(\ell+1)}}{\mathrm{Rm}} B_{x0}^{\mathrm{a}} \qquad \text{at } \ y = -H^\ell, \quad \text{(A.2.2a,b)}$$

for $\ell = 0, \ldots, n-1$, where we adopt the convention that $A_0^{\mathrm{i}0} = A_0^{\mathrm{i}}$, and

$$A_0^{\mathrm{i}n} = A_0^{\mathrm{i}-}, \qquad \frac{\partial A_0^{\mathrm{i}n}}{\partial y} = \frac{\chi^n}{\mathrm{Rm}} B_{x0}^{\mathrm{a}} \qquad \text{at } \ y = -H^n. \qquad \text{(A.2.3a,b)}$$

Starting with the nth layer, we find that

$$\frac{\partial A_0^{\mathrm{i}n}}{\partial y} = \frac{\chi^n}{\mathrm{Rm}} B_{x0}^{\mathrm{a}}. \qquad \text{(A.2.4)}$$

It then follows by induction that the ℓth layer satisfies

$$\frac{\partial A_0^{\mathrm{i}\ell}}{\partial y} = \frac{\chi^\ell}{\mathrm{Rm}} B_{x0}^{\mathrm{a}}. \qquad \text{(A.2.5)}$$

Then the ℓth layer is given by

$$A_0^{\mathrm{i}\ell} = A_0^{\mathrm{i}(\ell+1)}\Big|_{y=-H^\ell} + \frac{\chi^\ell}{\mathrm{Rm}} B_{x0}^{\mathrm{a}} \left(y + H^\ell\right). \qquad \text{(A.2.6)}$$

To evaluate the first term on the right-hand side of (A.2.6), we start with the nth layer. From (A.2.3) we know that

$$A_0^{\mathrm{i}n} = A_0^{\mathrm{i}-}|_{Y=0} + \frac{\chi^n}{\mathrm{Rm}} B_{x0}^{\mathrm{a}} \left(y + H^n\right). \qquad \text{(A.2.7)}$$

It then follows that

$$A_0^{\mathrm{i}(n-1)} = A_0^{\mathrm{i}-}|_{Y=0} + \frac{\chi^n h^n}{\mathrm{Rm}} B_{x0}^{\mathrm{a}} + \frac{\chi^{(n-1)}}{\mathrm{Rm}} B_{x0}^{\mathrm{a}} \left(y + H^{(n-1)}\right), \qquad \text{(A.2.8)}$$

and continuing inductively, we find that

$$A_0^{\mathrm{i}\ell} = A_0^{\mathrm{i}-}|_{Y=0} + \sum_{k=\ell+1}^{n} \frac{\chi^k h^k}{\mathrm{Rm}} B_{x0}^{\mathrm{a}} + \frac{\chi^\ell}{\mathrm{Rm}} B_{x0}^{\mathrm{a}} \left(y + H^\ell\right). \qquad \text{(A.2.9)}$$

We then deduce from (2.2.21a) that (2.2.24a) holds where (2.2.24b) takes the homogenised form

$$a(x,t) = \frac{B^{\mathrm{a}}_{x0}}{\mathrm{Rm}}\left[\sum_{k=1}^{n}\chi^k h^k + \chi h(x,t)\right]. \tag{A.2.10}$$

The first-order potential in each composite layer is again linear with respect to y, and is continuous with continuous derivatives (from (2.2.12)). Therefore the first-order potential is itself linear throughout the entire substrate and thus the substrate calculations remain the same as with a single layer. We must only ensure that (2.2.32b) is written in its general form, namely

$$b(x,t) = -B^{\mathrm{a}}_{Y0}(x)\overline{Q}(x,t) - \frac{\partial a}{\partial x}(x,t). \tag{A.2.11}$$

To summarise, the leading-order poloidal solution (2.2.34) retains its original form; the functions $a(x,t)$ and $b(x,t)$ are replaced by their homogenised forms (A.2.10) and (A.2.11), respectively.

A.2.2 Toroidal field

In this appendix we extend the leading-order toroidal solution detailed in § 2.3.5 to the case where the substrate is a composite material, comprising n layers. We adopt notation analogous to that in appendix A.2.1, whereby each layer has a different electrical conductivity and dimensionless thickness, denoted σ^{k*} and h^k, respectively. The induced magnetic field in the kth layer is denoted $B^{\mathrm{i}k}$, and we define the ratios

$$\Sigma^k_\ell = \frac{\sigma^{k*}}{\sigma^{\ell*}}, \qquad \Lambda^k_\ell = \frac{1+\chi^k}{1+\chi^\ell}. \tag{A.2.12a,b}$$

From (2.3.20) we find that the induced magnetic field is linear with respect to y in each substrate, and subject to the interface conditions (2.3.21) between layers k and $k+1$, which take the form

$$B^{\mathrm{i}k} = \Lambda^k_{k+1}B^{\mathrm{i}(k+1)}, \qquad \frac{\partial B^{\mathrm{i}k}}{\partial y} = \Lambda^k_{k+1}\Sigma^k_{k+1}\frac{\partial B^{\mathrm{i}(k+1)}}{\partial y} \qquad \text{at } y = -H^k, \tag{A.2.13a,b}$$

for $k = 0, 1, \ldots, n-1$, where $k = 0$ denotes values in the fluid and $H^0 = 0$, while $B^{\mathrm{i}n} = 0$ at $y = -H^n$.

It follows immediately that

$$\left.\frac{\partial B^{\mathrm{i}}}{\partial y}\right|_{y=0} = \Lambda_1^0 \Sigma_1^0 \frac{\partial B^{\mathrm{i}1}}{\partial y} = \Lambda_2^0 \Sigma_2^0 \frac{\partial B^{\mathrm{i}2}}{\partial y} = \cdots = \Lambda_k^0 \Sigma_k^0 \frac{\partial B^{\mathrm{i}k}}{\partial y}. \tag{A.2.14}$$

We can now find the induced field in the kth layer, starting from $k = n$:

$$B^{\mathrm{i}n} = \left(\left.\frac{\partial B^{\mathrm{i}}}{\partial y}\right|_{y=0} \right) \Lambda_0^n \Sigma_0^n \left(y + H^n\right). \tag{A.2.15}$$

Then for $k = n - 1$ we find that

$$B^{\mathrm{i}(n-1)} = \left(\left.\frac{\partial B^{\mathrm{i}}}{\partial y}\right|_{y=0} \right) \Lambda_0^{n-1} \left[\Sigma_0^{n-1} \left(y + H^{n-1}\right) + \Sigma_0^n \, h^n \right]. \tag{A.2.16}$$

Continuing inductively, we find that

$$B^{\mathrm{i}k} = \left(\left.\frac{\partial B^{\mathrm{i}}}{\partial y}\right|_{y=0} \right) \Lambda_0^k \left[\Sigma_0^k \left(y + H^k\right) + \sum_{j=k+1}^{n} \Sigma_0^j \, h^j \right], \tag{A.2.17}$$

from which the effective boundary condition is deduced by substituting $k = 0$ and evaluating at $y = 0$:

$$\frac{\partial B^{\mathrm{i}}}{\partial y} = a B^{\mathrm{i}} \quad \text{at} \;\; y = 0, \tag{A.2.18}$$

where

$$a = \frac{\sigma^*}{\sum_{j=1}^{n} h^j \sigma^{j*}}. \tag{A.2.19}$$

To summarise, the toroidal normalisation (2.3.29) and (2.3.30) remains identical; the parameter a is replaced by its homogenised form (A.2.19).

A.3 Velocity and magnetic field solutions (toroidal case)

The solution to the normalised leading order system with a toroidal applied field in an axisymmetric geometry (2.3.31), is given by

$$\mathcal{U}(Y; H, \zeta) = \frac{L(Y; H, \zeta)}{D(H, \zeta)}, \qquad \mathcal{B}(Y; H, \zeta) = \frac{M(Y; H, \zeta)}{2D(H, \zeta)}, \tag{A.3.1a,b}$$

where

$$
\begin{aligned}
L(Y;H,\zeta) = \sinh(HY)\Bigg(&\cos(HY)\Big\{2\sinh(H)\big[\zeta\cos(H)+\sin(H)\big] \\
&+2\cosh(H)\big[\zeta\sin(H)+\cos(H)\big]-\cos(2H)-1\Big\} \\
&-\sin(HY)\big[4\zeta\cos(H)\cosh(H)+\sin(2H)+\sinh(2H)\big]\Bigg) \\
&+2\sin(HY)\cosh(HY)\Big\{\sinh(H)\big[\zeta\cos(H)+\sin(H)\big] \\
&+\cosh(H)\big[\zeta\sin(H)-\cos(H)+\cosh(H)\big]\Big\}, \qquad \text{(A.3.2)}
\end{aligned}
$$

$$
\begin{aligned}
M(Y;H,\zeta) &= \sinh(H)\Big\{\zeta\sinh(H)+2\cos(HY)\sinh(HY)\big[\zeta\cos(H)+\sin(H)\big]\Big\} \\
&+\zeta\big[\cos(2H)+2\big]+\sin(2H)+\sinh(2H)+\cosh^2(H)\big[\zeta+2\cos(HY)\sinh(HY)\big] \\
&+2\cosh(H)\Bigg(\cos(HY)\sinh(HY)\big[\zeta\sin(H)-\cos(H)\big] \\
&-\cosh(HY)\Big\{\sin(HY)\big[\zeta\sin(H)+\cos(H)\big]+\cos(HY)\big[2\zeta\cos(H)+\sinh(H)\big]\Big\}\Bigg) \\
&-2\cosh(HY)\Big\{\sinh(H)\sin(HY)\big[\zeta\cos(H)+\sin(H)\big]+\cos(H)\sin(H-HY)\Big\}, \qquad \text{(A.3.3)}
\end{aligned}
$$

$$
D(H,\zeta) = 2\Big\{\zeta\big[\cos(2H)+\cosh(2H)+2\big]+\sin(2H)+\sinh(2H)\Big\}, \qquad \text{(A.3.4)}
$$

and the scaled coordinate $Y = y/h$ lies in the interval $Y \in [0,1]$.

A.4 Asymptotic expansions of wave-speeds

In this appendix we derive asymptotic expansions of the leading-order wave-speed $\mathfrak{c}_\infty$ and its first-order correction $\mathfrak{c}_{\infty 1}$ with respect to $\tilde{\alpha}$, given in (3.3.53) and (3.3.54). From equations (3.3.43) and (3.3.52) we know that the terms $\mathfrak{c}_\infty$ and $\mathfrak{c}_{\infty 1}$ satisfy

$$
\int_0^1 \frac{\mathrm{d}Y}{\big[\mathfrak{c}_\infty - \mathcal{U}(Y)\big]^2} = \frac{1}{H^4\tilde{\alpha}}, \quad \mathfrak{c}_{\infty 1} = -\frac{(\mathrm{i}\pm 1)}{2^{3/2}|\mathfrak{c}_\infty|^{5/2}} \Bigg/ \int_0^1 \frac{\mathrm{d}Y}{\big|\mathfrak{c}_\infty - \mathcal{U}(Y)\big|^3}. \qquad \text{(A.4.1a,b)}
$$

First, we consider the limit in which $\tilde{\alpha} \ll 1$. The integral on the left-hand side of (A.4.1a) is of magnitude $\mathcal{O}(1/\tilde{\alpha})$, which may be achieved either when $\mathfrak{c}_\infty = \mathcal{U}(1)+\delta$ or $\mathfrak{c}_\infty = \mathcal{U}(0)-\delta$, for some small correction term $1 \gg \delta(\tilde{\alpha}) > 0$.

In the first case, $\mathfrak{c}_\infty = \mathcal{U}(1) + \delta$, we enlist a small parameter $\varepsilon \ll 1$ to split the domain of integration. From the normalised problem (2.3.31) we see that $\mathcal{U}''(1) = -H^2$, while from the boundary conditions (2.3.31b), we see that $\mathcal{U}'(1) = 0$. Therefore

$$\int_{1-\varepsilon}^{1} \frac{\mathrm{d}Y}{\left[\mathfrak{c}_\infty - \mathcal{U}(Y)\right]^2} \sim \int_{1-\varepsilon}^{1} \frac{\mathrm{d}Y}{\left[\delta + H^2(1-Y)^2/2\right]^2} = \frac{\tan^{-1}(H\varepsilon/(2\delta))}{\delta^{3/2}H\sqrt{2}} + \frac{\varepsilon}{2\delta^2 + \delta\varepsilon^2 H^2}, \tag{A.4.2}$$

while the integral on the remainder of the domain $Y \in [0, 1-\varepsilon]$ is bounded by a term of order $\mathcal{O}((\delta + H^2\varepsilon^2/2)^{-2})$. Choosing ε such that $1 \gg \varepsilon \gg \delta^{3/8}$ suffices to give

$$\frac{1}{H^4\tilde{\alpha}} = \int_0^1 \frac{\mathrm{d}Y}{\left[\mathfrak{c}_\infty - \mathcal{U}(Y)\right]^2} \sim \frac{\pi}{(2\delta)^{3/2}H}, \tag{A.4.3}$$

from which it follows that $\delta = H^2(\tilde{\alpha}\pi)^{2/3}/2$. Substituting $\mathfrak{c}_\infty = \mathcal{U}(1)+\delta$ into (A.4.1b) and evaluating to leading-order (by splitting the domain as above) gives

$$\mathfrak{c}_{\infty 1} \sim -\frac{(\mathrm{i}+1)H^6\pi^{2/3}}{3\sqrt{2}\,\mathcal{U}(1)^{5/2}}\,\tilde{\alpha}^{5/3}. \tag{A.4.4}$$

In the second case, $\mathfrak{c}_\infty = \mathcal{U}(0) - \delta$, we proceed in a similar fashion. From the boundary conditions (2.3.31b), we know that $\mathcal{U}(0) = 0$, therefore

$$\int_0^{\varepsilon} \frac{\mathrm{d}Y}{\left[\mathfrak{c}_\infty - \mathcal{U}(Y)\right]^2} \sim \int_0^{\varepsilon} \frac{\mathrm{d}Y}{\left[\delta + \mathcal{U}'(0)Y\right]^2} = \frac{\varepsilon}{\delta^2 + \delta\varepsilon\,\mathcal{U}'(0)}, \tag{A.4.5}$$

while the integral on the remainder of the domain $Y \in [\varepsilon, 1]$ respects a bound of order $\mathcal{O}((\delta + \mathcal{U}'(0)\varepsilon)^{-2})$. Choosing ε such that $1 \gg \varepsilon \gg \sqrt{\delta}$ suffices to show that

$$\frac{1}{H^4\tilde{\alpha}} = \int_0^1 \frac{\mathrm{d}Y}{\left[\mathfrak{c}_\infty - \mathcal{U}(Y)\right]^2} \sim \frac{1}{\delta\,\mathcal{U}'(0)}, \tag{A.4.6}$$

from which it follows that $\delta = H^4\tilde{\alpha}/\mathcal{U}'(0)$. Substituting $\mathfrak{c}_\infty = -\delta$ into (A.4.1b), and evaluating to leading-order (by splitting the domain as above) gives

$$\mathfrak{c}_{\infty 1} \sim -\frac{(\mathrm{i}-1)\,\mathcal{U}'(0)^{3/2}}{H^2\sqrt{2\tilde{\alpha}}}. \tag{A.4.7}$$

We now consider the limit where $\tilde{\alpha} \gg 1$, in which case from (A.4.1a) we expect $\mathfrak{c}_\infty = \pm H^2\sqrt{\tilde{\alpha}} + \delta$ for some correction term $\delta \ll \sqrt{\tilde{\alpha}}$. To compute δ, we evaluate the integral

$$\frac{1}{H^4\tilde{\alpha}} = \int_0^1 \frac{\mathrm{d}Y}{\left[\mathfrak{c}_\infty - \mathcal{U}(Y)\right]^2} \sim \frac{1}{H^4\tilde{\alpha}} \int_0^1 1 \mp \frac{2(\delta - \mathcal{U}(Y))}{H^2\sqrt{\tilde{\alpha}}}\,\mathrm{d}Y. \tag{A.4.8}$$

Therefore, to leading order, we find that

$$\delta = \int_0^1 \mathcal{U}(Y)\,\mathrm{d}Y = \frac{F(H,\zeta)}{H}, \tag{A.4.9}$$

where the final equality comes from definition (2.3.34). The first-order wave-speed $\mathfrak{c}_{\infty 1}$ is then determined by substituting $\mathfrak{c}_\infty = \pm H^2\sqrt{\tilde{\alpha}} + F/H$ into (A.4.1b) to give

$$\mathfrak{c}_{\infty 1} \sim -\frac{(\mathrm{i} \pm 1)H}{2^{3/2}} \left[\tilde{\alpha}^{1/4} \mp \frac{5F(H,\zeta)}{2H^3}\,\tilde{\alpha}^{-1/4}\right]. \tag{A.4.10}$$

This completes the derivation of the asymptotic limits in (3.3.53) and (3.3.54).

A.5 Velocity and magnetic field solutions (three-dimensional cases)

The solution of the normalised leading-order three-dimensional gravity-driven system (4.1.39), is given by

$$u_{\mathcal{G}}(Y) = \frac{N^u_{\mathcal{G}}(Y)}{D_{\mathcal{G}}}, \qquad B^{\mathrm{i}}_{\mathcal{G}}(Y) = \frac{N^B_{\mathcal{G}}(Y)}{D_{\mathcal{G}}}, \tag{A.5.1}$$

where the numerators $N^u_{\mathcal{G}}$ and $N^B_{\mathcal{G}}$ and denominator $D_{\mathcal{G}}$ are shown overleaf.

Similarly, solutions of the normalised leading-order thermoelectric and thermocapillary systems (4.3.19) and (4.3.21), are given by

$$u_{\mathcal{S}}(Y) = \frac{N^u_{\mathcal{S}}(Y)}{\Upsilon D_{\mathcal{ST}}}, \qquad B^{\mathrm{i}}_{\mathcal{S}}(Y) = \frac{N^B_{\mathcal{S}}(Y)}{D_{\mathcal{ST}}}, \tag{A.5.2}$$

$$u_{\mathcal{T}}(Y) = \frac{N^u_{\mathcal{T}}(Y)}{D_{\mathcal{ST}}}, \qquad B^{\mathrm{i}}_{\mathcal{T}}(Y) = \frac{N^B_{\mathcal{T}}(Y)}{D_{\mathcal{ST}}}, \tag{A.5.3}$$

where

$$N_{\mathcal{T}}^{u} = \sqrt{\Upsilon^2+1}\Bigg\{$$
$$2\alpha\left[\sinh\left(H\sqrt{1-i\Upsilon}\right)\sinh\left(Y\sqrt{1+i\Upsilon}\right)+\sinh\left(H\sqrt{1+i\Upsilon}\right)\sinh\left(Y\sqrt{1-i\Upsilon}\right)\right]$$
$$+\cosh\left(Y\sqrt{1-i\Upsilon}\right)\left[\sqrt{1-i\Upsilon}\sinh\left(H\sqrt{1+i\Upsilon}\right)-\sqrt{1+i\Upsilon}\sinh\left(H\sqrt{1-i\Upsilon}\right)\right]$$
$$+\cosh\left(Y\sqrt{1+i\Upsilon}\right)\left[\sqrt{1+i\Upsilon}\sinh\left(H\sqrt{1-i\Upsilon}\right)-\sqrt{1-i\Upsilon}\sinh\left(H\sqrt{1+i\Upsilon}\right)\right]$$
$$+\sinh\left(Y\sqrt{1-i\Upsilon}\right)\left[\sqrt{1+i\Upsilon}\cosh\left(H\sqrt{1+i\Upsilon}\right)+\sqrt{1+i\Upsilon}\cosh\left(H\sqrt{1-i\Upsilon}\right)\right]$$
$$+\sinh\left(Y\sqrt{1+i\Upsilon}\right)\left[\sqrt{1-i\Upsilon}\cosh\left(H\sqrt{1+i\Upsilon}\right)+\sqrt{1-i\Upsilon}\cosh\left(H\sqrt{1-i\Upsilon}\right)\right]\Bigg\}, \tag{A.5.4}$$

$$N_{\mathcal{T}}^{B} = i\Upsilon\sqrt{\Upsilon^2+1}\Bigg\{$$
$$2\alpha\left[\sinh\left(H\sqrt{1-i\Upsilon}\right)\sinh\left(Y\sqrt{1+i\Upsilon}\right)-\sinh\left(H\sqrt{1+i\Upsilon}\right)\sinh\left(Y\sqrt{1-i\Upsilon}\right)\right]$$
$$+\cosh\left(Y\sqrt{1+i\Upsilon}\right)\left[\sqrt{1+i\Upsilon}\sinh\left(H\sqrt{1-i\Upsilon}\right)-\sqrt{1-i\Upsilon}\sinh\left(H\sqrt{1+i\Upsilon}\right)\right]$$
$$+\cosh\left(Y\sqrt{1-i\Upsilon}\right)\left[\sqrt{1+i\Upsilon}\sinh\left(H\sqrt{1-i\Upsilon}\right)-\sqrt{1-i\Upsilon}\sinh\left(H\sqrt{1+i\Upsilon}\right)\right]$$
$$-\sinh\left(Y\sqrt{1-i\Upsilon}\right)\left[\sqrt{1+i\Upsilon}\cosh\left(H\sqrt{1+i\Upsilon}\right)+\sqrt{1+i\Upsilon}\cosh\left(H\sqrt{1-i\Upsilon}\right)\right]$$
$$+\sinh\left(Y\sqrt{1+i\Upsilon}\right)\left[\sqrt{1-i\Upsilon}\cosh\left(H\sqrt{1+i\Upsilon}\right)+\sqrt{1-i\Upsilon}\cosh\left(H\sqrt{1-i\Upsilon}\right)\right]\Bigg\}, \tag{A.5.5}$$

$$
\begin{aligned}
N_{\mathcal{G}}^{u} = & -i\sqrt{1-i\Upsilon}\cosh\left(Y\sqrt{1-i\Upsilon}\right)\cosh\left(H\sqrt{1-i\Upsilon}\right)\left[\alpha(\Upsilon-i)\sinh\left(H\sqrt{1+i\Upsilon}\right)-i\sqrt{1+i\Upsilon}\cosh\left(H\sqrt{1+i\Upsilon}\right)+\Upsilon\sqrt{1+i\Upsilon}\right] \\
& -2i\alpha\Upsilon\sqrt{1+i\Upsilon}\cosh\left(H\sqrt{1+i\Upsilon}\right)\sinh\left(Y\sqrt{1-i\Upsilon}\right)-\alpha\sqrt{1+i\Upsilon}\cosh\left(H\sqrt{1+i\Upsilon}\right)\cosh\left(Y\sqrt{1+i\Upsilon}\right)\sinh\left(H\sqrt{1-i\Upsilon}\right) \\
& +\sinh\left(H\sqrt{1-i\Upsilon}\right)\left[2\sinh\left(H\sqrt{1+i\Upsilon}\right)-\sinh\left((H-Y)\sqrt{1+i\Upsilon}\right)\right]+i\Upsilon\sqrt{\Upsilon^2+1}\sinh\left(H\sqrt{1-i\Upsilon}\right)\sinh\left(Y\sqrt{1-i\Upsilon}\right) \\
& -i\alpha\Upsilon\sqrt{1+i\Upsilon}\sinh\left(H\sqrt{1-i\Upsilon}\right)\sinh\left(H\sqrt{1+i\Upsilon}\right)\sinh\left(Y\sqrt{1+i\Upsilon}\right)-i\Upsilon\sqrt{\Upsilon^2+1}\sinh\left(H\sqrt{1+i\Upsilon}\right)\sinh\left(Y\sqrt{1+i\Upsilon}\right) \\
& +2i\Upsilon\cosh\left(\frac{1}{2}(H-2Y)\sqrt{1+i\Upsilon}\right)\sinh\left(H\sqrt{1-i\Upsilon}\right)\sinh\left(\frac{1}{2}H\sqrt{1+i\Upsilon}\right)-i\Upsilon\sinh\left(Y\sqrt{1-i\Upsilon}\right)\sinh\left(H\sqrt{1+i\Upsilon}\right) \\
& +\Upsilon^2\sinh\left(Y\sqrt{1+i\Upsilon}\right)\sinh\left(H\sqrt{1-i\Upsilon}\right)+\Upsilon^2\sinh\left(H\sqrt{1+i\Upsilon}\right)\sinh\left(Y\sqrt{1-i\Upsilon}\right)-\sqrt{\Upsilon^2+1}\cosh\left(Y\sqrt{1-i\Upsilon}\right) \\
& +i\alpha\Upsilon\sqrt{1+i\Upsilon}\sinh\left(Y\sqrt{1-i\Upsilon}\right)+i\alpha\Upsilon\sqrt{1-i\Upsilon}\sinh\left(H\sqrt{1+i\Upsilon}\right)\sinh\left(H\sqrt{1-i\Upsilon}\right)\sinh\left(Y\sqrt{1-i\Upsilon}\right) \\
& -(1+i)\alpha\Upsilon\sqrt{1-i\Upsilon}\sinh\left(Y\sqrt{1+i\Upsilon}\right)-\sqrt{\Upsilon^2+1}\cosh\left(Y\sqrt{1+i\Upsilon}\right)-\alpha\sqrt{1+i\Upsilon}\sinh\left(Y\sqrt{1-i\Upsilon}\right) \\
& +\alpha\sinh\left(H\sqrt{1+i\Upsilon}\right)\sinh\left(H\sqrt{1-i\Upsilon}\right)\left[\sinh\left(Y\sqrt{1-i\Upsilon}\right)\sqrt{1-i\Upsilon}+\sinh\left(Y\sqrt{1+i\Upsilon}\right)\sqrt{1+i\Upsilon}\right] \\
& +\alpha\cosh\left(H\sqrt{1+i\Upsilon}\right)\sinh\left(H\sqrt{1-i\Upsilon}\right)\left[2\sqrt{1+i\Upsilon}+\sinh\left(Y\sqrt{1-i\Upsilon}\right)\sqrt{\Upsilon^2+1}\right]+2\sqrt{\Upsilon^2+1} \\
& -i\sqrt{1+i\Upsilon}\cosh\left(Y\sqrt{1-i\Upsilon}\right)\cosh\left(H\sqrt{1+i\Upsilon}\right)\left[\alpha(\Upsilon-i)\sinh\left(H\sqrt{1-i\Upsilon}\right)+\Upsilon\sqrt{1-i\Upsilon}\right] \\
& +\sqrt{1+i\Upsilon}\cosh\left(H\sqrt{1-i\Upsilon}\right)\cosh\left(H\sqrt{1+i\Upsilon}\right)\left[\alpha(1+i\Upsilon)\sinh\left(Y\sqrt{1-i\Upsilon}\right)+2\sqrt{1-i\Upsilon}\right] \\
& +i\alpha\sqrt{1-i\Upsilon}\cosh\left(H\sqrt{1-i\Upsilon}\right)\left[(i+\Upsilon)\sinh\left((H-Y)\sqrt{1+i\Upsilon}\right)+2\Upsilon\sinh\left(Y\sqrt{1+i\Upsilon}\right)\right] \\
& +i\Upsilon\cosh\left(H\sqrt{1+i\Upsilon}\right)\cosh\left(Y\sqrt{1+i\Upsilon}\right)\left[\sqrt{\Upsilon^2+1}+\alpha\sinh\left(H\sqrt{1-i\Upsilon}\right)\sqrt{1+i\Upsilon}\right] \\
& +\cosh\left(H\sqrt{1-i\Upsilon}\right)\sinh\left(H\sqrt{1+i\Upsilon}\right)\left[(1+i\Upsilon)\sinh\left(Y\sqrt{1-i\Upsilon}\right)+2\alpha\sqrt{1-i\Upsilon}\right] \\
& +\sqrt{\Upsilon^2+1}\cosh\left(H\sqrt{1-i\Upsilon}\right)\left[i\Upsilon\cosh\left(Y\sqrt{1+i\Upsilon}\right)-\cosh\left((H-Y)\sqrt{1+i\Upsilon}\right)\right] \\
& -(1+i\Upsilon)\cosh\left(Y\sqrt{1-i\Upsilon}\right)\sinh\left(H\sqrt{1+i\Upsilon}\right)\sinh\left(H\sqrt{1-i\Upsilon}\right),
\end{aligned}
\tag{A.5.6}
$$

$$
\begin{aligned}
N_{\mathcal{G}}^{B} = \Upsilon \Big\{ & - \cosh\left(Y\sqrt{1-i\Upsilon}\right)\cosh\left(H\sqrt{1-i\Upsilon}\right)\left[\alpha(\Upsilon-i)\sqrt{1-i\Upsilon}\sinh\left(H\sqrt{1+i\Upsilon}\right) - i\sqrt{\Upsilon^2+1}\cosh\left(H\sqrt{1+i\Upsilon}\right) + \Upsilon\sqrt{\Upsilon^2+1}\right] \\
& - \cosh\left(Y\sqrt{1-i\Upsilon}\right)\cosh\left(H\sqrt{1+i\Upsilon}\right)\left[\alpha(\Upsilon-i)\sqrt{1+i\Upsilon}\sinh\left(H\sqrt{1-i\Upsilon}\right) + \Upsilon\sqrt{\Upsilon^2+1}\right] + i\sqrt{\Upsilon^2+1}\cosh\left(Y\sqrt{1-i\Upsilon}\right) \\
& - \alpha\Upsilon\sqrt{1+i\Upsilon}\cosh\left(H\sqrt{1+i\Upsilon}\right)\cosh\left(Y\sqrt{1+i\Upsilon}\right)\sinh\left(H\sqrt{1-i\Upsilon}\right) - \Upsilon\sqrt{\Upsilon^2+1}\cosh\left(H\sqrt{1+i\Upsilon}\right)\cosh\left(Y\sqrt{1+i\Upsilon}\right) \\
& - i\alpha\sqrt{1-i\Upsilon}\sinh\left(H\sqrt{1-i\Upsilon}\right)\sinh\left(Y\sqrt{1-i\Upsilon}\right)\sinh\left(H\sqrt{1+i\Upsilon}\right) + \Upsilon\sqrt{\Upsilon^2+1}\sinh\left(H\sqrt{1-i\Upsilon}\right)\sinh\left(Y\sqrt{1-i\Upsilon}\right) \\
& + 2\alpha\Upsilon\sqrt{1+i\Upsilon}\cosh\left(H\sqrt{1+i\Upsilon}\right)\left[\sinh\left(H\sqrt{1-i\Upsilon}\right) - \sinh\left(Y\sqrt{1-i\Upsilon}\right)\right] + 2\Upsilon\sinh\left(H\sqrt{1+i\Upsilon}\right)\sinh\left(H\sqrt{1-i\Upsilon}\right) \\
& - i\sqrt{\Upsilon^2+1}\cosh\left(H\sqrt{1+i\Upsilon}\right)\sinh\left(H\sqrt{1-i\Upsilon}\right)\sinh\left(Y\sqrt{1-i\Upsilon}\right) + \Upsilon\sqrt{\Upsilon^2+1}\sinh\left(H\sqrt{1+i\Upsilon}\right)\sinh\left(Y\sqrt{1+i\Upsilon}\right) \\
& - 2\Upsilon\cosh\left(\frac{1}{2}(H-2Y)\sqrt{1+i\Upsilon}\right)\sinh\left(H\sqrt{1-i\Upsilon}\right)\sinh\left(\frac{1}{2}H\sqrt{1+i\Upsilon}\right) - \Upsilon\sinh\left(Y\sqrt{1-i\Upsilon}\right)\sinh\left(H\sqrt{1+i\Upsilon}\right) \\
& - i\sinh\left(H\sqrt{1-i\Upsilon}\right)\sinh\left((H-Y)\sqrt{1+i\Upsilon}\right) - i\alpha\sqrt{1-i\Upsilon}\sinh\left(Y\sqrt{1+i\Upsilon}\right) + i\alpha\sqrt{1+i\Upsilon}\sinh\left(Y\sqrt{1-i\Upsilon}\right) \\
& + i\alpha\sqrt{1+i\Upsilon}\sinh\left(H\sqrt{1-i\Upsilon}\right)\left[\sinh\left(H\sqrt{1+i\Upsilon}\right)\sinh\left(Y\sqrt{1+i\Upsilon}\right) - \cosh\left(H\sqrt{1+i\Upsilon}\right)\cosh\left(Y\sqrt{1+i\Upsilon}\right)\right] \\
& - i\Upsilon^2\sinh\left(Y\sqrt{1-i\Upsilon}\right)\sinh\left(H\sqrt{1+i\Upsilon}\right) + i\Upsilon^2\sinh\left(Y\sqrt{1+i\Upsilon}\right)\sinh\left(H\sqrt{1-i\Upsilon}\right) + 2\Upsilon\sqrt{\Upsilon^2+1} \\
& - \cosh\left(H\sqrt{1-i\Upsilon}\right)\left[\alpha\left(\Upsilon+i\right)\sqrt{1-i\Upsilon}\sinh\left((H-Y)\sqrt{1+i\Upsilon}\right) + i\sqrt{\Upsilon^2+1}\cosh\left((H-Y)\sqrt{1+i\Upsilon}\right)\right] \\
& + \alpha\Upsilon\sinh\left(H\sqrt{1+i\Upsilon}\right)\sinh\left(H\sqrt{1-i\Upsilon}\right)\left[\sqrt{1+i\Upsilon}\sinh\left(Y\sqrt{1+i\Upsilon}\right) + \sqrt{1-i\Upsilon}\sinh\left(Y\sqrt{1-i\Upsilon}\right)\right] \\
& + \alpha\Upsilon\sqrt{1+i\Upsilon}\sinh\left(Y\sqrt{1-i\Upsilon}\right) + \alpha\Upsilon\sqrt{1-i\Upsilon}\sinh\left(Y\sqrt{1+i\Upsilon}\right) - i\sqrt{\Upsilon^2+1}\cosh\left(Y\sqrt{1+i\Upsilon}\right) \\
& + \cosh\left(H\sqrt{1-i\Upsilon}\right)\cosh\left(H\sqrt{1+i\Upsilon}\right)\left[\alpha(\Upsilon-i)\sqrt{1+i\Upsilon}\sinh\left(Y\sqrt{1-i\Upsilon}\right) + 2\Upsilon\sqrt{\Upsilon^2+1}\right] \\
& - \Upsilon\cosh\left(H\sqrt{1-i\Upsilon}\right)\left[\sqrt{\Upsilon^2+1}\cosh\left(Y\sqrt{1+i\Upsilon}\right) + 2\alpha\sqrt{1-i\Upsilon}\sinh\left(Y\sqrt{1+i\Upsilon}\right)\right] \\
& + \cosh\left(H\sqrt{1-i\Upsilon}\right)\sinh\left(H\sqrt{1+i\Upsilon}\right)\left[(\Upsilon-i)\sinh\left(Y\sqrt{1-i\Upsilon}\right) + 2\alpha\Upsilon\sqrt{1-i\Upsilon}\right] \\
& + (i-\Upsilon)\cosh\left(Y\sqrt{1-i\Upsilon}\right)\sinh\left(H\sqrt{1-i\Upsilon}\right)\sinh\left(H\sqrt{1+i\Upsilon}\right)\Big\}, \qquad \text{(A.5.7)}
\end{aligned}
$$

$$
\begin{aligned}
D_{\mathcal{G}} = 2\left(1+\Upsilon^2\right)\Big\{&\sqrt{1+\Upsilon^2} + \sqrt{1-i\Upsilon}\cosh\left(H\sqrt{1-i\Upsilon}\right)\left[\alpha\sinh\left(H\sqrt{1+i\Upsilon}\right) + \cosh\left(H\sqrt{1+i\Upsilon}\right)\sqrt{1+i\Upsilon}\right] \\
&+ \sinh\left(H\sqrt{1-i\Upsilon}\right)\left[\sinh\left(H\sqrt{1+i\Upsilon}\right) + \alpha\cosh\left(H\sqrt{1+i\Upsilon}\right)\sqrt{1+i\Upsilon}\right]\Big\},
\end{aligned} \tag{A.5.8}
$$

$$
\begin{aligned}
N_{\mathcal{S}}^{u} = i\sqrt{\Upsilon^2+1}\Big\{&\sqrt{1+i\Upsilon}\sinh\left(Y\sqrt{1-i\Upsilon}\right) - \sqrt{1-i\Upsilon}\sinh\left(Y\sqrt{1+i\Upsilon}\right) \\
&+ \sinh\left(H\sqrt{1-i\Upsilon}\right)\sinh\left(H\sqrt{1+i\Upsilon}\right)\left[\sqrt{1-i\Upsilon}\sinh\left(Y\sqrt{1-i\Upsilon}\right) - \sqrt{1+i\Upsilon}\sinh\left(Y\sqrt{1+i\Upsilon}\right)\right] \\
&+ \cosh\left(H\sqrt{1+i\Upsilon}\right)\cosh\left(H\sqrt{1-i\Upsilon}\right)\left[\sqrt{1+i\Upsilon}\sinh\left(Y\sqrt{1-i\Upsilon}\right) - \sqrt{1-i\Upsilon}\sinh\left(Y\sqrt{1+i\Upsilon}\right)\right] \\
&- \cosh\left(Y\sqrt{1-i\Upsilon}\right)\left[\sqrt{1+i\Upsilon}\sinh\left(H\sqrt{1-i\Upsilon}\right)\cosh\left(H\sqrt{1+i\Upsilon}\right) + \sqrt{1-i\Upsilon}\sinh\left(H\sqrt{1+i\Upsilon}\right)\cosh\left(H\sqrt{1-i\Upsilon}\right)\right] \\
&+ \cosh\left(H\sqrt{1+i\Upsilon}\right)\left[\sqrt{1+i\Upsilon}\sinh\left(H\sqrt{1-i\Upsilon}\right)\cosh\left(Y\sqrt{1+i\Upsilon}\right) + \sqrt{1-i\Upsilon}\sinh\left(H\sqrt{1+i\Upsilon}\right)\cosh\left(H\sqrt{1-i\Upsilon}\right)\right]\Big\},
\end{aligned} \tag{A.5.9}
$$

$$
\begin{aligned}
N_{\mathcal{S}}^{B} = \sqrt{\Upsilon^2+1}\Big\{&\sqrt{1+i\Upsilon}\sinh\left(Y\sqrt{1-i\Upsilon}\right) + \sqrt{1-i\Upsilon}\sinh\left(Y\sqrt{1+i\Upsilon}\right) - \left[\cosh\left(Y\sqrt{1-i\Upsilon}\right) + \cosh\left(Y\sqrt{1+i\Upsilon}\right)\right]\times \\
&\left[\sqrt{1+i\Upsilon}\sinh\left(H\sqrt{1-i\Upsilon}\right)\cosh\left(H\sqrt{1+i\Upsilon}\right) + \sqrt{1-i\Upsilon}\sinh\left(H\sqrt{1+i\Upsilon}\right)\cosh\left(H\sqrt{1-i\Upsilon}\right)\right] \\
&+ \sinh\left(H\sqrt{1+i\Upsilon}\right)\sinh\left(H\sqrt{1-i\Upsilon}\right)\left[\sqrt{1+i\Upsilon}\sinh\left(Y\sqrt{1+i\Upsilon}\right) + \sqrt{1-i\Upsilon}\sinh\left(Y\sqrt{1-i\Upsilon}\right)\right] \\
&+ \cosh\left(H\sqrt{1+i\Upsilon}\right)\cosh\left(H\sqrt{1-i\Upsilon}\right)\left[\sqrt{1+i\Upsilon}\sinh\left(Y\sqrt{1-i\Upsilon}\right) + \sqrt{1-i\Upsilon}\sinh\left(Y\sqrt{1+i\Upsilon}\right)\right]\Big\},
\end{aligned} \tag{A.5.10}
$$

$$
\begin{aligned}
D_{\mathcal{ST}} = 2\Big\{&\Upsilon^2 + 1 + (\Upsilon+i)\cosh\left(H\sqrt{1-i\Upsilon}\right)\left[(\Upsilon-i)\cosh\left(H\sqrt{1+i\Upsilon}\right) - i\alpha\sqrt{1+i\Upsilon}\sinh\left(H\sqrt{1+i\Upsilon}\right)\right] \\
&+\sqrt{1-i\Upsilon}\sinh\left(H\sqrt{1-i\Upsilon}\right)\left[\alpha(1+i\Upsilon)\cosh\left(H\sqrt{1+i\Upsilon}\right) + \sqrt{1+i\Upsilon}\sinh\left(H\sqrt{1+i\Upsilon}\right)\right]\Big\}.
\end{aligned} \tag{A.5.11}
$$

A.6 Extended thermal problem

In this appendix, we solve the extended thermal problem (5.6.8) and (5.6.9) via separation of variables. To ensure that the boundary conditions are homogeneous, we decompose the temperature via

$$T = \hat{T} + T_0, \qquad\qquad T^{\mathrm{s}} = \hat{T}^{\mathrm{s}} + T_0^{\mathrm{s}}, \tag{A.6.1a,b}$$

where T_0 and T_0^{s} are the known quasi-steady solutions (4.3.10), while $\hat{T}$ and $\hat{T}^{\mathrm{s}}$ are unknown time-dependent components. Substituting the temperature decomposition (A.6.1) into the extended problem (5.6.8) and (5.6.9), we find that the time-dependent components in each layer satisfy

$$0 = \frac{\partial^2 \hat{T}}{\partial y^2}, \qquad \text{where } \ 0 < y < h, \tag{A.6.2a}$$

$$\Omega \frac{\partial \hat{T}^{\mathrm{s}}}{\partial t} = \frac{\partial^2 \hat{T}^{\mathrm{s}}}{\partial y^2} - \Omega \frac{k^*}{k^{\mathrm{s}*}} \left(y + h^{\mathrm{s}}\right) C \frac{\partial \boldsymbol{p}}{\partial t}(r, t), \qquad \text{where } \ -h^{\mathrm{s}} < y < 0, \tag{A.6.2b}$$

subject to the boundary conditions

$$\frac{\partial \hat{T}}{\partial y} = 0 \qquad \text{at } \ y = h, \tag{A.6.2c}$$

$$\hat{T} - \hat{T}^{\mathrm{s}} = \frac{\partial \hat{T}}{\partial y} - \frac{k^{\mathrm{s}*}}{k^*} \frac{\partial \hat{T}^{\mathrm{s}}}{\partial y} = 0 \qquad \text{at } \ y = 0, \tag{A.6.2d}$$

$$\hat{T}^{\mathrm{s}} = 0 \qquad \text{at } \ y = -h^{\mathrm{s}}, \tag{A.6.2e}$$

$$\hat{T}^{\mathrm{s}} = F(r, y) \qquad \text{at } \ t = 0, \tag{A.6.2f}$$

where we have defined

$$F(r, y) = f(r, y) - \frac{k^*}{k^{\mathrm{s}*}} \left(y + h^{\mathrm{s}}\right) C \boldsymbol{p}(r, 0) - C T^-(r), \tag{A.6.2g}$$

for an initial condition f.

We pose the eigenfunction expansion

$$\hat{T}^{\mathrm{s}} = \sum_{n \geq 1} a_n(r, t) \sin\left(\left(y + h^{\mathrm{s}}\right) \sqrt{-\lambda_n}\right), \qquad \lambda_n = -\left[\frac{\pi}{h^{\mathrm{s}}} \left(n - \frac{1}{2}\right)\right]^2, \tag{A.6.3}$$

and decompose $(y + h^{\mathrm{s}})$ in this basis via

$$y + h^{\mathrm{s}} = -\sum_{n \geq 1} b_n h^{\mathrm{s}} \sin\left((y + h^{\mathrm{s}})\sqrt{-\lambda_n}\right), \quad b_n = (-1)^n \frac{2}{\pi^2}\left(n - \frac{1}{2}\right)^{-2}. \quad \text{(A.6.4a,b)}$$

Equation (A.6.2b) and boundary condition (A.6.2f) may then be decomposed into

$$\frac{\partial a_n}{\partial t}(r,t) = \frac{\lambda_n}{\Omega} a_n(r,t) + \iota b_n C \frac{\partial p}{\partial t}(r,t), \qquad a_n(r,0) = F_n(r), \qquad \text{(A.6.5a,b)}$$

where

$$F_n(r) = \frac{2}{h^{\mathrm{s}}} \int_{-h^{\mathrm{s}}}^{0} F(r,y) \sin\left((y + h^{\mathrm{s}})\sqrt{-\lambda_n}\right) \mathrm{d}y. \qquad \text{(A.6.6)}$$

Problem (A.6.5) admits the solution

$$a_n(r,t) = F_n(r)\,\mathrm{e}^{\lambda_n t/\Omega} + \iota b_n C \int_0^t \frac{\partial p}{\partial t}(r,s)\,\mathrm{e}^{\lambda_n (t-s)/\Omega}\,\mathrm{d}s. \qquad \text{(A.6.7)}$$

This completes the solution for $\hat{T}^{\mathrm{s}}$. The time-dependent component $\hat{T}$ may be found from (A.6.2d) by calculating $\hat{T}^{\mathrm{s}}$ at $y = 0$. For completeness, we write out the complete solution to the extended thermal model. To this end, it is instructive to define the quantity

$$\Lambda_n = -\lambda_n (h^{\mathrm{s}})^2 = \left[\pi\left(n - \frac{1}{2}\right)\right]^2, \qquad \text{(A.6.8)}$$

which is independent of any system parameters. Then the ratio λ_n/Ω may be expressed as $-\Lambda_n/\Omega^{\mathrm{s}}$, where $\Omega^{\mathrm{s}} = (h^{\mathrm{s}})^2\,\Omega$ as defined in (5.6.7). Similarly, we may write $b_n = (-1)^n 2/\Lambda_n$. The full solution then takes the form

$$T(r,y,t) = (y + \iota)\,C p(r,t) + C T^-(r) - \iota C \nu(r,t) - \zeta(r,t), \qquad \text{(A.6.9a)}$$

$$T^{\mathrm{s}}(r,y,t) = \frac{k^*}{k^{\mathrm{s}*}}\,(y + h^{\mathrm{s}})\,C p(r,t) + C T^-(r) + \sum_{n \geq 1} \sin\left[\frac{y + h^{\mathrm{s}}}{h^{\mathrm{s}}}\pi\left(n - \frac{1}{2}\right)\right] \times \left(F_n(r)\,\mathrm{e}^{-\Lambda_n t/\Omega^{\mathrm{s}}} + (-1)^n \frac{2\iota C}{\Lambda_n} \int_0^t \frac{\partial p}{\partial t}(r,s)\,\mathrm{e}^{-\Lambda_n (t-s)/\Omega^{\mathrm{s}}}\,\mathrm{d}s\right), \qquad \text{(A.6.9b)}$$

where ν reflects the finite thermal storage capacity of the substrate, and ζ contains the initial conditions, defined respectively by

$$\nu(r,t) = \sum_{n\geq 1} \frac{2}{\Lambda_n} \int_0^t \frac{\partial p}{\partial t}(r,s)\, \mathrm{e}^{-\Lambda_n(t-s)/\Omega^{\mathrm{s}}}\, \mathrm{d}s, \quad \zeta(r,t) = \sum_{n\geq 1} (-1)^n F_n(r)\, \mathrm{e}^{-\Lambda_n t/\Omega^{\mathrm{s}}}. \tag{A.6.10a,b}$$

This completes the solution of the extended thermal problem.

References

[1] M. A. Abdou, M. S. Tillack, and A. R. Raffray. Thermomechanical problems in fusion reactor blankets. In *Fourth International Topical Meeting on Nuclear Reactor Thermal Hydraulics (NURETH-4)*, volume 2, 1989.

[2] M. J. Ablowitz and A. S. Fokas. *Complex variables: Introduction and applications*. Cambridge Texts in Applied Mathematics. Cambridge University Press, 2003.

[3] A. Agrachev and M. Sigalotti. On the local structure of optimal trajectories in R^3. *SIAM J. Control Optim.*, 42(2):513–531, 2003.

[4] H. Alfvén. Existence of electromagnetic-hydrodynamic waves. *Nature*, 150(3805):405–406, 1942.

[5] H. Alfvén. *Cosmical eletrodynamics*. The International series of monographs on physics. Clarendon Press, 1950.

[6] J. P. Allain and J. N. Brooks. Lithium surface-response modelling for the NSTX liquid lithium divertor. *Nucl. Fusion*, 51(2):23002, January 2011.

[7] J. P. Allain, M. D. Coventry, and D. N. Ruzic. Collisional and thermal effects on liquid lithium sputtering. *Phys. Rev. B*, 76(20):205434, November 2007.

[8] R. A. Alpher, H. Hurwitz, R. H. Johnson, and D. R. White. Some studies of free-surface mercury magnetohydrodynamics. *Rev. Mod. Phys.*, 32(4):758–769, October 1960.

[9] J. A. E. Andersson, J. Gillis, G. Horn, J. B. Rawlings, and M. Diehl. CasADi: a software framework for nonlinear optimization and optimal control. *Math. Program. Comput.*, 11(1):1–36, 2019.

[10] M. L. Apicella, V. B. Lazarev, I. Lyublinski, G. Mazzitelli, S. V. Mirnov, and A. Vertkov. Lithium capillary porous system behavior as PFM in FTU tokamak experiments. *J. Nucl. Mater.*, 386–388:821–823, 2009.

[11] M. L. Apicella, G. Mazzitelli, V. P. Ridolfini, V. B. Lazarev, A. Alekseyev, A. Vertkov, and R. Zagórski. First experiments with lithium limiter on FTU. *J. Nucl. Mater.*, 363–365:1346–1351, 2007.

[12] N. W. Ashcroft and N. D. Mermin. *Solid state physics.* Saunders College Publishing, 1976.

[13] G. Bartolini, A. Ferrara, and E. Usai. Chattering avoidance by second-order sliding mode control. *IEEE Trans. Automat. Contr.*, 43(2):241–246, 1998.

[14] M. J. Bluck and M. J. Wolfendale. An analytical solution to electromagnetically coupled duct flow in MHD. *J. Fluid Mech.*, 771:595–623, 2015.

[15] J. Blumm, A. Lindemann, B. Niedrig, and R. Campbell. Measurement of selected thermophysical properties of the NPL certified reference material stainless steel 310. *Int. J. Thermophys.*, 28(2):674–682, April 2007.

[16] H. G. Bock and K. J. Plitt. A multiple shooting algorithm for direct solution of optimal control problems. *IFAC Proc. Vol.*, 17(2):1603–1608, 1984.

[17] B. Bonnard and M. Chyba. *Singular trajectories and their role in control theory*, volume 40. Springer, 2003.

[18] R. Bowers. Magnetic susceptibility of copper metal at low temperatures. *Phys. Rev.*, 102(6):1486–1488, June 1956.

[19] S. I. Braginskii. Transport processes in a plasma. *Rev. Plasma Phys.*, 1:205–311, 1965.

[20] W. Braunbek. Eine neue Methode elektrodenloser Leitfähigkeitsmessung. *Zeitschrift für Phys.*, 73(5):312–334, 1932.

[21] C. E. Brennen. *Fundamentals of multiphase flow.* Cambridge University Press, 2005.

[22] L. Bühler. Inertialess magnetohydrodynamic flows in expansions and contractions. *Wissenschaftliche Berichte FZKA*, 6904, 2003.

[23] L. Bühler, S. Horanyi, and E. Arbogast. Experimental investigation of liquid-metal flows through a sudden expansion at fusion-relevant Hartmann numbers. *Fusion Eng. Des.*, 82(15–24):2239–2245, 2007.

[24] L. Bühler and S. Molokov. Magnetohydrodynamic flows in ducts with insulating coatings. Technical report, Kernforschungszentrum Karlsruhe, 1993.

[25] A. T. Burkov, A. Heinrich, P. P. Konstantinov, T. Nakama, and K. Yagasaki. Experimental set-up for thermopower and resistivity measurements at 100-1300 K. *Meas. Sci. Technol.*, 12(3):264, 2001.

[26] H. B. Callen. The application of Onsager's reciprocal relations to thermoelectric, thermomagnetic, and galvanomagnetic effects. *Phys. Rev.*, 73(11):1349–1358, June 1948.

[27] M. Caponigro, R. Ghezzi, B. Piccoli, and E. Trélat. Regularization of chattering phenomena via bounded variation controls. *IEEE Trans. Automat. Contr.*, 63(7):2046–2060, July 2018.

[28] B. A. Carreras. Plasma edge cross-field transport: experiment and theory. *J. Nucl. Mater.*, 337:315–321, 2005.

[29] S. Chandrasekhar. *Hydrodynamic and hydromagnetic stability.* Courier Corporation, 1961.

[30] C. C. Chang and T. S. Lundgren. Duct flow in magnetohydrodynamics. *Zeitschrift für Angew. Math. und Phys. ZAMP*, 12(2):100–114, 1961.

[31] F. L. Chernousko and A. A. Lyubushin. Method of successive approximations for solution of optimal control problems. *Optim. Control Appl. Methods*, 3(2):101–114, 1982.

[32] World Energy Council. *World energy resources.* The World Energy Council, 2016.

[33] R. V. Craster and O. K. Matar. Dynamics and stability of thin liquid films. *Rev. Mod. Phys.*, 81(3):1131–1198, August 2009.

[34] P. A. Davidson. Magnetohydrodynamics in materials processing. *Annu. Rev. Fluid Mech.*, 31(1):273–300, 1999.

[35] P. A. Davidson. *An introduction to magnetohydrodynamics.* Cambridge Texts in Applied Mathematics. Cambridge University Press, 2001.

[36] P. J. Davis and P. Rabinowitz. *Methods of numerical integration.* Dover Publications, second edition, 2007.

[37] H. W. Davison. Compilation of thermophysical properties of liquid lithium. Technical report, Lewis Research Center, NASA, Cleveland, Ohio, 1968.

[38] C. Day. Basics and applications of cryopumps. Technical report, Forschungszentrum Karlsruhe, 2007.

[39] P. J. Dellar. Planar channel flow in Braginskii magnetohydrodynamics. *J. Fluid Mech.*, 667:520–543, 2011.

[40] P. G. Drazin. Stability of parallel flow in a parallel magnetic field at small magnetic Reynolds numbers. *J. Fluid Mech.*, 8(1):130–142, 1960.

[41] P. G. Drazin and W. H. Reid. *Hydrodynamic stability.* Cambridge University Press, 2004.

[42] B. R. Duffy and H. K. Moffatt. A similarity solution for viscous source flow on a vertical plane. *Eur. J. Appl. Math.*, 8(1):37–47, 1997.

[43] T. Eich, B. Sieglin, A. Scarabosio, W. Fundamenski, R. J. Goldston, and A. Herrmann. Inter-ELM power decay length for JET and ASDEX Upgrade: Measurement and comparison with heuristic drift-based model. *Phys. Rev. Lett.*, 107(21):215001, November 2011.

[44] V. A. Evtikhin, I. E. Lyublinski, A. V. Vertkov, V. G. Belan, I. K. Konkashbaev, and L. B. Nikandrov. Calculation and experimental investigation of fusion reactor divertor plate and first wall protection by capillary-pore systems with Lithium. *J. Nucl. Mater.*, 271–272:396–400, 1999.

[45] V. A. Evtikhin, I. E. Lyublinski, A. V. Vertkov, S. V. Mirnov, and V. B. Lazarev. Technological aspects of lithium capillary-pore systems application in tokamak device. *Fusion Eng. Des.*, 56–57:363–367, 2001.

[46] V. A. Evtikhin, I. E. Lyublinski, A. V. Vertkov, S. V. Mirnov, V. B. Lazarev, N. P. Petrova, S. M. Sotnikov, A. P. Chernobai, B. I. Khripunov, V. B. Petrov, D. Y. Prokhorov, and V. M. Korzhavin. Lithium divertor concept and results of supporting experiments. *Plasma Phys. Control. Fusion*, 44(6):955, 2002.

[47] V. A. Evtikhin, I. E. Lyublinski, A. V. Vertkov, V. I. Pistunovich, L. G. Golubchikov, V. M. Korzhavin, V. A. Pozharov, and D. Y. Prokhorov. The liquid lithium fusion reactor. In *Sixteenth Conference Proceedings on Fusion Energy (Montreal, 7–11 October 1996) Vol. 3*, pages 659–665. International Atomic Energy Agency (IAEA), 1997.

[48] V. A. Evtikhin, A. V. Vertkov, I. E. Lyublinski, B. I. Khripunov, V. B. Petrov, and S. V. Mirnov. Research of lithium capillary-pore systems for fusion reactor plasma facing components. *J. Nucl. Mater.*, 307–311:1664–1669, 2002.

[49] P. Falsaperla, A. Giacobbe, S. Lombardo, and G. Mulone. Stability of hydromagnetic laminar flows in an inclined heated layer. *Ric. di Mat.*, 66(1):125–140, 2017.

[50] P. Farrell, Á. Birkisson, and S. Funke. Deflation techniques for finding distinct solutions of nonlinear partial differential equations. *SIAM J. Sci. Comput.*, 37(4):A2026–A2045, 2015.

[51] F. R. Fickett and R. P. Reed. Materials studies for magnetic fusion energy applications at low temperatures II. Technical report, National Bureau of Standards, NBSIR 79-1609, 1979.

[52] P. Fiflis, M. Christenson, M. Szott, K. Kalathiparambil, and D. N. Ruzic. Free surface stability of liquid metal plasma facing components. *Nucl. Fusion*, 56(10):106020, 2016.

[53] L. Fridman and A. Levant. Higher order sliding modes as a natural phenomenon in control theory. In F. Garofalo and L. Glielmo, editors, *Robust Control via Variable Structure and Lyapunov Techniques*, pages 107–133, Berlin, Heidelberg, 1996. Springer.

[54] A. T. Fuller. Study of an optimum non-linear control system. *J. Electron. Control*, 15(1):63–71, 1963.

[55] A. T. Fuller. Further study of an optimum non-linear control system. *J. Electron. Control*, 17(3):283–300, 1964.

[56] D. Gao and N. B. Morley. Equilibrium and initial linear stability analysis of liquid metal falling film flows in a varying spanwise magnetic field. *Magnetohydrodynamics*, 38(4):359–375, 2002.

[57] D. Gao, N. B. Morley, and V. Dhir. Numerical study of liquid metal film flows in a varying spanwise magnetic field. *Fusion Eng. Des.*, 63–64:369–374, 2002.

[58] D. Gao, N. B. Morley, and V. Dhir. Numerical simulation of wavy falling film flow using VOF method. *J. Comput. Phys.*, 192(2):624–642, 2003.

[59] R. A. Gardner and P. S. Lykoudis. Magneto-fluid-mechanic pipe flow in a transverse magnetic field. Part 1. Isothermal flow. *J. Fluid Mech.*, 47(4):737–764, 1971.

[60] R. A. Gardner and P. S. Lykoudis. Magneto-fluid-mechanic pipe flow in a transverse magnetic field Part 2. Heat transfer. *J. Fluid Mech.*, 48(1):129–141, 1971.

[61] L. Garzotti, P. Belo, G. Corrigan, D. Harting, F. Köchl, A. Loarte, E. Militello Asp, V. Parail, R. Ambrosino, M. Cavinato, M. Mattei, M. Romanelli, R. Sartori, and M. Valovič. Integrated core-SOL modelling of fuelling, density control and divertor heat loads for the flat-top phase of the ITER H-mode D-T plasma scenarios. *Nucl. Fusion*, 59(2):26006, December 2018.

[62] D. Giannakis, P. F. Fischer, and R. Rosner. A spectral Galerkin method for the coupled Orr–Sommerfeld and induction equations for free-surface MHD. *J. Comput. Phys.*, 228(4):1188–1233, 2009.

[63] D. Giannakis, R. Rosner, and P. F. Fischer. Instabilities in free-surface Hartmann flow at low magnetic Prandtl numbers. *J. Fluid Mech.*, 636:217–277, 2009.

[64] L. G. Golubchikov, V. A. Evtikhin, I. E. Lyublinski, V. I. Pistunovich, I. N. Potapov, and A. N. Chumanov. Development of a liquid-metal fusion reactor divertor with a capillary-pore system. *J. Nucl. Mater.*, 233:667–672, 1996.

[65] K. Gotoh. Hydromagnetic instability of a free shear layer at small magnetic Reynolds numbers. *J. Fluid Mech.*, 49(1):21–31, 1971.

[66] S. Grandison, D. T. Papageorgiou, and J.-M. Vanden-Broeck. The influence of electric fields and surface tension on Kelvin–Helmholtz instability in two-dimensional jets. *Zeitschrift für Angew. Math. und Phys.*, 63(1):125–144, February 2012.

[67] R. S. Graves, T. G. Kollie, D. L. McElroy, and K. E. Gilchrist. The thermal conductivity of AISI 304L stainless steel. *Int. J. Thermophys.*, 12(2):409–415, March 1991.

[68] D. J. Griffiths. *Introduction to electrodynamics.* Prentice–Hall, 3rd edition, 1998.

[69] H.-J. Güntherodt, H. U. Künzi, R. Müller, and R. Evans. Hall coefficient and electrical resistivity of liquid lithium. *Phys. Lett. A*, 54(2):155–156, 1975.

[70] A. A. Harms, G. H. Miley, K. F. Schoepf, and D. R. Kingdon. *Principles of fusion energy: An introduction to fusion energy for students of science and engineering.* World Scientific, 2000.

[71] R. Hartl, S. Sethi, and R. Vickson. A survey of the maximum principles for optimal control problems with state constraints. *SIAM Rev.*, 37(2):181–218, 1995.

[72] D. E. Hartley and W. Murgatroyd. Criteria for the break-up of thin liquid layers flowing isothermally over solid surfaces. *Int. J. Heat Mass Transf.*, 7(9):1003–1015, 1964.

[73] J. Hartmann. Hg-Dynamics I. Theory of the laminar flow of an electrically conductive liquid in a homogeneous magnetic field. *Math. Meddelelser*, 15(6):1–28, 1937.

[74] J. Hartmann and F. Lazarus. Hg-Dynamics II. Experimental investigations on the flow of mercury in a homogeneous magnetic field. *Math. Meddelelser*, 15(7), 1937.

[75] R. P. Haskett, T. P. Witelski, and J. Sur. Localized Marangoni forcing in driven thin films. *Phys. D Nonlinear Phenom.*, 209(1):117–134, 2005.

[76] V. Hauer, J.-C. Boissin, C. Day, H. Haas, A. Mack, D. Murdoch, R. Lässer, and M. Wykes. Design of the ITER torus prototype cryopump. *Fusion Eng. Des.*, 82(15–24):2113–2119, 2007.

[77] L. J. Haworth and L. D. P. King. The stopping power of lithium for low energy protons. *Phys. Rev.*, 54(1):48–50, July 1938.

[78] W. T. Hicks. Evaluation of vapor-pressure data for mercury, lithium, sodium, and potassium. *J. Chem. Phys.*, 38(8):1873–1880, 1963.

[79] C. Y. Ho and T. K. Chu. Electrical resistivity and thermal conductivity of nine selected AISI stainless steels. Technical report, CINDAS, 1977.

[80] E. Hoashi, S. Yoshihashi-Suzuki, T. Okita, T. Kanemura, H. Kondo, N. Yamaoka, and H. Horiike. Study on formation and development of surface wave of liquid metal lithium jet for IFMIF. *Mech. Eng. J.*, 1(4):TEP0017, 2014.

[81] L. M. Hocking. Spreading and instability of a viscous fluid sheet. *J. Fluid Mech.*, 211:373–392, 1990.

[82] J. T. Holgate, M. Coppins, and J. E. Allen. Electrohydrodynamic stability of a plasma-liquid interface. *Appl. Phys. Lett.*, 112(2):24101, 2018.

[83] R. J. Holroyd and J. S. Walker. A theoretical study of the effects of wall conductivity, non-uniform magnetic fields and variable-area ducts on liquid-metal flows at high Hartmann number. *J. Fluid Mech.*, 84(3):471–495, 1978.

[84] J. D. Huba. NRL: Plasma formulary. Technical report, Naval Research Laboratory, 2004.

[85] J. C. R. Hunt. Magnetohydrodynamic flow in rectangular ducts. *J. Fluid Mech.*, 21(04):577–590, 1965.

[86] J. C. R. Hunt. On the stability of parallel flows with parallel magnetic fields. *P. Roy. Soc. A – Math. Phy.*, 293(1434):342–358, 1966.

[87] J. C. R. Hunt and J. A. Shercliff. Magnetohydrodynamics at high Hartmann number. *Annu. Rev. Fluid Mech.*, 3(1):37–62, 1971.

[88] M. A. Jaworski, T. Abrams, J. P. Allain, M. G. Bell, R. E. Bell, A. Diallo, T. K. Gray, S. P. Gerhardt, R. Kaita, H. W. Kugel, B. P. LeBlanc, R. Maingi, A. G. McLean, J. Menard, R. Nygren, M. Ono, M. Podesta, A. L. Roquemore, S. A. Sabbagh, F. Scotti, C. H. Skinner, V. A. Soukhanovskii, D. P. Stotler, and the NSTX Team. Liquid lithium divertor characteristics and plasma–material interactions in NSTX high-performance plasmas. *Nucl. Fusion*, 53(8):83032, 2013.

[89] M. A. Jaworski, S. P. Gerhardt, N. B. Morley, T. Abrams, R. Kaita, J. Kallman, H. Kugel, R. Majeski, and D. N. Ruzic. Macroscopic motion of liquid metal plasma facing components in a diverted plasma. *J. Nucl. Mater.*, 415(1, Supplement):S985–S988, 2011.

[90] M. A. Jaworski, T. K. Gray, M. Antonelli, J. J. Kim, C. Y. Lau, M. B. Lee, M. J. Neumann, W. Xu, and D. N. Ruzic. Thermoelectric magnetohydrodynamic stirring of liquid metals. *Phys. Rev. Lett.*, 104(9):94503, March 2010.

[91] M. A. Jaworski, A. Khodak, and R. Kaita. Liquid-metal plasma-facing component research on the National Spherical Torus Experiment. *Plasma Phys. Control. Fusion*, 55(12):124040, 2013.

[92] A. R. Kantrowitz, T. R. Brogan, R. J. Rosa, and J. F. Louis. The magnetohydrodynamic power generator–Basic principles, state of the art, and areas of application. *IRE Trans. Mil. Electron.*, MIL-6(1):78–83, January 1962.

[93] H. J. Kelley, R. E. Kopp, and H. G. Moyer. Singular extremals. In Richard Bellman, editor, *Top. Optim.*, volume 31 of *Mathematics in Science and Engineering*, pages 63–101. Elsevier, 1967.

[94] Y. Y. Khine and J. S. Walker. Thermoelectric magnetohydrodynamic effects during Bridgman semiconductor crystal growth with a uniform axial magnetic field. *J. Cryst. Growth*, 183(1):150–158, 1998.

[95] A. C. King, E. O. Tuck, and J.-M. Vanden-Broeck. Air-blown waves on thin viscous sheets. *Phys. Fluids A Fluid Dyn.*, 5(4):973–978, 1993.

[96] A. F. Kolesnichenko. Electromagnetic processes in liquid material in the USSR and East European countries. *ISIJ Int.*, 30(1):8–26, 1990.

[97] M. Kono and P. H. Roberts. Recent geodynamo simulations and observations of the geomagnetic field. *Rev. Geophys.*, 40(4):4–53, 2002.

[98] K. S. Krane. *Introductory nuclear physics.* Wiley, 1987.

[99] S. I. Krasheninnikov. On scrape off layer plasma transport. *Phys. Lett. A*, 283(5–6):368–370, 2001.

[100] D. S. Krasnov, E. Zienicke, O. Zikanov, T. Boeck, and A. Thess. Numerical study of the instability of the Hartmann layer. *J. Fluid Mech.*, 504:183–211, 2004.

[101] J. J. Kriegsmann, M. J. Miksis, and J.-M. Vanden Broeck. Pressure driven disturbances on a thin viscous film. *Phys. Fluids*, 10(6):1249–1255, 1998.

[102] I. A. K. Kupka. The ubiquity of Fuller's phenomenon. In H. J. Sussman, editor, *Nonlinear Control. Optim. Control*, chapter 11, pages 313–350. CRC Press, 1990.

[103] M. Kuramae and M. Suzuki. Two-component heat pipes utilizing the Marangoni effect. *J. Chem. Eng. Japan*, 26(2):230–231, 1993.

[104] A. Kurganov and E. Tadmor. New high-resolution central schemes for nonlinear conservation laws and convection–diffusion equations. *J. Comput. Phys.*, 160(1):241–282, 2000.

[105] J. Lahjomri, K. Zniber, A. Oubarra, and A. Alemany. Heat transfer by laminar Hartmann's flow in thermal entrance region with uniform wall heat flux: the Graetz problem extended. *Energy Convers. Manag.*, 44(1):11–34, 2003.

[106] W. E. Langlois and K. J. Lee. Czochralski crystal growth in an axial magnetic field: effects of Joule heating. *J. Cryst. Growth*, 62(3):481–486, 1983.

[107] J. Larmor. How could a rotating body such as the Sun become a magnet? In *Rep. Br. Assoc. Adv. Sci. 87th Meet. Bournemouth*, pages 159–160. John Murray, 1919.

[108] J. D. Lawson. Some criteria for a power producing thermonuclear reactor. *Proc. Phys. Soc. Sect. B*, 70(1):6, 1957.

[109] L. G. Leal. *Advanced transport phenomena: Fluid mechanics and convective transport processes.* Cambridge University Press, 2007.

[110] D. Lee and H. Choi. Magnetohydrodynamic turbulent flow in a channel at low magnetic Reynolds number. *J. Fluid Mech.*, 439:367–394, 2001.

[111] P. Lehmann, R. Moreau, D. Camel, and R. Bolcato. A simple analysis of the effect of convection on the structure of the mushy zone in the case of horizontal Bridgman solidification. Comparison with experimental results. *J. Cryst. Growth*, 183(4):690–704, 1998.

[112] B. Lehnert. The decay of magneto-turbulence in the presence of a magnetic field and Coriolis force. *Q. Appl. Math.*, 12(4):321–341, 1955.

[113] D. Léonard and N. Long. *Optimal control theory and static optimization in economics*. Cambridge University Press, 1992.

[114] A. Levant. Higher-order sliding modes, differentiation and output-feedback control. *Int. J. Control*, 76(9-10):924–941, 2003.

[115] R. Lewis. Definitions of order and junction conditions in singular optimal control problems. *SIAM J. Control Optim.*, 18(1):21–32, 1980.

[116] Q. Li, L. Chen, C. Tai, and E. Weinan. Maximum principle based algorithms for deep learning. *J. Mach. Learn. Res.*, 18(1):5998–6026, 2017.

[117] C. Liao, M. S. Kazimi, and B. LaBombard. MHD effects on liquid metal film flow. *Nucl. Eng. Des.*, 146(1):325–335, 1994.

[118] D. Liberzon. *Calculus of variations and optimal control theory: A concise introduction*. Princeton University Press, 2011.

[119] O. Lielausis. Liquid metal in a strong magnetic field. In J. Lielpeteris and R. Moreau, editors, *Liquid Metal Magnetohydrodynamics*, pages 3–12. Springer, Dordrecht, 1989.

[120] J. H. Lienhard IV and J. H. Lienhard V. *A heat transfer textbook*. Phlogiston Press, fourth edition, 2018.

[121] D. Lunz and P. D. Howell. Dynamics of a thin film driven by a moving pressure source. *Phys. Rev. Fluids*, 3(11):114801, 2018.

[122] D. Lunz and P. D. Howell. Flow of a thin liquid-metal film in a toroidal magnetic field. *J. Fluid Mech.*, 867:835–876, 2019.

[123] I. Lyublinski, A. Vertkov, S. V. Mirnov, and V. B. Lazarev. Protection of tokamak plasma facing components by a capillary porous system with lithium. *J. Nucl. Mater.*, 463:1156–1159, 2015.

[124] D. J. C. MacKay. *Sustainable energy – without the hot air*. UIT Cambridge, 2009.

[125] H. Madarameb, K. Taghavi, and M. S. Tillack. The Influence of leakage currents on MHD pressure drop. *Fusion Sci. Technol.*, 8(1P2A):264–269, 1985.

[126] C. Marchal. Chattering arcs and chattering controls. *J. Optim. Theory Appl.*, 11(5):441–468, May 1973.

[127] R.A. Matula. Electrical resistivity of copper, gold, palladium, and silver. *J. Phys. Chem. Ref. Data*, 8(4):1147–1298, 1979.

[128] J. C. Maxwell. On physical lines of force. *Philos. Mag.*, 1861.

[129] M. McAsey, L. Mou, and W. Han. Convergence of the forward-backward sweep method in optimal control. *Comput. Optim. Appl.*, 53(1):207–226, September 2012.

[130] J. McDanell and W. F. Powers. Necessary conditions joining optimal singular and nonsingular subarcs. *SIAM J. Control*, 9(2):161–173, 1971.

[131] A. J. Mestel. Magnetic levitation of liquid metals. *J. Fluid Mech.*, 117:27–43, 1982.

[132] G. A. Mesyats and N. M. Zubarev. The Rayleigh–Plateau instability and jet formation during the extrusion of liquid metal from craters in a vacuum arc cathode spot. *J. Appl. Phys.*, 117(4):43302, 2015.

[133] D. H. Michael. Stability of plane parallel flows of electrically conducting fluids. *Math. Proc. Cambridge Philos. Soc.*, 49(1):166–168, 1953.

[134] J. Mikielewicz and J. R. Moszynskl. Minimum thickness of a liquid film flowing vertically down a solid surface. *Int. J. Heat Mass Transf.*, 19(7):771–776, 1976.

[135] G. V. Miloshevsky and A. Hassanein. Modelling of Kelvin–Helmholtz instability and splashing of melt layers from plasma-facing components in tokamaks under plasma impact. *Nucl. Fusion*, 50(11):115005, 2010.

[136] S. V. Mirnov, E. A. Azizov, V. A. Evtikhin, V. B. Lazarev, I. E. Lyublinski, A. V. Vertkov, and D. Y. Prokhorov. Experiments with lithium limiter on T-11M tokamak and applications of the lithium capillary-pore system in future fusion reactor devices. *Plasma Phys. Control. Fusion*, 48(6):821, 2006.

[137] H. K. Moffatt. Reflections on magnetohydrodynamics. In G. K. Batchelor, H. K. Moffatt, and M. G. Worster, editors, *Perspectives in Fluid Dynamics – A Collective Introduction to Current Research*, chapter 7, pages 347–391. Cambridge University Press, 2000.

[138] S. Molokov. Liquid metal flows in manifolds and expansions of insulating rectangular ducts in the plane perpendicular to a strong magnetic field. Technical report, Forschungszentrum Karlsruhe, 1994.

[139] S. Molokov, R. Moreau, and H. K. Moffatt. *Magnetohydrodynamics: Historical evolution and trends*, volume 80 of *Fluid Mechanics and Its Applications*. Springer, 2007.

[140] R. Moreau, O. Laskar, M. Tanaka, and D. Camel. Thermoelectric magnetohydrodynamic effects on solidification of metallic alloys in the dendritic regime. *Mater. Sci. Eng. A*, 173(1):93–100, 1993.

[141] P. Moresco and T. Alboussière. Weakly nonlinear stability of Hartmann boundary layers. *Eur. J. Mech. - B/Fluids*, 22(4):345–353, 2003.

[142] P. Moresco and T. Alboussière. Experimental study of the instability of the Hartmann layer. *J. Fluid Mech.*, 504:167–181, 2004.

[143] T. W. Morgan, A. Vertkov, K. Bystrov, I. Lyublinski, J. W. Genuit, and G. Mazzitelli. Power handling of a liquid-metal based CPS structure under high steady-state heat and particle fluxes. *Nucl. Mater. Energy*, 12:210–215, 2017.

[144] N. B. Morley and M. A. Abdou. Modeling of fully-developed, liquid metal, thin film flows for fusion divertor applications. *Fusion Eng. Des.*, 30(4):339–356, 1995.

[145] N. B. Morley and M. A. Abdou. Study of fully developed, liquid-metal, open-channel flow in a nearly coplanar magnetic field. *Fusion Technol.*, 31(2):135–153, 1997.

[146] N. B. Morley, A. A. Gaizer, and M. A. Abdou. Estimates of the effect of a plasma momentum flux on the free surface of a thin film of liquid metal. *Fusion Eng. Des.*, 28:176–180, 1995.

[147] N. B. Morley and P. H. Roberts. Solutions of uniform, open-channel, liquid metal flow in a strong, oblique magnetic field. *Phys. Fluids*, 8(4):923–935, 1996.

[148] N. B. Morley, S. Smolentsev, and D. Gao. Modeling infinite/axisymmetric liquid metal magnetohydrodynamic free surface flows. *Fusion Eng. Des.*, 63–64:343–351, 2002.

[149] N. B. Morley, S. Smolentsev, R. Munipalli, M.-J. Ni, D. Gao, and M. A. Abdou. Progress on the modeling of liquid metal, free surface, MHD flows for fusion liquid walls. *Fusion Eng. Des.*, 72(1–3):3–34, 2004.

[150] U. Müller and L. Bühler. *Magnetofluiddynamics in channels and containers*. Springer, 2001.

[151] W. Murgatroyd. CXLII. Experiments on magneto-hydrodynamic channel flow. *London, Edinburgh, Dublin Philos. Mag. J. Sci.*, 44(359):1348–1354, 1953.

[152] T. G. Myers. Thin films with high surface tension. *SIAM Rev.*, 40(3):441–462, 1998.

[153] M. D. Nornberg, H. Ji, J. L. Peterson, and J. R. Rhoads. A liquid metal flume for free surface magnetohydrodynamic experiments. *Rev. Sci. Instrum.*, 79(9):94501, 2008.

[154] E. F. Northrup. Some newly observed manifestations of forces in the interior of an electric conductor. *Phys. Rev. (Series I)*, 24(6):474–497, June 1907.

[155] N. Ohno. Plasma detachment in linear devices. *Plasma Phys. Control. Fusion*, 59(3):34007, 2017.

[156] J. Ongena and G. Van Oost. Energy for future centuries – Will fusion be an inexhaustible, safe and clean energy source? *Fusion Sci. Technol.*, 45(2T):3–14, 2001.

[157] M. Ono, R. Majeski, M. A. Jaworski, Y. Hirooka, R. Kaita, T. K. Gray, R. Maingi, C. H. Skinner, M. Christenson, and D. N. Ruzic. Liquid lithium loop system to solve challenging technology issues for fusion power plant. *Nucl. Fusion*, 57(11):116056, 2017.

[158] A. Oron, S. H. Davis, and S. G. Bankoff. Long-scale evolution of thin liquid films. *Rev. Mod. Phys.*, 69(3):931–980, July 1997.

[159] J. R. A. Pearson. On convection cells induced by surface tension. *J. Fluid Mech.*, 4(5):489–500, 1958.

[160] N. Pelekasis and L. Benos. Static arrangement of a capillary porous system (CPS): Modelling. *Fusion Eng. Des.*, 117:180–187, 2017.

[161] E. Platacis, A. Flerov, A. Klukin, S. Ivanov, A. Sobolevs, A. Shishko, L. Zaharov, and M. Gryaznevich. Gravitational flow of a thin film of liquid metal in a strong magnetic field. *Fusion Eng. Des.*, 89(12):2937–2945, 2014.

[162] L. S. Pontryagin, V. G. Boltyanskii, R. V. Gamkrelidze, and E. F. Mishchenko. *The mathematical theory of optimal processes*. John Wiley & Sons, New York, 1962.

[163] W. F. Powers. On the order of singular optimal control problems. *J. Optim. Theory Appl.*, 32(4):479–489, December 1980.

[164] J. Quintans Carou, S. K. Wilson, N. J. Mottram, and B. R. Duffy. Asymptotic and numerical analysis of a simple model for blade coating. *J. Eng. Math.*, 63(2):155, April 2008.

[165] C. B. Reed and P. S. Lykoudis. The effect of a transverse magnetic field on shear turbulence. *J. Fluid Mech.*, 89(1):147–171, 1978.

[166] K.-U. Riemann. The Bohm criterion and sheath formation. *J. Phys. D. Appl. Phys.*, 24(4):493, 1991.

[167] W. Ritchie. Experimental researches in voltaic electricity and electromagnetism. *Philos. Trans. R. Soc. London*, 122:279–298, 1832.

[168] H. M. Robbins. A generalized Legendre-Clebsch condition for the singular cases of optimal control. *IBM J. Res. Dev.*, 11(4):361–372, July 1967.

[169] P. H. Roberts. *An introduction to magnetohydrodynamics*. Longmans, London, 1967.

[170] P. H. Roberts. Magnetohydrodynamics. In D. Gubbins and E. Herrero-Bervera, editors, *Encyclopedia of Geomagnetism and Paleomagnetism*, pages 639–654. Springer, 2007.

[171] P. L. Roe. Characteristic-based schemes for the euler equations. *Annu. Rev. Fluid Mech.*, 18(1):337–365, 1986.

[172] M. Rosenberg, R. D. Smirnov, and A. Yu. Pigarov. On thermal radiation from fusion related metals. *Fusion Eng. Des.*, 84(1):38–42, 2009.

[173] D. N. Ruzic, W. Xu, D. Andruczyk, and M. A. Jaworski. Lithium–metal infused trenches (LiMIT) for heat removal in fusion devices. *Nucl. Fusion*, 51(10):102002, 2011.

[174] H. Schättler and U. Ledzewicz. *Geometric optimal control: Theory, methods and examples*, volume 38. Springer, 2012.

[175] H. Schättler and U. Ledzewicz. Synthesis of optimal controlled trajectories with chattering arcs. *Dynam. Cont. Dis. Ser. B*, 19(1-2):161–186, 2012.

[176] S. Sgobba. Physics and measurements of magnetic materials. Technical report, CERN, 2011.

[177] J. A. Shercliff. Steady motion of conducting fluids in pipes under transverse magnetic fields. *Math. Proc. Cambridge Philos. Soc.*, 49(1):136–144, 1953.

[178] J. A. Shercliff. The flow of conducting fluids in circular pipes under transverse magnetic fields. *J. Fluid Mech.*, 1(06):644–666, 1956.

[179] J. A. Shercliff. Thermoelectric magnetohydrodynamics. *J. Fluid Mech.*, 91(02):231, 1979.

[180] J. A. Shercliff. Thermoelectric magnetohydrodynamics in closed containers. *Phys. Fluids*, 22(4):635–640, 1979.

[181] J. A. Shercliff. Thermoelectric MHD with walls parallel to the magnetic field. *Int. J. Heat Mass Transf.*, 23(9):1219–1228, 1980.

[182] J. A. Shercliff. Non-uniqueness in thermoelectric magnetohydrodynamic heat convection. *Proc. R. Soc. London. A. Math. Phys. Sci.*, 382(1783):273–293, 1982.

[183] Y. Shi, G. Miloshevsky, and A. Hassanein. Boiling induced macroscopic erosion of plasma facing components in fusion devices. *Fusion Eng. Des.*, 86(2):155–162, 2011.

[184] K. Shimokawa, T. Itami, and M. Shimoji. On the temperature dependence of the magnetic susceptibility of liquid alkali metals. *J. Phys. F Met. Phys.*, 16(11):1811–1820, 1986.

[185] P. H. Sidles and G. C. Danielson. Thermal conductivity of metals at high-temperatures. Technical report, Ames Laboratory ISC, 1951.

[186] S. I. Sidorenkov, T. Q. Hua, and H. Araseki. Magnetohydrodynamics and heat transfer benchmark problems for liquid-metal flow in rectangular ducts. *Fusion Eng. Des.*, 27:711–718, 1995.

[187] P. C. Smith. A similarity solution for slow viscous flow down an inclined plane. *J. Fluid Mech.*, 58(2):275–288, 1973.

[188] S. Smolentsev, R. Moreau, L. Bühler, and C. Mistrangelo. MHD thermofluid issues of liquid-metal blankets: phenomena and advances. *Fusion Eng. Des.*, 85(7):1196–1205, 2010.

[189] C. Sozou. On the stability of plane flow of a conducting fluid in the presence of a coplanar magnetic field. *J. Fluid Mech.*, 43(3):591–596, 1970.

[190] J. T. Stuart. On the stability of viscous flow between parallel planes in the presence of a co-planar magnetic field. *P. Roy. Soc. A – Math. Phy.*, 221(1145):189–206, 1954.

[191] V. Surla, M. Tung, W. Xu, D. Andruczyk, M. Neumann, D. N. Ruzic, and D. Mansfield. Seebeck coefficient measurements of lithium isotopes. *J. Nucl. Mater.*, 415(1):18–22, 2011.

[192] H. J. Sussmann. The structure of time-optimal trajectories for single-input systems in the plane: The C^∞ nonsingular case. *SIAM J. Control Optim.*, 25(2):433–465, 1987.

[193] H. J. Sussmann. The Markov–Dubins problem with angular acceleration control. In *Proc. 36th IEEE Conf. Decis. Control*, pages 2639–2643, 1997.

[194] D. K. Sze, R. F. Mattas, A. B. Hull, B. Picologlou, and D. L. Smith. MHD considerations for a self-cooled liquid lithium blanket. *Fusion Sci. Technol.*, 21(3P2B):2099–2106, 1992.

[195] D. J. Temperley and L. Todd. The effects of wall conductivity in magneto-hydrodynamic duct flow at high Hartmann numbers. *Math. Proc. Cambridge Philos. Soc.*, 69(2):337–351, 1971.

[196] L. Todd. Hartmann flow in an annular channel. *J. Fluid Mech.*, 28(2):371–384, 1967.

[197] L. Todd. Magnetohydrodynamic flow along cylindrical pipes under non-uniform transverse magnetic fields. *J. Fluid Mech.*, 31(2):321–342, 1968.

[198] E. Trélat. Optimal control and applications to aerospace: Some results and challenges. *J. Optim. Theory Appl.*, 154(3):713–758, September 2012.

[199] S. M. Troian, E. Herbolzheimer, S. A. Safran, and J. F. Joanny. Fingering instabilities of driven spreading films. *Europhys. Lett.*, 10(1):25–30, September 1989.

[200] D. Tseluiko, M. G. Blyth, D. T. Papageorgiou, and J.-M. Vanden-Broeck. Effect of an electric field on film flow down a corrugated wall at zero Reynolds number. *Phys. Fluids*, 20(4):42103, 2008.

[201] D. Tseluiko, M. G. Blyth, D. T. Papageorgiou, and J.-M. Vanden-Broeck. Electrified viscous thin film flow over topography. *J. Fluid Mech.*, 597:449–475, 2008.

[202] E. O. Tuck and J.-M. Vanden Broeck. Influence of surface tension on jet-stripped continuous coating of sheet materials. *AIChE J.*, 30(5):808–811, 1984.

[203] United Nations, Department of Economic and Social Affairs, Population Division. World urbanization prospects: The 2014 revision. Technical Report ST/ESA/SER.A/366, 2014.

[204] United Nations, Department of Economic and Social Affairs, Population Division. World population prospects: The 2015 revision, key findings and advance tables. Technical Report ESA/P/WP.241, 2015.

[205] V. Utkin and H. Lee. Chattering problem in sliding mode control systems. *IFAC Proc. Vol.*, 39(5):1, 2006.

[206] G. G. van Eden, V. Kvon, M. C. M. van de Sanden, and T. W. Morgan. Oscillatory vapour shielding of liquid metal walls in nuclear fusion devices. *Nat. Commun.*, 8(1):192, 2017.

[207] J.-M. Vanden-Broeck. *Gravity–capillary free-surface flows*. Cambridge Monographs on Mechanics. Cambridge University Press, 2010.

[208] N. Vetcha, S. Smolentsev, and M. Abdou. Linear stability analysis for the hartmann flow with interfacial slip. *Magnetohydrodynamics*, 48(1):147–155, 2012.

[209] R. Vochten and G. Petre. Study of the heat of reversible adsorption at the air-solution interface. II. Experimental determination of the heat of reversible adsorption of some alcohols. *J. Colloid Interface Sci.*, 42(2):320–327, 1973.

[210] A. Vorobev and O. Zikanov. Instability and transition to turbulence in a free shear layer affected by a parallel magnetic field. *J. Fluid Mech.*, 574:131–154, 2007.

[211] A. Wächter and L. T. Biegler. On the implementation of an interior-point filter line-search algorithm for large-scale nonlinear programming. *Math. Program.*, 106(1):25–57, March 2006.

[212] H. J. Weber and G. B. Arfken. *Essential mathematical methods for physicists*. Elsevier Science, 2004.

[213] Q. Wei, M. Eddy, K.-D. Li, and L. Wang. Influence of surface morphology on sputtering yields. *J. Phys. D. Appl. Phys.*, 42(16):165304, July 2009.

[214] T. Weier, V. Shatrov, and G. Gerbeth. Flow control and propulsion in poor conductors. In S. Molokov, R. Moreau, and H. K. Moffatt, editors, *Magnetohydrodynamics: Historical Evolution and Trends*, pages 295–312. Springer, 2007.

[215] J. Wesson. The science of JET. Technical report, JET Joint Undertaking, 2000.

[216] D. G. Whyte, T. E. Evans, C. P. C. Wong, W. P. West, R. Bastasz, J. P. Allain, and J. N. Brooks. Experimental observations of lithium as a plasma-facing surface in the DIII-D tokamak divertor. *Fusion Eng. Des.*, 72(1–3):133–147, 2004.

[217] E. J. Williams. The induction of electromotive forces in a moving liquid by a magnetic field, and its application to an investigation of the flow of liquids. *Proc. Phys. Soc.*, 42(5):466, 1930.

[218] S. K. Wilson, B. R. Duffy, and S. H. Davis. On a slender dry patch in a liquid film draining under gravity down an inclined plane. *Eur. J. Appl. Math.*, 12(3):233–252, 2001.

[219] M. Wischmeier. *Simulating divertor detachment in the TCV and JET tokamaks.* PhD thesis, EPFL, 2005.

[220] W. M. Wonham. Note on a problem in optimal non-linear control. *J. Electron. Control*, 15(1):59–62, 1963.

[221] P. T. Wooler. Instability of flow between parallel planes with a coplanar magnetic field. *Phys. Fluids*, 4(1):24–27, 1961.

[222] B. Xu and M. J. Verstraete. First principles explanation of the positive seebeck coefficient of lithium. *Phys. Rev. Lett.*, 112(19):196603, May 2014.

[223] L. Xu and W. Lan. On the nonlinear stability of plane parallel shear flow in a coplanar magnetic field. *J. Math. Fluid Mech.*, 19(4):613–622, 2017.

[224] W. Xu, D. Curreli, D. Andruczyk, T. Mui, R. Switts, and D. N. Ruzic. Heat transfer of TEMHD driven lithium flow in stainless steel trenches. *J. Nucl. Mater.*, 438:S422–S425, 2013.

[225] C.-S. Yih. Stability of liquid flow down an inclined plane. *Phys. Fluids*, 6(3):321–334, 1963.

[226] A. Ying, A. S. Lavine, and M. Tillack. The effect of Hartmann and side layers on heat transfer in magnetohydrodynamic flow. *Fusion Technol.*, 15(2P2B), 1989.

[227] S. Yoshihashi-Suzuki, H. Sugiura, E. Hoashi, H. Kondo, T. Kanemura, N. Yamaoka, M. Ida, H. Nakamura, K. Nakamura, I. Matsushita, and H. Horiike. Overview: Free surface measurement with renewed nozzle of Osaka Li loop. *Fusion Eng. Des.*, 86(9–11):2577–2580, 2011.

[228] Y. Yuan, B. Xu, B. Q. Fu, H. Greuner, B. Böswirth, H. Y. Xu, C. Li, Y. Z. Jia, S. L. Qu, G.-N. Luo, G. H. Lu, and W. Liu. Suppression of cavitation in melted tungsten by doping with lanthanum oxide. *Nucl. Fusion*, 54(8):83026, 2014.

[229] M. I. Zelikin and V. F. Borisov. *Theory of chattering control: with applications to astronautics, robotics, economics, and engineering.* Birkhäuser Boston, 1994.

[230] L. Zhornitskaya and A. L. Bertozzi. Positivity-preserving numerical schemes for lubrication-type equations. *SIAM J. Numer. Anal.*, 37(2):523–555, 1999.

[231] J. Zhu, E. Trélat, and M. Cerf. Planar tilting maneuver of a spacecraft: Singular arcs in the minimum time problem and chattering. *Discret. Contin. Dyn. Syst. - B*, 21(4):1347–1388, 2016.

[232] J. Zhu, E. Trélat, and M. Cerf. Geometric optimal control and applications to aerospace. *Pacific J. Math. Ind.*, 9(1):8, July 2017.

[233] K. Zniber, A. Oubarra, and J. Lahjomri. Analytical solution to the problem of heat transfer in an MHD flow inside a channel with prescribed sinusoidal wall heat flux. *Energy Convers. Manag.*, 46(7–8):1147–1163, 2005.

[234] G. Z. Zuo, J. S. Hu, J. G. Li, N. C. Luo, L. E. Zakharov, L. Zhang, and A. Ti. First results of lithium experiments on EAST and HT-7. *J. Nucl. Mater.*, 415(1, Supplement):S1062–S1066, 2011.

[235] S. J. Zweben and R. W. Gould. Structure of edge-plasma turbulence in the Caltech tokamak. *Nucl. Fusion*, 25(2):171, 1985.